Nanomaterials and Nanotechnology in 2021

Editors: Khalid Lafdi and Mahendra Rai

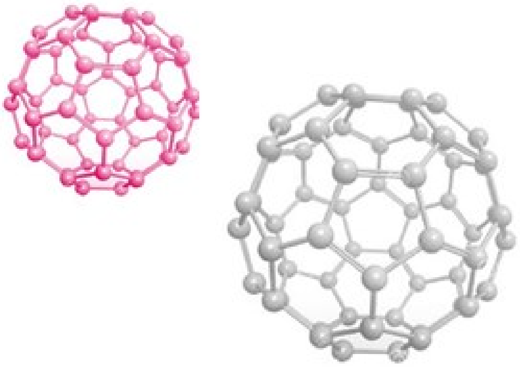

Nanotechnology Centre

Centre for Energy and Environmental Technologies

VSB-Technical University of Ostrava

Ostrava, Czech Republic

ISBN 978-80-248-4585-2

DOI: 10.31490/9788024845852

e-monography

Nanomaterials and Nanotechnology in 2021

Available on:
https://cnt.vsb.cz/en/science-and-research/publications/

Revised by:
Monika Šupová

Edited by:
Khalid Lafdi and Mahendra Rai

Designed by:
Sylva Holešová, Jana Kupková, Marianna Hundáková, Gražyna Simha Martynková,
Daniela Plachá, Karla Čech Barabaszová, Gabriela Kratošová

Published by Vydavatelství VŠB – TU Ostrava
17. listopadu 15/2172, 708 33 Ostrava
Czech Republic

Content

Part 1 – Advances in Nanomaterials and Nanotechnology

Part 2 – Progress in Nanomaterials Characterizations

Part 3 – Nanotechnology in Medicine and Pharmacy

Part 4 – Nanotechnology for Environmental Solution

Preface

It is an indisputable fact that nanotechnology and the concept of nanoparticles have become one of the most frequently used terms of the 21st century. On the other hand, it must be admitted that nanoparticles were here already in the deep past; an example is purple of Cassius, which has been used since the 17th century to make red glass and Meissen porcelain. The first surviving term for this type of particles - colloid - comes from the Greek word for glue and was first used by "the father of colloid chemistry", Italian chemist Francesco Selmi (1817–1881) in 1845 and further in 1861 by Scottish chemist and dialysis discoverer Thomas Graham (1805–1869), who in the study of the rate of diffusion of substances across the parchment membrane denoted a group of substances behaving similarly to glue by this term. In 1906, based on the classification of dispersion systems according to the size of dispersed particles, Wilhelm Oswald (1853–1932) came to the conclusion that the so-called colloidal properties are not exhibited by a certain group of substances, but that any substance can be brought into colloidal state. The development of more sensitive methods and theories enabled the rapid development of colloid chemistry, which was renamed to nanotechnology at the turn of the new millennium.

Oswald's hypothesis is confirmed by the fact that research in the field of various nanomaterials has been growing exponentially in recent years; thus, it can be even said that nanotechnology is changing the world. These materials have found widespread use in many areas of human activity: from energy, construction, various industries, agriculture to cosmetics and healthcare. They are even beginning to be applied for environmental protection. Developments in nanomaterials and nanotechnologies are constantly advancing, with many scientists pushing forward the idea that truly revolutionary nanotechnology products, materials, and applications are within reach. On the other hand, it must be acknowledged that we still know nothing about the wider impacts of the products of these nanotechnologies on the environment and humans, and the discussion on this topic often resembles learned disputations of old university masters.

Based on the latest works of scientists from the Nanotechnology Centre of CEET of the VŠB-Technical University of Ostrava and other colleagues from around the world, a book, which you are currently holding in your hand, has been compiled. It does not aim to solve the problem of whether nanotechnologies and nanomaterials are salvation or destruction for humanity, but seeks to be a valuable contribution discussing the potential of nanoparticles and nanomaterials and deals with new knowledge in the development of advanced nanomaterials and nanotechnologies, their characterization, and applications in nanomedicine and the environment.

Prof. Ing. Daniela Plachá, Ph.D.
head of department

Nanotechnology Centre

Centre for Energy and Environmental Technologies

VSB-Technical University of Ostrava

VSB TECHNICAL UNIVERSITY OF OSTRAVA | ENERGY AND ENVIRONMENTAL TECHNOLOGY CENTRE | NANOTECHNOLOGY CENTRE

Part 1

Advances in Nanomaterials and Nanotechnology

Preparation of light conversion materials from aluminosilicate nanoparticles

M. Čičkan*[1], M. Janek[1,2]

[1]Comenius University in Bratislava; Faculty of Science; Department of Theoretical and Physical chemistry; Slovak Republic;

[2]Slovak Technical University; Faculty of Chemical and Food Technology; Department of Inorganic Materials; Slovak Republic

ABSTRACT

Aluminosilicates are among the hydrated oxide inorganic materials commonly found in nature and can be also prepared synthetically. The structure of aluminosilicates is formed by building blocks network of tetrahedrons and octahedrons. Due to the isomorphous substitutions occurring in the structure, the negative charge of the net oxygen network is changed, and therefore is balanced by cations located close to the structure surface. These cations compensating e.g. negative charge can be exchanged for other cations in cation exchange reaction. The number of exchangeable cations is referred to as cation-exchange capacity. Rare earth elements (REE) are known as suitable phosphors used in light-emitting devices. Their ability to emit light after excitation of their valence electrons and subsequent relaxation to the ground levels was intensively studied many years already. REE show their spectral properties due to the numerous possible energy states of f-orbital levels. In presented study, aluminosilicates were used for REE doping, to modify their optical properties. These materials can be used in several interesting applications, e.g. medicine, photovoltaic panels, etc. In this work, the optical properties of selected aluminosilicates after their REE modification were studied with respect to the changes of their structural and optical properties after their exchange and fixation by material thermal treatment.

Keywords: aluminosilicates; nanoparticles; up-conversion; down-conversion; rare earth elements

INTRODUCTION

The synthetic and natural aluminosilicates were used in this work, isomorphous substitutions occurring in the structure are responsible for the negative charge of the net oxygen network, which is balanced by cations located close to the structure surface. Aluminosilicates form typically microcrystals. However, the variability in structural substitutions and various hydration state of the exchangeable cations are responsible for observable microcrystal disorder, typically investigated by X-ray powder diffraction. This is able to deliver e.g. information about the mean interatomic distances. The content of exchangeable cations is expressed by the value of the cation exchange capacity (CEC). These cations interact with the negatively charged structural oxygens by electrostatic interactions or are strongly bound to the surface by a bridging oxygen [1]. The possibilities of cations adsorption to aluminosilicate surfaces as well as the possibilities of their modification have been widely studied [2]. In dependence of new used cation properties for the cation exchange reaction as published by Janek et al. 2014 [3] (Fig.1), it is possible to obtain new materials with interesting physical-chemical properties. When creating light-emitting materials, it is necessary also pay attention to the material final chemical, photochemical and thermal stability [4].

---

* Corresponding Author´s Email: cickan2@uniba.sk

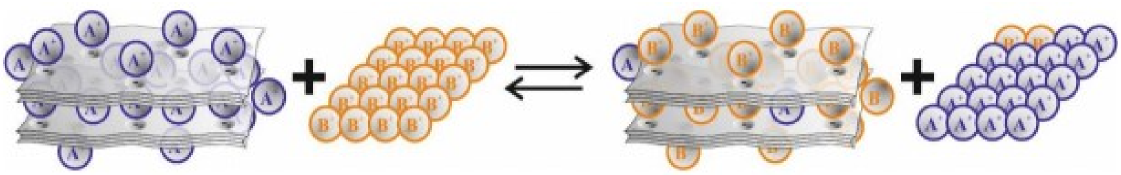

Figure 1. Scheme of cation exchange reaction principle [3].

Lanthanides (REE) are known as phosphors due to their high density of energy states of 4f electron energy levels [5]. The atoms of REE are characterized by the f orbitals being shielded by s and p valence electrons in their pure metallic form, but these are typically used for bonds and forming divalent and/or trivalent cations [6]. Availability of rich 4f electron energy states in REE compounds with energy differences corresponding to the (UV)VIS photons, makes them ideal elements for use in light emitting devices with broad field of application including medical detection applications.

The aim of this work was to verify the suitability of aluminosilicates used as support matrices for REE cations. The ability to incorporate REE cations into the framework of used aluminosilicate samples was verified in this work, including the spectral analysis in the infrared region. By observing the OH structural groups vibration changes caused by the presence of REE cations in used aluminosilicates samples.

EXPERIMENTAL STUDY

To properly estimate the present amounts of REE cations in the interlayer space after cation exchange reaction, it was necessary to quantify the CEC value of the aluminosilicate samples used. The CEC value was quantified by visible spectroscopy (VIS) analysis of blue triethylenetetraamine copper complex before and after its reaction with dispersions of all aluminosilicate samples used.

Samples were prepared from 2 % w/w aluminosilicate dispersions by saturating them several times with solutions containing 0.33 M concentration of the desired REE cations. The modified dispersions were then washed several times with distilled water. In the next step, the samples were dried in an oven at 110 °C, crushed in an agate mortar, sieved through 100 µm rectilinear sieve and stored in a polyethylene flask. A detailed description of CEC, sample preparation and processing has been also described elsewhere [7].

The infrared spectra of modified aluminosilicate powders were measured by Attenuated Total Reflection Fourier Transform Infrared Spectroscopy (ATR-FTIR) and by Raman spectroscopy in the middle-IR region of 4000 to 400 cm^{-1} using a Nicolet 6700 FTIR spectrometer.

RESULT AND DISCUSSION

Using ATR-FTIR spectral measurements and comparing them with the literature data, we approved strong absorption in the range of 3600 - 3200 cm^{-1} caused by stretching water vibration and at 1630 cm^{-1} associated with water bending vibration. The antisymmetric - ν_3 and symmetric - ν_1 stretching modes for differently bounded water molecules and $2\nu_2$ overtone of bending - ν_2 vibration were identified in FTIR spectra of aluminosilicates. The positions of these vibrations are reflecting the strength of hydrogen bonding between water molecules, that is affected by the interlayer cations and the charge density located at the aluminosilicate oxygen surface. The intensity and vibrational energy of these

---

* Corresponding Author´s Email: cickan2@uniba.sk

bands vary with the type of interlayer cation and the water continuous network involved in H-bond formation. The bands observed in material used in our study are in a good agreement with the aluminosilicate vibrations reported in the literature [8] (Fig. 2).

The specific absorption band at 3623 cm^{-1} is observed due to the stretching of the structural OH groups, the band observed at 3417 cm^{-1} belongs to the antisymmetric stretching of the water located on the hydrated interlayer cations. The band at 3241 cm^{-1} represents the symmetric stretching of water located at the hydration shell of exchangeable cations and surface of the aluminosilicate. Accordingly, band at 1631 cm^{-1} represents the deformation vibration of present water. The vibration at 1115 and at 981 cm^{-1} belongs to the structural Si-O stretching vibrations. The bands recorded at 912, 875 and 839 cm^{-1} represent the deformation vibrations of the bridging Al-Al-OH, Al-Fe-OH and Al-Mg-OH groups. Vibration band at 798 cm^{-1} belongs possibly to quartz admixture of this natural sample [9,10].

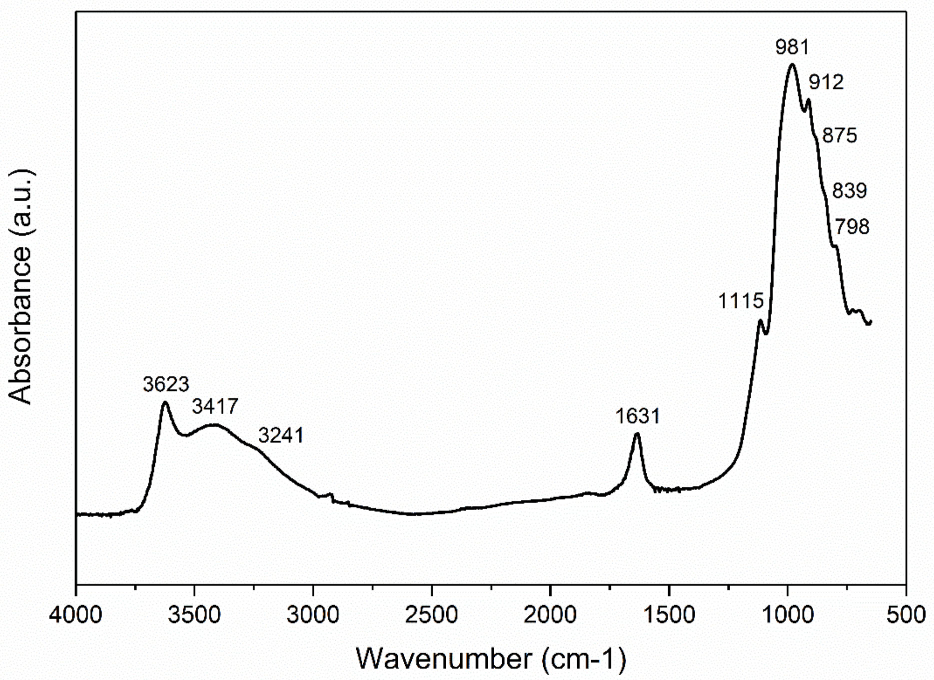

Figure 2. ATR-FTIR spectra of original aluminosilicate sample.

The area size under the bands located in the range of 3420 - 3240 cm^{-1} is associated with water content in the samples influenced also by the amount and type of exchangeable cations. Samples with a higher content of exchangeable cations adsorb more water compared to samples containing fewer exchangeable cations. For the identical material, the increased strength of hydrogen bonding between water molecules is accompanied by a shift of the water stretching bands to lower wavenumbers, while the water bending band is shifted to higher wavenumbers. Here, the cation type having higher surface charge density have increased values of hydration enthalpies, hence shall induce more water bound as compared to cations having the lesser charge. This water binding ability must reflect the cation polarising ability and their hydration number. According to the Xu et al. [11] the polyvalent cations adsorb water molecules more firmly compared to monovalent cations. As the water content in the solvating shells of exchangeable cations in the interlayer increases enhanced intensity of absorption band should be observed. Our results are in good agreement with the discussion above.

The modification of the material using different REE cations caused a different binding of the water content to the analysed samples and affected its structural vibrations (Fig.3). This was reflected in the

---

* Corresponding Author´s Email: cickan2@uniba.sk

observation of decreasing intensity of the deformation vibration of water located at 1631 cm^{-1}. This can indicate the decreased water amount in their hydration sphere even though all of them were trivalent REE cations. All samples were treated by the same manner, but interestingly the Si-O stretching vibration shifted from 981 cm^{-1} to 995 cm^{-1}. At the same time, the deformation vibrations of Al-Al-OH groups shifted from 912 cm^{-1} to 915 cm^{-1}, deformation vibrations of Al-Mg-OH groups shifted from 838 cm^{-1} to 846 cm^{-1} and deformation vibration band of the Al-Fe-OH groups shifted from 798 cm^{-1} to 796 cm^{-1}. Such systematic shift towards higher wavenumbers, indicate more intensive interaction of new REE cations with aluminosilicate oxygen surface than previous cations present.

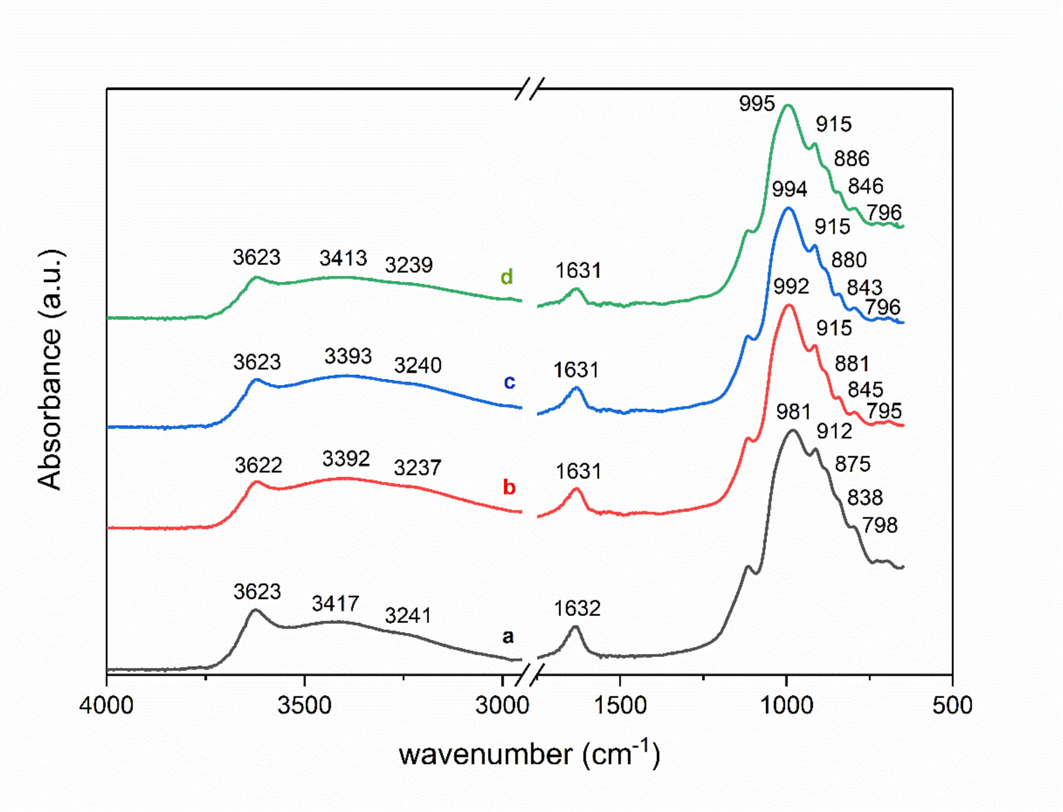

Figure 3. Spectroscopic recording of ATR-FTIR measurements of treated sample materials 1.a) pure sample b) sample modified with REE-1, c) sample modified with REE-2, d) sample modified with REE-1,2.

A lower band intensity was observed in all investigated samples for the stretching vibrations of structural OH groups, which indicate the presence of REE cations in modified samples. The trend of wavenumbers increasing of the absorption bands described above and decreasing the intensities of the stretching vibrations was proportional to the decreasing radius REE used for the modification. We therefore assume a tighter incorporation of smaller REE cations onto the oxygen surface of the aluminosilicate sample used. The investigation of trivalent cations such as the REE cations, which form stronger hydrogen bonds, compared to the monovalent and divalent cations originally present in the interlayer such as sodium or calcium, are in good agreement with the results reported in the literature [8].

CONCLUSION

In this work, we confirmed that the originally occurring cations of the aluminosilicate sample can be successfully replaced by REE cations. The data obtained correlate well with the data reported in the literature [8]. Modification of the materials by REE cations changed the ratios of both the tightly and

---

weakly bound water molecules, in comparison to material starting state. The bands of the original aluminosilicate sample showed a detectable shift to higher wavelengths after aluminosilicate modification by REE elements. Lowering intensities of the stretching vibrations of structural OH groups were also detected. This indicates the existence of stronger interactions between the trivalent cations of the REE elements and the charged aluminosilicate layers. The data are in good agreement with the results of hydrated cations reported in the literature [8]. Trivalent cations with smaller diameters have shown regular behaviour having better selectivity to the aluminosilicate layers compared to the original cations with larger ionic radius. The successful cation exchange is important for preparation of new materials by REE cations.

ACKNOWLEDGMENTS

This work was supported by the Slovak Research and Development Agency under contract No. APVV-18-0075. Support from the VEGA grant agency 1/0227/20 and 1/0342/21, and grant UK/177/2021 are also gratefully acknowledged. Our thanks also belong to Assoc. prof. Dr. Jozef Tatiersky, PhD. for his kind assistance during spectroscopic measurements of samples.

REFERENCES

[1] Finck, N., Dardenne, K., Geckeis, H. 2015. Am(III) coprecipitation with and adsorption on the smectite hectorite. *Chemical Geol*ogy, 409:12-19.

[2] Bradbury, M.H., and Baeyens, B. 2002. Sorption of Eu on Na- and Ca-montmorillonites: experimental investigations and modelling with cation exchange and surface complexation. *Geochimica et Cosmochimica Acta,* 66(13):2325-2334.

[3] Janek, M., Zich, D., Naftaly, M. 2014. Terahertz time-domain spectroscopy response of amines and amino acids intercalated smectities in far-infrared region. *Materials Chemistry and Physics,* 145(3):278-287.

[4] Okada, T., Miyamoto, Y., Kurihara, H., Mochiduki, Y., Katsumi, S., Ito, F. 2020. Electronic interactions between a quaternary pyridyl-β-diketonate and anionic clay nanosheets facilitate intense photoluminescence. *Photochemical & Photobiological Sciences,* 19(10):1280-1288.

[5] Bailey, M.P., Rocks, B.F., Riley, C. 1984. Terbium chelate for use as a label in fluorescent immunoassays. *Analyst,* 109(11):1449-1450.

[6] Sabbatini, N., Guardigli, M., Lehn, J. M. 1993. Luminescent lanthanide complexes as photochemical supramolecular devices. *Coordination Chemistry Reviews,* 123(1-2):201-228.

[7] Čičkan, M., and Janek, M. 2020. Príprava fotoluminiscenčných materiálov s využitím syntetických a prírodných hlinitokremičitanov (Preparation of photoluminescent materials using synthetic and natural aluminosilicates). In Student scientific conference PriF UK 2020: collection of peer-reviewed papers, Bratislava: Univerzita Komenského v Bratislave, pp. 643-648.

[8] Madejová, J., Janek, M., Komadel, P., Herbert, H.J., Moog, H.C. 2002. FTIR analyses of water in MX-80 bentonite compacted from high salinary salt solution systems. *Applied Clay Science,* 20:255-271.

[9] Madejová, J., and Komadel, P. 2001. Baseline studies of the clay minerals society source clays: Infrared methods. *Clays and Clay Minerials,* 49(5):410-432.

[10] Farmer, V.C. 1974. The layer silicates. In: *The lnfrared spectra of minerals*, edited by Farmer, V.C., 331-363. London, UK: Mineralogical Society.

[11] Xu, W., Johnson, C.T., Parker, P., Agnew, S.F. 2000. Infrared study of water sorption on Na-, Li-, Ca-, and Mg-exchanged (Swy-1 and Saz-1) montmorillonite. *Clays and Clay Minerals,* 48:120-131.

---

* Corresponding Author´s Email: cickan2@uniba.sk

Development studies of silver nanocomposite-based sensors for acid penetration

***Q. Fang**[*1], K. Lafdi*[1,2]

[1]Chemical and Materials Engineering Department University of Dayton, Dayton, OH 45469-USA;

[2]Department of Mechanical and Construction Engineering, Northumbria University, Newcastle upon Tyne, UK

ABSTRACT

Polymer composites are widely used to store liquid chemicals. Monitoring their structural health has attracted a lot of attention recently. The geometry of nanomaterial in polymer composites plays an important role in affecting the penetration progress, thus altering the durability of polymer composite. In this study, the silver nanocomposite-based SHM sensors are designed to detect the progress of chemical diffusion and material degradation as a function of time. A comparison between the AgNW sensor and AgNP sensors is used to study the geometry of silver nanomaterial's effect on acid penetration. It appeared that the SHM sensors' resistance decrease in three stages with the diffusion time increase. Moreover, with the volume percentage of silver nanomaterial increase, the response time decrease. And the AgNW based sensors have shown a shorter response time. An aggregation model was developed to better understand the nanomaterial's geometry effect on acid penetration progress.

Keywords: silver nanocomposite; sensors; acid penetration; structural health monitoring

INTRODUCTION

Structural health monitoring is a critical research area in polymer composite applications [1-3]. The lifetime of composite containers for chemicals like acid attracts attention recently [4, 5]. The acid diffusion mechanism is studied by many groups, and the sensors are used to monitor the structural health monitoring of composite [6-9]. The electrical network affects the sensing behavior a lot, and our group's previous work on CNT sensing behavior could not be well interpreted [10]. The CNT was so flexible and entangled then formed a complex electrical network; thus, the simulation results on a simple geometry-formed electrical network were hard to explain the complex experimental result. Compare to CNT, AgNW is much stiff, and its geometry is simple, thus a better choice to study this problem. This study carried out work on the comparison of AgNW and AgNP at various concentrations experimentally and numerically. A simulation was carried out to better understand the effect of nanofillers' geometry and concentration on sensing behavior.

EXPERIMENTAL/THEORETICAL STUDY

1. Preparation of nanocomposite sensors

Epon 862 (epoxy) and Jeffamine D230 (hardener) were used to prepare the epoxy resin system, and the ratio of epoxy to hardener was 20:7. As shown in figure 1, the procedure of preparing sensors was strictly followed as below: (1) Calculated amount Ag nanofillers and 5 g acetone were added in 20 g epoxy and stirred for 3 hours; (2) 7 g Jeffamine D230 was added in the solution and stirred for 75 minutes; (3) In 20 minutes, the mixed solution was used to form a layer by layer structure with a copper electrode inserted; (4) The sensors were cured in a vacuum bay for three days. Non-woven fabric layers were used in constructing the layer-by-layer structure and keep the copper electrode at the center of the sensor.

---

* Corresponding Author´s Email: fangq1@udayton.edu

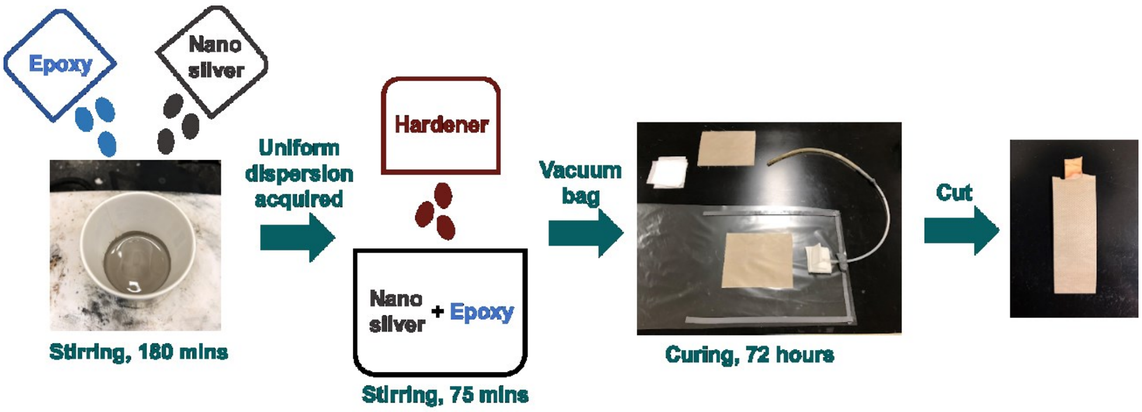

Figure 1. Schematic illustration of silver nanocomposite sensor.

2. Testing method and characterization

A Phenom desktop SEM (15kv, Pro X, Phenom) was used to characterize the morphology of Ag nanofillers and sensors. The wide-angle X-ray diffraction (WAXD, Smartlab X-ray diffractometer, Rigaku) was used to examine the crystallinity of AgNW and AgNP. As shown in figure 2, a sensing system was built by connecting a KEITHLEY 2700 Multimeter, a signal recording software, and the experimental part. The experimental part consisted of the sensor, the copper electrode, and a 1 M H_3PO_4 solution in a beaker. The recording intervals were 1s. 180 to 300 minutes was needed for the resistance to decrease to the lowest value (1 kΩ in this study), which means the sensor was completely degraded.

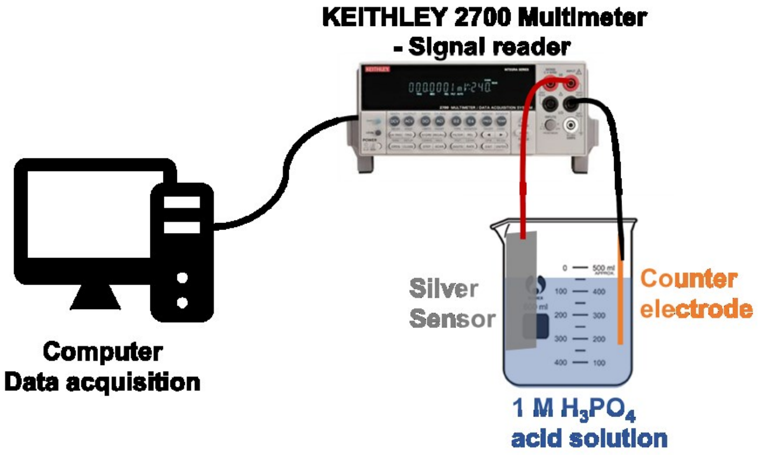

Figure 2. Schematic illustration of the testing system.

3. Theoretical study

The modeling work is based on Fick's second law. The equation is shown below.

$$\partial \Phi \partial d = De2t2 \qquad (1)$$

φ is the concentration of ion, *d* is the thickness of a calculated layer, *t* is the time, *De* is the effective diffusion coefficient of ion in the composite.

---

* Corresponding Author´s Email: fangq1@udayton.edu

The Fricke-Hamilton-Crosser model is used to study the nanofiller's shape effect on Effective diffusion coefficient, thus the acid penetration process. Part a and part b are polymer matrix and nanofiller. The *De* can be interpreted as:

$$De=xva\phi-1+\phi+xva1-\phi+\phi+xDb \quad (2)$$

D_b is the diffusion coefficient of part b, v_a is the volume percentage of part at. x is a function of D_a/D_b, and ϕ equals D_a/D_b. An empirical relationship was applied, and the sphericity of a particle is used to describe x. ϕ was set as 100 to obtain a clear observation on geometry effect on effective diffusion coefficient.

RESULTS AND DISCUSSION

1. Morphology

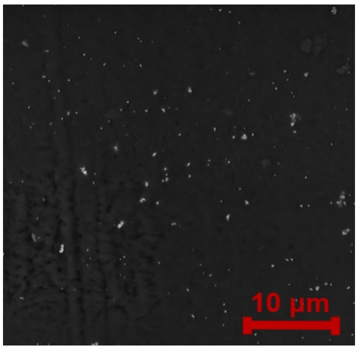

Figure 3. SEM image of silver sensors surface.

In figure 3, a good dispersion of silver nanofiller is shown, and tiny aggregation is obvious, which will affect the acid penetration process.

2. Experimental and modeling result

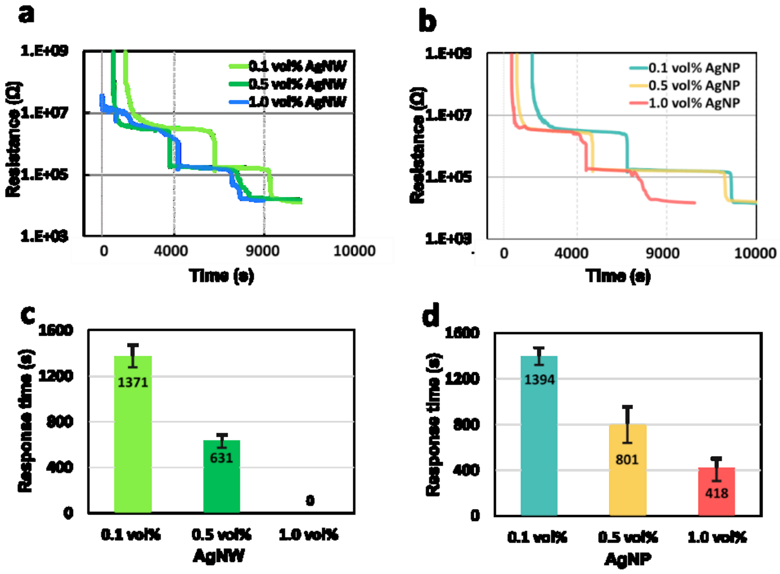

Figure 4. The recorded resistance of (a) AgNW sensors, (b) AgNP sensors; The response time of (c) AgNW sensors, (d) AgNP sensors.

---

* Corresponding Author´s Email: fangq1@udayton.edu

As shown in Figures 4(a), (b), the silver nanocomposite sensors clearly exhibited three stages in the electrical resistance-time curve. According to our group's previous study, the three stages can be caused by different ion diffusion processes [10]. The first drop and stage were caused by a typical ion diffusion and led to the resistance change, and the second and third stages did not appear as the nanofiller's concentration increase in carbon nanocomposite sensors. This can be affected by the easy entanglement and aggregation of carbon nanomaterial, thus affect the result. In this work, the 2nd and 3rd stages appeared with the concentration increase, which highly approved the ion stages guess, and the conductivity of nanocomposite can be treated as an important indicator for structural health monitoring. Compare to carbon nanomaterial, the AgNP has a low structure aggregation, the AgNW is stiff, and the network is formed by wire overlapping, not the entanglements.

In figure 4 (c), (d), the response time decreases with the nanosilver concentration increase, and the AgNW sensors had a shorter response time than AgNP sensors. With the concentration increase, the difference between the AgNW sensor and AgNP sensors becomes bigger. At 1.0 vol%, the response time of AgNW sensors is 0 seconds, and the response time of AgNP sensors is still 418±101 seconds. The conductive network can be formed in 1 vol% AgNW sensor, which provided the conductive pathway for the ions, lead to 0 seconds response time. However, the concentration is still relatively low, and the number of conductive pathways is lack, then the resistance of AgNW sensors was still as high as 3.5×10^{8} Ω. With diffusion processing, more pathways are formed, thus decrease the electrical resistance.

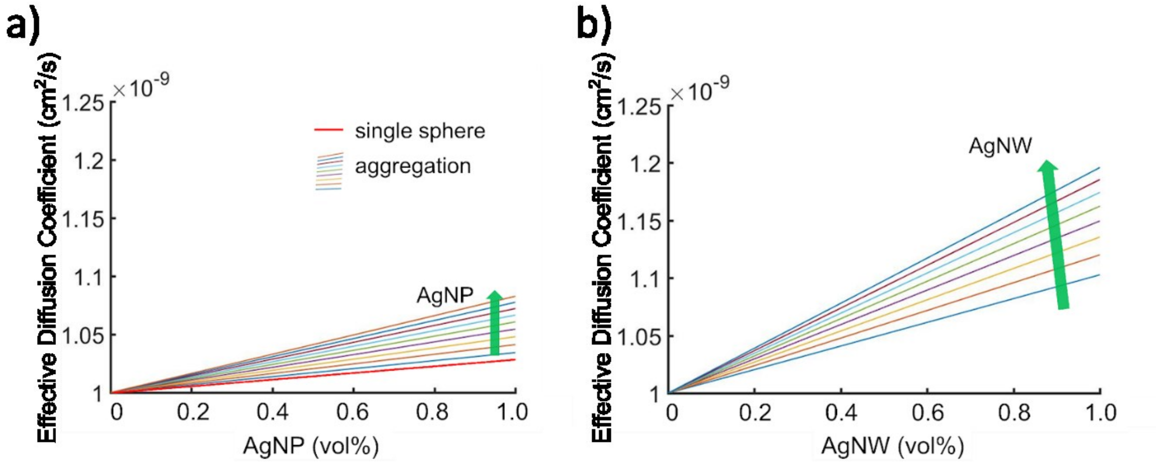

Figure 5. The nanofiller's geometry effect on effective diffusion coefficient. The arrow shows the aspect ratio of AgNP aggregation increment and aspect ratio increment of AgNW. (a) AgNP aggregation's aspect ratio 4 to 20 with an interval of 2; (b) AgNW's aspect ratio 30 to 100 with an interval of 10.

In figure 5(a), the increment of the effective diffusion coefficient is dominant as the aspect ratio of AgNP aggregation increasing. The red line at the bottom shows that no aggregation nanofiller's effective diffusion coefficient is the lowest. In other words, the sphere particle nanofiller's sensor will have the slowest acid penetration and longest response time compared to other shapes. Moreover, the AgNP aggregation will increase the acid diffusion. The aspect ratio is an important factor. However, acid diffusion was affected by many factors. In general, with AgNP aggregation size increase, the number of particles decreases at a certain concentration. According to our previous work, with the aggregation size increasing, the probability of forming a network increase and decrease [11]. The factor is that the anisotropic property of aggregation is dominant while the aggregation size is very small. It is hard to interpret a comprehensive statement for aggregation's overall effect on acid diffusion. However, the aggregation increases the acid diffusion by its shape. In figure 5(b), the increment of the effective diffusion coefficient is significant as the aspect ratio of AgNW increases. The higher effective diffusion coefficient at 1 vol% is one factor that affects the ion diffusion, which confronts to the experiment result.

The average length of AgNW used is 15±5 µm, and average diameter is 0.15 µm, and the simulation is done within this aspect ratio range.

CONCLUSION

In this study, the AgNW nanocomposite sensor and AgNP nanocomposite sensor are used to study the geometry of nanofiller's effect on acid penetration. The experimental result shows that the AgNW sensor has a shorter response time compare to the AgNP sensor, and with the concentration increase, the difference becomes dominant. The modeling work shows that the AgNP aggregation will accelerate the acid penetration, and the AgNW has a much higher effective diffusion coefficient which needs a shorter time to get a response. Moreover, the acid diffusion process is determined by a lot of factors. With some interesting findings during the study, we plan to explore the thickness's effect on acid diffusion. With more research on this problem, this type of sensor will become more reliable, and the application becomes much clear.

ACKNOWLEDGMENTS

We gratefully thank Chang Liu (Lerner Research Institute, Cleveland Clinic Foundation) for his help in the simulation.

REFERENCES

[1] Rashetnia, R., Hallaji, M., Smyl, D., Seppänen, A., Pour-Ghaz, M. 2017. Detection and localization of changes in two-dimensional temperature distributions by electrical resistance tomography. *Smart Materials and Structures,* 26:115021.

[2] Diamanti, K., and Soutis, C. 2010. Structural health monitoring techniques for aircraft composite structures. *Progress Aerospace Sciences,* 46:342-352.

[3] Chiacchiarelli, L.M., Rallini, M., Monti, M., Puglia, D., Kenny, J.M., Torre, L. 2013. The role of irreversible and reversible phenomena in the piezoresistive behavior of graphene epoxy nanocomposites applied to structural health monitoring. *Composites Science and Technology,* 80:73-79.

[4] Lindgren, M., Wallin, M., Kakkonen, M., Saarela, O., Vuorinen, J. 2016. The influence of high-temperature sulfuric acid solution ageing on the properties of laminated vinyl-ester joints. *International Jouurnal of Adhesion and Adhesives,* 68:298-304.

[5] Liu, C., Fang, Q., Lafdi, K. 2020. Novel wireless sensing design for composite durability study. *Composites Communications,* 22:100511.

[6] Abacha, N., Kubouchi, M., Sakai, T., Tsuda, K. 2009. Diffusion behavior of water and sulfuric acid in epoxy/organoclay nanocomposites. *Journal of Applied Polymer Science,* 112:1021-1029.

[7] Chanakul, A., Traiphol, R., Traiphol, N. 2016. Colorimetric sensing of various organic acids by using polydiacetylene/zinc oxide nanocomposites: Effects of polydiacetylene and acid structures. *Colloids and Surfaces A – Physicochemical and Engineering Aspects,* 489:9-18.

[8] Luo, Y., Lin, Z., Guo, G. 2019. Biodegradation assessment of poly (lactic acid) filled with functionalized titania nanoparticles (PLA/TiO 2) under compost conditions. *Nanoscale Research Letters,* 14:1-10.

[9] Liu, C., Sergeichev, I., Akhatov, I., Lafdi, K. 2018. CNT and polyaniline based sensors for the detection of acid penetration in polymer composite. *Composites Science and Technology,* 159:111-118.

[10] Liu, C., Lafdi, K., Chinesta, F. 2020. Durability sensor using low concentration carbon nano additives. *Composites Science and Technology,* 195:108200.

[11] Fang, Q., and Lafdi, K. 2021. Effect of nanofiller morphology on the electrical conductivity of polymer nanocomposites. *Nano Express,* 2:010019.

---

* Corresponding Author´s Email: fangq1@udayton.edu

Fabrication and characterization of graphene-based de-icing heater

A. Muhsan* [1,2], ***K. Lafdi***[1,3]

[1]University of Dayton, Dayton, Department of Chemical and Materials Engineering, OH, 45469, USA;
[2]University of Technology, Department of Materials Engineering, Baghdad, 10066, Iraq;
[3]Northumbria University, Department of Mechanical Engineering, Newcastle upon Tyne, NE1 8ST, UK

ABSTRACT

In this study, graphene-based paper was utilized as a potential de-icing material. Vacuum bagging technique was used to fabricate the composite panel which consisted of graphene-based paper and epoxy/glass fiber. The techniques were used to fabricate graphene-based paper were chemical vapor deposition (CVD) and hot-pressing techniques. Scanning electron microscopy (SEM), optical microscopy, X-ray diffraction and Raman spectroscopy were used to characterize graphene based paper and composite panels. The thermal conductivity and electrical conductivity were measured for graphene-based paper. The temperature distribution in the composite panel during de-icing tests was studied using infrared thermal imaging. The de-icing test based on the joule heating of the composite panel by applying electrical potential. Various electrical potential applied to the composite panel to investigate the role of potential applied on the de-icing process. Based on the results, the optimum potential applied 5 V was sufficient to remove ice from panel's surface with low power consumption. The temperature profile of composite panels showed higher temperature for composite panel of CVD graphene-based paper compared by hot pressing sample because of higher in-plane thermal conductivity for CVD graphene-based paper.

Keywords: de-icing technique; graphene-based paper; composite panel; Joule heating

INTRODUCTION

Aeronautical structures may fail because of ice accumulation that lead to aerodynamic degradation [1]. With the accumulation of ice onto structures, the weight and wing surface roughness increase, which not only affect the aerodynamic performance but also induces air foil distortion and high energy consummation. Several thermal, chemical and mechanical methods have been used to eliminate ice accumulative such as chemical fluid system, pneumatic boots, electro impulsive, hot air system, ultrasound system, microwave technology and electro-thermal de-icing system [2-5]. The most effective technique is the electro-thermal de-icing due to its ability to control the temperature and heat dissipation by joule heating [6]. The electrothermal de-icing system is one of the most promising de-icing systems for polymer composites, as it doesn't cause delamination and damage to composite structure [7]. Many studies have reported using of conductive polymers with metals and carbons additives. However, they showed low thermal and electrical conductivity and higher energy consumption [8] is still an issue. Various materials used as heating element to enhance the performance of de-icing technique including carbon nanotubes (CNTs) [9], graphene [10], carbon fiber [11], sprayable metal layer [12], electro-conductive textile [13] and constantan wire [14]. Delamination of composite panel is the main issue in using metallic films and wires despite higher thermal conductivity. Therefore, it is required to use conductive material that can provide excellent electro-thermal properties as well as can achieve desired temperature without jeopardizing the mechanical and thermal properties of composites. Unique electro-thermal properties of carbon nanomaterials make them potential heating element materials for de-icing. The structures of graphite derivatives papers are designed by controlling stacking processes and assembling orientations of the multilayers; therefore, these materials can bear relatively large deformations with outstanding flexibility and mechanical robustness [15]. Currently, 2D graphite derivatives films can be directly fabricated by chemical vapor deposition process [16], oxide paper

---

* Corresponding Author´s Email: muhsana1@udayton.edu

reduction [17], directly aqueous dispersion [18], electrophoretic deposition [19], and roll-to-roll producing strategy [20]. Raji et. al. used graphene nanoribbon (GNR) stacks/epoxy composite to enhance the efficiency of de-icing performance. They stated that tunable conductivity of the GNR/epoxy composites and low GNR content were required [21]. Tarfaoui *et al.* utilized CNTs bucky paper as a heating element for preparing composite panel for de-icing. They reported that this self-heating composite provided excellent electric heating properties at different temperature with a rapid heating reaction and structure stability after heating–cooling cycles [22]. Karim *et al.* investigated the role of glass fibers roving coated by graphene ink for de-icing. They reported that low resistance of graphene-based glass roving and efficient heating to a desired temperature at lower power consumption [2]. Vertuccio *et al.* prepared composite panel which consisted of graphene paper/carbon fibers/epoxy. They stated that this carbon heater was very efficient and highly competitive to the current resistive heater [23]. Yao *et al.* investigated the de-icing/anti-icing system using incorporated carbon nanotubes web into carbon reinforced composites. They showed that the high heating rate, reliable and predictable performance and low thermal mass of the CNT web structure were particularly suited to the anti-icing/ de-icing application [24].

Herein we used graphene-based paper as a potential material for de-icing technique and we investigated the role of fabrication method of graphene on the efficiency of composite panels for de-icing process. Also, we studied the optimum potential applied into the composite panel during de-icing technique.

EXPERIMENTAL SETUP

Graphene based paper used as a heating element for composite panel. Two types of graphene papers were made. The first paper uses a high temperature chemical vapor deposition. The process consisted of cracking methane and hydrogen at 1000 °C at reduced pressure of 3 torr followed by a subsequent annealing around 3000 ° C to form graphene-based paper. Hot pressing technique used to prepare graphene-based paper. Exfoliated graphite was dispersed into water with 2% PVA and stirred using both mechanical and ultrasonic stirrings for 2 hours. Once the suspension was homogenized, it was filtered using vacuum filtration method forming an even filtered cake. Then, the cake was hot pressed in silicon mold at temperature of 60 °C and pressure of 80 psi for a period of 30 min. Once the pressure is released, the material appeared very glossy with a metal shiny look. Vacuum bagging technique was utilized to fabricate the composite panel. The curing of composite panel occurred at room temperature for one day. de-icing test included applying an electrical potential through composite panel which covered by ice to show the role of the heating element on the of de-icing process. The composite panels drilled at both edges then screwed to connect the electrical power to the heating element. Figure 1 depicts the experimental setup of de-icing technique which consisted of power supply, composite panel and thermal camera to determine the temperature of composite panel during de-icing process. The composite panel surface covered by ice then applying potential to panel using power supply. The composite panel is heated to remove the ice from panel's surface. Infra-red thermal camera (FLIR) used to study thermal distribution through composite panel at various voltages applied.

---

* Corresponding Author´s Email: muhsana1@udayton.edu

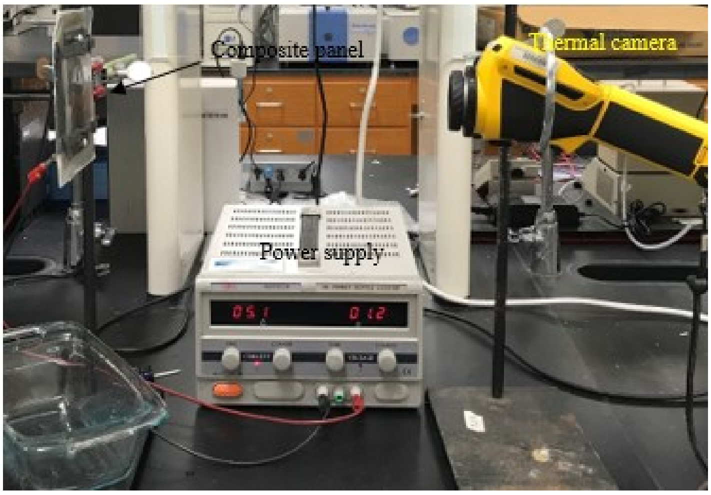

Figure 1. The experimental setup of de-icing test.

The composite panels and graphene-based paper were characterized using scanning electron microscopy (SEM), optical microscopy, X ray diffraction (XRD) and Raman spectroscopy. Also, the thermal conductivity and electrical conductivity of the heating elements determined by in-plane thermal conductivity and chemical analysis technique respectively.

RESULTS AND DISCUSSION

The morphology of graphene-based papers was characterized using SEM. Figure 2(a) shows graphene sheets structure of CVD graphene-based paper. However, a corrugated structure was observed in hot pressing graphene-based paper figure 2(b).

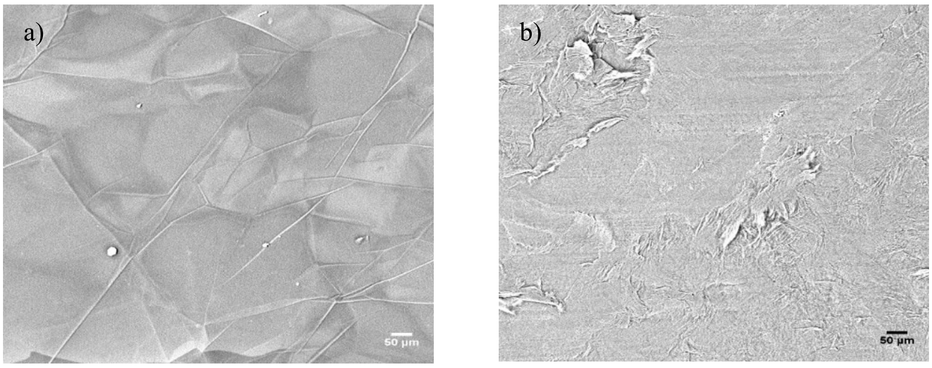

Figure 2. SEM images for graphene-based paper, a) CVD graphene-based paper and b) hot pressing graphene-based paper.

* Corresponding Author´s Email: muhsana1@udayton.edu

Figure 3 shows the images of optical microscopy for cross section of composite panels to indicate the morphology of panels. As shown in figure 3, there are no defects during fabrication technique and graphene-based paper totally adhered to glass fiber/epoxy composite.

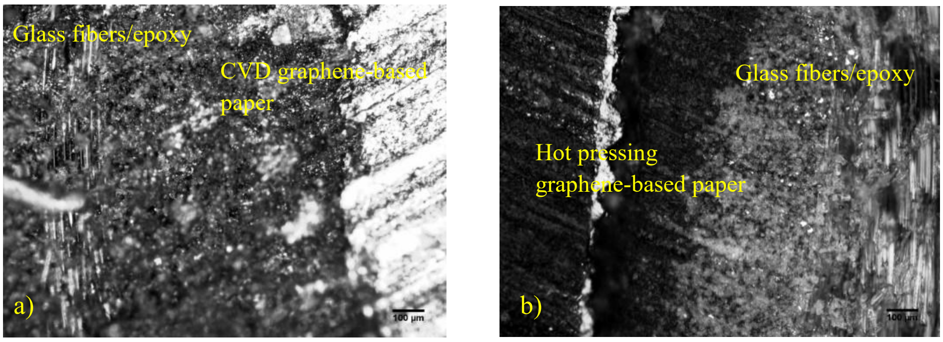

Figure 3. Optical microscopy for graphene-based paper composite panel. a) CVD graphene-based paper and b) hot pressing graphene-based paper.

SEM images of composite panels to indicate graphene-based paper and the glass fiber/epoxy composite as shown in figure 4 the cross section of composite panels. Obviously, the images show the glass fiber/epoxy and graphene-based paper.

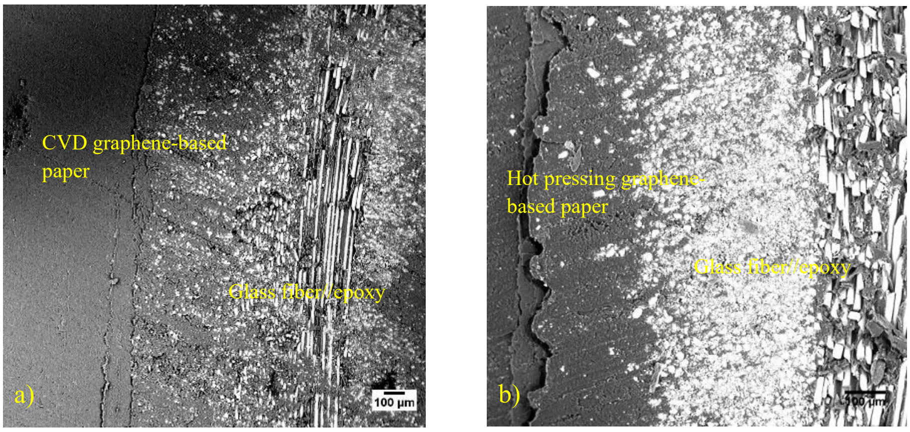

Figure 4. SEM images for cross section of graphene-based paper composite panels. a) CVD graphene-based paper and b) hot pressing graphene-based paper.

---

* Corresponding Author´s Email: muhsana1@udayton.edu

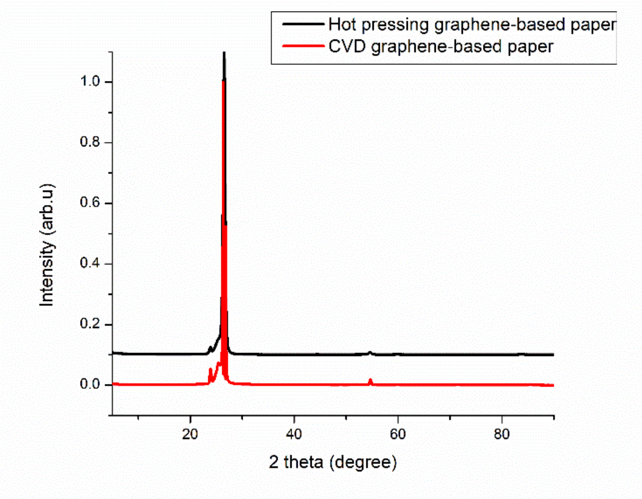

Figure 5. XRD patterns for graphene-based papers.

Figure 5 shows X-ray diffraction patterns for graphene-based papers to indicate the crystallinity of used materials for composite panels. As shown in this figure, the patterns of graphene-based papers have a main peak at 26.5° with d-spacing $0.335nm$.

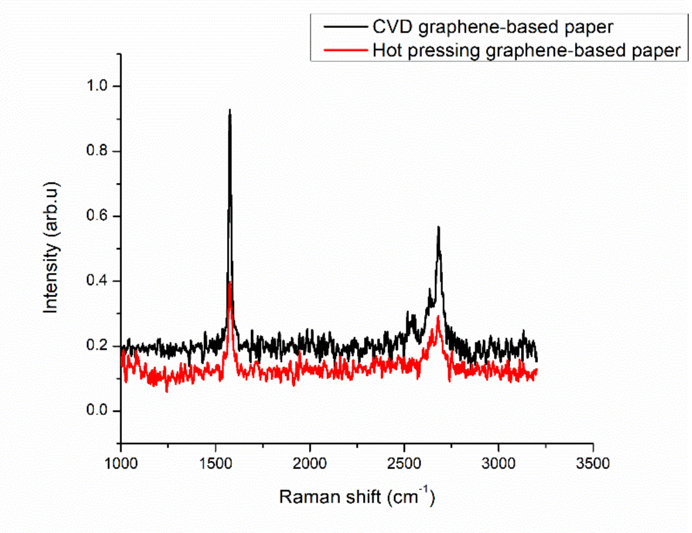

Figure 6. Raman spectrum for graphene-based papers.

The Raman spectrum indicate the quality of carbon materials used in the composite panels. The D peak originates from the breathing mode of six-atom rings and requires a defect for activation, therefore the intensity of the D peak depends on the disorder of the graphene. The 2D peak is the second order of the D peak and the shape of the 2D peak varies with different thicknesses of few layers of graphene sheets. The G peak represents the E_{2g} phonons vibration mode in the center of the Brillouin zone of sp^2 hybrid carbon atom [25]. The spectrum of CVD graphene-based paper shows the main peaks G and 2D at Raman shift 1585 cm^1, 2700 cm^1 respectively which indicated it had high quality due to disappearing the D peak that related to the presence of defects as shown in figure 6. Also, the Raman spectrum for

---

* Corresponding Author´s Email: muhsana1@udayton.edu

hot pressing graphene-based paper shows G and 2D peaks at Raman shift 1580 cm^1, 2700 cm^1 respectively with lower intensity compared by Raman spectrum of CVD graphene-based paper.

The electrical conductivity of graphene-based papers measured using 4-pins method. The electrical conductivity measurements for CVD graphene-based paper and hot-pressing graphene-based paper were 7.8*10^5 S/cm and 4.5*10^4 S/cm, respectively. Also, the electrical resistance measurements for CVD graphene-based paper and hot-pressing graphene-based paper were 0.5*10^{-3} Ω and 1.159*10^{-2} Ω, respectively. Thermal conductivity for graphene-based papers measured using in-plane steady state thermal conductivity device [26]. The measurements of in-plane thermal conductivity of CVD graphene-based paper and hot-pressing graphene-based paper were 1293 W m^{-1} k^{-1} and 983 W m^{-1} k^{-1}, respectively. The high quality and absence of defects for CVD graphene-based paper made it had higher thermal and electrical conductivities compared to hot pressing technique.

The heat was generated when the potential applied to the composite panel due to joule heating. The heat transported in the composite panel through graphene-based paper because of high in-plane thermal conductivity then the heat conducted to the surface of composite panel to melt the accumulated ice. Figures 7 and 8 indicate the role of joule heating for composite panel as a function of potential applied and time.

The potential applied to composite panels was (3,4,5,8,10) V for a period at room temperature to show the thermal distribution through composite panels.

As shown in figure 7 the temperature profile of composite panel is increased proportionally with potential applied. The joule heating of CVD graphene-based paper composite panels had highest temperature at 10 V around 170°F. On the other words, the composite panel reached to suitable temperature to remove ice at a short time as shown in figure 7.

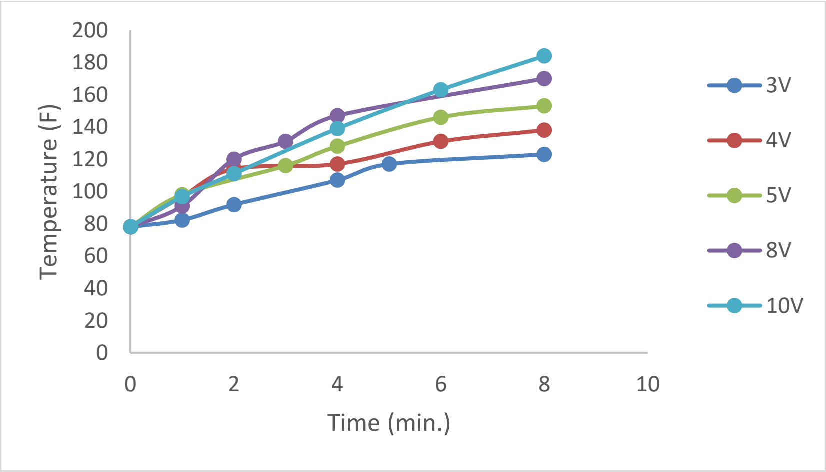

Figure 7. Effect of potential applied on the joule heating of CVD graphene-based paper composite panel.

Figure 8 depicts the temperature profile for hot pressing graphene-based paper / glass fibers/epoxy composite panel. As shown in this figure the temperature increased slightly as the current increased. The temperature profile for hot pressing graphene-based paper at different electrical potential applied (3,4,5,8,10) V showed low temperatures of the surface of composite panel. Due to in-plane thermal conductivity of hot-pressing graphene-based paper is lower than that for CVD graphene-based paper.

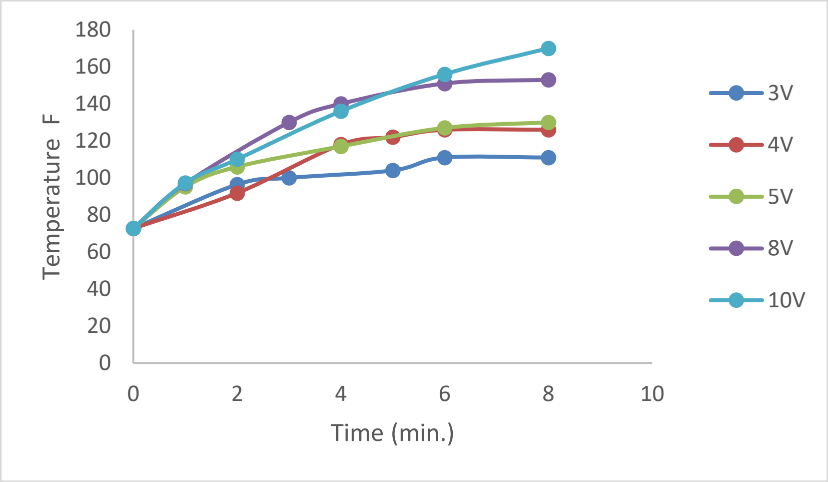

Figure 8. Effect of potential applied on the joule heating of hot-pressing graphene-based paper composite panel.

During the de-icing technique, the joule heating of composite panels started when the current applied to the panel which covered by ice. The mechanism of de-icing technique involved the following stages: stage (1) increasing the temperature of panel's surface gradually at constant current applied, then stage (2) formation interfacial layer between panel's surface and layer of ice which allowed for ice to melt, then stage (3) finally removal ice form panel's surface. Figures 9 and 10 show the temperature profile of de-icing process for composite panels and thermal images for composite panels during de-icing process. It shows the temperature of composite panel before applying potential then increasing temperature of panel's surface at constant potential applied 5V to remove the ice from its surface. Graphene based paper composite panels have lost its temperature when the power supply turns off because of high thermal conductivity of graphene paper.

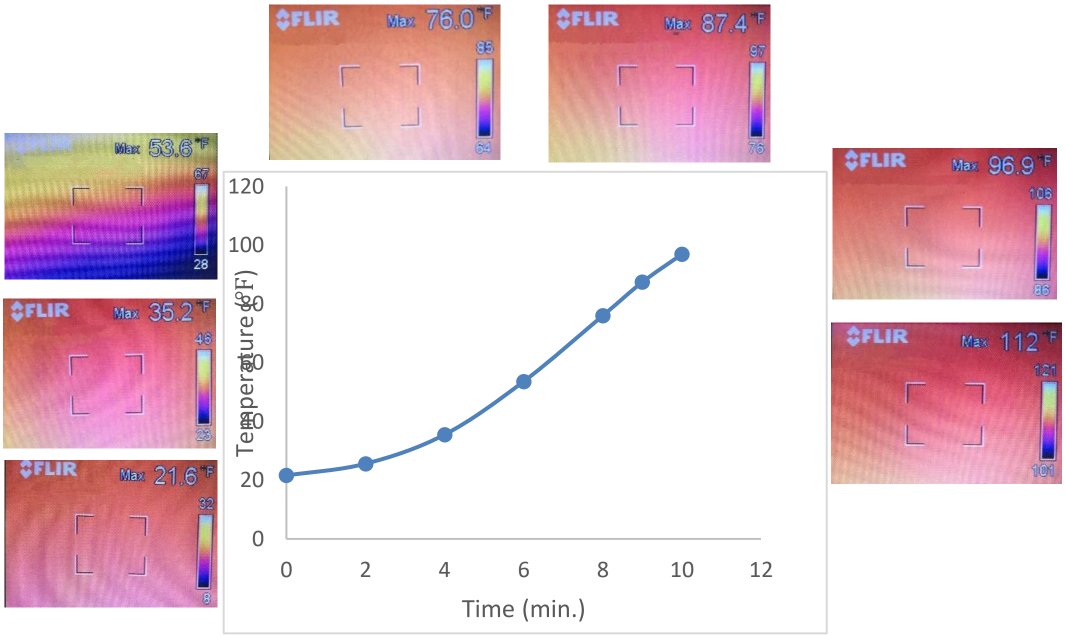

Figure 9. Deicing technique for CVD graphene-based paper composite panel.

---

* Corresponding Author´s Email: muhsana1@udayton.edu

As shown in figure 10 the temperature for surface of hot-pressing graphene-based paper composite panel before applying constant potential 5V was 14.2 F then the temperature of surface increased gradually to remove the ice from the surface. The temperature profile for composite panels showed higher temperature for composite panel of CVD graphene-based paper compared by hot pressing sample because of higher in-plane thermal conductivity for CVD graphene-based paper.

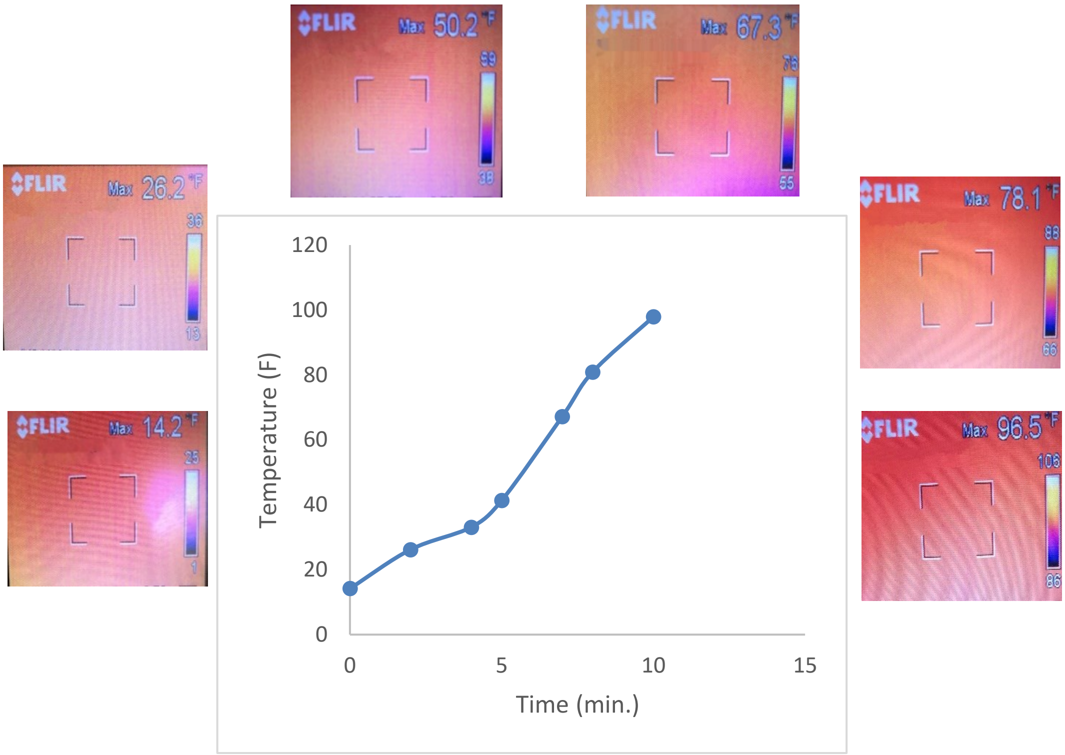

Figure 10. Deicing technique for hot pressing graphene-based paper composite panel.

The efficiency of graphene-based paper composite panel for deicing technique totally based on the in-plane thermal conductivity of graphene paper, current applied and time of deicing process which depended on the thickness of accumulated ice.

CONCLUSION

Composite panels based on graphene-based paper were made in order to improve the mechanism of deicing technique. Vacuum bagging technique was used to fabricate composite panels. CVD graphene-based paper exhibit higher in-plane thermal and electrical conductivities than hot pressing graphene-based paper due to absence of defects. Investigation of effect of potential applied on the joule heating of composite panels showed that the CVD composite panel has higher efficiency than hot pressing composite panel. During deicing test, the temperature of composite panel's surface was increased to melt the ice and uniform temperature distribution along the composite panel was observed.

---

* Corresponding Author´s Email: muhsana1@udayton.edu

Chapter 3

Part 1: Advances in Nanomaterials and Nanotechnology

REFERENCES

[1] Lynch, F.T., and Khodadoust, A. 2001. Effects of ice accretions on aircraft aerodynamics. *Progress in Aerospace Sciences,* 37:669-767.

[2] Karim, N., Zhang, M., Afroj, S., Koncherry, V., Potluri, P., Novoselov, K.S. 2018. Graphene-based surface heater for de-icing applications. *RSC Advances,* 8:16815–16823.

[3] Volman, V., Zhu, Y., Raji A., Genorio, B., Lu, W., Xiang, C., Kittrell, C., Tour, J.M. 2014. Radio-frequency-transparent, electrically conductive graphene nanoribbon thin films as deicing heating layers. *ACS Applied Materials & Interfaces,* 6:298−304.

[4] Fan, S., Jiang, X., Sun, C., Zhang, Z., Shu, L. 2011. Temperature Characteristic of DC Ice-Melting Conductor. *Cold Regions Science and Technology*, 65:29−38.

[5] Gupta, R., Rao, K.D.M., Srivastava, K., Kumar, A., Kiruthika, S., Kulkarni, G.U. 2014. Spray coating of crack templates for the fabrication of transparent conductors and heaters on flat and curved surfaces. *ACS Applied Materials & Interfaces,* 6:13688−13696.

[6] Botura, G.C., Sweet, D., Folsdorf, D. 2005. Development and demonstration of low power electrothermal de-icing system. Meeting paper presented at the 43rd AIAA Aerospace Sciences Meeting and Exhibit, Reno, Nevada, January 10 - 13. https://doi.org/10.2514/6.2005-1460.

[7] Thomas, S.K., Cassoni R.P., MacArthur, C.D. 1996. Aircraft anti-icing and de-icing techniques and modeling. *Journal of Aircraft,* 33:841-854.

[8] Perepelkin, K.E. 2005. Polymer fibre composites, basic types, principles of manufacture, and properties. Part 2. Fabrication and properties of polymer composite materials. *Fibre Chemistry,* 37:381-400. https://doi.org/10.1007/s10692-006-0012-5.

[9] Chu, H., Zhang, Z., Liu, Y., Leng, J. 2014. Self-heating fiber reinforced polymer composite using meso/macropore carbon nanotube paper and its application in deicing. *Carbon,* 66:154-163. https://doi.org/10.1016/j.carbon.2013.08.053.

[10] Sui, D., Huang, Y., Huang, L., Liang, J., Ma, Y., Chen, Y. 2011. Flexible and transparent electrothermal film heaters based on graphene materials. *Small,* 7(22):3186-3192. https://doi.org/10.1002/smll.201101305.

[11] Kim, T., and Chung, D.D.L. 2003. Carbon fiber mats as resistive heating elements. *Carbon,* 41(12):2436-2440. https://doi.org/10.1016/S0008-6223(03)00288-4.

[12] Sloan, J. 2009. 787 integrates new composite wing deicing system. *High Performance Composites,* 17:27-29.

[13] Falzon, B.G., Robinson, P., Frenz, S., Gilbert, B. 2015. Development and evaluation of a novel integrated anti-icing/de-icing technology for carbon fibre composite aerostructures using an electro-conductive textile. *Composites Part. A: Applied Science and Manufacturing,* 68:323-335. https://doi.org/10.1016/j.compositesa.2014.10.023.

[14] Mohseni, M., and Amirfazli, A. 2013. A novel electro-thermal anti-icing system for fiber-reinforced polymer composite airfoils. *Cold Regions Science and Technology,* 87:47-58. https://doi.org/10.1016/j.coldregions.2012.12.003.

[15] Davami, K., Zhao, L., Lu, E., Cortes, J., Lin, C., Lilley, D.E., Purohit, P.K., Bargatin, I. 2015. Ultralight shape-recovering plate mechanical metamaterials. *Nature Communications,* 6(1):10019. https://doi.org/10.1038/ncomms10019.

[16] Kim, K.S., Zhao, Y., Jang, H., Lee, S.Y., Kim, J.M., Kim, K.S., Ahn, J.-H., Kim, P., Choi, J.-Y., Hong, B.H. 2009. Large-scale pattern growth of graphene films for stretchable transparent electrodes. *Nature,* 457(7230):706-710. https://doi.org/10.1038/nature07719.

[17] Dikin, D.A., Stankovich, S., Zimney, E.J., Piner, R.D., Dommett, G.H.B., Evmenenko, G., Nguyen, S.T., Ruoff, R.S. 2007. Preparation and characterization of graphene oxide paper. *Nature,* 448(7152):457-460. https://doi.org/10.1038/nature06016.

[18] Chen, H., Müller, M.B., Gilmore, K.J., Wallace, G.G., Li, D. 2008. Mechanically strong, electrically conductive, and biocompatible graphene paper. *Advanced Materials,* 20(18):3557-3561. https://doi.org/10.1002/adma.200800757.

[19] Yao, Y., Fu, K.K., Yan, C., Dai, J., Chen, Y., Wang, Y., Zhang, B., Hitz, E., Hu, L. 2016. Three-dimensional printable high-temperature and high-rate heaters. *ACS Nano,* 10(5):5272-5279. https://doi.org/10.1021/acsnano.6b01059.

[20] Bae, S., Kim, H., Lee, Y., Xu, X., Park, J.-S., Zheng, Y., Balakrishnan, J., Lei, T., Ri Kim, H., Song, Y.I., Kim, Y.-J., Kim, K.S., Özyilmaz, B., Ahn, J.-H., Hong, B.H., Iijima, S. 2010. Roll-to-roll production of 30-inch graphene films for transparent electrodes. *Nature Nanotechnology,* 5(8):574-578. https://doi.org/10.1038/nnano.2010.132.

---

* Corresponding Author´s Email: muhsana1@udayton.edu

[21] Raji, A.-R. O., Varadhachary, T., Nan, K., Wang, T., Lin, J., Ji, Y., Genorio, B., Zhu, Y., Kittrell, C., Tour, J.M. 2016. Composites of graphene nanoribbon stacks and epoxy for joule heating and deicing of surfaces. *ACS Applied Materials & Interfaces,* 8(5):3551-3556. https://doi.org/10.1021/acsami.5b11131.

[22] Tarfaoui, M., El Moumen, A., Boehle, M., Shah, O., Lafdi, K. 2019. Self-heating and deicing epoxy/glass fiber based carbon nanotubes buckypaper composite. *Journal of Materials Science,* 54(2):1351-1362. https://doi.org/10.1007/s10853-018-2917-9.

[23] Vertuccio, L., De Santis, F., Pantani, R., Lafdi, K., Guadagno, L. 2019. Effective de-icing skin using graphene-based flexible heater. *Composites Part B: Engineering,* 162:600-610. https://doi.org/10.1016/j.compositesb.2019.01.045.

[24] Yao, X., Hawkins, S.C., Falzon, B.G. 2018. An advanced anti-icing/de-icing system utilizing highly aligned carbon nanotube webs. *Carbon,* 136:130-138. https://doi.org/10.1016/j.carbon.2018.04.039.

[25] Ferrari, A.C., Meyer, J.C., Scardaci, V., Casiraghi, C., Lazzeri, M., Mauri, F., Piscanec, S., Jiang, D., Novoselov, K.S., Roth, S.,Geim, A.K. 2006. Raman spectrum of graphene and graphene layers. *Physical Review Letters,* 97(18):187401. https://doi.org/10.1103/PhysRevLett.97.187401.

[26] Völklein, F., Reith, H., Meier, A. 2013. Measuring methods for the investigation of in-plane and cross-plane thermal conductivity of thin films. *Physica Status Solidi A: Applidations and Materials Science,* 210(1):106-118. https://doi.org/10.1002/pssa.201228478.

---

* Corresponding Author´s Email: muhsana1@udayton.edu

Study of interactions between bioapatite from human bone and Ca – deficient hydroxyapatite

L. Pazourková*[1], G. Simha Martynková[2], M. Šupová[3]

[1]IT4 Innovation Centre, VŠB – Technical University of Ostrava, Czech Republic;
[2]Nanotechnology Centre, CEET, VŠB – Technical University of Ostrava, Czech Republic;
[3]Institute of Rock Structure and Mechanic, Academy of Science of the Czech Republic, Czech Republic

ABSTRACT

Bioapatites (A), prepared from natural bones, are used as implants for bone grafts or powder bone fillings. The bioapatites are obviously obtained by calcinations of natural bones. The main advantage of BA from natural bones is the right ration between Ca, P and other minerals. The Ca-deficient hydroxyapatite (CDH) is biocompatible and cheap material very often used in biological and non-biological applications. The aim of this study is to prepare CDH particles on surface of bioapatites. The bioapatites are prepared by two calcinations temperatures (500 and 700°C, respectively) and subsequently crushed in mortar or milled in jet mill. The Ca-deficient hydroxyapatite is prepared on the surface of bioapatites by easy precipitation route to decrease possible influence of more invasive preparation techniques. The resulting composites of A + CDH were characterised by X-ray powder diffraction (XRD), infrared spectroscopy with Fourier transformation (FTIR) and scanning electron microscopy (SEM). The XRD shows broadening of basal reflection of A in composite, which could confirm presence of CDH. The scanning electron microscopy shows creation of small CDH particles and film-like structure. The interactions between CDH and A are probably by physical and non-bonding base.

Keywords: bioapatite; bone; Ca-deficient hydroxyapatite

INTRODUCTION

The bones are often used in biomedicine applications as implant for bone grafts or powder bone fillings. The bones are natural source of hydroxyapatite (Hap) in the nature. The advantage of the Hap from this source is the right ratio between Ca and P and trace amount of other minerals (e.g.: Mg^{2+}, Na^{+}, K^{+}) and also absence of impurities caused by by-products. Hap obtained from natural sources is inexpensive and uncomplicated in contrary with synthetic ways. The commonly route to obtain hydroxyapatite from natural sources is thermal calcinations. The lot of study were done about thermal calcinations of bones (e.g.:1,2,3). The Hap obtained from the natural source is suitable candidate as implantation material.

Ca-deficient hydroxyapatite is poor crystalline compound with variable composition with Ca/P ratio in range 1.33 – 1.67. The extent of this ratio is done by variability of chemical composition due to e.g. lattice substitution or surface absorption. The Ca deficit is accompanied with OH deficit and protonation of some PO_4 groups [4].

The literature about interaction between bones and hydroxyapatites are very extensive, but the literature about interaction between CDH and bioapatite is very spare.

The aim of this study is preparation of Ca-deficient hydroxyapatite on calcinated bioapatite from human bone. The interaction between bioapatite and Ca-deficient hydroxyapatite is studied. The coverage and/or interaction between these two materials are crucial for utilization in biomedical usage. The prepared composites are studied by infrared spectroscopy with Fourier transformation (FTIR), X-ray powder diffraction (XRD) and scanning electron microscopy (SEM).

---

* Corresponding Author´s Email: lenka.pazourkova@vsb.cz

EXPERIMENTAL/THEORETICAL STUDY

The bioapatite (A) were prepared from human bones by leasing in acid mixture and then calcination at desired temperature (500 or 700 °C) to remove organic residues (samples marked as A5 and A7, respectively). The prepared powders were then crushed in mortar or milled in jet mill. The samples of bioapatite were marked by P for crushed in mortar or M for milled bioapatite (A5P, A5M, A7P, and A7M, respectively). Then CDH was prepared with bioapatite samples. The CDH was prepared according to our previous study [5]. Shortly solution of $CaCl_2$ was slowly added into the solution Na_2HPO_4 containing 0.1 g of bioapatite. The suspension was settled down for 24 h.

The samples were characterised by XRD powder diffraction (Miniflex 600, Bragg-Brentano arrangement with scintilation detector, Cu Kα radiation, NiK-beta filter). The infrared spectra were measured on Infrared spectrometer with Fourier transformation (Nicolet iS50 (ThermoFisher, USA) with DTGS detector by ATR technique). The images of samples were performed with Scanning electron microscope (EOL JSM-7610F Plus (JEOL, Japan).

RESULTS AND DISCUSSION

The pure bioapatites, calcinated at 500 °C, show fibrous like structure with relatively smooth particles. The milled sample exhibits larger amount of small particles than bioapatite crushed in mortar. After CDH preparation, bioapatite surface is visibly covered by small particles and film-like covering of CDH. The particles are completely covered by CDH because no fibrous like structure is visible.

Calcination of bone at 700 °C leads to creation small particles and no fibrous structure is visible (Fig. 1 a)). The milling process produces smaller and uniform particles than apatite crushed in mortar. The bioapatite particles are covered by CDH film-like layer after CDH preparation (Fig. 1b)). In comparison with A5 + CDH composites, the A7 + CDH composites show no single CDH particles on its surface.

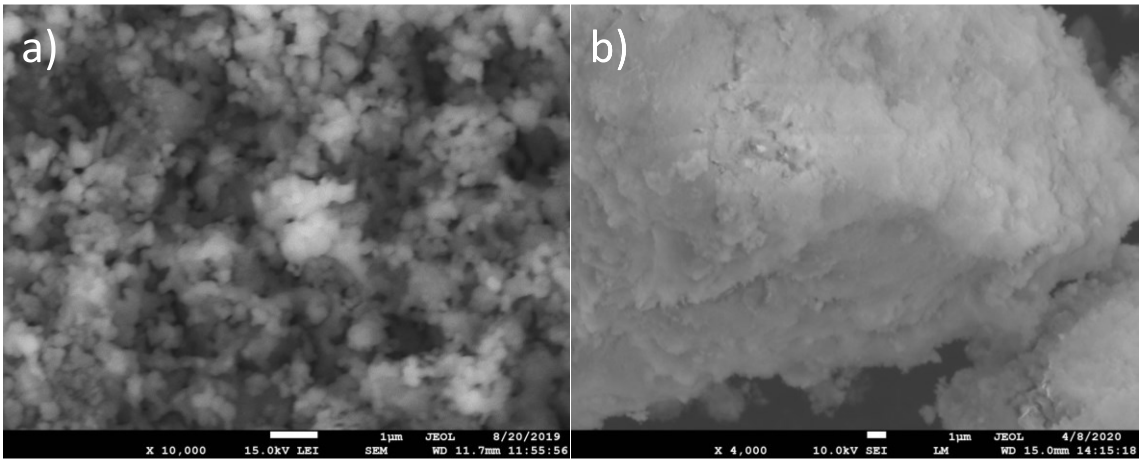

Figure 1. SEM images of a) A7P and b) A7MP.

Diffraction patterns of bioapatite with CDH composites are very similar with diffraction patterns of original bioapatite. The diffraction patterns of composites exhibit decreasing of peak intensity in comparison with pure bioapatites, which is visible primarily in 30 – 35° 2Θ region. The peaks at that region also show extension of basal reflections corresponds to presence of CDH [6].

The FTIR spectra of composites with CDH show bands very similar to pure calcinated bone and CDH. The spectra do not show significant shifts, but the intensity of the bands decreased probably due to presence of CDH.

---

* Corresponding Author´s Email: lenka.pazourkova@vsb.cz

CONCLUSION

The XRD and FTIR results revealed that interaction between A and CDH is probably based only on physical or non-bonding ways. The scanning electron microscopy showed creation of CDH particles of submicron size and film-like covering of A surface. The type of A preparation did not exhibit significant charges in CDH shape or size of particles. The result obtained at this study will be used as starting material for following study – deeper investigation of interaction forces between A and CDH.

ACKNOWLEDGMENTS

This work was supported by the European regional development fund in the IT4Innovations national supercomputing center – path to exascale project, project number CZ.02.1.01/0.0/0.0/16_013/0001791 within the operational programme research, development and education.

REFERENCES

[1] Manalu, J., Soegijono, B., Indrani, D.J. 2015. Article Characterization of Hydroxyapatite Derived from Bovine Bone. *Asian Journal of Applied Sciences*, 3(4):758-765.

[2] Baco, S., Bambang, L., Joseph, N., Yassin, F.M., Basri, N.F. 2013. Structural and composition of natural hydroxyapatite (HA) at different sintering temperatures. *Malaysian Journal of Fundamental and Applied Sciences,* 9(4):216-220.

[3] Venkatesan, J., and Kim, S.K. 2010. Effect of Temperature on Isolation and Characterization of Hydroxyapatite from Tuna (Thunnus obesus) Bone. *Materials,* 3(10):4761-4772.

[4] Dorozhkin, S. 2016. *Calcium orthophosphate-based bioceramics and biocomposites*. Weinheim, Germany: Wiley-VCH Verlag GmbH & Co.KGaA.

[5] Pazourková, L., Hundáková, M., Peikertová, P., Simha Martynková, G. 2017. Preparation of calcium-deficient hydroxyapatite particles on vermiculite by precipitation and sonication. *Journal of Australian Ceramic Society*, 53(2): 775-785.

[6] Pazourková, L. 2018. Nanokompozitní plniva na bázi jílových minerálů a hydroxyapatitu pro polymerní kompozity (Nanocomposite fillers based on clay minerals and hydroxyapatite for polymer composites). PhD diss., VSB-TUO Ostrava, Czech Republic.

* Corresponding Author´s Email: lenka.pazourkova@vsb.cz

Effect of CNT additives on the electrical properties of derived nanocomposites (experimentally and modelling)

S. Tamayo-Vegas*[1], A. Muhsan[2], L. Chang[2], M. Tarfaoui[3], K. Lafdi[1]
[1]Department of Mechanical Engineering, Northumbria University, United Kingdom;
[2]Department of chemical engineering, University of Dayton, United States;
[3]Department of Mechanical Engineering, ENSTA Bretagne, France

ABSTRACT

Polymeric nanocomposites (PNCs) are in continuous demand in many industrial applications. Especially with the rapid progress in electronics, PNCs with enhanced electrical and mechanical properties are being developed with the help of nanotechnology. Among carbon fillers, carbon nanotubes (CNTs) are extraordinarily superior in their physical properties. With the addition of small amounts into polymeric matrices, the electrical conductivity is greatly improved. However, different parameters affect the final conductivity. Thus, in this study, we have investigated the effects of MWCNT parameters i.e. aspect ratio, orientation, and intrinsic conductivity throughout modelling in DIGIMAT software with two approaches, mean-field homogenization and finite element method. In addition, the numerical data were compared with our experimental data finding a great correlation. Also, the findings suggest that the mean field homogenization has a good accuracy below the percolation threshold while FE simulations showed an exceptional correlation above the percolation threshold. Moreover, the intrinsic conductivity of the MWCNT was found is the critical parameter to correlate with experimental data. Finally, this study provides sufficient evidence that both tools are powerful to predict the electrical conductivity of nanocomposites.

Keywords: nanocomposites; carbon nanotubes; electrical properties; modelling

INTRODUCTION

Nanocomposites have attracted considerable research interest in the last decades. With the help of nanotechnology, novel polymeric nanocomposites (PNCs) are being developed to obtain enhanced physical properties [1-2]. These materials are widely employed in different industrial applications e.g. microelectronics, aerospace, structural health monitoring [3]. Normally, the material composition consists of a polymer matrix and different types of carbon fillers i.e. graphene, graphite, carbon fiber, and carbon nanotubes (CNT) [2]. With the addition of such fillers the composite's mechanical, electrical and thermal properties are enormously improved [4].

Among carbon fillers, carbon nanotubes are the most attractive because of their unique physical properties i.e. high strength to weight ratio and aspect ratio [5]. Moreover, due to their superior mechanical and electrical properties, CNTs are widely employed for tailoring multifunctional properties of polymer nanocomposites for nanoelectromechanical sensors [6-7]. Additionally, it is well known that the addition of CNTs into dielectric polymeric matrices will result in a drastic improvement in the electrical conductance of the composite [8]. Nevertheless, the resulting electrical properties of the matrix depend completely on several factors such as filler percentage, aspect ratio, particle orientation, particle dispersion, the morphology of nanotube network, and the number of nanotube contact points [9-10].

Furthermore, the critical volume fraction of CNT that triggers a severe escalation in the conductivity of the composite is called the electrical percolation threshold (EPT). At the percolation threshold, the electrical conductivity (S/m) is exponentially increased due to the formation of connected

---

* Corresponding Author´s Email: w18002002@northumbria.ac.uk

networks [11]. When these percolation networks are formed, electron conduction takes place due to three different sources: the intrinsic conductance of the nanotubes, direct contact conductance, and conductance resulting from electron tunnelling. The contact and the intrinsic conductance are the critical factors to obtain highly conductive polymer nanocomposites (PNCs), however, the electron tunnelling is not negligible [8-9].

Experimental values of electrical conductivity have been reported as high as 10000 S/m in composites containing 10 wt.% of single-walled carbon nanotube (SWCNT) in a PMMA matrix and a maximum conductivity of 2000 S/m with 15 wt.% of multi-walled carbon nanotubes in PU matrices [12]. Similarly, percolation thresholds have been reported to range from 0.0025 wt.% to 10.5 wt.% [7]. Although percolation threshold has been widely studied, the variation of CNT's characteristics (i.e. type, synthesis method, dimensions, polymer type, etc.) impedes a complete understanding of the process involved [12].

Predicting the properties of PNCs through modelling and simulations is a potent and useful tool. Moreover, the percolation phenomena and their characteristics can be studied in a low-cost and effective way. Electrical conductivity in polymer-based composites can be modelled via finite element method, Monte Carlo, resistor model, etc [13]. In this article, we study the electrical properties of MWNT with different aggregation percentages (i.e. 0.5, 1, 2, 4, 5 wt.%) in an epoxy matrix. Experimental measurements revealed that the percolation threshold occurs at around 1.7 wt.% of MWNT. Additionally, using DIGIMAT software two different approaches: Mean-field homogenization and finite element simulations were carried out to investigate the effects of aspect ratio, clustering, filler concentration, and orientation in relation to the electrical conductivity of the nanocomposite. Thus, this study aimed to investigate the correlation between DIGIMAT simulations and experimental data.

EXPERIMENTAL/NUMERICAL STUDY

Experimental details.

The CNT/Polymer composites were fabricated by mixing CNTs into an epoxy matrix. Multi-walled carbon nanotubes (MWCNT) from Applied sciences INC were dispersed into the commercial Epoxy 862 with different percentage i.e. 0.5, 1, 2, 4 ,5 wt.% The MWCNT dimensions range from 100 nm to 200 nm for the diameter and 30 um to 100 um for the length. The samples electrical conductivity was obtained through four-probe measurements and recorded using a voltmeter (Loresta equipment).

Simulation methodology.

To calculate the electrical conductivity of the polymeric nanocomposites the MSC DIGIMAT software was chosen as it offers accurate and reliable results [14]. The modelling and simulation were performed with two different methods: mean-field homogenization (MFH) and finite element analysis (FEA). The former models and estimates the multi-phase material properties through the Mori-Tanaka approach and the latter through the generation of a realistic Representative Volume Element (RVE) and implementation of the well-known finite element method [15].

Both approaches calculate the electrical properties based on the constituent's parameters i.e. matrix and filler properties, filler mass fraction, filler aspect ratio, filler orientation, and filler clustering. Besides, on mean-field homogenization, the percolation threshold and the critical exponent can be modified to predict the electrical conductivity. During MFH simulations the modelling enclosed a two-phase composite, the matrix and the nanofillers; the properties of the constituent are summarized in Table 1. The values of the Epoxy were obtained from (Govorov *et al.*, 2018) [16] and MWCNT properties come from (Bao *et al.*, 2011; Loos, 2015) [4,17].

The finite element analysis was performed in the DIGIMAT FE environment, where an RVE was created with two constituents i.e. Epoxy Epon 862 and MWCNT. A cuboid RVE, whose dimensions were modified accordingly, with fillers randomly distributed was generated to estimate the electrical

---

* Corresponding Author´s Email: w18002002@northumbria.ac.uk

conductivity of the PNCs. Figure 3 shows the RVEs with the distribution of the filler for different mass percentage. Additionally, the nanofillers were created using a cylinder inclusion shape, where the size was set to vary from 30 um to 100 um. Also, random distribution and agglomeration (clustering) was considered in the setting. Finally, the mesh parameters were set to 420 000 elements as the calculated conductivity converges at this point.

RESULTS AND DISCUSSION

For the simulations, the effects of the MWCNT parameters (i.e. aspect ratio, orientation and intrinsic conductivity) were investigated for both modelling approaches. First, in the mean field homogenization simulations, the influence of the CNT's intrinsic electrical conductivity was studied, the values were modified according to the experimental result reported in the literature [4,17], and are shown in table 1.

Table 1. Properties of the constituents.

	Epoxy EPON 862	Carbon nanotubes (MWCNT)
Density	1.21 g/cm^3	2.1 g/cm^3
Electrical conductivity	2.1 x 10^{-7} S/cm	5 x 10^1 S/cm - 5 x 10^5 S/cm

The study clearly shows a remarkable influence in the prediction on the final PNC conductivity, which is depicted in Figure 1. Moreover, it can be evidently seen that above the percolation threshold these values greatly increment and would differ from the experimental results. Nonetheless, the optimal value for the electrical conductivity (σ) was found to be 2000 S/Cm. Also, based on our experimental results, the sharp increase in the conductivity is observed to begin just before 2 wt.%, and it was confirmed to be 1.7 wt.% from the simulations. Besides, the critical exponent, found in the percolation theory, was detected to be 1.15 for a perfect agreement with experimental results.

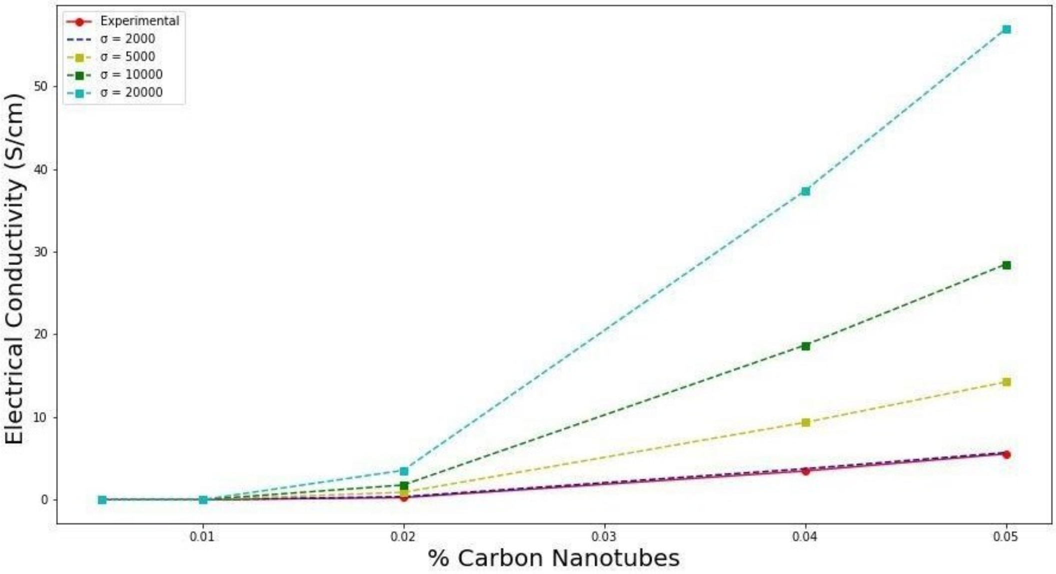

Figure 1. Comparison of electrical conductivity from MFH with experimental data.

In the same manner, the variation of the aspect ratio (AR) was studied during the simulations. The values were altered within the upper and lower limits according to the manufacturer values, i.e. AR = 150, 1000 respectively. This parameter was observed to only influence below the percolation threshold, figure 2 shows the increment of the conductivity when the AR is higher. On the other hand, above the percolation threshold, the final electrical conductivity remains the same in the MFH simulations. Finally, the AR ideal value was found to be 1000, and along with random orientation and the intrinsic conductivity previously stayed, the best agreement with the experimental data is shown in figure 1, with a blue line.

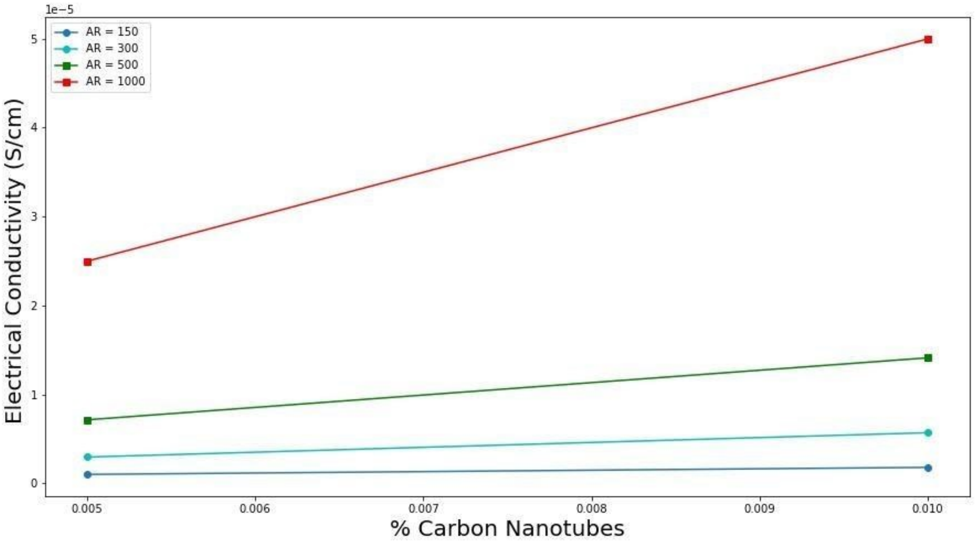

Figure 2. Electrical conductivity with different Aspect Ratio below the percolation threshold.

---

* Corresponding Author´s Email: w18002002@northumbria.ac.uk

Subsequently, in the FE simulations, different RVEs with random CNT distribution were created. Figure 3 portrays the different percentage of CNT inside the cuboid RVE. The RVE dimensions were varied according to the changes in the AR, as the RVE size is extremely important to obtain reliable data. The intrinsic conductivity of MWCNT was set up to be 2000 S/Cm to be in accordance with the MFH simulations.

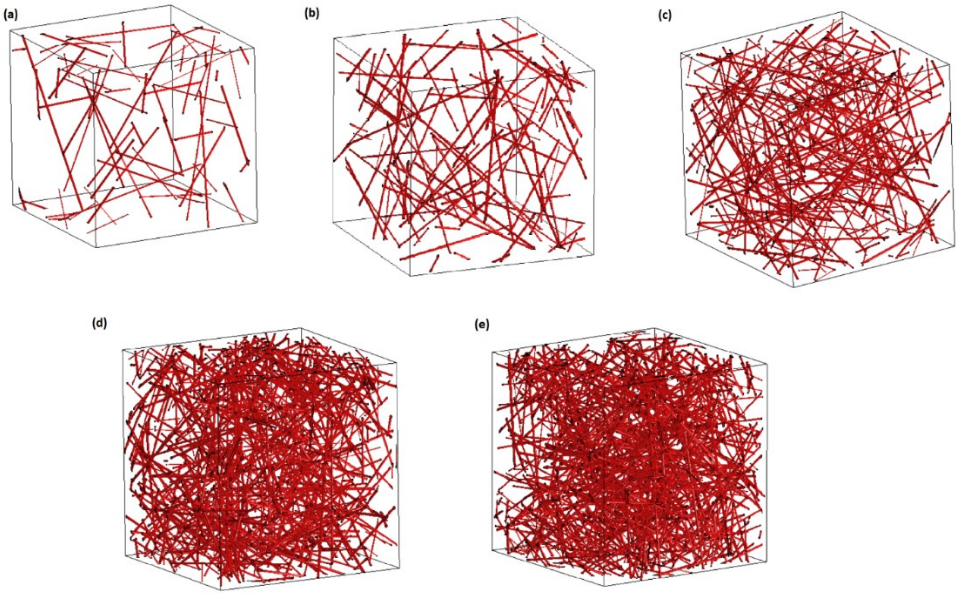

Figure 3. (a) 0.5 wt.%; (b) 1 wt.%; (c) 2 wt.%; (d) 4 wt.%; (e) 5 wt.%.

The simulations in the FE were performed with the influence of the orientation of the fillers, aspect ratio and the intrinsic conductivity. The former was set to randomly distributed and the aspect ratio changed to find the best possible match. The values of the aspect ratio were varied according to the upper and lower limits, however, when the aspect ratio is increased the RVE must be also increased to obtain isotropic calculations, resulting in a tremendous increment of the calculation time. Thus, an optimal value with an excellent agreement to the experimental results was found to be 150 for AR and 50 um for the RVE length.

Table 2. Electrical conductivity (S/cm) results.

Samples	Experimental	Mean Field Homogenization	Finite Element
0.5 wt.%	$2.123\ x10^{-5}$	$2.497\ x10^{-5}$	$2.15\ x10^{-7}$
1 wt.%	$5.195 \text{ x } 10^{-4}$	$4.997 \text{ x } 10^{-4}$	$1.167\ 10^{-6}$
2 wt.%	0.2512	0.354	0.222
4 wt.%	3.472	3.738	3.160
5 wt.%	5.549	5.698	5.2190

The simulated values are summarized in table 2, where it can be clearly seen that above the percolation threshold FE simulations match the experimental results accurately. Nevertheless, below this critical limit, FE simulations underestimate the intrinsic conductivity of CNT, resulting in that the final conductivity equals to the Epoxy. The disagreement for the 0.5 wt. % and 1 wt.% have an error of 2 orders, this is due to at low concentrations percentages the probability that a network of fillers connect two opposite size of the RVE is very low. Finally, the best predictions from both approaches

* Corresponding Author´s Email: w18002002@northumbria.ac.uk

(i.e. MFH and FE) are shown in figure 3. Both approaches have a magnifico agreement with experimental results.

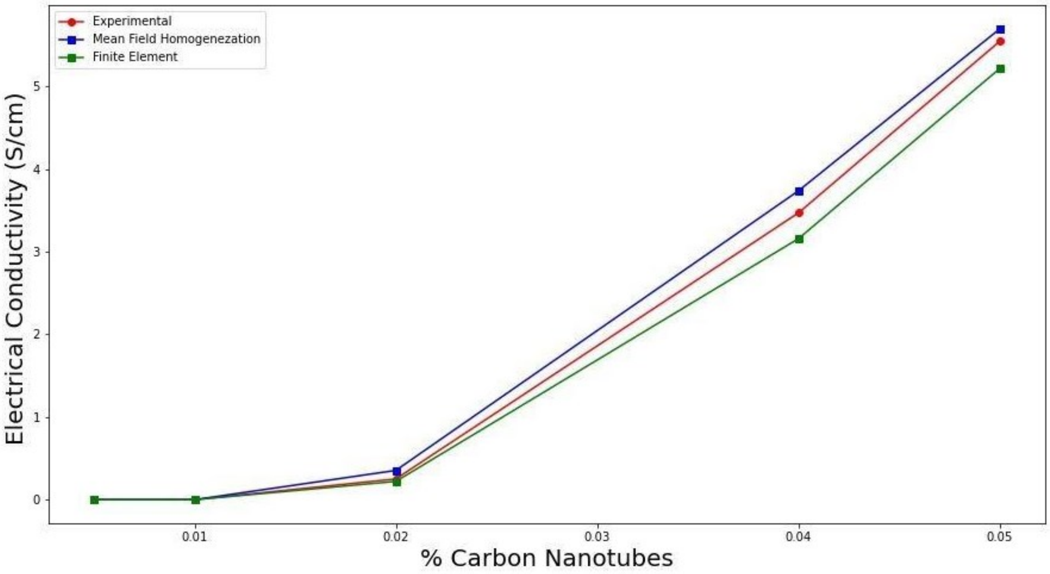

Figure 4. Comparison of electrical conductivity of Mean-field Homogenization and Finite Element with experimental data.

CONCLUSION

The prediction of the final electrical conductivity of a PNC with various percentages was performed utilizing two different simulation approaches, where the intrinsic conductivity of the MWCNT was found to be the critical parameter. Also, mean field homogenization showed great correlation and consistency below and after percolation threshold with the experimental results. However, the aspect ratio did not influence the findings above percolation, which according to theory it cannot be neglected. On the other hand, the FE simulations underestimated the intrinsic conductivity below the percolation threshold, a possible explanation is due to that at a low percentage the probability that a network is formed inside the RVE is very low, as the parameters were set to randomly distributed with a certain degree of agglomeration. Moreover, the disagreement might also be due to that the electron tunnelling cannot be negligible, and this was not investigated. In the same manner, agglomeration was found to not highly impact the outcome, nevertheless, further investigation can be done where the effects of curvature, potential agglomeration and direct contact resistance should be investigated. Besides, the above percolation threshold FE simulations showed an isotropic behaviour matching the experimental data accurately. Finally, the simulations inside the DIGIMAT software demonstrated the capacity and the ability to predict the electrical conductivity of PNC when the two tools are combined.

REFERENCES

[1] Meguid, S.A., and Weng, G.J., editors. 2017. Micromechanics and nanomechanics of composite solids. Switzerland: Springer Nature: Cham.

[2] Tjong, S.C. 2010. Electrical and dielectric behavior of carbon nanotube-filled polymer composites. In *Physical Properties and Applications of Polymer Nanocomposites*, edited byTjong, S.C., and Mai, Y.-W., 495-528. Cambridge, UK: Woodhead Publishing.

[3] Theodosiou, T.C., and Saravanos, D.A. 2010. Numerical investigation of mechanisms affecting the piezoresistive properties of CNT-doped polymers using multi-scale models. *Composites Science and Technology*, 70(9):1312-1320.

[4] Bao, W.S., Meguid, S.A., Zhu, Z.H., Meguid, M.J. 2011. Modeling electrical conductivities of nanocomposites with aligned carbon nanotubes. *Nanotechnology,* 22(48):485704.

[5] Maghsoudlou, M.A., Barbaz Isfahani, R., Saber-Samandari, S., Sadighi, M. 2019. Effect of interphase, curvature and agglomeration of SWCNTs on mechanical properties of polymer-based nanocomposites: experimental and numerical investigations. *Composites Part B: Engineering,* 175*:*107-119.

[6] Gong, S., Wang, Y., Xiao, Z., Li, Z., Wang, Z.X., Lei, R.S., Zhu, Z.H. 2017. Effect of temperature on the electrical property of epoxy composites with carbon nanotube. *Composites Science and Technology,* 149:48-54.

[7] Fang, W., Jang, H.W., Leung, S.N. 2015. Evaluation and modelling of electrically conductive polymer nanocomposites with carbon nanotube networks. *Composites Part B: Engineering,* 83:184-193.

[8] Bao, W.S., Meguid, S.A., Zhu, Z.H., Pan, Y., Weng, G.J. 2012. A novel approach to predict the electrical conductivity of multifunctional nanocomposites. *Mechanics of Materials*, 46:129-138.

[9] Mohiuddin, M., and Hoa, S.V. 2013. Estimation of contact resistance and its effect on electrical conductivity of CNT/PEEK composites. *Composites Science and Technology,* 79:42-48.

[10] Nilsson F., Krückel, J., Schubert, D.W., Chen, F., Unge, M., Gedde, U.W., Hedenqvist, M.S. 2016. Simulating the effective electric conductivity of polymer composites with high aspect ratio fillers. *Composites Science and Technology,* 132:6-23.

[11] Zeng, X., Xu, X., Shenai, P.M., Kovalev, E., Baudot, Ch., Mathews, N., Zhao, Y. 2011. Characteristics of the electrical percolation in carbon nanotubes/polymer nanocomposites. The *Journal of Physical Chemistry C*, 115(44):21685-21690.

[12] Bauhofer, W., and Kovacs, J.Z. 2009. A review and analysis of electrical percolation in carbon nanotube polymer composites. *Composites Science and Technology,* 69:1486-1498.

[13] Taherian, R. 2016. Experimental and analytical model for the electrical conductivity of polymer-based nanocomposites. *Composites Science and Technology,* 123:17-31.

[14] Khammassi, S., and Tarfaoui, M. 2020. Influence of exfoliated graphite filler size on the electrical, thermal, and mechanical polymer properties. *Journal of Composie Materials,* 54:3731-3741.

[15] Lesiuk, I., and Katunin, A. 2020. Numerical analysis of electrically conductive fillers of composites for aircraft lightning strike protection. *Aircraft Engineering and Aerospace Technology,* 92:1441-1450.

[16] Govorov, A., Wentzel, D., Miller, S., Kanaan, A., Sevostianov I. 2018. Electrical conductivity of epoxy-graphene and epoxy-carbon nanofibers composites subjected to compressive loading. *International Journal of Engineering Science,* 123:174-180.

[17] Loos, M. 2015. *Carbon Nanotube Reinforced Composites*. Oxford, UK: William Andrew.

[18] Theodosiou, T.C., and Saravanos, D.A. 2010. Numerical investigation of mechanisms affecting the piezoresistive properties of CNT-doped polymers using multi-scale models. *Composites Science and Technology,* 70 (9):1312-1320.

* Corresponding Author´s Email: w18002002@northumbria.ac.uk

Preparation of polylactide nanoparticles by supercritical fluid technology

J. Zágora*[1], D. Plachá[1], K. Čech Barabaszová[1], S. Holešová[1], R. Gabor[1], M. Fernández García[2], A. Muñoz Bonilla[2]

[1]Nanotechnology Centre, CEET, VSB – Technical University of Ostrava, Czech Republic;
[2]ICTP, CSIC, Spain

ABSTRACT

Development of new antimicrobial materials that are not toxic to higher living organisms is a major challenge today. Newly developed materials can have a high application potential in biomedicine, coatings, packaging etc. Combination of commonly used biopolymer polylactide with cationic polymers seems to be very successful in the fight against antimicrobial resistance. PLA will play a key role in fulfilling the intention set out in the Green Deal announced by the EU commission, as it is a bioplastic that is easily degradable, recyclable, and mass-produced. Also, the development of 3D printing in the context of this initiative, and the actual use of PLA as one of the main materials used for this printing, make the technology around the preparation and modification of PLA quite logical. Moreover, the environmentally friendly and energy saving technology like supercritical fluid process (SFP) will be used for their preparation. In a first approach, polylactide nano- and microparticles and structures were prepared by supercritical fluid extraction. The RESS (rapid expansion supercritical fluid solution) method is easier to optimize and shows better particle size control. On the contrary, a highly porous structure was obtained using the SAS (supercritical antisolvent) method.

Keywords: polylactide; antimicrobial polymers; supercritical fluid technology; RESS; micronization

INTRODUCTION

Increasing antimicrobial resistance to antibiotics is a worrying phenomenon. The costs associated with prevention and cure of these infections exceed 1.500 million euros per year. And more important, the timeline for the development of resistance to a new antibiotic is unpredictable. Excessive use of antibiotics has caused an increase in antimicrobial resistance due to the ability of microorganisms to adapt rapidly [1–3]. The development of other materials enabling the elimination of pathogenic microorganisms is a challenge of the present time and is an issue addressed by many scientists worldwide [4]. Such materials include for example bio-based polymers or composites containing an antimicrobial moiety of natural origin or synthesized to mimic a natural antimicrobial material [1,4–6]. Bio-based polymers such as polylactic acid are excellent candidates for these purposes [7]. To mimic natural antimicrobial polymers, low molecular weight polymers bearing groups with positive charges (ammonium, imidazolium etc.) were studied.

Supercritical fluid technology (SFT) is an alternative technology with minimal environmental impact, reduced energy consumption, non-toxic residues, and efficient conversion of reactants to products. Among its major advantages is the possibility of adjusting thermophysical properties such as diffusivity, viscosity, density, and dielectric constant by simply varying the operating pressure and/or temperature. The most used supercritical fluid is non-toxic and inexpensive carbon dioxide. Micronization, impregnation, extraction as well as chemical reactions are among technologies where supercritical process can be used [8-10]. The two supercritical particle formation techniques that are most used: rapid expansion of supercritical solution (RESS) process, where the supercritical CO_2 is used as a solvent for solute, and supercritical antisolvent (SAS) process, where supercritical CO_2 is used as an antisolvent for the precipitation of materials dissolved in organic solvents [9]. In a RESS process,

---

* Corresponding Author´s Email: jakub.zagora@vsb.cz

the solute is first dissolved in supercritical CO_2. The fluid saturated with solute is then depressurized into ambient conditions through a nozzle to cause a substantial lowering of the solvent power of CO_2, leading to very high supersaturation of solute, precipitation, nucleation and particle growth, consequently generating the microparticles or nanoparticles [11]. Expanding the supercritical solution into a liquid solution instead of a gas is an interesting variation of the RESS process. The main hurdle in utilizing the RESS process for producing polymer particles is the poor solubility or even non-solubility of polymers in the supercritical CO_2, since most polymers are insoluble in supercritical CO_2 at temperatures below 80 °C [9]. In addition, the RESS process is a batch process, which means it cannot produce the particles continuously; thus, it is hard to scale-up the process.

In a SAS process, the polymer is firstly dissolved in organic solvents, which would pass the limitation of poor solubility of polymer in the supercritical CO_2. The organic solution is then inserted into supercritical CO_2 to cause a contact between the two media. This generates a higher super-saturation ratio of the solution, resulting in fast nucleation and growth, and consequently creates fine particles [11]. However, it is possible for a polymer partially soluble in the supercritical CO_2 when a SAS process is performed, that only a very small amount or even no product of polymer may be found in the high-pressure vessel. Probably, very small droplets of organic solution are dispersed into the supercritical CO_2 fluid, and/or the organic solvent acts as a co-solvent. It would increase the polymer solubility in the supercritical CO_2, resulting in a molecular dispersion of polymer in the supercritical CO_2, and leading to the loss of polymer via the vent [9].

The aim of this work is to micronize pellets of commercially available PLA, using SFT. It is a first step for a preparation of antimicrobial materials. The micronization process was optimized using variable conditions (pressure, temperature, time, polymer concentration).

EXPERIMENTAL

The RESS and SASS supercritical processes were used to optimize the micronization of polactide pellets (Ingeo^{TM} 4032D, RESINEX Czech Republic, diameter cca 0.5 cm). Dichloromethane (Merck) was used as a solvent for the PLA pellets dissolution in the SAS method. During the RESS method, the micronized PLA particles were captured into ethanol (Merck). The experiments were performed at temperatures ranging from 40 to 80 ° C, and at pressures from 120 to 360 bar. The reaction time was from 10 to 80 minutes. The prepared materials were characterized for their physico-chemical (ie, structural, morphological, thermal, and mechanical) properties.

The following methods were used for the micronization of PLA pellets and characterizations of all materials:

- Supercritical fluid extractor Spe-ed SFE 4 positions (Applied Separations)
- HORIBA Nanopartica SZ-100 laser diffraction device
- The SEM JEOL JSM-7610F Plus (JEOL, Japan) with auto emission source

RESULTS AND DISCUSSION

The supercritical processes of micronization were optimized. It was found that RESS is more suitable method than SAS one. The conditions (temperature, pressure, time) used for the preparation of the individual samples, only RESS method, are ranged in Table 1.

---

* Corresponding Author´s Email: jakub.zagora@vsb.cz

Table 1. Overview of samples and their preparation conditions.

Sample No.	Method	Pressure [Bar]	Temperature [°C]	Reaction time [min]	Extraction	Mean [nm]	Mode [nm]
13	RESS	240	80	80	Ethanol	397	383
14	RESS	240	80	80	Ethanol		479
15	RESS	240	80	120	Ethanol	418	382
16	RESS	120	80	120	Ethanol	228	228
17	RESS	360	80	80	Ethanol	464	436
18	RESS	360	80	50	Ethanol	240	237

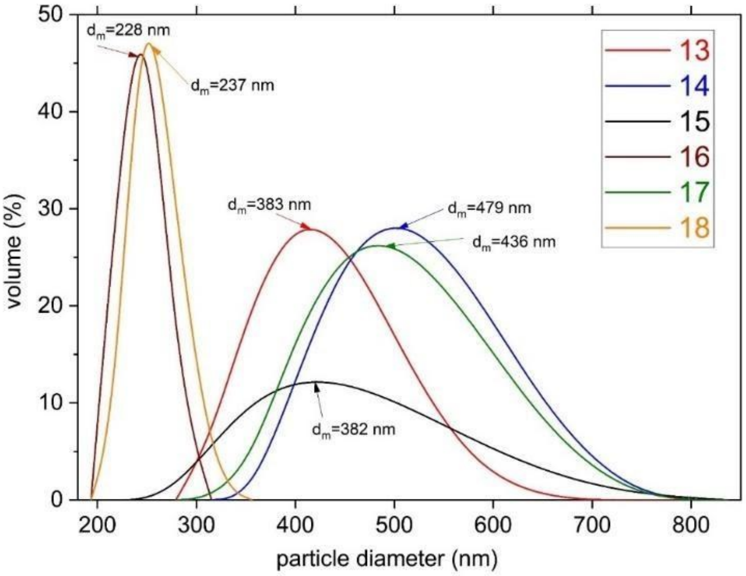

Figure 1. Particle size distribution of samples.

The particle size distribution of the samples No.13-18 is shown in Figure 1. Evidently, we observed the narrowest particle size distribution at the samples 16 and 18. The best conditions (at 80 °C) for the micronization are: 1) the highest selected pressure (360 bar) for 50 min or 2) the lowest selected pressure (120 bar) for 120 min. Thus, the higher pressure is the shorter time is needed to achieve demanded results.

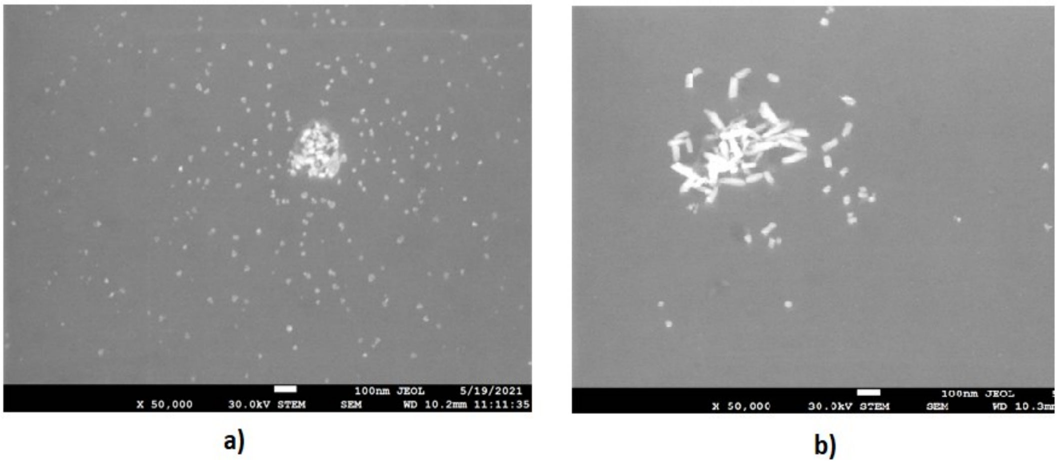

Figure 2. STEM images of PLA nanoparticles, a) sample 16, b) sample 17.

---

* Corresponding Author´s Email: jakub.zagora@vsb.cz

In Figure 2, the STEM images of obtained samples 16 and 17 are shown. It is clearly visible that PLA pellets were micronized, and even their size is smaller than it was observed via the particle size distribution measurement. In case of the sample 16, particles were of quasi spherical shape with particle size under 100 nm. In case of the sample 17, the particle size of the individual particles was much higher (~100 nm) comparing to the sample 16 and they were rod-shaped. Evidently, the RESS processes of the micronization were successful comparing to the size of the original PLA pellets used for these experiments. It is clear that very small particles/nanoparticles are formed during the process, but they form agglomerates.

CONCLUSION

In these experiments, it was proven that the PLA micro- and nanoparticles were prepared by supercritical fluid technology, using RESS and SAS methods. The SAS method is not very suitable for the preparation of nanoparticles. In case of higher concentration of PLA in ethanolic solution, particles of about 680 nm in size are formed, accompanied even by fibers with a length of 8-9 µm. Using the RESS method, particles and agglomerates with particle size distributions of 200 nm to 500 nm were obtained, depending on the conditions used (pressure, reaction time). In general, the most significant parameters are pressure and time of the extraction.

ACKNOWLEDGMENTS

This work was supported by the Doctoral grant competition VSB - Technical University of Ostrava, reg. no. CZ.02.2.69/0.0/0.0/19_073/0016945 within the Operational Programme Research, Development and Education, under project DGS/INDIVIDUAL/2020-001 "Development of antimicrobial biobased polymeric material using supercritical fluid technology" and Programme i-LINK+ 2020: Design of novel antimicrobial biobased materials using supercritical fluids processes, LINKA20364.

REFERENCES

[1] SAWAN, SP et al. Materials. 2012. *Contribution to the Fifth Assessment Report of the Intergovernmental Panel on Climate Change* Cambridge: Cambridge University Press. doi:10.1017/CBO9781107415324.004

[2] Muñoz-Bonilla, A., and Fernández-García M. 2012. Polymeric Materials with Antimicrobial Activity. *Progress in Polymer Science,* 37(2):281-339.

[3] Muñoz-Bonilla, A., and Fernández-García M. 2018. Poly(ionic liquid)s as antimicrobial materials. *European Polymer Journal*, 105:135-149.

[4] Surveillance of antimicrobial resistance in Europe 2018. 2019. Annual report of the European Antimicrobial Resistance Surveillance Network (EARS-Net). European Centre for Disease Prevention and Control: Stockholm, Sweden, doi:10.2900/22212.

[5] Lagarón, J.M., Ocio, M.J., López-Rubio, A. 2011. Antimicrobial Packaging Polymers. A General Introduction. In *Antimicrobial Polymers*, edited by Lagarón, J.M., Ocio, M.J., and López-Rubio, A., 1-22. Hoboken, New Jersey: John Wiley & Sons, Inc.

[6] Fang, H., Li, L., Wang, J., Xu, L., Wu, Y., Wang, Y., Fei, X., Tian, J., Li, Y. 2019. A novel high-strength poly(ionic liquid)/PVA hydrogel dressing for antibacterial applications. *Chemical Engineering Journal,* 365:153-164.

[7] Škrlová, K., Malachová, K., Muñoz-Bonilla, A., Měřinská, D., Rybková, Z., Fernández-García, M., Plachá, D. 2019. Biocompatible polymer materials with antimicrobial properties for preparation of stents. *Nanomaterials,* 9(11):1548.

[8] Knez, Ž., Pantić, M., Cöa, D., Novak, Z., Knez Hrnčič, M. 2019. Are supercritical fluids solvents for the future? *Chemical Engineering and Processing – Process Intensification,* 141:107532.

[9] Chen, A.Z., Zhao, Z., Wang, S.-B., Li, Y., Zhao, Ch., Liu, Y.-G. 2011. A continuous RESS process to prepare PLA–PEG–PLA microparticles. *Journal of Supercritical Fluids,* 59:92-97.

---

* Corresponding Author´s Email: jakub.zagora@vsb.cz

[10] Velasco, D., Benito, L., Fernández-Gutiérrez, M., San Román, J., Elvira, C. 2010. Preparation in supercritical CO_2 of porous poly(methylmethacrylate)–poly(l-lactic acid) (PMMA–PLA) scaffolds incorporating ibuprofen. *Journal of Supercritical Fluids,* 54(3):335-341.

[11] Higginbotham, C.L., Yons, J.G.L., Kennedy, A.J.E. 2009. Polymer processing using supercritical fluids. In *Advances in Polymer Processing: from macro to nano scales*, edited by Thomas, S., and Weimin, Y., 384-401. Cambridge, UK: Woodhead Publishing Limited.

* Corresponding Author´s Email: jakub.zagora@vsb.cz

Part 2

Progress in Nanomaterials Characterization

Structural and phase variability study of the PVDF nanocomposite materials

K. Čech Barabaszová*[1], S. Holešová[1], L. Plesník[1]

[1]Nanotechnology Centre, CEET, VŠB - Technical University of Ostrava, 17. listopadu 15/2172, 708 00 Ostrava - Poruba, Czech Republic

ABSTRACT

The PVDF nanocomposite materials were prepared in the form of thin films. The natural PVDF were modified by various inorganic and organic nanofiller materials with known antimicrobial properties. The structural changes were investigated using scanning electron microscope (SEM). The hydrophilic character was demonstrated by water contact angle and the phase changes were evaluated by the Fourier transform infrared spectroscopy (FTIR) and X-ray diffraction analyses. The PVDF nanocomposite samples had spherulites structure with a prevailing α and γ phases.

Keywords: PVDF nanocomposites; structural and phase changes; crystallite

INTRODUCTION/THEORETICAL STUDY

The poly(vinylidene fluoride) is semi-crystalline polymer with zig-zag chain. Many ways of chaining allow creation of several types of phases (α, β, γ, δ and ε), Fig 1. These phases are different by the positions of the fluor in the polymer chain. The polymer reaction and crystallization condition (especially temperature) determine the final crystalline phase. A change in phase can be caused by mechanical processing such as tension or high pressure, but also a change in polarization. These processes cause the conversion of non-polar α-phase to the electroactive β-phase. Usually, however during crystallization from the melt, the phase is converted from β-phase to α-phase [1].

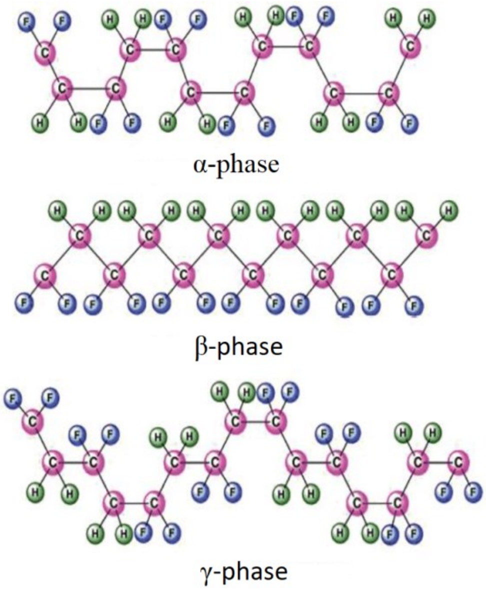

Figure 1. Structural formulas of individual phases of PVDF [2].

---

* Corresponding Author´s Email: karla.cech.barabaszova@vsb.cz

PVDF are used in several medical applications. One of the applications of PVDF is a sewing material for stitches for their biocompatibility and high mechanical durability during sterilization and medical treatment. For its porous structure it can be used as a filter material. The PVDF nanocomposite with the β and γ phase shows piezoelectric properties. These properties combined with the PVDF durability and lightweight allow their use as sensors, intelligent skin, and an alternative of conventional materials for prosthetic applications or ear prostheses. Biocompatibility allows using PVDF directly in the human body. It is already used today in tissue engineering to replace and stimulate bone or muscle healing using a mechanical or electrical stimulus [3, 4, 5].

In this study, the structural and phase changes of the PVDF nanocomposites with respect to the external condition, which are used in medicine mainly during sterilization of medical accessories, were tested.

EXPERIMENTAL STUDY

The PVDF granules (from Sigma Aldrich) were used for PVDF nanocomposites preparation. The granules were dissolved in presence of *N,N*-dimethylformamide and acetone as a solvent. This mixture was dissolved with constant mixing at temperature 80 ºC. After complete dissolution of PVDF, mixture was transferred on Petri dish and dried at constant temperature 160 ºC for 24 hours. The result of this process was PVDF thin film.

For the preparation of samples with modified materials, these materials were added to dissolve mixture and this mixture was exposed to ultrasound in ultrasonic bath. Result of this process was dispersion of modified material into dissolved PVDF. Rest of the process of preparation was the same as process of preparation of non-modified samples. In this study there were PVDF nanocomposites modified by clay particles of the vermiculite (V), zinc oxide (ZnO) and chlorhexidine (CH) or various combination of this materials.

RESULTS AND DISCUSSION

The structural changes of the PVDF nanocomposite thin films were evaluated by the SEM (Fig. 2). The pure PVDF films have spherulite structure with spherulites crystal size from 10 to 50 μm and micropores at their edges with an average size about 5 μm. The vermiculite (V) in the PVDF/V nanocomposite materials caused refinement of the spherulite structure, the average spherulites crystal size was smaller than 5 μm. The PVDF/V/CH nanocomposite formed a compact film with pores. A homogeneous distribution of the V/CH nanofiller particles in the volume of the PVDF matrix is visible. The PVDF/ZnO/V/CH nanocomposites have spherulite structure with big spherulite crystals, whose surfaces are formed by unevenly distributed cavities. The spherulitic structure resulting from differentially modified vermiculite nanofillers predicts the use of these PVDF nanocomposite films for membrane technologies.

The hydrophilic character of the pure PVDF and PVDF nanocomposite materials was demonstrated by the water contact angle (WCA, wettability angle), smaller than 90°. The similar values of the WCA were measured for pure PVDF 65° ± 2.1 and 64° ± 1.9 for PVDF/ZnO/V/CH samples, while 74° ± 2.9 for PVDF/V and 76° ± 3.5 for PVDF/V/CH nanocomposite materials were measured. These WCA values correspond to the structural changes in the PVDF nanocomposite materials.

---

* Corresponding Author´s Email: karla.cech.barabaszova@vsb.cz

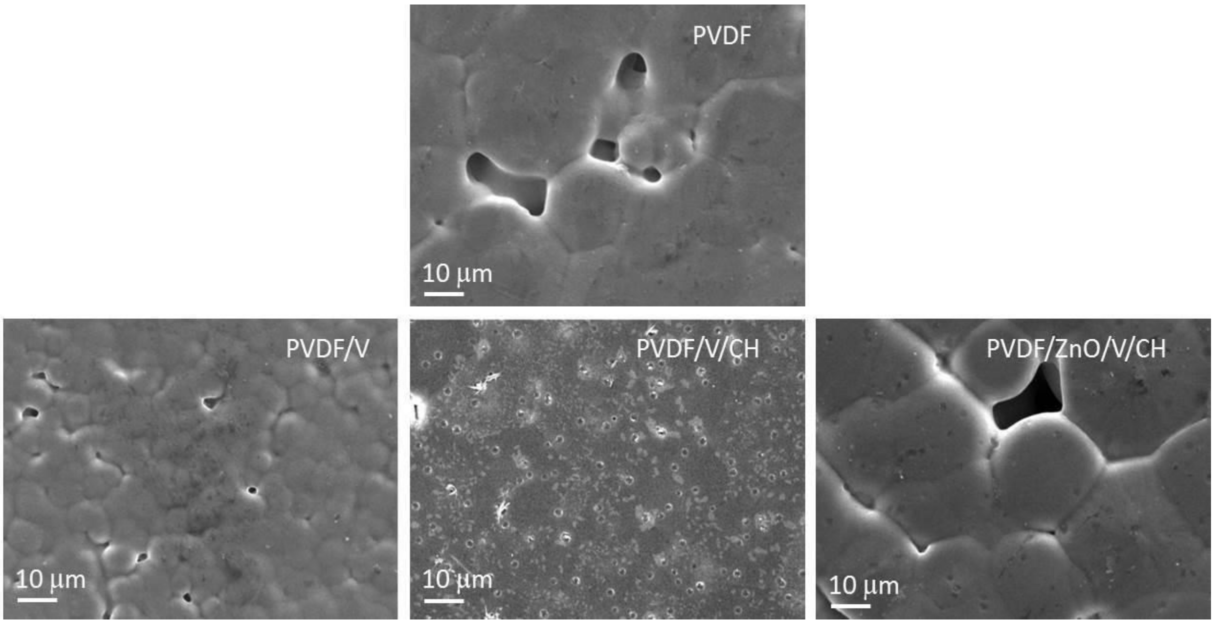

Figure 2. SEM images of the pure PVDF a); b) PVDF/V;(c) PVDF/V/CH and d) PVDF/ZnO/V/CH nanocomposite materials.

FTIR analysis helps us to determinate type of PVDF phase which was produced in each sample. The typical bands for given crystal phases obtained from FTIR spectra for each sample are shown in Table 1. Prevailing phases were α and γ or their combination. Mainly wavenumbers 763 and 614 cm^{-1}, and furthermore 532, 795, 975 and 1150 cm^{-1} indicate predominantly the presence of α-phase. The typical wavenumber for γ-phase is 1231 cm^{-1}, and also 1429, 813 cm^{-1} indicate the presence of this phase. It can be seen that the presence of the specific phase depends on the type of used nanofiller.

Table 1. PVDF phases in each sample.

Sample	WAG (°)	phase	wavenumbers (cm^{-1})
PVDF		γ	1429, **1231**, 813
PVDF_V		γ+α	**1231**, 813, 795, **763**, **614**
PVDF_V_CH		α	795, **763**, **614**, 531
PVDF_ZnO_V_CH		γ+α	**1230**, 975, 813, 796, **763**, **614**

XRD analysis confirmed the presence of the PVDF phase and ZnO, V and CH nanofillers in the PVDF matrix. However, this analytical method did not provide information on the interaction between the evaluated phases and changes in the crystalline phases of the PVDF matrix.

Regarding to the future use of PVDF nanocomposite materials in medical devices, it was monitored a number of factors which can cause a phase change as degradation by ultraviolet radiation, ultrasound radiation and/or surface degradation in physiological solutions. In our study it was found that the addition of V, ZnO and CH nanoparticles (as nanofillers in the PVDF) stabilized the nanocomposite structures and did not cause phase changes in the structure. In contrast, in the pure PVDF material due to different degradation processes, the phase changes from γ-phase to α-phase were evaluated.

CONCLUSION

The spherulite structure predominates in the PVDF nanocomposite film. This structure is variable and can be modified by several types of nanofillers, which obtain different properties of the final material

---

* Corresponding Author´s Email: karla.cech.barabaszova@vsb.cz

and increases resistance to phase transformation during exposure to extreme external influences. This material has great promise in applications in the medical and pharmaceutical fields.

ACKNOWLEDGMENTS

This work was supported by the project No. SP2020/08 “Hybrid clay nanofillers for antimicrobial polymer films” and project No. SP2021/106 “Study and development of composite nanomaterials and nanofillers”. Authors thank to M. Heliová for SEM micrographs.

REFERENCES

[1] Cardoso, V.F., Correia, D.M., Ribeiro, C., Fernandes, M.M., Lanceros-Méndez, S. 2018. Fluorinated Polymers as Smart Materials for Advanced Biomedical Applications. *Polymers*, 10:161.
[2] Mishra, S., Unnikrishnan, L., Kumar Nayak, S. 2018. Structural configuration of three major phases of PVDF. In: *Wiley Online Library*. Bengaluru: Wiley.
[3] Mishra, S., Unnikrishnan, L., Kumar Nayak, S., Mohanty, S. 2018. Advances in Piezoelectric Polymer Composites for Energy Harvesting Applications: A Systematic Review. *Macromolecular Materials and Engineering,* 304:1800463.
[4] Mirfakhrai, T., Madden, J.D.W., Baughman, R.H. 2007. Polymer artificial muscles. *Materials Today*, 10:30-38.
[5] Suaste-Gómez, E., Rodríguez-Roldán, G., Reyes-Cruz, H., Terán-Jiménez, O., Lanceros-Méndez, S. 2013. Developing an ear prosthesis fabricated in polyvinylidene fluoride by a 3d printer with sensory intrinsic properties of pressure and temperature. *Sensors,* 16:332.
[6] Ribeiro, C., Sencadas, V., Correia, D.M., Lanceros-Méndez, S. 2015. Piezoelectric polymers as biomaterials for tissue engineering applications. *Colloids and Surfaces B: Biointerfaces,* 136:46-55.

---

* Corresponding Author´s Email: karla.cech.barabaszova@vsb.cz

Micromechanical characterization of Carbon Black reinforced epoxy nanocomposite using micro indentation

S. Khammassi*[1], M. Tarfaoui[1]

[1]ENSTA Bretagne, FRE CNRS 3744, IRDL, F-29200 Brest, France

ABSTRACT

The effect of carbon black reinforcement on the Vickers hardness of epoxy resin-based composites was studied. The micro-indentation dynamic mechanical analysis test measures the micromechanical properties of carbon black reinforced DGEBA epoxy nanocomposites with varying weight percentages (0, 1, 2 and 5 wt%). The micro-indentation deformation was studied by in-situ imaging of the impression using KEYENCE. Mechanical properties, such as hardness, elastic modulus, and stiffness, gradually increase as the mass fraction of filler (CB) continuously increases. This progress depends on various parameters, such as nanoparticle- reinforced polymer composites' dispersion, interfacial bonding, and load transfer.

Keywords: carbon black; nanocomposite; micro-indentation; micro-hardness

INTRODUCTION

With the wide application of polymers and their composite materials, the demand for materials with excellent mechanical properties is growing. Therefore, improving the mechanical properties through appropriate methods can benefit the design of composite materials and lead to the wide application of materials in different fields. Matrix strengthening is mainly one of the methods to improve the mechanical properties of composite materials by adding nanoparticles [1] [2]. It has been proved that adding a small number of rigid nanoparticles to the polymer matrix can significantly improve its mechanical properties [2-7].

A nanocomposite material can be defined as a composite material in which the size of at least one phase (mainly filler) is in the nanometer range. Like traditional composite materials, nanocomposites have two parts: filler and matrix. Traditional composite materials usually use fibers such as carbon fibers or glass fibers as fillers. In nanocomposites, the fillers are nanomaterials. The size range of nanomaterials is 1-100 nm. Some examples of nanomaterials are CNT, carbon nanofibers and nanoparticles, such as gold, silver, diamond, copper and silicon. Of particular interest are carbon black nanocomposites because they have high strength and stiffness and can be produced at relatively low CB concentrations [1,2,7,8].

As the filler size reaches the nanometer scale, the interaction at the interface becomes quite large relative to the inclusions' size, so the final performance shows a significant change [9,4].

Carbon Black-reinforced polymer composites' mechanical properties are significantly lower than their theoretically predicted potential [10]. For the CB mentioned in [11-15], maiking the nanoparticles fully play a reinforcing role requires a good dispersion of the nanoparticles in the polymer matrix and a strong bond with the polymer matrix. But to achieve high-quality scores, including carbon nanoparticles' inclusion in a polymer matrix, which usually gathers into weakly interaction due to van der Waals force attraction [15, 16]. However, a threshold represents the nanocomposite's resistance limit, which defines the beginning of agglomeration. The threshold depends on the type and mass fraction of nanoparticles [3, 17-19, 20].

It has been proven that the micro indentation technique is the most accurate way to evaluate the influence of carbon nanoparticles on the deformation behavior [20-22]. In this study, a micro-indenter was used to extend the hardness and elastic modulus of nanoparticle-reinforced epoxy composites.

---

* Corresponding Author´s Email: sabrine.khammassi@ensta-bretagne.org

EXPERIMENTAL STUDY

The epoxy resin chosen in this work is DGEBA, and MOMENTIVE provides epoxy resin in a liquid, low viscosity and good adhesive form. In this study, the weight ratio between the resin and the curing agent Jeffamine D230 is 2:1. Carbon black was used in this study. Table 1 lists the different composition ratios of our reinforced nanocomposites. DEGUSSA provides carbon black. Besides, the nanocomposite structure was developed by RESCOLL. In Figure 1, the process of the indentation test is introduced.

Table 1. Weight ratio of nanocomposite constitution.

Resin 1		Nanifiller			Hardener		Polymerisation cycle
G		g	% mass.		g		
100	DGEBA	-	-	-	32	Jeffamine D230	16h à 23°C + 1h à 120°C
100	DGEBA	1.6	1.2	CBs	32	Jeffamine D230	16h à 23°C + 1h à 120°C
100	DGEBA	3.2	2.4	CBs	32	Jeffamine D230	16h à 23°C + 1h à 120°C
100	DGEBA	8	5.7	CBs	32	Jeffamine D230	16h à 23°C + 1h à 120°C

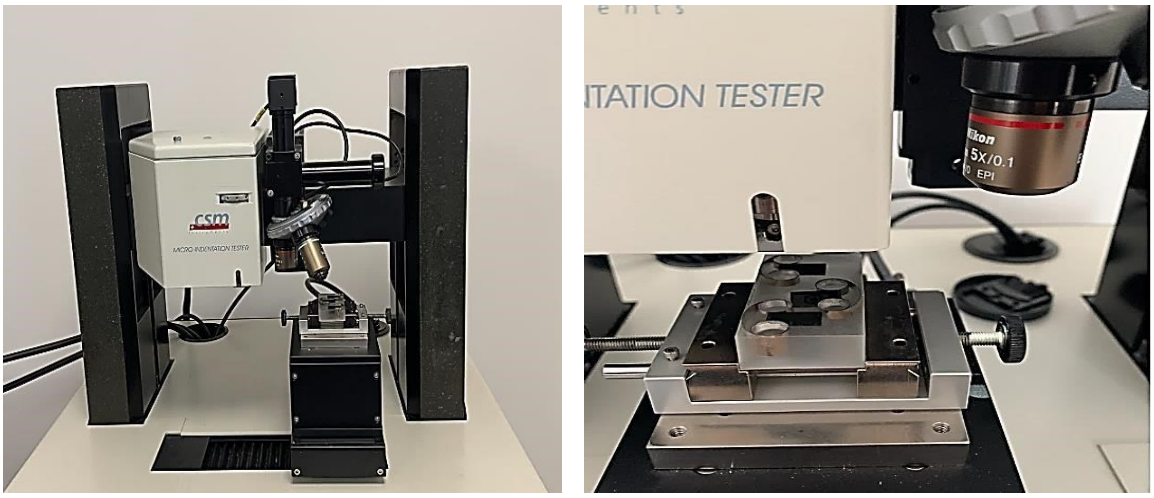

Figure 1. Image of the indentation machine and specimens under test.

RESULTS

The load-displacement curves of the neat and the reinforced prepared composites, obtained from the micro indentation tests, are presented in Figure 2.

The slope of the unloaded section of the curve is directly related to the modulus of elasticity. It can be seen that in addition to the pure epoxy composite material and the reinforced epoxy nanocomposite material, the addition of carbon black to the matrix increases the slope of the unloading curve, thus

---

* Corresponding Author´s Email: sabrine.khammassi@ensta-bretagne.org

increasing the stiffness of the material, as shown in Figure 3, where it has been increased from 282 mN / µm to 295 mN / µm.

Allowing to these results, Young's modulus of the composite material was measured and shown in Fig. 3 that, compared with the pure matrix, the carbon black reinforced epoxy nanocomposite increased from 4GPa to 5GPa, respectively. This increase may be due to the higher strength bonds between the CB nanoparticles and the epoxy resin. These results are related to the results obtained with the hardness value. Figure 6 also illustrates that the carbon black reinforced composite material's microhardness increases significantly with the supplementary increase of the filler content. The microhardness of CB-reinforced nanocomposites increases significantly with the increase of CB content in the matrix. The micro-hardness increased from 32Hv of pure epoxy resin to 40Hv of CBs filler concentration of 5 wt% in the nanocomposite. This value has increased due to the resistance of relatively hard CB particles to the epoxy matrix's plastic deformation [31]. Therefore, the reduction in plastic deformation can be confirmed by reducing plastic energy defined in Figure 6. The significant increase in microhardness can be attributed to the better distribution of the CB particles and the excellent adhesion between the epoxy resin and the CB particles. KEYENCE's optical microscope confirmed the better dispersion of CB particles in the matrix.

Some observations can be drawn from simulation results and test samples. Contour displacement maps and stress maps can be drawn around the open position. For this reason, this area can be reflected as a place where cracks happen. Carbon Black increases the interface's resistance and reduces the stress concentration, which in turn delays the onset of damage.

As shown in Figure 7, due to the polymer's viscosity, the shape of the indentation pattern is slightly different from the standard Vickers indenter. Matrix cracking is the type of damage observed around recessed areas. The indentation print of each mass fraction shows the difference in the surface homogeneousness.

* Corresponding Author´s Email: sabrine.khammassi@ensta-bretagne.org

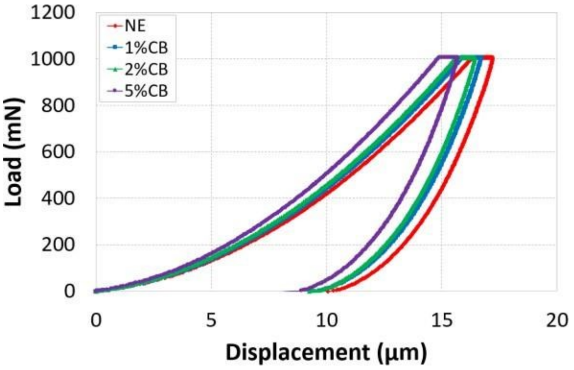

Figure 2. P– δ interactions of CBs/epoxy specimen computed with a different mass fraction.

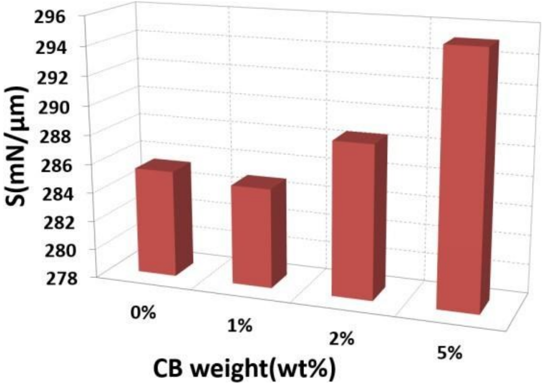

Figure 3. Effect of CBs nanoparticles on stiffness.

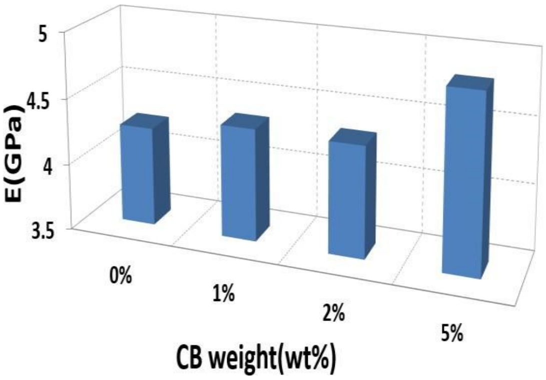

Figure 4. Effect of CBs nanoparticles on Young modulus.

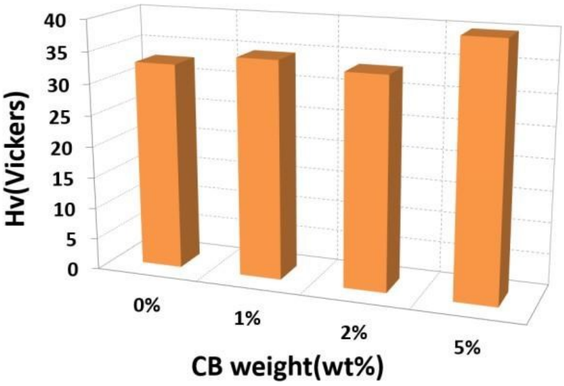

Figure 5. Effect of CBs nanoparticles on microhardness.

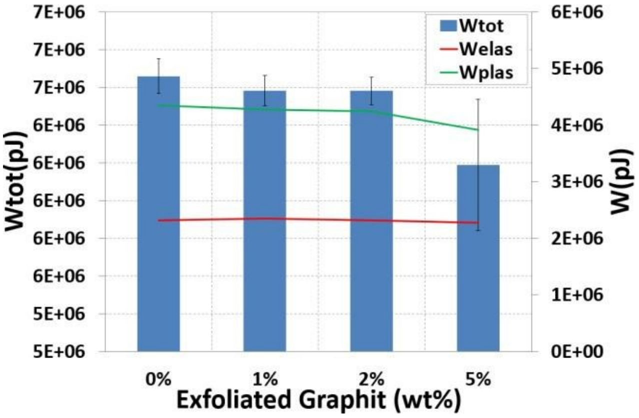

Figure 6. Effect of different mass fraction of CBs on the Welas and Wplas.

---

* Corresponding Author´s Email: sabrine.khammassi@ensta-bretagne.org

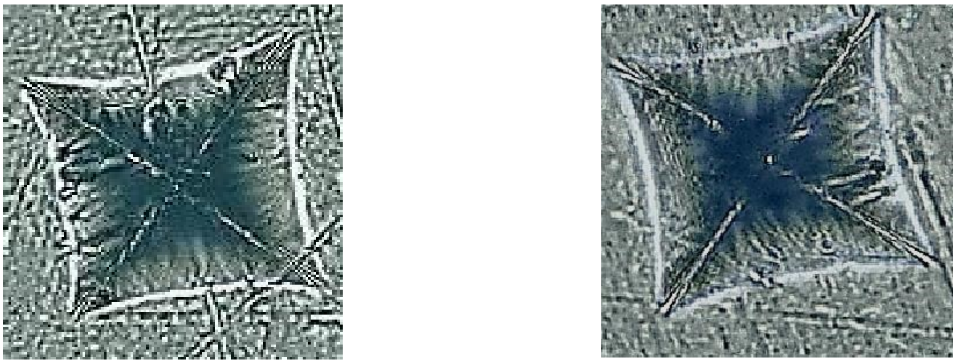

a) NE (0wt.%CB)

b) 1wt.%CB

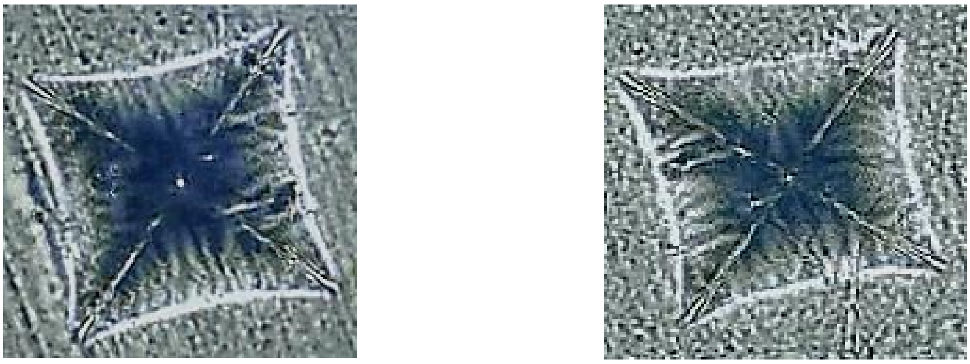

c) 2wt.%CB

d) 5wt.%CB

Figure 7. The KEYENCE image of the indentation print.

CONCLUSION

The experimental results of our research show that carbon black reinforced epoxy resin improves the performance of nanocomposites at different mass fractions, depending on the following factors: the type of distributed additive, its performance characteristics, and the interface properties between the matrix and the reinforcing additive. Compared with pure epoxy resin, epoxy resin reinforcement by 5wt.% CB showed a visual increase in hardness.

KEYENCE analyzed and observed the microstructure of indentation. This microstructure analysis can recognize the fracture mode and crack propagation of CBs reinforced epoxy nanocomposites. Microscopic observation showed that cracks appeared from the position of the indenter and extended laterally along with the microstructure. Compare the profile of the indentation test. Therefore, CBs tend to enhance the interface resistance and fracture toughness of composite materials. Adding a small amount of CB seems to improve the modulus of elasticity, fracture toughness, and crack resistance. By adding 5 wt.% of CB, the rigidity of the nanofiller-modified polymer composite material is significantly enhanced.

FUNDING

The Region Bretagne, through the PhD projects, collaborated with ENSTA Bretagne kindly supported this work.

---

* Corresponding Author´s Email: sabrine.khammassi@ensta-bretagne.org

Chapter 8

Part 2: Progress in Nanomaterials Characterization

REFERENCES

[1] Bryning, M.B. 2007. *Carbon nanotube networks in epoxy composites and aerogels.* PhD diss., University of Pensylvania.

[2] Hissam, A., and Bower, M. 2003. Analysis of a preloaded bolted joint in a ceramic composite combustor. *Paper presented at 39th AIAA/ASME/SAE/ASEE Joint Propulsion Conference and Exhibit*, Huntsville, Alabama, July 20-23.

[3] Tarfaoui, M., Lafdi, K., Beloufa, I., Daloia, D., Muhsan, A. 2018. Effect of graphene nano-additives on thelocal mechanical behavior of derived polymer nanocomposites. *Polymers,* 10(6):667.

[4] Khammassi, S., and Tarfaoui, M. 2020. Influence of exfoliated graphite filler size on the electrical, thermal, and mechanical polymer properties. *Journal of Composite Materials,* 54(25):3731-3741.

[5] Lau, K.-T., Shi, S.-Q., Zhou, L.-M., Cheng, H.-M. 2003. Micro-hardness and flexural properties of randomly oriented carbon nanotube composites. *Journal of Composite Materials,* 37(4):365-376.

[6] Samal, S.S., and Bal, S. 2008. Study of mechanical and morphological properties of aligned and randomly oriented carbon nanotube composites. *Paper presented at The International Conference on Emerging Scenarios in Space Technology & Applications,* India, Chennai, Satyabama university, November 13-15.

[7] Chihi, M., Tarfaoui, M., Bouraoui, C, El Moumen, A. 2003. Effect of CNTs additives on the energy balance of carbon/epoxy nanocomposites during dynamic compression test. *Polymers,* 12(1):194.

[8] Tricas, N., Vidal-Escales, E., Borros, S., Gerspacher, M. 2003. Influence of carbon black amorphous phase content on rubber filled compounds. *Composites Science and Technology,* 63(8):1155-1159.

[9] Uzunpinar, C. 2010. Effect of dispersion of swcnts on the viscoelastic and final properties of epoxy-based nanocomposites. Master thesis, Auburn University, Alabama.

[10] Ojha, S., Acharya, S.K., Raghavendra, G. 2015. Mechanical properties of natural carbon black reinforced polymer composites. *Journal of Applied Polymer Science,*132(1):41211.

[11] Zhang, W., Blackburn, R.S., Dehghani-Sanij, A.A. 2007. Effect of carbon black concentration on electrical conductivity of epoxy resin-carbon black-silica nanocomposites. *Journal of Materials Science,* 42(18):7861-7865.

[12] Afzal, A., Kausar, A., Siddiq, M. 2016. Perspectives of polystyrene composite with fullerene, carbo black, graphene, and carbon nanotube: a review. *Polymer-Plastics Technology and Engineering,* 55(18):1988-2011.

[13] Lohar, G.S., and Jogi, B.F. 2018. Influence of carbon black (cb) on mechanical behaviour and microscopic analysis of poly-propylene (pp)/ acrylonitrile-butadiene-styrene (abs) nanocomposites. *Procedia Manufacturing*, 20:85-90.

[14] Savetlana, S., Zulhendri, H., Sukmana, I., Saputra, F.A. The effect of carbon black loading and structure on tensile property of natural rubber composite, in *IOP Conference Series Materials Science and Engineering,* 2017, *223*:012009.

[15] Dong, M., Li, Q., Liu, H., Liu, Ch., Wujcik, E.K., Shao, Q., Ding, T., Mai X., Shen, Ch., Guo, Z. 2018. Thermoplastic polyurethane-carbon black nanocomposite coating: Fabrication and solidparticle erosion resistance. Polymer, 158:381-390.

[16] Rahmat, M., and Hubert, P. 2011. Carbon nanotube–polymer interactions in nanocomposites: a review. *Composites Science and Technology,* 72(1):72-84.

[17] El Moumen, A., Tarfaoui, M., Lafdi, K., Benyahia, H. 2017. Dynamic properties of carbon nanotubes reinforced carbon fibers/epoxy textile composites under low velocity impact. *Composites Part B-Engineering,* 125:1-8.

[18] Nachtane, M., Tarfaoui, M., Saifaoui, D., El Moumen, A., Hassoon, O.H., Benyahia, H. 2018. Evaluation ofdurability of composite materials applied to renewable marine energy: Case of ducted tidal turbine. *Energy Reports*, 4:31-40.

[19] El Moumen, A.; Tarfaoui, M.; Lafdi, K. Mechanical characterization of carbon nanotubes-basedpolymer composites using indentation tests. *Composites Part B-Engineering,* 114:1-7.

[20] Khammassi, S., Tarfaoui, M., Lafdi, K. 2021. Study of mechanical performance of polymer nanocomposites reinforced with exfoliated graphite of different mesh sizes using micro-indentation. *Journal of Composite Materials,* 55(19):2617-2629.

[21] Kaszowska, Z., Kot, M., Białek-Kostecka, D., Forczek-Sajdak, A. 2019. Application of micro-indentation tests to assess the consolidation procedure of historic wall paintings. *Journal of Cultural Heritage,* 36:286-296.

[22] Kossman, S., Chicot, D., Lost, A. 2017. Indentation instrumentée multi-échelles appliquée à l'étude des matériaux massifs métalliques. *Matériaux Techniques,* 105(1):104.

---

* Corresponding Author´s Email: sabrine.khammassi@ensta-bretagne.org

The photochemical reactions of 4-aminobenzenethiol on the plasmonic nanostructured surfaces

I. Kopal*[1], M. Švecová[2], T. Čapková[3], M. Dendisová[1]

[1]Department of Physical Chemistry, University of Chemistry and Technology Prague, Czech Republic;
[2]Department of Analytical Chemistry, University of Chemistry and Technology Prague, Czech Republic;
[3]Centre of Polymer Systems, University Institute, Tomas Bata University in Zlín, Czech Republic

ABSTRACT

The increasingly dynamic development in the field of Surface-enhanced spectroscopies leads to the preparation of innovative nano-featured enhancing substrates, tested using suitable model analytes. 4-aminobenzenethiol (4-ABT) is widely used for this purpose, mainly due to its optical properties and adsorption abilities onto the surface of plasmonic substrates. On the other hand, there is not negligible risk of the photochemical dimerization of 4-ABT as a result of the incident radiation under certain circumstances. Therefore, it is desirable to assess the extent of dimerization on the selected plasmonic metals, same as the role of the excitation wavelength used.

As part of this work, we studied the photochemical reaction of prepared large-scaled substrates covered by 4-ABT molecules. The morphology of these substrates was monitored using optical and electron microscopy. Furthermore, we have measured the Surface-enhanced Raman scattering (SERS) spectra of the deposited molecules on the prepared Ag, Au, and Cu surfaces using five different excitation wavelengths.

The results showed that the formation of dimer molecules occurs most abundantly on the silver substrate, disproportionately less on the Au and Cu surfaces. In all cases, the degree of dimerization is strongly dependent on the morphology of the nanostructures and the excitation wavelength used.

Keywords: surface-enhanced Raman spectroscopy; 4-aminobenzenethiol; plasmonic surface photochemistry

INTRODUCTION

Decades have passed since the discovery of the influence of plasmonic metals on the enhancement of Raman scattering. This phenomenon was first reported (although misinterpreted) by Martin Fleischmann when observing a more intense signal of pyridine molecules adsorbed on a silver electrode [1]. Since then, surface-enhanced Raman scattering (SERS) has become a technique used in many fields of chemical, physical, and biomedical research [2]. The unlimited possibilities of SERS spectroscopy applications lead to a constant need to develop new nanostructured plasmonic substrates [3]. For the development of plasmonic metal substrates, molecules with a good spectral response and the potential to form uniform layers on the substrates serve as model analytes. Such a substance is, for example, 4-aminobenzenethiol (4-ABT), popular in the professional community mainly due to its tendency to form self-assembled monolayers [4]. However, a photochemical reaction of 4-ABT to 4,4´-dimercaptoazobenzene (4,4´-DMAB) can occur on the surface of plasmonic metals under certain conditions [5]. So far, many factors influencing the course of this photochemical reaction, such as the effect of the excitation wavelength, pH of deposition solution, a plasmonic metal used, or input potential, have been studied [6-9]. However, there are often incomplete studies.

This work aimed to monitor 4-ABT and 4,4´-DMAB bands on prepared Ag, Au, and Cu large-scaled substrates, characterized by optical and electron microscopy, and to use them to assess the influence of the used plasmonic metal and excitation wavelength (455, 532, 633, 780 and 1064 nm) on the course of photochemical reaction of 4-ABT.

---

* Corresponding Author´s Email: kopali@vscht.cz

EXPERIMENTAL STUDY

Preparation of nanostructured substrates

Large-scaled Ag, Au, and Cu SERS substrates were prepared by electrodeposition on platinum targets. Pt supports were first sanded with metallographic papers, polished with Al_2O_3 and $CaCO_3$, and cleaned by immersion in a mixture of H_2SO_4 and H_2O_2 (3:1 v:v, “piranha” solution) for 30 minutes. Then, they were rinsed with miliQ water and dried. They were metalcoated in the appropriate electrochemical baths using various current sequences (Table 1). The prepared substrates were then immersed in a deposition bath of 4-ABT (10^{-5} mol·dm^{-3} in methanol) for 24 hours. Subsequently, the covered targets were removed from the solutions and dried by nitrogen.

Table 1. Current sequences used for the preparation of plasmonic substrates.

$[Ag(NH_3)_2]^+$		$[Au(NH_3)_4]^{3+}$		$[Cu(NH_3)_4]^{2+}$	
I (mA)	*t* (min)	*I* (mA)	*t* (min)	*I* (mA)	*t* (min)
5	10	5	5	10	10
10	5	10	5	20	10
		15	5	30	10
				40	10
				50	10

Optical and scanning electron microscopy

Surface images were taken using an Olympus microscope equipped with four objectives (10 × / 0.25 BD, 20 × / 0.40 BD, 50 × / 0.50 BD and 100 × / 0.90 BD) included in the Raman microscope. A lens with 100× magnification was used.

A Scanning Electron Microscope (SEM) S-4800 (Hitachi, Japan) was used to study nanostructures morphology. The images were taken at a set electron acceleration voltage of 10 kV.

SERS spectroscopy

A Fourier transform spectrometer (FT-spectrometer) EQUINOX 55 (Bruker, Germany), connected to a Raman module FRA 106/S, and a dispersive Raman microscope DXR (Nicolet, USA) were used to obtain SERS spectra. FT-spectrometer is equipped with Nd:YAG (Neodymium-Doped Yttrium Aluminum Garnet) laser emitting 1064nm radiation and by germanium detector cooled by liquid nitrogen. The dispersive spectrometer uses various radiation sources. A diode laser (455 nm), an Nd:YAG laser excited by laser diodes (532 nm), a gaseous He:Ne laser (633 nm), or a diode laser (780 nm) serves as excitation sources emitting radiation of different wavelengths. Scattered radiation is collected by a CCD detector. The measurement parameters for both instruments are in Table 2. The spectra were measured at 12 points on each substrate and subsequently processed and averaged using Omnic 9 software.

---

* Corresponding Author´s Email: kopali@vscht.cz

Table 2. Measurement parameters of individual SERS spectra of 4-ABT on different surfaces.

	Excitation wavelength (nm)	Resolution (cm^{-1})	Metal	Laser power (mW)	Number of aquisitions	Exposure time (s)
FT-spectrometer	1064	4		300	1024	1800
Dispersive spectrometer	780	< 5	Ag	1	20	2
			Au	5	20	2
			Cu	5	20	2
	633	< 5	Ag	0.1	20	2
			Au	5	20	2
			Cu	5	20	2
	532	< 5	Ag	0.1	20	2
			Au	5	20	10
			Cu	5	20	2
	455	< 5	Ag	1	20	2
			Au	5	20	10
			Cu	5	20	2

RESULTS AND DISCUSSION

The rate of photochemical dimerization was studied using SERS spectra measured on individual plasmonic metals. Based on previously published works, we can say that the formation of 4,4´-DMAB is demonstrable by the occurrence of several selected bands in the spectrum (Fig. 1) [6,10]. In the figure, the colored bands show the spectral regions in which bands of 4,4´-DMAB (Fig. 2) appear.

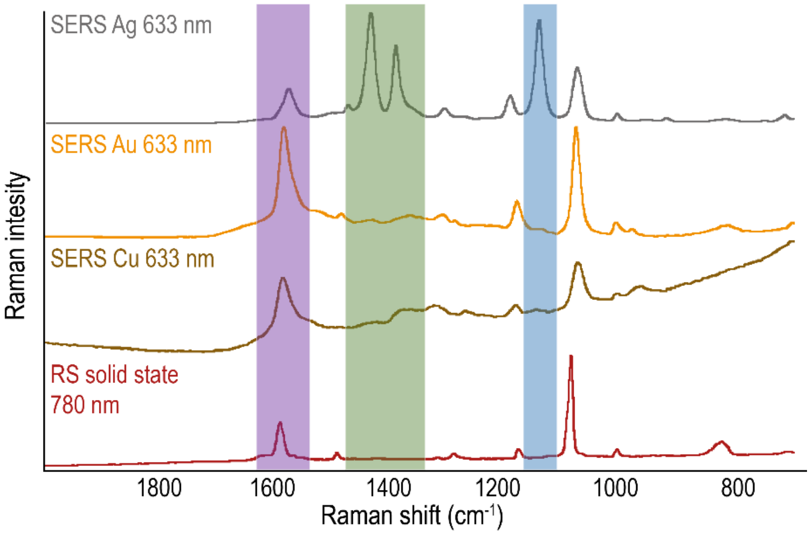

Figure 1. Comparison of SERS spectra of 4-ABT measured on Ag, Au, and Cu surfaces at the settings given in Table 2 and Raman spectra of solid-state 4-ABT measured with excitation wavelength of 780 nm, laser power of 80 mW, and exposure time 10×1 s.

The formation of 4,4´-DMAB affects the position and shape of the band at 1594 cm^{-1} (Fig. 1, purple bar), which belongs to the stretching vibration of C=C bond of the aromatic ring of the monomer. This type of vibration of the dimerized molecule occurs around 1580 cm^{-1}. For this reason, in most cases, this vibration of the dimer is not independently observable in the spectra but is manifested by the deformation of the more intense monomer band. In the spectral region 1450 to 1350 cm^{-1} (Fig. 1, green bar), bands of stretching N=N bond (usually ~ 1434 and 1390 cm^{-1}) can be observed in the case of the formation of 4,4´-DMAB. These bands tend to be very intense due to the large change in polarizability during the vibrational motion of the molecule. The similarly intense band is located around 1141 cm^{-1}

---

* Corresponding Author´s Email: kopali@vscht.cz

(Fig. 1, blue bar) that corresponds to the deformation vibration of the C-H bond of the ortho-hydrogens on the aromatic rings of the dimer. In all cases, a relatively intensive band of C-S stretching of 4-ABT (~ 1080 cm^{-1}) occurs [6].

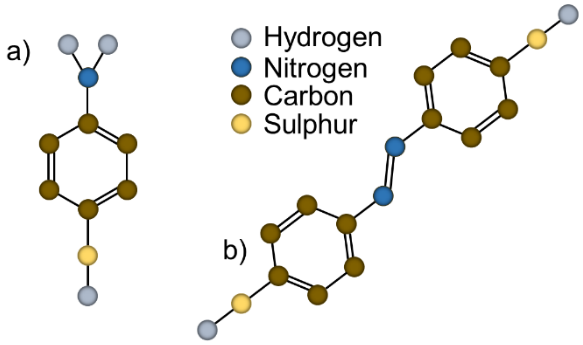

Figure 2. Molecular structure of a) 4-aminobenzenethiol and b) 4,4´-dimercaptoazobenzene.

Silver substrate

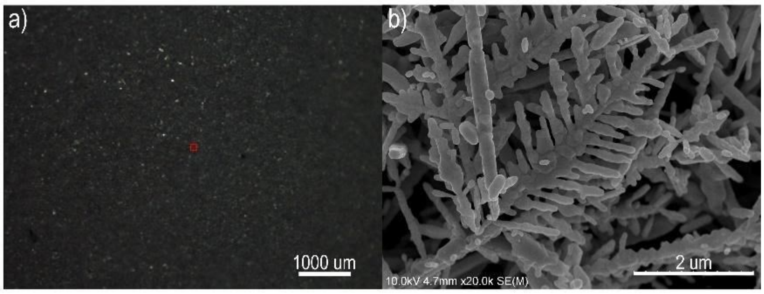

Figure 3. Images of Ag surface taken by a) optical and b) scanning electron microscope. The red square indicates the laser spot.

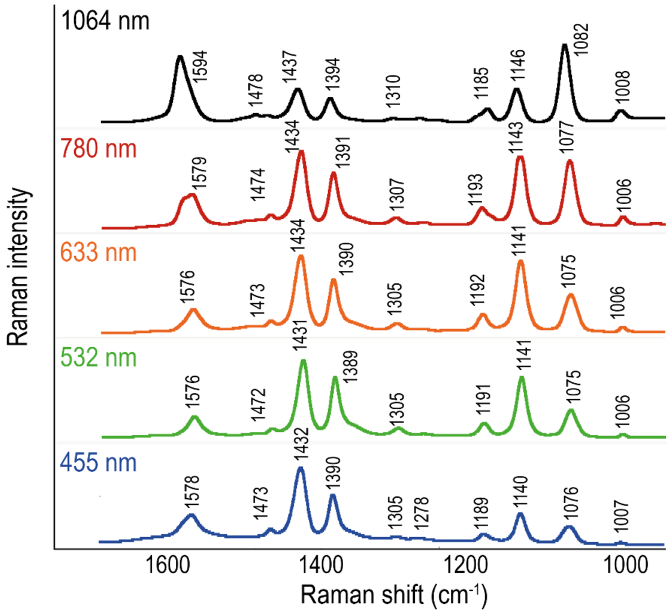

Figure 4. SERS spectra of 4-ABT/4,4´-DMAB on Ag surface.

* Corresponding Author´s Email: kopali@vscht.cz

Optical and electron microscopy images of silver substrates are shown in Fig. 3. Dendritic Ag structures have formed. The silver surface is covered continuously by the displayed nanostructures.

The SERS spectra of 4-ABT on the Ag surface taken using different excitation wavelengths are shown in Figure 4. In the highest observed spectral region, it is evident that the 1594 cm^{-1} band deformation occurs. In the spectrum measured with an excitation wavelength of 780 nm, two-band maxima, due to the presence of 4,4´-DMAB, are well observable. Along with another shift to lower wavelengths, the maximum of this band moves to lower values of the Raman shift. Bands with maxima at 1437, 1394, and 1146 cm^{-1} are also present in the spectrum. Given these findings, we can clearly state that 4,4´-DMAB forms on the Ag surface. Even from the dependence of the ratio of the 1437/1082 (4,4´-DMAB/4-ABT) band areas on the excitation energy, we can say that the amount of dimer on the substrate surface is linearly dependent on the radiation energy (Fig. 5).

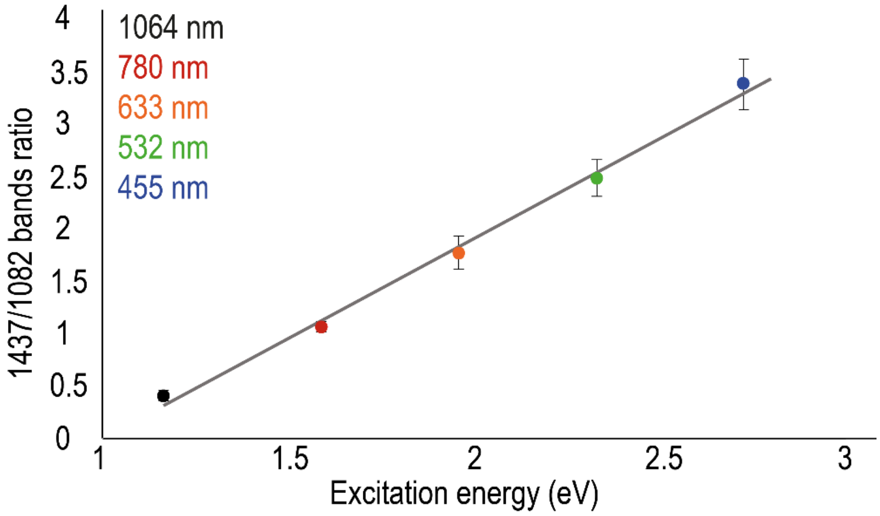

Figure 5. Dependence of the ratio of band areas 1437/1082 (4,4´-DMAB/4-ABT) on the excitation energy.

Gold substrate

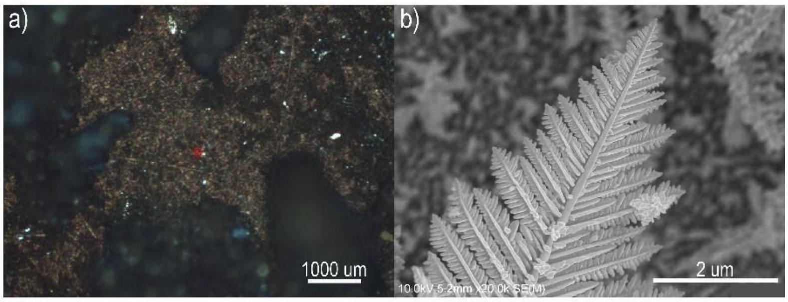

Figure 6. Images of Au surface taken by a) optical and b) scanning electron microscope. The red square indicates the laser spot.

---

* Corresponding Author´s Email: kopali@vscht.cz

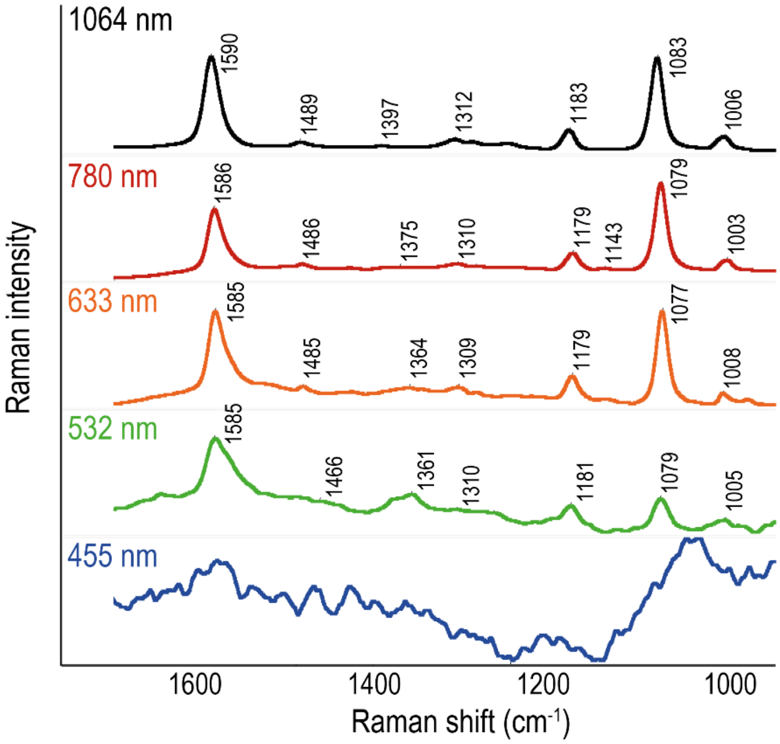

Figure 7. SERS spectra 4-ABT/4,4´-DMAB on Au surface.

Dendritic Au structures formed on the Pt target, are obvious in Fig. 6. These features are smaller and differently arranged than in the case of the Ag substrate. The golden "islands" form on the target surface and the SERS spectra have been measured from these areas. In SERS spectra of 4-ABT on Au surface (Fig. 7) we observe only a slight evidence of the 4,4´-DMAB bands. The band at the 1590 cm^{-1} gradually widens together with the decreasing value of the excitation wavelength, which indicates an increase in the percentage of the dimer. In the spectrum measured with an excitation wavelength of 633 nm, we can also observe a slightly increased background at 1430, 1364, and 1140 cm^{-1} where 4,4-’DMAB bands should appear. It is likely that in the spectra measured with excitation wavelengths of 455 and 532 nm, the dimer bands would already be visible. However, these wavelengths are no longer suitable for gold surfaces prepared in this way, and their surface plasmon resonance maximum tuned to the longer wavelength. But in the spectrum measured with excitation wavelength 532 nm, we can sense another 1590 cm^{-1} band broadening and 1430 and 1364 cm^{-1} bands intensity increase. It is also evident that at the excitation wavelength of 455 nm, the SERS phenomenon no longer occurs here and even bands of analyte in the monomeric form are not observable. For these reasons, it was not possible to determine the exact dependence of the amount of dimer on the excitation wavelength. Likely, the reaction appears more frequently with increasing radiation energy, similarly as in the case of Ag substrate.

---

* Corresponding Author´s Email: kopali@vscht.cz

Copper substrate

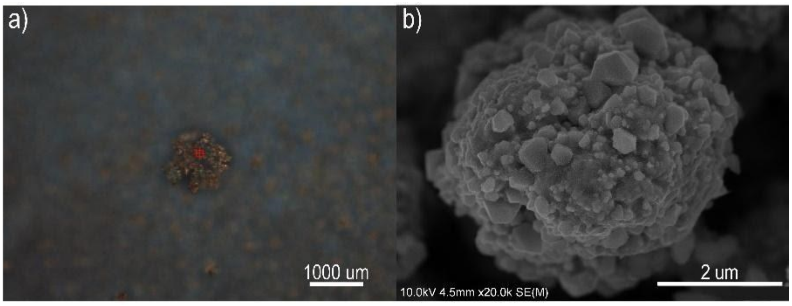

Figure 8. Images of Cu surface taken by a) optical and b) scanning electron microscope. The red square indicates the laser spot.

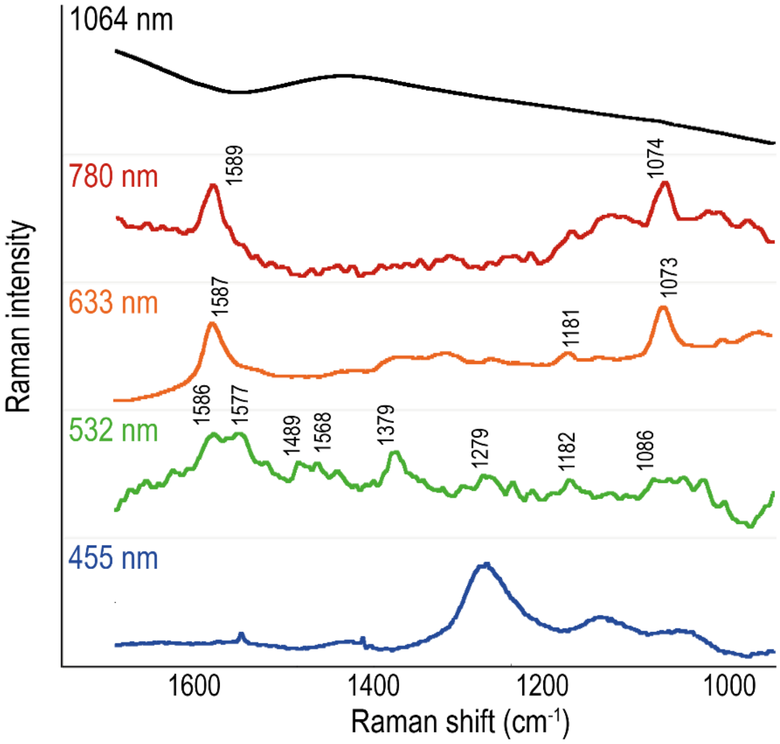

Figure 9. SERS spectra 4-ABT/4,4´-DMAB on Cu surface.

Unlike Ag and Au surfaces, spherical ("cauliflower-like") structures of various heights formed on the Cu surface (Fig. 8). The best SERS spectra were measured when focusing the laser at the points of contact of elevated objects. When focusing on the vertices of these structures, the resulting signal was disproportionately weaker. The Cu substrate did not enhance the signal 4-ABT to such asextent as can be seen from the SERS spectra on Ag and Au surfaces that is due to the optical properties of Cu (Fig. 9). Bands of 4-ABT were observed in the spectra measured with excitation wavelengths of 780 and 633 nm, although the signal in the first-mentioned spectrum was relatively weak. In the spectra measured with an excitation wavelength of 633 nm, again, we observe a relatively wide band at 1587 cm^{-1} indicating possible dimer formation. Although it occurs rather to a less extent, more at the incidence of radiation at lower wavelengths (532 and 455 nm). However, the analyte signal in these spectra was not observable despite the high noise intensity. For these reasons, there is not possible to indication about any trend regarding the formation of 4,4´-DMAB on Cu nanostructures.

---

* Corresponding Author´s Email: kopali@vscht.cz

CONCLUSION

In this work, photochemical dimerization of 4-ABT on large-scaled Ag, Au, and Cu surfaces prepared by electrodeposition was studied using SERS spectroscopy. In addition to the effect of plasmonic metal used, the influence of the excitation wavelength was also investigated.

The dimerization occurs most on silver substrates, less on gold substrates that is consistent with our previous experiments. In the case of the copper substrate, there is also small evidence of dimer creation, which happens after the interaction of visible light radiation with surface-bonded molecules. Due to the differences between the published literature and the Cu substrate examined here, we concluded that the physical properties like the size and shape of the formed nanostructure play an important role.

The assumption that the degree of conversion of the photochemical reaction increases with the energy of the incident radiation was confirmed.[9] The 4,4´-DMAB signal was very well observable in the spectra measured on the Ag substrate, the linear dependence of the amount of dimer on the energy of the incident radiation was obtained. For the remaining two surfaces, it was not possible to obtain a similar value due to the lower response of 4,4´-DMAB.

Further planned experiments will also investigate the dependence of the degree of dimerization on differently prepared plasmonic nanostructures, e.g. on metal colloidal systems or large-scaled substrates prepared by galvanic deposition. The effect of the gradual change in pH, applied voltage, and other reaction variables would be assessed. Based on these experiments, it should be possible to compile an approximate reaction model that could serve to estimate dimerization on previously unexplored substrates.

ACKNOWLEDGMENTS

The authors acknowledge the assistance provided by the Research Infrastructure NanoEnviCz, supported by the Ministry of Education, Youth and Sports of the Czech Republic under Project No. LM2018124. The author T.C. is especially thankful to the Ministry of Education, Youth and Sports of the Czech Republic – DKRVO (RP/CPS/2020/006). The authors also acknowledge the institutional financial support of the University of Chemistry and Technology Prague.

REFERENCES

[1] Fleischmann, M., Hendra, P.J., McQuillan, A.J. 1974. Raman spectra of pyridine adsorbed at a silver electrode. *Chemical Physics Letters,* 26(2):163-166.

[2] Procházka, M. 2016. *Surface-enhanced Raman spectroscopy: Bioanalytical, Biomolecular and Medical Applications*, edited by Greenbaum E. Switzerland: Springer International Publishing.

[3] Švecová, M., Ulbrich, P., Dendisová, M., Matějka, P. 2018. SERS study of riboflavin on green-synthesized silver nanoparticles prepared by reduction using different flavonoids: What is the role of flavonoid used? *Spectrochimica Acta Part A-Molecular and Biomolecular Spectroscopy,* 195:236-245.

[4] Dendisová-Vyškovská, M., Prokopec, V., Člupek, M., Matějka, P. 2012. Comparison of SERS effectiveness of copper substrates prepared by different methods: what are the values of enhancement factors? *Journal of Raman Spectroscopy,* 43(2):181-186.

[5] Shin, D. 2017. Two different behaviors in 4-ABT and 4,4′-DMAB surface enhanced Raman spectroscopy. *Journal of Raman Spectroscopy,* 48(2):343-347.

[6] Dendisová, M., Havránek, L., Ončák, M., Matějka, P. 2013. In situ sers study of azobenzene derivative formation from 4-aminobenzenethiol on gold, silver, and copper nanostructured surfaces: What is the role of applied potential and used metal? *Journal of Physical Chemistry C,* 117:21245-21253.

[7] Kim, K., Yoon, J.K., Lee, H.B., Shin, D., Shin, K.S. 2011. Surface-enhanced Raman scattering of 4-aminobenzenethiol in Ag sol: relative intensity of a1- and b2-type bands in variant against aggregation of Ag nanoparticles. *Langmuir,* 27(8):4526-4531.

[8] Kim, K., Kim, K.L., Shin, D., Choi, J.-Y., Shin, K.S. 2012. Surface-enhanced Raman scattering of 4-aminobenzenethiol on Ag and Au: pH dependence of b2-type bands. *Journal of Physical Chemistry C, 116(7):*4774-4779.

---

* Corresponding Author´s Email: kopali@vscht.cz

[9] Kim, K.L., Lee, S.J., Kim, K. 2004. Surface-enhanced Raman scattering of benzyl phenyl sulfide in silver sol: excitation-wavelength-dependent surface-induced photoreaction. *Journal of Physical Chemistry B,* 108(26):9216-3220.

[10] Novák, V., Dendisová, M., Matějka, P., Bouř, P. 2016. Explanation of surface-enhanced Raman scattering intensities of p-aminobenzenethiol by density functional computations. *Journal of Physical Chemistry C,* 120:18275-18280.

Chapter 10

Part 2: Progress in Nanomaterials Characterization

Surface zeta potential analysis of novel graphene oxide coatings for membranes

T. Luxbacher*[1], R. Kohl[1],
[1]Anton Paar GmbH, Austria

ABSTRACT

2D materials such as graphene and graphene oxide introduce new pathways for the development of novel materials with superior properties. Nanocomposite coatings containing graphene oxide are investigated for their capability to enhance the performance of membranes for water treatment applications. We use the analysis of the zeta potential to confirm the presence of graphene oxide at the surface of such nanocomposite membrane coatings, which is a requirement for their activity and interaction with the aqueous environment.

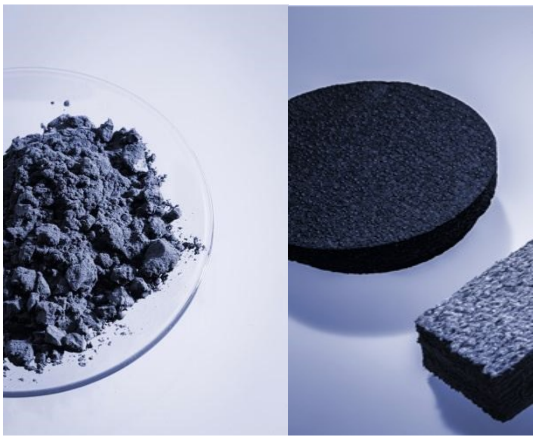

Keywords: surface zeta potential; graphene oxide; coatings; membranes

INTRODUCTION

The discovery of graphene has opened completely new technological pathways in material science. Nowadays graphene and its derivates can be found in a large number of applications due to their outstanding properties. Such applications can be found in the fields of electronics and batteries but also in biomedical applications including drug delivery, biosensing, bioimaging, and scaffolds for tissue engineering.

The hydrophilic nature of graphene oxide makes this graphene derivative also attractive for the advancement of membrane technology. Graphene oxide is expected to increase the water permeability, to suppress membrane fouling, and to introduce a reinforcement of polymer membranes.

We report on the modification of a polymer membrane by a graphene oxide-polyelectrolyte composite coating and its effect on the charging behaviour at the membrane-water interface. A second example considers the formation of a ceramic membrane composed of graphene oxide and aluminium oxide.

---

* Corresponding Author´s Email: pc-application@anton-paar.com

Chapter 10

Part 2: Progress in Nanomaterials Characterization

The characterization of the surface and interfacial charge of polymer and ceramic membranes employs the measurement of the streaming potential for the calculation of the surface zeta potential.

Graphene oxide composite membranes

Graphene with its two-dimensional planar structure increases the mechanical strength, the thermal stability and the electrical properties of composites, and has thus received attention as a suitable candidate for the development of membranes for water treatment processes. In contrast to graphene, graphene oxide (GO) exhibits an increased hydrophilicity due to the oxygen-containing functional groups (C=O, C–OH). The latter lead to a better dispersion of GO in water and other polar solvents thereby maintaining the superior properties of graphene. The amphiphilic character of GO makes it compatible with polymers, which are used as the base material in the low-cost membrane production process, and enhances the water permeability and the antifouling properties of membranes Additionally, graphene and GO are low-cost alternatives to carbon nanotubes (CNT) or carbon nanofibers (CNF).

These properties make GO a potential modifier for polymer but also ceramic membranes for wastewater treatment processes.

Membranes and the zeta potential

The zeta potential is a solid-water interfacial parameter and representative for the material surface charge. The zeta potential helps to predict electrostatic interactions between material surfaces and solutes in a surrounding aqueous solution. Furthermore, the analysis of the zeta potential is a sensitive method to detect changes in the surface chemistry. In the field of membrane applications, the zeta potential contributes to the rejection of solutes and to membrane fouling. With the help of zeta potential analysis, it is possible to determine the coverage of the membrane surface by a thin-film coating and the stability of such coating.

EXPERIMENTAL

Two types of nanocomposite coatings containing graphene oxide where prepared as potential candidates for novel membrane materials. A multilayer coating with alternating layers of GO and the cationic polyelectrolyte polyethylenimine (PEI) was deposited on a flat sheet polymer ultrafiltration membrane. A second nanocomposite coatings was of ceramic nature and composed of GO and nanocrystalline aluminium oxide (Al_2O_3).

The instrument SurPASS 3 was used for the zeta potential analyses of flat sheet membranes with different GO nanocomposite coatings. Small sample pieces of 20 mm x 10 mm were adhered to the sample holders of the Adjustable Gap Cell with the active coating facing upwards (Figure 1).

Streaming potential measurements were performed with an aqueous 0.001 mol/l KCl solution used as the background electrolyte. The pH dependence of the zeta potential was recorded automatically with the integrated dosing unit to determine the isoelectric point (IEP, pH value where the zeta potential is 0 mV and a charge reversal takes place) of each GO coating.

---

* Corresponding Author´s Email: pc-application@anton-paar.com

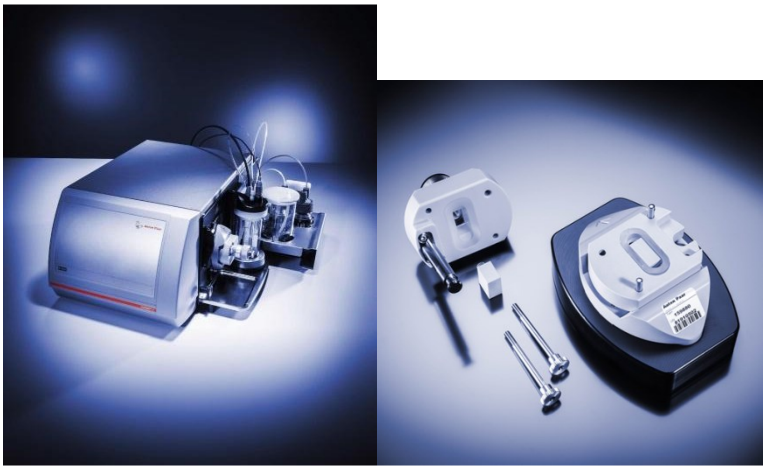

Figure 1. Left: SurPASS 3 equipped with dosing unit. Right: Adjustable Gap Cell with sample holders with a cross-section of 20 x 10 mm^2.

RESULTS

GO coating on a polymer membrane

The combination of GO nanoparticles with the cationic polyelectrolyte poly(ethylene imine), PEI, was used to improve the rejection of a polyacrylontrile membrane (PAN) for ultrafiltration (UF) thereby maintaining the high water permeability [1]. Figure 2 shows the pH dependence of the zeta potential for such a PAN UF membrane with a GO│PEI coating deposited by a layer-by-layer method. Above the IEP at pH 3.3, the coating is negatively charged with the zeta potential approaching ς = –40 mV at neutral and alkaline pH.

In order to interpret the observed zeta potential as a representative for the surface charge of the GO│PEI coating and to understand the composition of this coating, Figure 2 also displays the zeta potential for a pristine PAN membrane, for the PAN membrane coated solely with PEI, and for a membrane coated with a stand-alone film of GO.

We find significant differences in the zeta potential for each of these membrane samples. Although the zeta potential and therefore the electrokinetic charge density $\square_{ek}$ of the pristine and GO│PEI-coated PAN membranes are similar at pH 8-9 (ζ ~ -40 mV, σ_{ek} ~ -0.34 µC/cm^2), the pH dependences and the isoelectric points give evidence for the modification of PAN by the GO│PEI coating.

The sole coating of the PAN membrane by the cationic polyelectrolyte PEI shifts the IEP from pH 4.6 for the pristine PAN membrane to pH 8.9. The secondary amine groups of PEI get protonated at low and medium pH. Due to their strongly basic character, rather highly alkaline conditions are required to suppress this protonation. At pH 8.9 of the bulk aqueous solution we find an electroneutral condition at the membrane-water interface and thus the IEP for the PEI-coated PAN membrane. Since the IEP for the GO│PEI-coated membrane is shifted to even lower pH compared to the IEP of PAN, we conclude that PEI obviously does not contribute to the charge at the outermost surface of the GO│PEI coating.

A comparison of the zeta potential for the GO│PEI-coated PAN membrane with the zeta potential for a stand-alone membrane of graphene oxide reveals the apparent nature of the GO│PEI coating, which is dominated by the presence of GO. Obviously, the layer-by-layer coating achieves a well separated stack of polymer (PEI) and GO layers with GO determining the terminal layer.

---

* Corresponding Author´s Email: pc-application@anton-paar.com

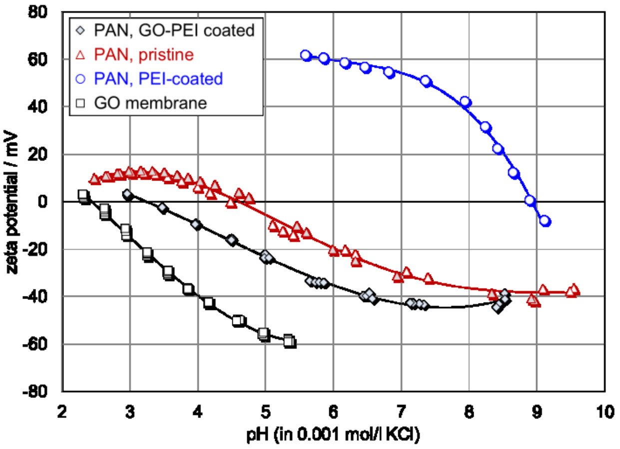

Figure 2. pH dependence of the zeta potential for a pristine polyacrylonitrile (PAN) membrane for UF, for the PAN membrane coated with a multilayer of GO and PEI, for a PEI- coated PAN membrane, and for a GO membrane.

GO│Al_2O_3 composite membrane

In another example we use the same zeta potential results for a membrane coated with a stand-alone porous film of GO shown in Figure 2 to explain the composition of a composite layer of GO and Al_2O_3. Figure 3 shows the pH dependence of the zeta potential for such a GO|Al_2O_3 coating and compares this result with the zeta potential of the GO coated membrane and with the zeta potential obtained for a single-channel tubular alumina ceramic membrane for microfiltration (MF). While all measurements of the streaming potential for flat membrane surfaces employ the Adjustable Gap Cell, the zeta potential analysis of the microporous ceramic membrane utilizes the measuring cell for tubular membranes [2].

The IEP 5.2 of the GO│Al_2O_3 composite layer is found in between the IEP 2.4 for the GO stand-alone film and the IEP 6.5 for the alumina MF membrane. To conclude on the composition of the GO│Al_2O_3 layer, we first elucidate the zeta potential of the Al_2O_3 ceramic membrane. For this purpose, we add another dependence of the zeta potential on the pH of the aqueous KCl solution, which was obtained for a sample plug of corundum powder. The difference in the IEPs of ΔpH = 1.5 for corundum powder and the alumina membrane may be explained by an ageing effect for the membrane surface. Note that surface of Al_2O_3 exhibits a rather complex behaviour and the IEP may range from pH 4 for single-crystalline sapphire [3] to pH > 9 for Al_2O_3 nanoparticles in dispersion [4].

For the interpretation of the composition of the outermost surface of the GO│Al_2O_3 layer, we refer to the IEP 8 of corundum powder and to the IEP 2.4 of the purely GO membrane. Based on the comparison of these materials and their IEPs, we conclude on a homogeneous composition of the layer with a contribution of 50% by GO and 50% by Al_2O_3.

* Corresponding Author´s Email: pc-application@anton-paar.com

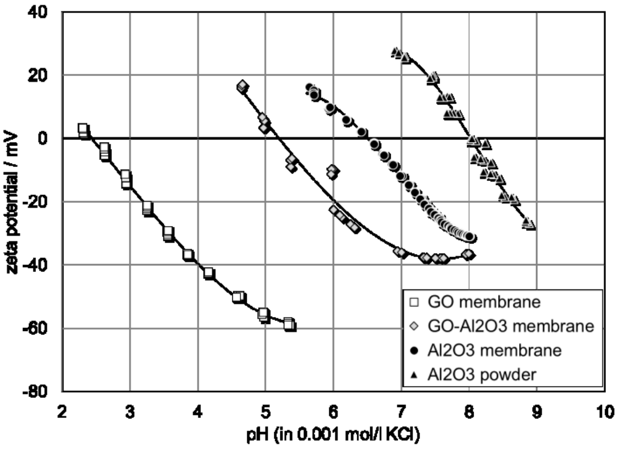

Figure 3. pH dependence of the zeta potential for a GO|Al_2O_3 nanocomposite coating, a stand-alone film of GO on a membrane, and two samples of Al_2O_3 (a single-channel tubular ceramic MF membrane and corundum powder).

SUMMARY

New generation 2D materials such as graphene oxide offer a high potential for the development of novel materials with advanced properties. The tunability of GO makes it a promising candidate for the modification of membranes for water treatment to improve the water transport and to suppress membrane fouling. The transfer of knowledge about the correlation of the surface zeta potential with salt rejection and the fouling propensity of (primarily) polymer membranes, which was developed in the past decades, to the characterization of novel coatings containing GO is straightforward. This report illustrates results for graphene oxide and GO-containing surface coatings for both polymeric and ceramic films. The IEPs summarized in Table 1 demonstrate the variability of surfaces prepared by using GO as a composite material. A comparison of the IEP of the composite material with the IEPs of the individual components enables an estimation of the surface composition. The derived contribution of GO of the composite layers to the zeta potential is also shown in Table 1.

Table 1. Isoelectric points of materials discussed in this report and surface contribution of GO to composite layers.

Sample	**IEP**	**GO contribution**
GO membrane	2.4	100 %
PAN membrane	4.6	n/a
GO│PEI LbL-coated PAN	3.3	85 %
PEI-coated PAN	8.9	n/a
GO-Al_2O_3 composite	5.2	50 %
Al_2O_3 MF membrane	6.5	n/a
Corundum powder	8	n/a

---

* Corresponding Author´s Email: pc-application@anton-paar.com

REFERENCES

[1] Andreeva, D.V., Trushin, M., Nikitna, A., Costa, M.C.F., Cherepanov, P.V., Holwill, M., Chen, S., Yang, K., Chee, S.W., Mirsaidov, U., Castro Neto, A.H., Novoselov, K.S. 2021. Two-dimensional adaptive membranes with programmable water and ionic channels. *Nature Nanotechnology,* 16(2):174-180.

[2] *From pottery to membranes: Characterization of ceramic powders and surfaces*. 2020. Application report XPCIA005EN. Anton Paar GmbH.

[3] Lützenkirchen, J., Zimmermann, R., Preočanin, T., Filby, A., Kupcik, T., Küttner, D., Abdelmonem, A., Schild, D., Rabung, T., Plaschke, M., Brandenstein, F., Werner, C., Geckeis, H. 2010. An attempt to explain bimodal behaviour of the sapphire c-plane electrolyte interface. *Advances in Colloid and Interface Science,* 157(1-2):61-74.

[4] Kosmulski, M. 2002. The pH-dependent surface charging and the points of zero charge. J*ournal of Colloid and Interface Science,* 253(1):77-87.

---

* Corresponding Author´s Email: pc-application@anton-paar.com

Nanoscale Investigation of Multilayer Graphene Flakes using Contactless Electrical Modes of Tosca Atomic Force Microscope

Gregor Plohl*
Anton Paar Gmbh / Austria

ABSTRACT

Graphene is a 2D material with promising physical and electronic properties and has been widely studied because of its potential applications in next-generation electronics, photovoltaics and life science. The contactless electrical modes of atomic force microscope Tosca were used to accurately characterize the material and functional properties of graphene flakes on nanometer scale.

Keywords: AFM; KPFM; EFM; two pass technique; work function; surface potential microscopy; thin films

INTRODUCTION

Graphene was discovered, isolated and characterized by A.K Geim and K.S. Novoselov in 2004 [1]. They were able to isolate a monolayer of graphene from a piece of graphite by using an ordinary Scotch tape. The authors received the 2010 Nobel Prize in Physics for "*groundbreaking experiments regarding the two-dimensional graphene*" [2].

Graphene is made of sp^2 – hybridized carbon atoms arranged in a one-atom-thick hexagonal (honeycomb) lattice structure [3], as shown in Figure 1. This two-dimensional (2D) material is a basic building block for all graphitic materials of other dimensionalities; it can form a zero-dimensional (0D) quantum dots, it can be rolled into one-dimensional (1D) nanotubes or stacked to form three-dimensional (3D) graphite.

Graphene has remarkable mechanical, electrical, magnetic and thermal properties. It is one of the thinnest (thickness of 0.345 nm), strongest (about 100 times stronger than steel) and lightest material known to exist with excellent electrical and thermal conductivity. Due to its unique electronic characteristics, graphene has been viewed as a promising candidate to replace conventional silicon-based electronics. Moreover, graphene has an enormous potential in many applications such as semiconductors, photovoltaics, life science, energy storage, printable transparent electronics and many others.

Nevertheless, the widespread implementation of graphene is, overall, still in the research and development stage. Therefore, there is a great scientific interest for an in-depth understanding and characterization of various physical properties of graphene-based materials on a nanoscale. The advanced modes of atomic force microscopy (AFM) are powerful tools which enable a great progress in the field of graphene related research. This report demonstrates the application of contactless electrical modes, namely the electrostatic force microscopy and Kelvin probe microscopy of Tosca atomic force microscope for nano-characterization of material functional properties of graphene flakes.

---

* Corresponding Author´s Email: support-nsp@anton-paar.com

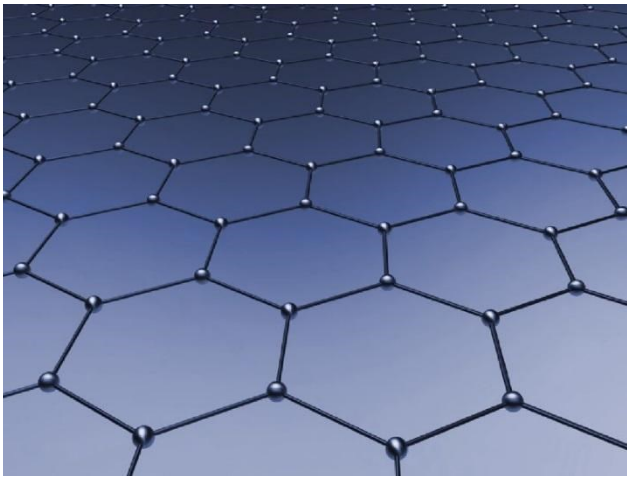

Figure 1. Hexagonal lattice structure of graphene made of carbon atoms.

EXPERIMENTAL/THEORETICAL STUDY

Electrical modes are techniques derived from atomic force microscopy (AFM) used to measure local electric properties together with the topography of the sample at nanoscale. First measurements of the contact potential difference between different materials using AFM were reported by Nonnenmacher, O'Boyle and Wickramasinge in 1991 [4] shortly after invention of AFM [5]. They simultaneously measured the topography and contact potential difference of gold, platinum and palladium surfaces. Electrical modes require a conductive cantilever and an electrical contact between the sample and sample table must be established. No special sample preparation is necessary and the measurements can be performed under ambient conditions.

The Kelvin probe force microscopy (KPFM) and electrostatic force microscopy (EFM) record the long-range electrostatic forces and provide information about electric properties such as contact potential difference, electric surface potential, work function and electric charge distribution.

Both EFM and KPFM can operate in two different ways, known as single pass and two pass techniques. Single pass technique records the topography and the surface potential concurrently, while the traditional two pass techniques requires two scanning passes. Figure 2 schematically shows the principle of the two-pass technique.

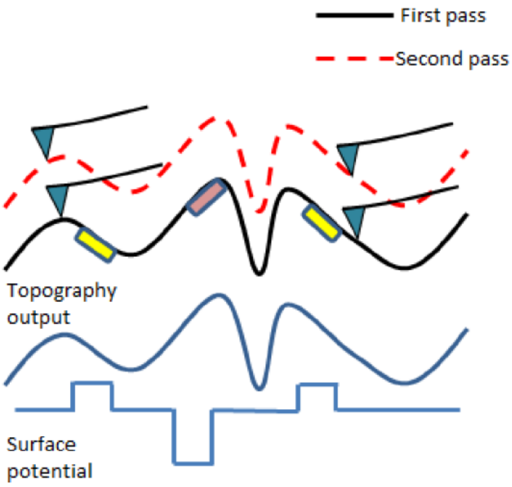

Figure 2. Two pass technique AFM.

* Corresponding Author´s Email: support-nsp@anton-paar.com

The two-pass technique, implemented in Tosca atomic force microscope, uses the first pass to record the surface line profile by tapping mode. Then the cantilever is lifted to a predefined distance above the surface, the so-called lift offset, and follows the recorded surface line profile to measure the signal of long-range electrostatic forces in the second pass. This two-pass technique effectively minimizes crosstalk from topographic effects.

Tapping mode is a form of dynamic imaging. In general, the dynamic imaging mode oscillates the cantilever near its resonance frequency. The interaction forces (either mechanical, van der Walls, electric or magnetic) between the probe and sample produce a frequency shift of the resonance frequency, amplitude and phase between excitation and oscillation of the cantilever. This variation in the cantilever oscillation behavior provides information about the probe-sample interaction forces. The changes can be monitored either by amplitude modulation (AM) or frequency modulation (FM) techniques and used to reconstruct height and other physical properties. Tapping mode uses the AM detection technique, where the cantilever oscillation amplitude is kept constant via a feedback loop.

Electrostatic Force Microscope (EFM)

Electrostatic force microscopy maps the local electric potential and charge distribution by probing the electrostatic force between the biased tip and the sample.

During the lift pass an external bias voltage is applied between the cantilever tip and the sample while the cantilever continues to oscillate at the tapping frequency. As the cantilever tip scans over a surface, its oscillation is affected by the electrostatic forces. Measured amplitude and phase shifts reveal the electric potential distribution on the sample surface. EFM provides qualitative information about electric field variations and is used for electrical failure analysis, detecting trapped charges, mapping electric polarization, etc.

Kelvin Probe Force Microscope (KPFM)

While the EFM mode is used mainly for the qualitative measurements of surface potential, the KPFM mode provides the quantitative mapping of the contact potential difference:

$$V_{CPD} = \frac{\varphi_{tip} - \varphi_S}{e} \qquad (1)$$

where e is the elementary charge and and φ_{tip} and φ_S are the work functions of the probe and sample, respectively. The work function is the minimum energy needed to remove an electron from a solid surface.

In contrast to EFM, the cantilever in lift pass of KPFM is no longer excited mechanically but electrically by applying an external voltage V_{ext} between the tip and the sample as

$$V_{ext} = V_{DC} + V_{AC}\sin(\omega_{mod}t) \qquad (2)$$

where and ω_{mod} is the modulation frequency, and V_{DC} and V_{AC} are amplitudes of DC and AC components, respectively. The modulation frequency is (usually) selected to be equal to the resonant frequency of the AFM cantilever. The electrostatic force between the sample and the tip is given as

---

* Corresponding Author´s Email: support-nsp@anton-paar.com

$$F_e(Z) = -\frac{1}{2}(\Delta V)^2 \frac{dC}{dz} \tag{3}$$

where C denotes the capacitance between the tip and the sample, z is the tip-sample distance and $\Delta V = V_{ext}$ - V_{CPD} is the potential difference between the tip and the sample. The feedback electronics, based on AM detection mechanism, adjusts the bias voltage V_{DC} until the oscillation amplitude at the modulation frequency ω_{mod} is nullified, thus $V_{DC} = V_{CPD}$.

Further, the work function of the sample φ_S can be calculated using Eq. (1) when the tip work function φ_{tip} is is known. The work function influences many surface phenomena (adsorption, charge transfer, photoelectric activity, catalytic activity, etc.) and is a critical parameter in solid-state electronics. Therefore, KPFM is often used to study metallic and semi-conducting nanostructures in a variety of devices from biosensors to solar cells [7].

The exfoliated graphene flakes deposited on a silicon wafer were investigated by Tosca atomic force microscope under ambient conditions. An acoustic enclosure and active vibration table isolated the AFM device from surrounding vibrations. The measurements were performed using a standard Arrow-EFM silicon AFM cantilever with platinum iridium coating. The cantilever has a typical resonance frequency of 75 kHz and a force constant of 2.8 N/m.

Graphene flakes of various shapes and surface areas were deposited on a silicon wafer. The flake thickness ranges from one graphene layer to some hundreds of nm. Figure 3 shows a microscopic image of the deposited multilayer graphene flakes.

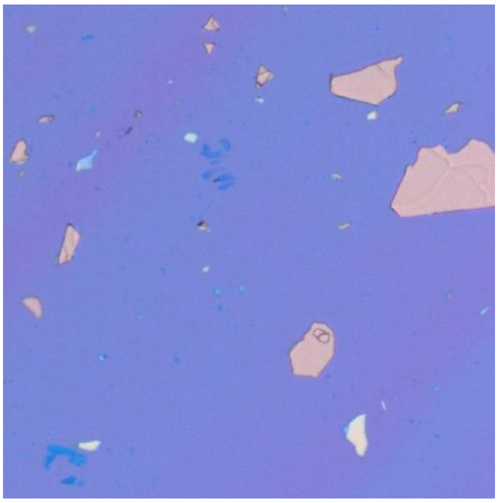

Figure 3. Optical image (1000 x 1000 µm) of the exfoliated graphene flakes on a silicon wafer.

RESULTS AND DISCUSSION

The AFM investigation of graphene flakes was performed on a 15 x 15 µm area with a resolution of 750 x 750 pixels and a scan rate of 0.5 line/second. Both electric modes, EFM and KPFM, were employed at the same position.

---

* Corresponding Author´s Email: support-nsp@anton-paar.com

Topography

The topography data was recorded during the first pass of the two-pass technique by tapping mode. The same topographic results were obtained by both methods, EFM and KPFM. In addition to the height profile, the tapping mode also provides the phase contrast of the surface, which is related to the mechanical interaction between the tip and the sample and thus represents the distribution of the mechanical properties of the surface. Hence, the phase contrast data allows distinguishing regions with different mechanical properties.

Figure 4 shows the results of tapping mode investigations of the 15 x 15 µm scan area. The topographic image shows elevated graphene structures on a flat silicon wafer. Overall, the graphene flake has a very smooth surface with some residues, presumably coming from the graphene synthesis process.

Figure 4 (middle) shows the 2D height profile extracted from the topography data presented in Figure 4 (top). The investigated graphene flake is composed of about 3 to 6 layers of graphene and reach up to around 2 nm in height. The height difference of a single graphene layer, which is about 0.345 nm, is clearly visible.

The phase contrast image, Figure 4 (bottom), clearly displays a two phase separated structures. From the knowledge about material properties of graphene and silicon it may be concluded that the brighter regions correspond to the stiffer graphene flakes and darker regions to silicon wafer. As expected, the phase contrast does not depend on the thickness of the graphene flakes.

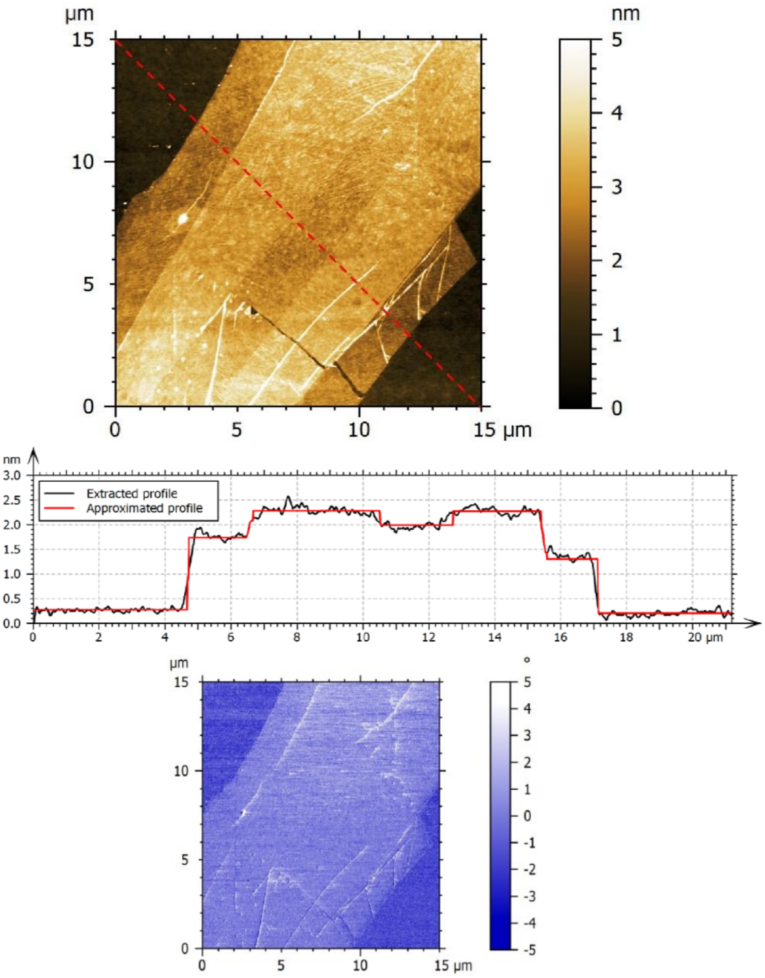

Figure 4. Results of the tapping mode investigations of graphene flakes. The height image (top), where the red line indicates the position of the extracted 2D height profile shown in the middle. Phase contrast image (bottom) indicates two mechanically different materials.

---

* Corresponding Author´s Email: support-nsp@anton-paar.com

EFM results

EFM method provides qualitative information about electric field variations by applying an external bias voltage, in the range from -10 V to 10 V, between the tip and the sample.
Figure 5 presents the results of EFM mode measurements performed at the lift offset of 15 nm and DC bias voltage set to 8 V.

A 3D superposition of the EMF phase signal and the topography is shown in Figure 5 (top). A highly contrasted, stepwise phase shift at silicon-graphene transition can be observed. On the surface of a single graphene flakes practically no phase shift between different height levels of graphene layers can be observed. These findings are confirmed by analyzing the extracted 2D EFM phase profile shown in Figure 5 (bottom).

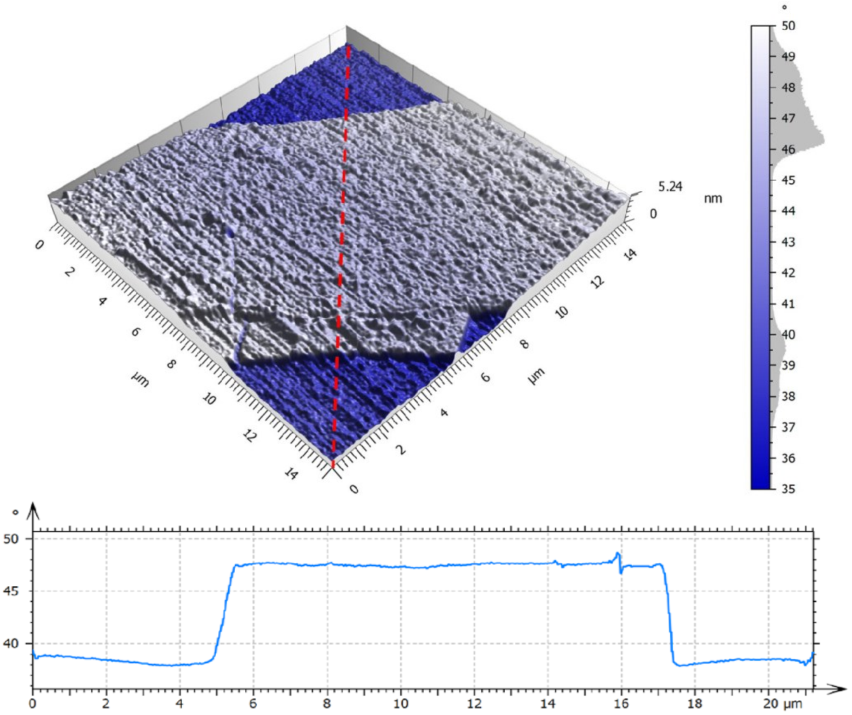

Figure 5. Results of EFM mode investigations of graphene flakes. Superposition of 3D topography and EFM phase signal (top), where the red line indicates the position of the extracted 2D phase profile shown below. A sharp, stepwise phase shift at the silicon-graphene transition can be observed.

---

* Corresponding Author´s Email: support-nsp@anton-paar.com

KPFM results

The KPFM signal was obtained in the lift pass with the lift offset of 15 nm and AC excitation amplitude to 9 V. The results of KPFM investigations are presented in Figure 6.

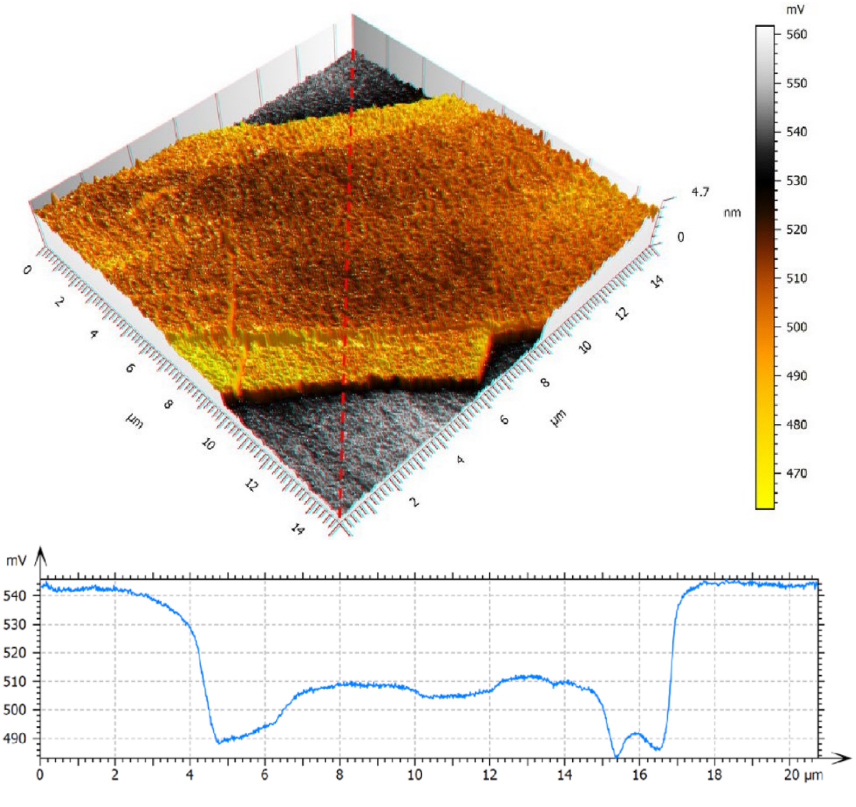

Figure 6. Results of KPFM mode investigations of graphene flake. Superposition of 3D topography and contact potential distribution (top), where the red line indicates the position of the extracted 2D profile shown below. The electric potential difference between graphene and silicon depends on the flake thickness and lies between 30 and 60 mV.

Figure 6 (top) presents a 3D superposition of the contact potential distribution and the topography, while Figure 6 (bottom) shows the extracted 2D profile of the contact potential difference.

By analyzing the KPFM results, similar conclusion can be made as in the case of EFM investigation. The data obtained by KPFM confirms the findings of EFM method and adds the quantitative aspects. KPFM resolves the contact potential difference on sub-nm scale to precisely distinguish graphene layers of around 0.35 nm.

The electric potential difference between the graphene flakes and silicon wafer is between 30 and 60 mV and shows to depend on the graphene flake thickness. Higher contact potential difference corresponds to the thinner graphene flakes and vice versa. This is in agreement with literature [7] where it has been shown that increasing the number of layer of graphene can eventually shield completely the substrate potential.

---

* Corresponding Author´s Email: support-nsp@anton-paar.com

CONCLUSION

This short section should summaries the work based on the facts in evidence and point out the main areas covered in the writing. It may also contain the future directions of the work.

The electric modes of the atomic force microscope Tosca were used to image nanoscale topographic and electrostatic properties of multilayer graphene flakes. The topography measurements were able to resolve single layers of graphene in the composition of the examined graphene flake. The electrostatic force microscopy (EFM) provides qualitative information about local electric potential by detecting the electrostatic force between the biased tip and the sample.

In contrast, the Kelvin probe force microscopy (KPFM) provides quantitative information about contact potential difference by using additional feedback control. Further, KPFM was able to precisely distinguish single graphene layers on a sub-nanometer scale due to the contact potential difference. The contact potential difference is related to the material work function which can be determined when the tip work function is known.

ACKNOWLEDGMENTS

The author would like to express his gratitude to colleagues in NSP team in Graz (Austria) for their invaluable help.

REFERENCES

[1] Novoselov, K.S., Geim, A.K., Morozov, S.V., Jiang, D., Zhang, Y., Dubonos, S.V., Grigorieva, I.V., Firsov, A.A. 2004. Electric Field Effect in Atomically Thin Carbon Films. *Science,* 306(5696):666-669.

[2] Geim, A., and Novoselov, K.S. 2019. *Graphene – the perfect atomic lattice*. The Nobel Prize in Physics 2010. www.nobelprize.org/prizes/physics/2010/

[3] *Graphene - Synthesis, Characterization, Properties and Applications*, 2011, edited by Gong, J.R., Rijeka, Croatia: InTech.

[4] Nonnenmacher, M., O'Boyle, M.P., Wickramasinghe, H.K. 1991. Kelvin probe force microscopy. *Applied Physics Letters,* 58:2921-2923.

[5] Binning, G., Quate, C.F., Gerber, Ch. 1986. Atomic Force Microscope. Physical Review Letters, 56:930.

[6] *Conductive Atomic Force Microscopy – Applications in Nanomaterials*. 2017, edited by Lanza, M., Weinheim, Germany: Wiley-VCH Verlag GmbH & Co.KGaA.

[7] Lee, N.J., Yoo, J.W., Choi, Y.J., Kang, C.J., Jeon, D.Y., Kim, D.C., Seo, S., Chung, H.J. 2009. The interlayer screening effect of graphene sheets investigated by Kelvin probe force microscopy. *Applied Physics Letters,* 95:222107.

---

* Corresponding Author´s Email: support-nsp@anton-paar.com

Part 3

Nanotechnology in Medicine and Pharmacy

Encapsulation of hydrophobic drugs in hyaluronic acid nanofibers: effect of the solution preparation procedure

L. Bardoňová[1,2], A. Kotzianová[1], J. Kulhánek[1], O. Židek[1], K. Mamulová Kutláková[2], V. Velebný[1]*
[1]Contipro a.s, Czech Republic;
[2]Nanotechnology Centre, CEET, VŠB - Technical University of Ostrava, VŠB – Technical University of Ostrava, Czech Republic

ABSTRACT

Perspective application of nanofibrous mats composed of hydrophilic polymers are the fast-dissolving drug delivery systems for immediate release of a wide spectrum of additives, including poorly soluble drugs. For the effective preparation of drug carriers, it is necessary to load additives with high encapsulation efficiency. In our study, we aimed to prepare hyaluronic acid/polyethylenoxide nanofibers with a hydrophobic antiseptic agent (ANT). We have used several approaches of solution preparation to achieve ideally 100 % encapsulation efficiency of ANT. The approaches included dispersing ANT in polymer solution (dispersion), creating an emulsion with the surfactant Tween 60 in water before dissolving the polymers (emulsion), and dissolving all the components in a single solvent system (blend). The morphology of the nanofibers was characterized by SEM, amount of encapsulated ANT was analyzed by HPLC, and the distribution of ANT was mapped by Raman spectroscopy. The best results were obtained by blend electrospinning. The encapsulation efficiency of ANT was over 95 % and ANT was distributed in the nanofiber mat homogeneously. The yield of the electrospinning process was also 3-fold higher than the yield of dispersion and emulsion electrospinning.

Keywords: hyaluronic acid; antiseptics; nanofiber; electrospinning

INTRODUCTION

The electrospinning method (ES) allows the preparation of nanofibrous mats from a wide range of polymers and the incorporation of active pharmaceutical ingredients (API) [1]. There are several approaches commonly mentioned in the literature to incorporate API into nanofibrous mats [2-5]. The blend and dispersion electrospinning are the simplest. For blend systems, both polymers and API are dissolved in a single solvent mixture and spun. However, it is not always possible to find a suitable solvent system for the chosen polymer and API combination. For dispersion, the polymers are dissolved in a suitable solvent, and the API is dispersed in the polymer solution, but the sedimentation of API during ES might occur. Therefore, more complex systems are implemented. Emulsion electrospinning is often used for the incorporation of lipophilic APIs into a hydrophilic matrix. The polymers are dissolved in water, API is the so-called oil phase (or vice versa). Surfactants or amphiphilic compounds are used for the emulsification of API [6, 7]. Other options mentioned in the literature include the core-shell structure or surface immobilization.

We have used the combination of hyaluronic acid (HA) and polyethylenoxide (PEO) to prepare nanofibrous mats. Both these polymers are hydrophilic, and their nanofiber form dissolves in the aqueous medium immediately, releasing the incorporated API. As an additive, a hydrophobic chlorinated aromatic compound with antiseptic effect was used. The aim of the study was to test different approaches to solution preparation and electrospinning to achieve the highest API encapsulation possible. The nanofiber mat has a potential to be used as a fast-dissolving drug delivery system.

---

* Corresponding Author´s Email: bardonova@contipro.com

EXPERIMENTAL

For the preparation of ES solution, the emulsion, dispersion, and blend methods were used. The solution concentration was 6 wt%, other parameters of the prepared solutions are presented in Table 1. For the preparation of emulsion solutions, Tween 60 was dissolved in distilled water (DW), ANT was added, and the solution was stirred until the emulsion was formed. The polymers were dissolved afterwards. In the case of dispersion solution, the polymers were dissolved in water, then ANT was dispersed. For blend solutions, ANT was dissolved in solvent mixture (DW/isopropanol (IPA) 70:30 wt%), and polymers were added.

Table 1. Composition of the prepared solutions.

Method	Solution	HA (wt%)	ANT (wt%)	Tween 60 (wt%)	PEO (wt%)	Solvents
dispersion	HA-ANT-D	75	5	-	20	water
	HA-ANT-E1	75	5	4	16	water
emulsion	HA-ANT-E2	75	5	4,5	15.5	water
	HA-ANT-E3	75	5	5	15	water
blend	HA-ANT-B	75	5	-	20	water/IPA (70:30 w/w)

The polymer solutions were electrospun using a 4SPIN® LAB device (Contipro, Czech Republic) in a configuration of a linear needleless multi-jet spinning nozzle as the emitter and a rotating cylinder (width of 25 cm, diameter of 12 cm) as the collector. The collector was covered with wax paper; the rotating speed was 500 rpm. The electrospinning process was conducted under the following conditions: emitter-collector distance of 18 cm, accelerating voltage of 58 kV, airflow of 70–90 L/min, temperature of 24–26 °C, humidity below 20 %. Solution feed rate was optimized for each process and ranged between 100–200 µL/min. Each nanofibrous mat was electrospun for 60 minutes.

The morphology of the prepared mats was characterized by scanning electron microscopy (Zeiss Ultra Plus, Carl ZEISS, applied voltage 3,5 kV). From SEM images (5000 x), the diameter of fibers was evaluated using ImageJ 1.48 (average of 30 fibers). The amounts of ANT in the prepared nanofibrous mats were determined using HPLC. The encapsulation efficiency of ANT in the prepared nanofibrous mats was calculated according to the following formula (w_d [%] is the weight concentration of ANT determined by HPLC and w_i [%] is the initial weight concentration of the API in the solution used to make the nanofibrous mats):

$$\text{Encapsulation efficiency } [\%] = w_d / w_i \times 100\% \qquad (1)$$

To determine the yield of the process, three (2 × 2) cm^2 samples from each nanofibrous mat were weighed. The yield was calculated as the ratio of weight to area. The distribution of ANT in the prepared mats was analyzed by Raman microscopy (inVia Qontor, Renishaw). The maps consisted of (20 × 20) spectra with a step of 1 µm. For qualitative analysis, the acquired spectra were normalized (to the band of HA at 1123 cm^{-1}) and a distribution of the ANT characteristic band intensity (at 706 cm^{-1}) was generated.

RESULTS AND DISCUSSION

The parameters of the prepared mats are summarized in Table 2. The fiber diameter (after considering error) was comparable for samples obtained by dispersion and emulsion ES. The fiber diameter of HA-ANT-B was higher and less homogeneous. Although no defects were observed, it was not possible to remove the HA-ANT-D mat from the substrate, thus the yield could not be determined. The yield of the ES process was approximately 6,6 g/m^2 for HA-ANT-E mats, for HA-ANT-B mats the yield was more than 3-fold higher. There is no significant connection between the amount of encapsulated ANT and the yield of the electrospinning process. The lowest encapsulation efficiency was

---

* Corresponding Author´s Email: bardonova@contipro.com

achieved by dispersion ES (HA-ANT-D). Using emulsion ES, the encapsulation efficiency increased with the content of surfactant, but even when the amount of Tween 60 equals ANT in the solution (HA-ANT-E3), the encapsulation efficiency was not higher than 75 %. The use of surfactant is thus not efficient. Using the blend solution, the encapsulation efficiency of ANT was over 95 %.

Table 2. The fiber diameter, yield, and encapsulation efficiency of the prepared samples.

Method	Sample	Tween 60 (wt%)	Fiber diameter (nm)	Yield (g/m^2)	Encapsulation efficiency
dispersion	HA-ANT-D	-	121 ± 21	-	3%
emulsion	HA-ANT-E1	4	124 ± 24	6.51 ± 0,47	58.60%
	HA-ANT-E2	4.5	149 ± 31	6.8 ± 0,60	67.90%
	HA-ANT-E3	5	143 ± 28	6.53 ± 0,06	70.40%
blend	HA-ANT-B	-	270 ± 128	22.8 ± 1,14	96.20%

Figure 1 represents the distribution of ANT in the nanofibrous layers (Raman spectroscopy mapping). ANT was not detected in the analyzed area of HA-ANT-D. The differences in intensity could be attributed to the signal baseline subtraction. Due to the surfactant, ANT was incorporated into the HA-ANT-E mats in the form of clusters (Figure 1 HA-ANT-E2). In the case of blend electrospinning, ANT is distributed relatively homogeneously throughout the mapped area.

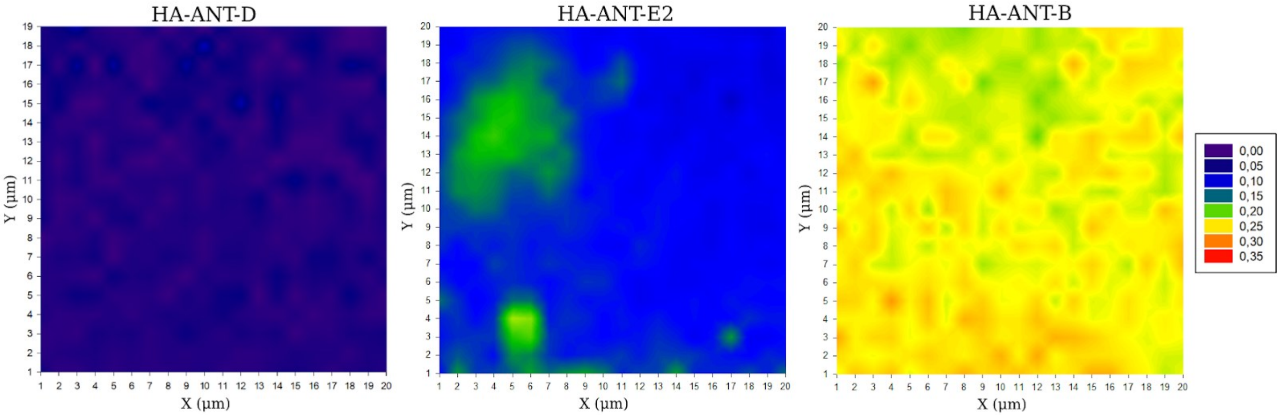

Figure 1. Distribution of ANT in the nanofibrous layers HA-ANT-D, HA-ANT-E2, and HA-ANT-B. The scale represents the normalized intensity of ANT band at 706 cm^{-1}.

CONCLUSION

Nanofiber mats of HA/PEO/ANT were prepared. Several approaches (dispersion, emulsion, blend) were used for solution preparation and electrospinning. The properties of nanofibrous mats were assessed and compared to choose the most suitable process. The most important parameters were the encapsulation efficiency and the yield of the electrospinning process, which ensure that the preparation of nanofibrous mats will be both cost- and time-effective. The dispersion electrospinning is not convenient, the encapsulation efficiency was merely 3 %, and the mat was not self-supporting. By adding the surfactant Tween 60 (emulsion electrospinning), the encapsulation efficiency increased up to 70 % (ratio between Tween 60 and ANT 1:1). Using blend electrospinning, we were able to achieve both the highest the encapsulation efficiency (over 95 %) and yield. The blend electrospinning is thus the most viable approach for the preparation of HA/PEO/ANT mats.

Chapter 12

Part 3: Nanotechnology in Medicine and Pharmacy

REFERENCES

[1] Ding, Y., Li, W., Zhang, F., Liu, Z., Zanjanidazeh Ezazi, N., Liu, D., Santos, H.A. 2019. Electrospun fibrous architectures for drug delivery, tissue engineering and cancer therapy. *Advanced Functional Materials,29*:1802852.

[2] Miguel, S.P., Figueira, D.R., Simões, D., Ribeiro, M.P., Coutinho, P., Ferreira, P., Correia, I. 2018. Electrospun polymeric nanofibres as wound dressings: A review. *Colloids Surfaces B: Biointerfaces,169*:60-71.

[3] Ulubayram, K., Calamak, S., Shahbazi, R., Eroglu, I. 2015. Nanofibers based antibacterial drug design, delivery and applications. Current Pharmaceutical Design, *21(15)*:1930-1943.

[4] Haider, A., Haider, S., Kang, I.-K. 2018. A comprehensive review summarizing the effect of electrospinning parameters and potential applications of nanofibers in biomedical and biotechnology. *Arabian Journal of Chemistry, 11*(8):1165-1188.

[5] Yu, D.-G., Li, J.-J., Williams, G.R., Zhao, M. 2018. Electrospun amorphous solid dispersions of poorly water-soluble drugs: a review. *Journal of Controlled Release, 292*:91-110.

[6] Aadil, K.R., Nathani, A., Sharma, C.S., Lenka, N., Gupta, P. 2018. Fabrication of biocompatible alginate-poly(vinyl alcohol) nanofibers scaffolds for tissue engineering applications. *Materials Technology, 33(8)*:507-512.

[7] Akbarzadeh, M., Pezeshki-Modaress, M., Zandi, M. 2020. Biphasic, tough composite core/shell PCL/PVA-GEL nanofibers for biomedical application. *Journal of Applied Polymer Scence, 137*(21):48713.

---

* Corresponding Author´s Email: bardonova@contipro.com

Study of UDD under experimental carcinogenesis

L.V. Batyuk[1], **N.N. Kizilova**[2,3]*

[1]Department of Medical and Biological Physics and Medical Information Science/Kharkiv National Medical University, Ukraine;

[2]Warsaw University of Technology, Institute of Aviation and Applied Mechanics, Poland;

[3]PoreLab, Department of Chemistry, Norwegian University of Science and Technology, Norway

ABSTRACT

In article the protection ability of the ultra-disperse nanodiamonds (UDD) is studied based on the measurements of content of electrolytes in plasma and erythrocytes of Wistar rats with Guerin's carcinoma under conditions of irradiation by 10.0 Gy and use of UDD. The groups of rats with Guerin's carcinoma and with X-ray irradiation and both with used UDD and X-ray irradiation treatments were compared to the control group. In the experiment, the content of electrolytes in blood plasma and erythrocytes of rats was measured by flame photometry. Hematological control of radiation reactions and the effectiveness of UDD out by studies of the morphological composition of peripheral blood was studied. The content of collagen metabolites (hydroxyproline) in daily urine and glycosaminoglycan metabolites was determined. It was shown, that UDDs have a radioprotective effect under conditions of external exposure of the body of rats. The radiation activities of UDDs are based on its specific membranotropic properties, which integrally increases the general nonspecific resistance of the organism.

Keywords: carcinoma; X-ray, erythrocytes; blood plasma; nanodiamonds; collagen metabolites

INTRODUCTION

Pronounced changes in the body that precede and promote cell malignancy, as well as the powerful remote effect of the tumor on organs and systems, affect the erythrocyte in the pathogenesis of tumor growth [1-3]. In our studies, special attention was paid to the structural and functional state of erythrocytes during tumor growth in the experiment (transplanted carcinoma). It is known that a number of physical, biochemical and structural changes occur in the tumor-carrying organism. The presence of areas with different oxygenation in a malignant tumor is one of the leading factors in radiation therapy of tumors. Use to enhance the radiation effect of electron-acceptor compounds, such as UDD, active under conditions of hypoxia (anoxia), causes damage and death of hypoxic tumor cells, which is observed in the biochemical changes in the state of blood cells [4, 5].

EXPERIMENTAL STUDY

Experimental studies were performed on 20 Wistar rats, 4 months of age, weighing 160-180 g with subcutaneously transfused 20% suspension of Guerin's carcinoma cells. A series of experiments was performed, the animals were divided into three groups: 1 group - animals with vaccinated Guerin's carcinoma; Group 2 - animals whose tumors were subjected to local fractional X-ray irradiation (the total dose per carcinoma growth zone was 10 Gy); Group 3 - animals that were injected a diluted suspension of UDD in doses of 2.0 ml (C=0.02 % of dry weight of UDD in saline) of a one hour before irradiation once per day with food during 5 days prior to the radiation treatment. A group of intact rats was a control. In the experiment, the content of electrolytes in blood plasma and erythrocytes was measured by method of flame photometry [7]. Hematological control of radiation reactions and the effectiveness of the drug were carried out by clinical studies of the morphological composition of peripheral blood before, in the middle and after the course. The content of collagen metabolites

---

* Corresponding Author´s Email: lv.batyuk@knmu.edu.ua

(hydroxyproline) in daily urine was determined by the method [7]; the content of glycosaminoglycan metabolites (non-hexuronic acids) by the method [8].

RESULTS AND DISCUSSION

Malignant tumors require a significant amount of water and basic electrolytes Na^+ and K^+ for their development. Under conditions of carcinoma growth and local fractional X-ray irradiation of 10 Gy, there is a decrease in the content of K^+ in erythrocytes of rats and an increase in Na^+. In plasma, the coefficient of their ratio increased relative to control (Table 1). Water - electrolyte imbalance may be due to the side effects of a large number of decay products of carcinoma cells [9]. The destruction of membranes of cells can be caused by defects such as “through” pores. The radius of such a pore increases depending on the voltage to a certain value, after which the defect continues to expand spontaneously under the influence of radiation-induced factors [10].

Table 1. The content of electrolytes in plasma and erythrocytes of rats on irradiation and use of UDD.

Experiment	n	K (*mmol/l*)	K (*mmol/l*)	Na (*mmol/l*)	Na (*mmol/l*)	Na / K	K / Na
		plasma	erythrocyte	plasma	erythrocyte	plasma	erythrocyte
Biological control	5	5.3±1.4	87.9±4.8	144.8±13.5	21.7±2.9	27.52	4,04
Carcinoma	5	4.5±0.1	95.6±4.7	162±26.3	25.7±5.0	36±6.1	3.3±0.9
Carcinoma + X-ray (at a dose 10 Gy)	5	5.0±0.2	82.1±5.6	178.7±13.8	18.9±11.3	36±2.7	3.3±0.5
Carcinoma + X-ray (at a dose of 10 Gy) + UDD	5	4.7±0.4	97.6±1.3*	164.7±31.4	23.8±3.3	35.1±7.5	4.2±0.6

Note. * - probably in comparison with the control $p \le 0.05$

The use of UDD in local fractional X-ray irradiation of rats at a dose of 10 Gy leads to an increase in the level of K^+ in erythrocytes by an average of 11% and an increase in the level of Na^+ in plasma by 14%, which differs little from the biological control group. The obtained data show that simultaneously with the decrease in the level of radiation damage, the nanoparticles of UDD reduces the stability and promotes the increase of membrane of cells permeability for ions, thus showing both protective and toxic effects. UDD in contact with erythrocyte membranes due to its membraneotropy, it strengthens them and increases the resistance of cells to current loads and to the effects of ionizing radiation. Obviously, such protection is universal and similar phenomena will occur under the influence of other damaging factors, including destabilizing processes within the body. No significant difference between the actions of the drug in different doses was found.

The results of dynamic studies of the morphological composition of peripheral blood in the process of local fractional X-ray irradiation show that the most significant changes are in the state of leukopoiesis. These changes are characterized by a progressive decrease in the number of leukocytes in 40% in Group 1 (on average up to 59% in Group 2). At the same time there was a marked decrease in the number of lymphocytes: their level decreased more than 2 times from baseline in Group 2. The results of studies of the peculiarities of the development of hematological reactions in the conditions of application of UDD in comparison with the indicators in the control groups indicate a significant hemostimulating activity of the drug. This activity is realized in reducing the frequency of leukopenia reactions during of local fractional X-ray irradiation (1.5 times). It was found that under the influence of UDD the frequency of leukopenia reactions in the range from 3.0 to 2.0 $x10^9$ /l leukocytes decreases 1.6 times (from 50 to 27 %), and their duration is reduced by 3 times. The level of daily urinary excretion of markers of collagen (oxyproline) and glycosaminoglycans (hexuronic acids) is constantly increasing in the dynamics of local fractional X-ray irradiation and DDD use. Since the basis of radiation damage to connective tissue are violations of the synthesis of protein-carbohydrate components and reducing the content of functionally active forms, it is realized in reducing the urinary excretion of major

* Corresponding Author´s Email: lv.batyuk@knmu.edu.ua

metabolites. The revealed growth of the latter when using the developed methods confirms the prevention of the processes of disintegration of synthesis and catabolism of the main structures of the organic matrix of the skin and a significant restructuring in their composition towards dissolved forms. This is connected with the activation of repair systems of biochemical and physiological functions of connective tissue.

CONCLUSION

The revealed patterns of structural and functional parameters of erythrocytes indicate that changes in the state of erythrocyte membranes may be associated with changes in the composition and specific structure of the erythrocyte membrane during the formation and growth of carcinoma of rats. Used doses of the drug of UDD have radiosensitizing activity, which is inherent in the electron-acceptor compound. Membrane structures of blood cells of rats under conditions of local fractional X-ray irradiation of carcinoma and the use of nanoparticles of UDD are characterized by less abrupt changes in conformation than the membrane structures of cells of rats under the action of carcinoma and irradiation. Thus, it can be summarized that the use of UDA contributes to a significant increase in the effectiveness of treatment of rats with Guerin's carcinoma under experimental carcinogenesis.

REFERENCES

[1] Batyuk, L.V. 2015. Influence of cancer disease on dielectric characteristics of structural-functional state of erythrocyte membranes. *Science Rise,* 7(4-12):11-17.

[2] Tsyrlina, E.V., Kriukova, O.G., Poroshina, T.E., Tyrkevich, E.A., Barash, N.I., Mullakhmetova, Z.I., Semiglazov, V.F., Bershteĭn, L.M. 2014. Microviscosity of erythrocyte membranes in breast cancer patients: connection with the receptor phenotype of the tumor. *Voprosy Onkologii,* 60:504-509.

[3] Nagasawa, T., Kobayashi, T., Kimura, E. 1982. Detection of reversible and irreversible changes of erythrocyte osmotic fragility induced by Yoshida tumor cells in rats. *European Journal of Cancer and Clinical Oncology,* 18(8):711-775.

[4] Voycheva, C. 2017. Detonation nanodiamonds: opportunity for pharmaceutical and medical application. *Journal of Pharmaceutical Research*, 1(2):000108.

[5] Tsai, L.-W., Lin, Yu-Ch., Perevedentseva, E., Lugovtsov, A., Priezzhev, A., Cheng, Ch.-L. 2016. Nanodiamonds for medical applications: interaction with blood in vitro and in vivo. *Intrernational Journal of Molecular Science,* 17(7):9072-9077.

[6] Batyuk, L.V. 2004. Influence of local fractionated X-ray irradiation on the hydration and structural state of erythrocytes at experimental models of carcinoma. *Bulletin of Problems in Biology and Medicine, 4*:135-140.

[7] Martin, C.J., and Axelrod, A.E. 1953. A modified method for determination of hydroxyproline. *Society for Experimental Biology and Medicine,* 83(3):461–462.

[8] Bitter, T., and Muir, H. 1962. A modified uronic acid carbazole reaction. *Analytical Biochemistry,* 4:330-334.

[9] Shahid, S. 2016. Review of hematological indices of cancer patients receiving combined chemotherapy & radiotherapy or receiving radiotherapy alone. *Critical Reviews in Oncology/Hematology,* 105:145–155.

[10] Villa, C.H., Anselmo, A.C., Mitragotri, S., Muzykantov, V. 2016. Red blood cells: Supercarriers for drugs, biologicals, and nanoparticles and inspiration for advanced delivery systems. *Advanced Drug Delivery Reviews,* 106:88-103.

---

* Corresponding Author´s Email: lv.batyuk@knmu.edu.ua

Multifunctional Harmonic Nanoparticles for Cell Tracking and Theranostic Applications

***A. Gheata*[1]*, G. Gaulier*[2]*, G. Campargue*[2]*, J. Vuilleumier*[1]*, D. Staedler*[3]*, D. Diviani*[3]*, L. Bonacina*[2]*, S. Gerber-Lemaire**[1]**
[1]Group for Functionalized Biomaterials, Institute of Chemical Sciences and Engineering, Ecole Polytechnique Fédérale de Lausanne, Switzerland;
[2]Department of Applied Physics, Université de Genève, Switzerland;
[3]Department of Biomedical Sciences, University of Lausanne, Switzerland

ABSTRACT

In comparison with luminescent probes, harmonic nanoparticles (HNPs), which are based on metal oxide nanocrystals lacking of inversion symmetry, benefit from excitation spectral flexibility, fully coherent emission and high photostability. These appealing properties constitute unique assets for bioimaging protocols beyond the classical NIR I tissue transparency window. Surface functionalization of HNPs offers the possibility to exploit these unique capabilities in highly demanding applications such as cell tracking in tissue depth, multiscale and multimodal imaging and on-demand light-triggered release of therapeutic payloads. We herein disclose efficient conjugation protocols for surface coating and post-functionalization of HNPs toward the development of theranostic nanodevices.

Keywords: multifunctional nanoparticles; multimodal imaging probes; cell labelling; NIR-light triggered uncaging

INTRODUCTION

The recent progress in nanotechnologies have paved the way for intense investigation of nanomaterials in clinical settings for the early detection, diagnosis and treatment of several diseases. The ability to produce inorganic nanostructures of tunable size and composition, combined with their high agent loading capacity and surface properties amenable to tailored chemical modification, have generated high expectations that nanomaterials could provide unprecedented diagnosis and therapeutic tools [1]. HNPs, which are composed by non-centrosymmetric inorganic nanocrystals presenting a highly efficient non-linear response, have recently emerged in multiphoton imaging applications with the aim of overcoming some limitations of fluorescent probes [2, 3]. HNPs exhibit a number of favorable properties for bioimaging applications including the ability to image their second harmonic signal in response to excitation from the UV to mid-IR, the absence of photo-bleaching, blinking and saturation, and spectrally narrow emission signals. We previously exploited these unique features for cell labelling [4], tissue imaging [5] and selective phototherapeutic protocols [6]. We herein disclose novel demonstrations of surface functionalized HNPs for the controlled release of therapeutic payloads, dual imaging applications and cell tracking.

EXPERIMENTAL/THEORETICAL STUDY

Most of the reported light-responsive drug carriers rely on high-energy UV light excitation of photosensitive scaffolds, thus limiting their practical biomedical applications due to poor penetration potential and direct cytotoxicity. The inherent flexibility of HNP with respect to the excitation wavelength, associated with the possibility to apply double excitation protocols, make them ideal systems for light-triggered release applications making use of the second harmonic emission of the NP harmonic core to uncage surface-conjugated molecular cargos [7]. In addition, the optical imaging

---

* Corresponding Author´s Email: sandrine.gerber@epfl.ch

capabilities of HNPs in multiphoton microscopy can be nicely complemented by contrast performance in T_1-weighted magnetic resonance (MR) images through surface functionalization with chelated Gd(III) ions. This combination offers the possibility to exert efficient contrast for both whole body imaging, and microscopy observation at the cellular and subcellular spatial resolution.

RESULTS AND DISCUSSION

Surface silanization of $BiFeO_3$ (BFO) and $LiNbO_3$ (LNO) nanocrystals [8] was performed in the presence of (3-aminopropyl)-triethoxysilane (APTES) and its azido analogue to ensure colloidal stability of the resulting coated NPs in aqueous and alcoholic media and display a high density of azide functionalities amenable to downstream functionalization through click reaction (azide to alkyne [3+2] cycloaddition). Model molecular cargo (tryptophan) and anticancer chemotherapeutics (chlorambucil, erlotinib derivative) [9] were conjugated to silica coated HNPs, and efficiently released by the interaction of the second harmonic emission of the inorganic core with coumarinyl caging units, upon NIR pulsed irradiation (15 minutes) (Fig. 1A). The potential of this strategy was demonstrated *in vitro* in the presence of human prostate cancer cells (DU145). Similar functionalization strategy allowed the conjugation of chelated Gd^{3+} ions to the surface of LNO NPs (Fig. 1B). The resulting nanoconstructs exhibited intense SHG signals for cancer cells imaging in the NIR-II window and strong contrast enhancement in T_1-weighted images of agarose gel-based phantoms at 14.1 T MRI.

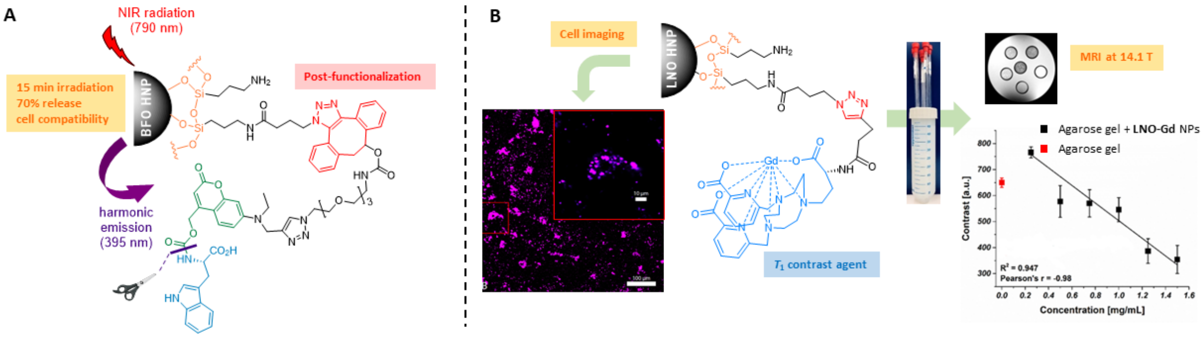

Figure 1. A. Controlled release of caged molecular cargo triggered by the harmonic emission of surface functionalized BFO NPs upon NIR radiation; B. LNO-Gd nanoconjugates exert contrast in MRI (14.1 T) and nonlinear multiphoton microscopy (SHG image of labelled DU145 human prostate cancer cells).

In addition, the simultaneous detection of the second and third harmonic emission of functionalized HNPs offers the possibility to track individual cells in optically congested environment such as muscle tissues [10].

CONCLUSION

We herein demonstrated the capabilities of surface functionalized BFO and LNO NPs for advanced imaging applications combining multi-order multiphoton microscopy and MR imaging at high field. The possibility to complement these contrast properties with efficient drug loading and on-demand release capacities pave the way for further development of multifunctional HNPs as theranostic nanoplatforms for clinical applications.

ACKNOWLEDGMENTS

We acknowledge financial support from the France-Switzerland Interreg program (Interreg fédéral, Vaud state, Geneva state, projects NANOFIMT and OncoNanoScreen).

---

* Corresponding Author´s Email: sandrine.gerber@epfl.ch

Chapter 14

Part 3: Nanotechnology in Medicine and Pharmacy

REFERENCES

[1] Nguyen, K.T., and Zhao, Y. 2015. Engineered hybrid nanoparticles for on-demand diagnostics and therapeutics. *Accounts of Chemical Research,* 48(12):3016-3025.

[2] Bonacina, L. 2013. Nonlinear nanomedecine: harmonic nanoparticles toward targeted diagnosis and therapy. *Molecular Pharmaceutics,* 10(3):783-792.

[3] Meyer, T., Schmitt, M., Dietzek, B., Popp, J. 2013. Accumulating advantages, reducing limitations: Multimodal nonlinear imaging in biomedical sciences – The synergy of multiple contrast mechanisms. *Journal of Biophotonics,* 6(11-12):887-904.

[4] Passemard, S., Staedler, D., Sonego, G., Magouroux, T., Schneiter, G.S., Juillerat-Jeanneret, L., Bonacina, L., Gerber-Lemaire, S. 2015. Functionalized bismuth ferrite harmonic nanoparticles for cancer cells labelling and imaging. *Journal of Nanoparticle Research,* 17:414.

[5] Rogov, A., Irondelle, M., Ramos-Gomes, F., Bode, J., Staedler, D., Passemard, S., Courvoisier, S., Yamamoto, Y., Waharte, F., Ciepielewski, D., Rideau, P., Gerber-Lemaire, S., Alves, F., Salamero, J., Bonacina, L., Wolf, J.-P. 2015. Simultaneous Multiharmonic Imaging of Nanoparticles in Tissues for Increased Selectivity. *ACS Photonics.* 2(10):1416-1422.

[6] Staedler, D., Magouroux, T., Passemard, S., Schwung, S., Dubled, M., Schneiter, G.S., Rytz, D., Gerber-Lemaire, S., Bonacina, L., Wolf, J.-P. 2014. Deep UV generation and direct DNA photo-interaction by harmonic nanoparticles in labelled samples. *Nanoscale,* 6:2929-2936.

[7] Vuilleumier, J., Gaulier, G., De Matos, R., Ortiz, D., Menin, L., Campargue, G., Mas, C., Constant, S., Le Dantec, R., Mugnier, Y., Bonacina, L., Gerber-Lemaire, S. 2019. Two-photon-triggered photorelease of caged compounds from multifunctional harmonic nanoparticles. *ACS Applied Materials & Interfaces,* 11(30):27443-27452.

[8] Staedler, D., Magouroux, T., Hadji, R., Joulaud, C., Extermann, J., Schwung, S., Passemard, S., Kasparian, C., Clarke, G., Gerrmann, M., Le Dantec, R., Mugnier, Y., Rytz, D., Ciepielewski, D., Galez, C., Gerber-Lemaire, S., Juillerat-Jeanneret, L., Bonacina, L., Wolf, J.-P. 2012. Harmonic nanocrystals for biolabeling: a survey of optical properties and biocompatibility. *ACS Nano*, 6(3):2542-2549.

[9] Vuilleumier, J., Gaulier, G., De Matos, R., Mugnier, Y., Campargue, G., Wolf, J.-P., Bonacina, L., Gerber-Lemaire, S. 2020. Photocontrolled release of the anticancer drug chlorambucil with caged harmonic nanoparticles. *Helvetica Chimica Acta,* 103(1):e1900251.

[10] Dubreil, L., Leroux, I., Ledevin, M., Schleder, C., Lagalice, L., Lovo, C., Fleurisson, R., Passemard, S., Kilin, V., Gerber-Lemaire, S., Colle, A. M., Bonacina, L., Rouger, K. 2017. Multi-harmonic imaging in the second near-infrared window of nanoparticle-labeled stem cells as a monitoring tool in tissue depth. *ACS Nano,* 11(7):6672-6681.

---

* Corresponding Author´s Email: sandrine.gerber@epfl.ch

Nanomaterials as antiparasitics

J. Jampílek[1,2], **D. Plachá**[3,4]*

[1]Faculty of Natural Sciences, Comenius University in Bratislava, Slovakia;
[2]Department of chemical biology, Faculty of Science, Palacky University Olomouc, Czech Republic;
[3]Nanotechnology Centre, CEET, VSB-Technical University of Ostrava, Czech Republic;
[4]Centre ENET, CEET, VSB-Technical University of Ostrava, Czech Republic

ABSTRACT

For many decades, diseases caused by parasites were among the so-called neglected diseases, and the development of antiparasitic drugs was minimal. However, with climate change, travel and global food distribution, more and more species of parasites are becoming a serious problem. In general, parasites can be classified into three main groups: ectoparasites (e.g., lice and fleas), helminths (i.e. worm parasites, e.g., roundworm, tapeworm, fluke) and protozoa (i.e. the single-celled organism, e.g., *Plasmodium*, *Trypanosoma*, *Leishmania*, *Entamoeba*, *Toxoplasma*, *Trichomonas*). Thus, it is evident that they are not only parasites causing tropical diseases, but many parasites also occur in temperate regions, although their diversity and activity increase with increasing temperature. The number of parasites harmful to agricultural/food valuable plants or animals is even greater. The choice of appropriate drugs is very limited, and therefore development is logically focused on reformulating older drugs to reduce toxicity, increase efficacy, and target distribution to parasite-affected tissues. Nanoscale science and nanotechnology have unambiguously demonstrated to have a great potential in providing novel and improved solutions. Nano-size materials change their physical and chemical properties in comparison with bulk materials and have helped to improve and innovate a variety of pharmaceutical, medical, industrial, and agricultural products. Thus, this contribution deals with the biological activity of various types of nanoparticles/nanomaterials against parasites.

Keywords: antiparasitics; helmints; nanoparticles; protozoa

INTRODUCTION

Parasites are organisms that live on or in the host organism and obtain food from or on behalf of the host. They can be divided into three main groups: ectoparasites, helminths and protozoa. Ectoparasites (ticks, fleas, lice and mites) are organisms that attach or burrow into the skin and remain there for weeks or months. Arthropods can also be included in this group, especially mosquitoes, which can also cause diseases, but are much more important as vectors of many other parasites. Helminths are large multicellular organisms that are generally visible to the naked eye in adulthood. Parasitic worms are classified into three main groups: i) flatworms (tapeworms and flukes), ii) thorny-headed worms (adult forms live in the intestines of vertebrates, are rare in humans, but are common in birds and fish), and iii) roundworms (nematodes - adult forms live in the gastrointestinal tract, blood, lymphatic system or subcutaneous tissues; larvae can cause infections in various body tissues). Helminths in humans are usually found in the intestines and muscles, but can also be found in the liver, lungs, brain, skin, blood, lymph, or eyes. Human can be for the helminths intermediate host (*Echinococcus*) or the final host (*Nematoda*, *Cestoda*, *Trematoda*, *Filaria*). Protozoa are microscopic unicellular organisms that are able to reproduce in humans (the reproductive cycle consists of asexual or sexual reproduction and depends on the type of particular host) and are the cause of serious infections. They can be divided into: i) intestinal protozoa transmitted by the faecal-oral route (e.g., contaminated food, water or personal contact), and ii) blood or tissue protozoa transmitted by vectors (mosquito bites, flies). Some protozoan diseases can be found all over the world, e.g., amebiasis, giardiasis, coccidiosis, trichomoniasis,

---

* Corresponding Author´s Email: josef.jampilek@gmail.com

toxoplasmosis, while some occur mainly in subtropical or tropical parts of the world: malaria, trypanosomiases (sleeping sickness, Chagas disease), leishmaniasis [1-8].

Repellents and antiseptics can be used against ectoparasites with varying degrees of success. Anthelmintics are either drugs that eliminate parasitic worms from the body by either stunning (vermifuges) or killing (vermicides). In folk medicine, plant extracts were used, e.g., from mustard, fern, goosefoot. Anthelmintically active synthetic compounds belong to piperazines, amidines/guanidines, halogenated phenols and structurally different (e.g., oxamniquine, suramine, ivermectin, etc.). They affect muscle function, reproduction, metabolism, proteosynthesis and nucleic acids. Antiprotozoals are drugs used to treat protozoal infections. In addition to typical antiprotozoals, antimicrobial chemotherapeutics are used, e.g., from the groups of tetracyclines, macrolides, imidazoles/triazoles, sulfonamides, nitroimidazoles/nitrofuranes. Classical antiprotozoal drugs include organometallic compounds (based on arsenic and antimony), halogenated 8-hydroxyquinolines, amino acids, amide-based agents, naphthoquinones, and antimalarials (especially based on quinine and artemisinin). Drugs inhibit the function of enzymes, interfere with metabolism, proteosynthesis and nucleic acids [9-12].

From the above list, it can be seen that these are not only parasites causing tropical diseases, but many parasites also occur in temperate areas. Nevertheless, the diversity and activity of the parasites increases with increasing temperature. However, parasitic infections have begun to affect people living in developed countries due to climate change and travel, global trade, the spread of vectors and pathogens. The WHO has included this type of disease among the so-called neglected diseases, i.e. those to which minimal attention is paid by public health and the pharmaceutical industry. These diseases significantly affect more than 1 billion people worldwide, disrupt physical and cognitive development, contribute to other diseases, cause maternal and child deaths, make farming or livelihoods more difficult and reduce overall productivity. In addition to prevention, thorough diagnosis and appropriate (prophylactic, causal) treatment are necessary. It is important to note that most clinically used drugs are relatively old (some are obsolete) and in addition to high parasite resistance, the drugs have significant side effects (toxic at effective doses) and have an unfavorable pharmacokinetic profile. Many used antiparasitic drugs in conventional drug formulations are unstable and poorly absorbed from the gastrointestinal tract (due to their poor solubility), rapidly metabolized (first-pass effect), difficult to cross biological membranes, resulting in overall reduced bioavailability and poor therapeutic effect [2, 4, 9-12].

NANOMATERIALS AS POTENTIAL ANTIPARASITIC AGENTS

Thus, it seems ideal to use nanoparticle drug delivery systems for reformulation. Such an approach using innovative nanoparticle (NP) systems for old drugs will allow the overall improvement of the therapeutic effects of antiparasitics by increasing bioavailability, increasing intracellular penetrability, increasing stability and efficacy. In addition, many nanoformulations allow for targeted drug delivery and sustained release. All these factors will make it possible to reduce the dose and thus reduce the systemic intrinsic toxicity of the drug [13-16]. From this point of view, mainly formulations based on nanoliposomes, solid lipid nanoparticles, nanosuspensions and polymeric nanosystems are investigated. However, nanosystems based on graphene and its derivatives and nanoformulations based on metals (e.g., Ag, Au, Cu, Zn, Fe, etc.) are not omitted either [15-17]. The properties of nano-antiparasitics are significantly affected by: i) size, ii) shape, iii) surface charge, and iv) surface hydro/lipophilic characteristics [13 - 17].

The size of NPs plays an important role in *in vivo* transport/distribution, e.g., <100 nm nanocarriers have a longer circulation time, on the other hand >100 nm nanocarriers are easily removed from the blood by the reticuloendothelial system [17]. Therefore, it is not surprising that the fact has been exploited and nifurtimox NPs with a particle size <100 nm have a significantly prolonged time in the bloodstream, which increases its activity against *Trypanosoma cruzi* [18]. The shape of NP affects the rate of diffusion and distribution of NPs in the body and their interactions with macrophages. For example, NPs are phagocytosed in the following order: flattened ellipsoid > spherical > rod-shaped. This is important for the treatment of intracellular parasitic infections (e.g., spherical NPs with amphotericin B are preferred for the treatment of leishmaniasis) [17]. The surface charge of NPs affects distribution

---

* Corresponding Author´s Email: josef.jampilek@gmail.com

in the body and metabolism. NPs with a negative surface charge are trapped in the liver and eliminated faster than NPs with a neutral surface charge (e.g., fenbendazole nanoliposomes, with a neutral surface charge, have a longer blood circulation time and easily penetrate the blood–brain barrier. On the other hand, negatively charged nanoliposomes are easily accumulated in muscles and can be used as drug carriers for the treatment of toxocariasis [17, 19]. Hydro/lipophilic surface properties affect protein binding, resulting in a rate of distribution and elimination. Thus, by modifying the surface, the desired pharmacokinetics can be achieved. For example, surface modification with polyethylene glycol (PEG) improves hydrophilicity and reduces protein binding, prolonging the biological half-life of the nanosystems (up to 36-fold) [13-17, 20-22].

Nano-antiparasitic agents are absorbed in three basic ways: i) transcellular pathway (the most important, realized by the mechanisms of endocytosis, such as phagocytosis and pinocytosis), ii) paracellular pathway (tight junctions opened by components of the formulations, e.g., unsaturated fatty acids or surfactants), iii) direct molecular absorption of the drug (due to the small particle size, the more soluble drug transferred directly to the bloodstream due to the concentration gradient on both sides of the membrane) [17].

Ullio-Gamboa et al. encapsulated ivermectin (0.11 and 0.28% w/v) in spherical lipid nanocapsules composed of Labrafac® WL 1349, Lipoid® S75-3 and Kolliphor® HS-15 with a particle size of approx. 55 nm. This formulation proved to be 150- to 300-fold more effective compared to permethrin 1% (w/w) against permethrin-resistant lices [23].

Although the exact mechanism of interactions between graphene-based materials and biosystems has not been elucidated, these types of nanomaterial have become a very popular for various biomedical applications [24, 25]. For example, graphene oxide (GO) nanosheets have been found to significantly inhibit the invasion of *Plasmodium falciparum* into red blood cells. GO nanosheets have also been shown to arrest the development of trophozoite-stage plasmodia. Antiplasmoidal activity was also found for graphene quantum dots (GQDs), which were evaluated against chloroquine- (CQ) sensitive and CQ-resistant *P. falciparum* strains with IC_{50} 82.43 µg/mL (CQ-s) and 85.17 µg/mL (CQ-r), respectively. In addition, GQDs have been shown to be effective against vectors; LD_{50} values against *Anopheles stephensi* ranged from 0.157 to 6.323 ppm [26-28].

AgNPs synthesized using a reducing leaf aqueous extract of *Tinospora cordifolia* Miers (*Menispermaceae*) with a particle size of 55–80 nm were tested against *Pediculus humanus capitis* De Geer. The activity of starting $AgNO_3$ was not detected, the leaf aqueous extract had a pediculocidal activity LC_{50} = 52.09 mg/L, while the AgNPs showed LC_{50} = 12.46 mg/L [29]. Spherical AgNPs synthesized using a fungal extract from *Duddingtonia flagrans* with an average particle size in the range of 14.51–1.18 nm showed *in vitro* anthelmintic activity against *Ancylostoma caninum* larvae. At concentrations of 10.85, 21.70 and 43.4 µg/mL, they showed a 100% nematicidal effect compared to levamisole. The fungal extract contained chitinases, which were absorbed on the surface of NPs and thus facilitated the penetration of NPs into nematodes, where NPs caused the death of the parasite. This presumed effect was supported by the observed extensive morphological changes in the worm cuticle [30]. Polyphenols from an aqueous extract of *Isatis tinctoria* L. (*Brassicaceae*) resulted in spherical AgNPs with a particle size of 10–20 nm, which were surface modified with amphotericin B. This nanosystem showed significant activity (IC_{50} 2.43 µg/mL) against *Leishmania tropica* [31]. Spherical green synthesized AgNPs with a particle size in the range of 2–8 nm were effective against *P. falciparum* with an IC_{50} of 8 g/mL [32]. Iron oxide NPs modified with artesunate was effective at one-eighth of the concentration of bulk artesunate on artemisinin-resistant *P. falciparum* R539T in a mouse model [33]. Cylindrical and spherical MgO NPs on the surface modified with CQ with a particle size of approx. 10 nm were effective in an *in vivo* assay on mice infected with *Plasmodium berghei* [34]. *In vitro* acaricidal activity against *Hyalomma* spp. (ticks common in Asia, Europe and Africa responsible for the transmission of protozoal, bacterial, rickettsial and viral diseases) was demonstrated for ZnO NPs with a particle size of 15 nm. The tests were performed at concentrations of 50, 125 and 250 mg/mL against the control (distilled water and cypermethrin) after 10, 30 and 60 minutes. Concentrations of 125 mg/mL after 30 minutes of exposure and concentrations of 250 mg/mL after 10 minutes had a 100% acaricidal effect [35].

CONCLUSION

The encapsulation of antiparasitics in nanoparticles or the immobilization of antiparasitics on nanoparticles leads to the emergence of innovative effective potential antiparasitic chemotherapeutics. Also, "new" antiparasitically effective metal-based nanonoformulations seem to be a promising way to develop effective and commercially available drugs. Even in this case, nanotechnologies are becoming an effective tool for increasing efficiency and reducing side effects. In addition to their own effective nano-antiparasitics, it is possible to further improve the therapeutic effects of antiparasitics by modifying their pharmacokinetic profile by influencing the size and shape of the nanoparticles and by modifying their surface properties.

ACKNOWLEDGMENTS

This study was supported by the Slovak Research and Development Agency; project APVV-17-0373.

REFERENCES

[1] Paniker, C.K.J. Paniker´s Textbook of Medical Parasitology, 8th ed.; Ghosh, S., Ed.; Jaypee Brothers Medical Publishers: New Delhi, India, 2017, pp.276.

[2] Centers for Disease Control and Prevention, U.S. Department of Health & Human Services. *About Parasites*. https://www.cdc.gov/parasites/about.html.

[3] WHO. *World Health Statistics 2021.* https://www.who.int/data/gho/publications/world-health-statistics.

[4] WHO. *Neglected tropical diseases 2020*. https://www.who.int/neglected_diseases/en.

[5] WHO. *World Malaria Report 2020*. https://www.who.int/publications/i/item/9789240015791.

[6] WHO. *Human African trypanosomiasis 2021*. https://www.who.int/trypanosomiasis_african/en.

[7] WHO. *Chagas disease - American trypanosomiasis 2021*. https://www.who.int/health-topics/chagas-disease#tab=tab_1.

[8] WHO. *Leishmaniasis 2021*. https://www.who.int/leishmaniasis/disease/en/.

[9] Roche, V.F., Zito, S.W., Lemke, T.L., Williams, D.A. 2019. *Foye's Principles of Medicinal Chemistry*, Philadelphia: Wolters Kluwer Health.

[10] Jampílek J. 2014. Recent advances in design of potential quinoxaline anti-infectives. *Current Medical Chemistry*, 21(38):4347–4373.

[11] Jampílek, J. 2017. Design of antimalarial agents based on natural products. *Current Organic Chemistry*, 21(18):1824–1846.

[12] Jampílek, J. 2018. Design and Discovery of New Antibacterial Agents: Advances, Perspectives, Challenges. *Current Medical Chemistry*, 25(38):4972–5006.

[13] Jampílek, J., and Kráľová, K. 2017. Nano-antimicrobials: Activity, benefits and weaknesses. In: *Nanostructures for Antimicrobial Therapy*, edited by Ficai, A., and Grumezescu, A.M., 23-54. Elsevier, Amsterdam, Netherland.

[14] Jampílek J., and Kráľová K. 2018. Application of nanobioformulations for controlled release and targeted biodistribution of drugs In: *Nanobiomaterials: Applications in Drug Delivery*, edited by Sharma, A.K., Keservani, R.K., and Kesharwani, R.K., 131-208. Apple Academic Press Inc.: Warentown, USA.

[15] Jampílek, J., and Kráľová, K. 2019. Campos, E.V.R.; Fraceto, L.F. Bio-based nanoemulsion formulations applicable in agriculture, medicine, and food industry. In: *Nanobiotechnology in Bioformulations*, edited by Prasad, R., Kumar, V., Kumar, M., and Choudhary, D.K., 33-84. Springer: Cham, Switzerland.

[16] D. Plachá, J. Jampilek, in: M. Rai, M. Patel, R. Patel (Eds.), Nanotechnology in Medicine: Toxicity and Safety, Wiley, 2022, pp. 67–108.

[17] Sun, Y., Chen, D., Pan, Y., Qu, W., Hao, H., Wang, X., Liu, Z., Xie, S. 2019. Nanoparticles for antiparasitic drug delivery. *Drug Delivery, 26(1)*:1206-1221.

[18] Gonzalez-Martin, G., Merino, I., Rodriguez-Cabezas, M.N. 2011. Pharmaceutics: Characterization and Trypanocidal Activity of Nifurtimox-containing and Empty Nanoparticles of Polyethylcyanoacrylates. *Journal of Pharmacy and Pharmacology*, 50:29–35.

[19] Velebny, S., Hrckova, G., Tomasovicova, O., Dubinsky, P. 2000. Treatment of larval toxocarosis in mice with fenbendazole entrapped in neutral and negativêly charged liposomes. *Helminthologia*, 37:119–125.

---

* Corresponding Author´s Email: josef.jampilek@gmail.com

[20] Pensel, P.E., Ullio, G.G., Fabbri, J., Ceballos, L., Bruni, S.S., Alvarez, L.I., Allemandi, D., Benoit, J.P., Palma, S.D., Elissondo, M.C. 2015. Cystic echinococcosis therapy: Albendazole-loaded lipid nanocapsules enhance the oral bioavailability and efficacy in experimentally infected mice. Acta Tropica. 152:185–194.

[21] Kumar, R., Pandey, K., Sahoo, G.C., Das, S., Das, V., Topno, R.K., Das, P. 2017. Development of high efficacy peptide coated iron oxide nanoparticles encapsulated amphotericin B drug delivery system against visceral leishmaniasis. *Materials Science and Engineering: C Materials for Biological Application*, 75:1465–1471.

[22] Fulop, V., Jakab, G., Bozo, T., Toth, B., Endresik, D., Balogh, E., Kellermayer, M., Antal, I. 2018. Study on the dissolution improvement of albendazole usingreconstitutable dry nanosuspension formulation. *European Journal of Pharmaceutical Sciences*, 123:70–78.

[23] Ullio-Gamboa, G., Palma, S., Benoit, J.P., Allemandi, D., Picollo, M.I., Toloza, A.C. 2017. Ivermectin lipid-based nanocarriers as novel formulations against head lice. *Parasitology Research*, 116:2111–2117.

[24] Placha, D., and Jampílek, J. 2019. Graphenic Materials for Biomedical Applications. *Nanomaterials*, 9:1758-1794.

[25] Jampílek, J., and Kráľová, K. 2021. Advances in drug delivery nanosystems using graphene-based materials and carbon nanotubes. *Materials*, 14:1059-1097.

[26] Kenry, K., Lim, Y.B., Nai, M.H., Cao, J., Loh, K.P., Lim, C.H.T. 2017. Graphene oxide inhibits malaria parasite invasion and delays parasitic growth in vitro. *Nanoscale*, 9:14065–14073.

[27] Murugan, K., Nataraj, D., Jaganathan, A., Dinesh, D., Jayashanthini, S., Samidoss, C.M., Paulpandi, M., Panneerselvam, C., Subramaniam, J., Aziz, A.T., Nicoletti, M., Kumar, S., Higuchi, A., Benelli, G. 2017. Nanofabrication of Graphene Quantum Dots with High Toxicity Against Malaria Mosquitoes, Plasmodium falciparum and MCF-7 Cancer Cells: Impact on Predation of Non-target Tadpoles, Odonate Nymphs and Mosquito Fishes. *Journal of Cluster Science*, 28:393–411.

[28] Jampílek, J., Kráľová, K., Fedor, P. 2020. Bioactivity of Nanoformulated Synthetic and Natural Insecticides and Their Impact on Environment. In: *Nanopesticides - From Research and Development to Mechanisms of Action and Sustainable Use in Agriculture*, edited by Fraceto, L.F., S.S. de Castro, V.L., Grillo, R., Avila, D., Oliveira, H.C., de Lima R., 165-225. Springer, Cham, Switzerland.

[29] Jayaseelan, C., Rahuman, C., Rajakumar, A.A., Kirthi, G., Santhoshkumar, A.V., Marimuthu, T., Bagavan, S., Kamaraj, A., Zahir, A.A., Elango, G. 2011. Synthesis of pediculocidal and larvicidal silver nanoparticles by leaf extract from heartleaf moonseed plant, Tinospora cordifolia Miers. *Parasitology Research*, 109:185–194.

[30] Barbosa, A.C.M.S., Silva, L.P.C., Ferraz, C.M., Tobias, F.L., de Araujo, J.V., Loureiro, B., Braga, G.M.A.M., Veloso, F.B.R., Soares, F.E.F., Fronza, M., Braga, F.R. 2019. Nematicidal activity of silver nanoparticles from the fungus Duddingtonia flagrans. *International Journal of Nanomedicine*, 14:2341–2348.

[31] Ahmad, A., Wei, Y., Syed, F., Khan, S., Khan, G.M., Tahir, K., Khan, A.U., Raza, M., Khan, F.U., Yuan, Q. 2016. Isatis tinctoria mediated synthesis of amphotericin B-bound silver nanoparticles with enhanced photoinduced antileishmanial activity: A novel green approach. *Journal of Photochemistry Photobiology B, Biology*, 161:17–24.

[32] Mishra, A., Kaushik, N.K., Sardar, M., Sahal, D. 2013. Evaluation of antiplasmodial activity of green synthesized silver nanoparticles, Colloids and Surfaces B: Biointerfaces, 111:713–718.

[33] Kannan, D., Yadav, N., Ahmad, S., Namdev, P., Bhattacharjee, S., Lochab, B., Singh, S. 2019. Pre-clinical study of iron oxide nanoparticles fortified artesunate for efficient targeting of malarial parasite. *EBioMedicine*, 45:261–277.

[34] Hadiza, A.M., Taura, D.W., Mohammed, B. 2018. Antiplasmodial activity of nanoparticles enhanced chloroquine on Plasmodium berghei in vivo. *Bayero Journal of Pure Applied Sciences*, 11:27–32.

[35] Norouzi, R., Ataei, A., Hejazy, M., Shahbazi, P. 2019. Acaricidal activity of zinc oxide nanoparticles against Hyalomma spp. in vitro. *Nanomedicine Research Journal*, 4:234–238.

Chapter 16

Part 3: Nanotechnology in Medicine and Pharmacy

Structure-property relationship study of silver nanoparticles stabilised with ammonium and phosphonium surfactants

M. Pisárčik*
Department of Chemical Theory of Drugs, Faculty of Pharmacy, Comenius University, Bratislava, Slovakia

ABSTRACT

Investigations of physicochemical properties and biological activity of silver nanoparticles (AgNPs) stabilised with tetra- and hexadecyltrimethylphoshonium bromide surfactants and tetra- and hexadecyltrimethylammonium bromide surfactants revealed their dependence on the molecular structure of stabilising surfactants. The size of surfactant stabilised AgNPs was in the range 50 – 80 nm with slightly higher values found for AgNPs stabilised with alkyltrimethylphoshonium bromide surfactants. These AgNPs showed somewhat smaller positive zeta potential values less than +50 mV which indicates weaker association of alkyltrimethylphosphonium surfactant molecules on AgNPs surface. On the other hand, this weaker association is responsible for increased cytotoxicity of AgNPs stabilised with alkyltrimethylphosphonium surfactant molecules. The dependence of physical parameters of AgNPs and their cytotoxicity on the alkyl chain length of stabilising surfactant shows the increased stability of AgNPs and their better cytotoxic action for stabilising ammonium and phosphonium surfactants with longer hexadecyl chains in surfactant molecular structure.

Keywords: silver nanoparticles; phosphonium, ammonium; cytotoxicity

INTRODUCTION

Silver nanoparticles (AgNPs) represent an attractive branch of nanomaterials suitable for the use in biomedical, industrial, and scientific areas. Despite a limited toxicity information and *in vivo* biological data of AgNPs, they turned out to be proven antibacterial agents in medical applications [1]. They were also found to have anticancer [2], antioxidative [3] and anti-inflammatory [4] effects. The main problems related to AgNPs are the low application concentration and poor particle stability in aqueous solutions over longer periods of time which results in the limitation of their potential applications. A promising solution to this issue turned out to be a stabilisation of AgNPs by various types of chemical stabilisers such as polymers and surfactants.

Cationic surfactants of various chemical composition exert strong stabilising effect on AgNPs. Due to the strong electrostatic interaction of surfactant headgroups with the surface of AgNPs, a protective bilayer composed of surfactant molecules is formed around AgNP. This surfactant bilayer protects AgNPs from agglomeration and subsequent phase separation of silver nanodispersions. Of the broad family of cationic surfactants, surfactant molecules containing quaternary nitrogen or phosphorus atom in the polar part of surfactant molecule (ammonium and phosphonium surfactants) turned out to be potent stabilisers of silver nanodispersions. Among phosphonium surfactants, alkyltriphenylphosphonium surfactants are of special importance because they are widely explored as a tool in mitochondrial bioenergetics, particularly in the strategy to target bioactive molecules to mitochondria by the attachment to the lipophilic triphenylphosphonium headgroups through alkyl linkers [5].

As our experimental results indicate [6-8], there is a relationship between ammonium and phosphonium surfactant molecular structure and physical properties, biological activity, and stability of surfactant-stabilised AgNPs. This relationship is rather complex and reveals the effect of various features in surfactant molecular structure on properties and stability of AgNPs.

---

* Corresponding Author´s Email: pisarcik@fpharm.uniba.sk

EXPERIMENTAL

The size of AgNPs stabilised with alkyltrimethylammonium and alkyltrimethylphosphonium cationic surfactants was determined using dynamic light scattering method (Brookhaven BI9000 correlator, 200SM goniometer) at 25°C and at the scattering angle 90°. Translational diffusion coefficient of AgNPs was obtained from time correlation curves. Hydrodynamic diameter values of nanoparticles were calculated from translational diffusion coefficient using the Stokes-Einstein formula. The mean values of AgNPs diameter were calculated from the set of five independent recordings of time correlation curve for each silver-to-surfactant molar ratio and plotted in the figures. Zeta potential of AgNPs was determined using a Brookhaven ZetaPlus equipment. Zeta potential was calculated from the measured electrophoretic mobility using the Smoluchowski approximation for charged colloidal particles. The plotted zeta mean values were calculated from the set of 20 repeated measurements. AgNPs cytotoxicity was determined on HepG2 cell line (ATCC HB-8065). After cells preparation and incubation, the cell proliferation was evaluated utilising the published procedure [9].

RESULTS AND DISCUSSION

Figures 1a and 1b show the influence of quaternary nitrogen and phosphorus atoms in surfactant headgroup on physical properties of AgNPs. For this purpose, size and zeta potential of AgNPs stabilised with tetradecyltrimethylphosphonium bromide (14m3) and hexadecyltrimethylphosphonium bromide (16m3) surfactants are compared with those of AgNPs stabilised with ammonium surfactants of identical alkyl chain length - tetradecyltrimethylammonium bromide (TTAB) and hexadecyltrimethylammonium bromide (CTAB).

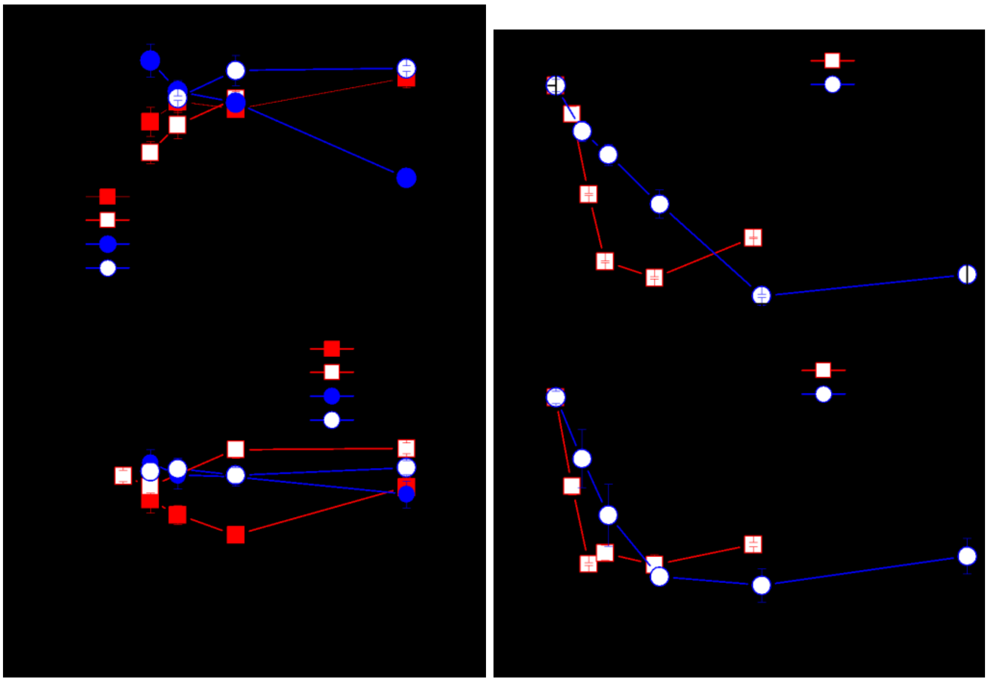

Figure 1. (a) Hydrodynamic diameter d of AgNPs stabilised with tetra- (TTAB) and hexadecyltrimethylammonium bromide (CTAB) surfactants; tetra- (14m3) and hexadecyltrimethylphosphonium bromide (16m3) surfactants plotted as a function of the molar ratio n_{Ag}/n_{surf} (b) zeta potential of AgNPs plotted as a function of n_{Ag}/n_{surf} (c) Comparison of *in vitro* cytotoxicity of AgNPs stabilised with TTAB and 14m3 (d) Comparison of *in vitro* cytotoxicity of AgNPs stabilised with CTAB and 16m3.

The interaction of tetra- and hexadecyltrimethylphoshonium bromide surfactant molecules with AgNPs (solid data symbols for Ag/14m3 and Ag/16m3 in the plot) results in a slightly larger particle

---

* Corresponding Author´s Email: pisarcik@fpharm.uniba.sk

diameter and a less positive zeta potential value, especially for shorter C_{14}-homologs of the investigated surfactant series (Fig. 1a and 1b). The stabilising effect of cationic surfactants on AgNPs is provided by the formation of a protective bilayer composed of surfactant molecules that surrounds silver nanoparticle. Physical properties of surfactant stabilised AgNPs depend on the molecular composition of this protective bilayer. The results shown in Fig. 1a and 1b indicate that the possible reason for this effect could be a less dense steric arrangement of alkyltrimethylphosphonium bromide molecules in the bilayer due to their bulkier phosphorus headgroup parts when compared with the molecular parameters of ammonium surfactant headgroup. Smaller electronegativity of phosphorus atom and larger size of phosphonium headgroup represent some level of a steric hindrance in the dense arrangement of alkyltrimethylphosphonium bromide molecules within surfactant bilayer surrounding AgNPs. On the other hand, higher electronegativity of nitrogen atom, stronger bonds in headgroup parts of alkyltrimethylammonium bromides and smaller headgroup size contribute to a stronger hydrophobic and electrostatic interactions between adjacent surfactant molecules in the bilayer. This results in a more positive zeta potential and smaller diameter of AgNPs stabilised with tetra- and hexadecyltrimethylammonium surfactant molecules.

The plots of cytotoxicity study of alkyltrimethylammonium and alkyltrimethylphosphonium stabilised AgNPs atoms show the percentage of surviving cancer cells plotted against surfactant concentration for surfactant alkyl chain length 14 (Figure 1c) and 16 (Figure 1d) carbon atoms. As the plots indicate, the steeper onset of the decrease in surviving cells percentage is observed for C_{14}- and C_{16}-trimethylphosphonium stabilised AgNPs (data symbols for Ag/14m3 and Ag/16m3). This is to relate to weakly-associated phosphonium headgroup cations on AgNPs surface which may facilitate the interactions of phosphonium surfactant stabilised AgNPs with cancer cell membranes, thus increasing biological effect of phosphonium surfactant stabilised AgNPs.

Beside the effect of different surfactant headgroup composition on the physical properties and cytotoxicity of surfactant stabilised AgNPs, hydrophobic interactions affect the size, zeta potential and cytotoxicity of surfactant stabilised AgNPs, as well. Figure 1b shows more positive zeta potential for AgNPs stabilised with C_{16}-homologs (16m3, CTAB, open data symbols) of ammonium and phosphonium surfactant series than for AgNPs stabilised with C_{14}-homologs (14m3, TTAB). This indicates better stabilising effect of longer surfactant alkyl chain on AgNPs. The difference in AgNPs size in favour of C_{16}-homologs is not that dominant (Fig. 1b). However, AgNPs stabilised by cationic surfactants with hexadecyl chains (16m3, CTAB) show cytotoxicity significantly higher than that of AgNPs stabilised by surfactants with a shorter tetradecyl hydrophobic chain (open circle data symbols in Fig. 1c, 1d).

CONCLUSIONS

The present study shows the effect of alkyltrimethylammonium bromide and alkyltrimethylphosphonium bromide surfactants on physical properties and cytotoxicity of surfactant stabilised AgNPs. As the results indicate, the interaction of alkyltrimethylphosphonium surfactant molecules with AgNPs results in a slightly larger particle diameter and a less positive zeta potential value which is to relate to weaker association of bulkier phosphonium headgroups on AgNPs surface. Weaker association of alkyltrimethylphosphonium bromides on AgNPs surface is responsible for the increased cytotoxicity when compared with the cytotoxicity level of AgNPs stabilised with alkyltrimethylammonium bromide surfactants.

ACKNOWLEDGMENTS

This work was supported by the Grant Agency of Ministry of Education and Academy of Science of Slovak republic (VEGA), Projects No. 1/0686/21 and 1/0054/2019 and by the Slovak Research and Development Agency Grant No. APVV-17-0373.

---

* Corresponding Author´s Email: pisarcik@fpharm.uniba.sk

Chapter 16

Part 3: Nanotechnology in Medicine and Pharmacy

REFERENCES

[1] Lara, H.H., Garza-Trevino, E.N., Ixtepan-Turrent, L., Singh, D.K. 2011. Silver nanoparticles are broad-spectrum bactericidal and virucidal compounds. *Journal of Nanobiotechnology*, 9:30-37.

[2] Yeşilot, Ş., and Acar, Ç.A. 2019. Silver nanoparticles; a new hope in cancer therapy? *Eastern Journal of Medicine*, 24:111–116.

[3] Soni, N., and Dhiman, R.C. 2017. Phytochemical, Anti-oxidant, Larvicidal, and Antimicrobial Activities of Castor (Ricinus communis) Synthesized Silver Nanoparticles. *Chinese Herbal Medicines*, 9:289–294.

[4] Jiang, Q., Yu, S., Li, X., Ma, C., Li, A. 2018. Evaluation of local anesthetic effects of Lidocaine-Ibuprofen ionic liquid stabilized silver nanoparticles in Male Swiss mice. *Journal of Photochemistry and Photobiology B: Biology*, 178:367–370.

[5] Bakshi, M.S., Singh, J., Singh, K., Kaur, G. 2004. Mixed Micelles of Cationic Gemini with Tetra Alkyl Ammonium and Phosphonium Surfactants: The Head Group and Hydrophobic Tail Contributions. *Colloids and Surfaces A: Physicochemical and Engineering Apects*, 234:77–84.

[6] Pisárčik, M., Jampílek, J., Lukáč, M., Horáková, R., Devínsky, F., Bukovský, M., Kalina, M., Tkacz, J., Opravil, T. 2017. Silver nanoparticles stabilised by cationic gemini surfactants with variable spacer length. *Molecules*, 22:1794-1812.

[7] Pisárčik, M., Jampílek, J., Lukáč, M., Bilka, F., Bilková, A., Pašková, Ľ., Devínsky, F., Horáková, R., Opravil, T. 2018. Silver nanoparticles stabilised with cationic single-chain surfactants. Structure-physical properties-biological activity relationship study. *Journal of Molecular Liquids*, 272:60–72.

[8] Pisárčik, M., Lukáč, M., Jampílek, J., Bilka, F., Bilková, A., Pašková, Ľ., Devínsky, F., Horáková, R., Opravil, T. 2020. Phosphonium surfactant stabilised silver nanoparticles. Correlation of surfactant structure with physical properties and biological activity of silver nanoparticles. *Journal of Molecular Liquids*, 314:113683.

[9] Raspotnig, G., Fauler, G., Jantscher, A., Windischhofer, W., Schachl, K., Leis, H.J. 1999. Colorimetric determination of cell numbers by Janus green staining. *Analytical Biochemistry,* 275:74–83.

---

* Corresponding Author´s Email: pisarcik@fpharm.uniba.sk

Gold nanorods with organosilica shell as potential dual-therapeutic agents

N.A. Salavatov**, *O.V. Dement'eva, V.M. Rudoy

Frumkin Institute of Physical Chemistry and Electrochemistry, Russian Academy of Sciences, Moscow

ABSTRACT

The main features of the formation of mesoporous $SiO_{1.5}SH$-shell with the tailored thickness on the gold nanorod surface with the use of 3-mercaptopropyltrimethoxysilane as a precursor have been systematically studied. Quantitative data of the cisplatin sorption by the synthesized composite particles has been obtained. Such multifunctional nanostructures are of considerable interest from the point of view of combining photothermal and chemotherapy of cancer.

Keywords: nanocomposite; plasmonic; nanorods, core-shell

INTRODUCTION

The application of nanoparticles in the biomedical field opens up new possibilities in the diagnosis and treatment of cancer and other socially significant diseases. Recently, special attention has been paid to more complex composite nanoparticles. Such structures can combine several functions, for example, serve as diagnostic and therapeutic agents of dangerous diseases [1].

The common known type of composite nanoparticles is nanoparticles with a noble metal core (for example, gold nanorod) and a silica shell.

The main property of gold nanorods is longitudinal localized surface plasmon resonance (LSPR). The position of the LSPR band depends on their aspect ratio and can be easily "tuned" in a wide spectral range, including the near-IR spectral region (i.e. the region of biological tissue optical window). Therefore, gold nanorods are used in optical diagnostics and photothermal therapy of cancerous tumors. Silica shells of composite nanoparticles can serve as the container for dye molecules, drugs, etc. Tetraethoxysilane (TEOS) is usually used as a precursor for silica shells. In this case, to obtain a mesoporous shell, it is necessary to use a surfactant.

We propose to use for this purpose another precursor, 3-mercaptopropyltrimethoxysilane (MPTMS), which has several advantages over TEOS. First, the triol group has a chemical affinity for the surface of gold nanorods. Second, the asymmetric structure of MPTMS molecule provides the formation of a porous shell without the use of surfactants in comparison with TEOS. Also, it should be noted that reactive SH-group of the MPTMS can be used for shell functionalization with various compounds. For example, it is well known that thiol groups coordinate the ions of different metals.

In this work, we demonstrate the advantages of $SiO_{1.5}SH$-shells by loading a popular and weel-studied chemotherapy drug – cisplatin.

EXPERIMENTAL STUDY

Gold nanorods were obtained by the seedless synthesis in micellar solutions of cetyltrimethylammonium bromide (CTAB) [2]. $SiO_{1.5}SH$-shells were formed on the surface of gold nanorods using MPTMS as a precursor in an alkaline medium. The scheme of such composite nanoparticle synthesis is shown in Fig. 1.

---

* Corresponding Author´s Email: gop--nick@yandex.ru

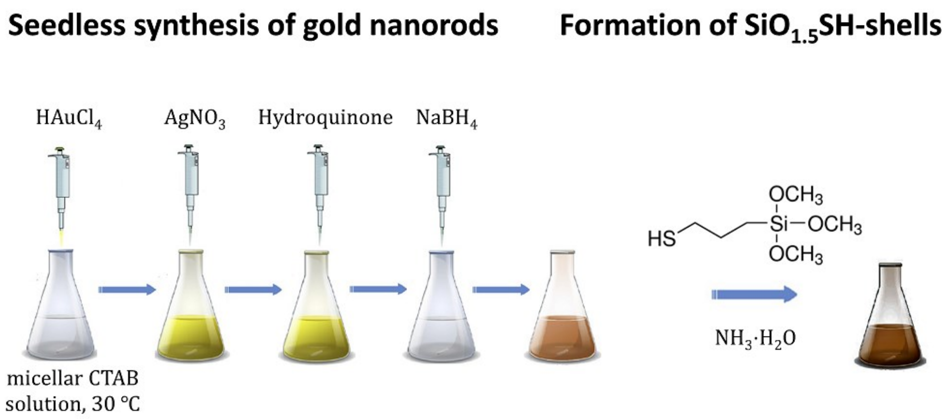

Figure 1. Scheme of the composite nanoparticle synthesis.

Cisplatin was loaded into $SiO_{1.5}SH$-shells by sorption from aqueous solutions. To increase the aggregative stability of the sol during the sorption of cisplatin, the composite nanoparticles were modified with methoxypolyethylene glycol maleimide.

UV-vis-NIR Spectroscopy was used to study the optical properties of the nanoparticles and to determine the cisplatin concentration. The morphology and particle size distribution were studied using a high-resolution transmission electron microscope (HRTEM) and an atomic force microscope. The presence and distribution of cisplatin in composite nanoparticles were determined using energy dispersive X-ray analysis.

RESULTS AND DISCUSSION

In the seedless synthesis of gold nanorods, in contrast to the classical “seeded approach”, particle nucleation and growth occur in one pot, which greatly simplifies the process. This protocol allows us to obtain monodisperse gold nanorods and to tune the position of the LSPR in a wide wavelength range. During the synthesis of $SiO_{1.5}SH$-shells, the formation of by-products as coreless organosilica nanoparticles is detected. To solve this problem, it is necessary to suppress homogeneous nucleation. We succeeded in achieving this aim by drop-wise injection MPTMS, increasing the concentration of gold nanorods (i.e. centers of heterogeneous nucleation) and the amount of ethanol in the reaction system. Moreover, the synthesis was carried out at an elevated temperature (40–60 °C). The optimized synthesis protocol allows us not only to completely suppress the formation of organosilica nanoparticles but also to provide fine control of the $SiO_{1.5}SH$-shell thickness of composite nanoparticles (Fig. 2). The formation of $SiO_{1.5}SH$ shells predictably leads to a bathochromic shift of the longitudinal LSPR, which is associated with a change in the dielectric constant near the gold nanorods (Fig. 3).

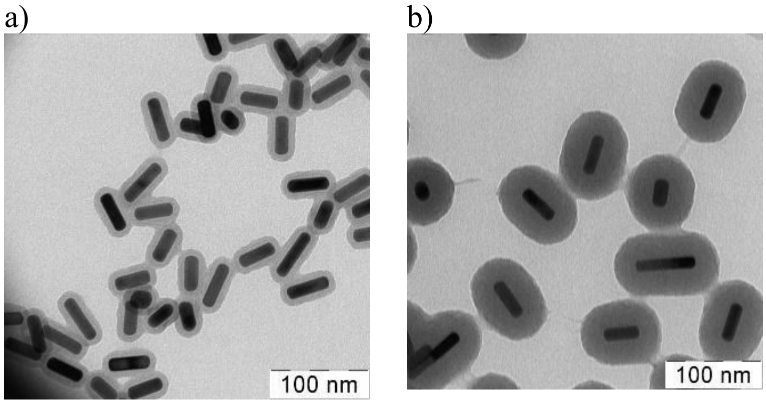

Figure 2. HRTEM-images of gold nanorods coated $SiO_{1.5}SH$-shell with thickness 13 nm (a) and 28 nm (b).

---

* Corresponding Author´s Email: gop--nick@yandex.ru

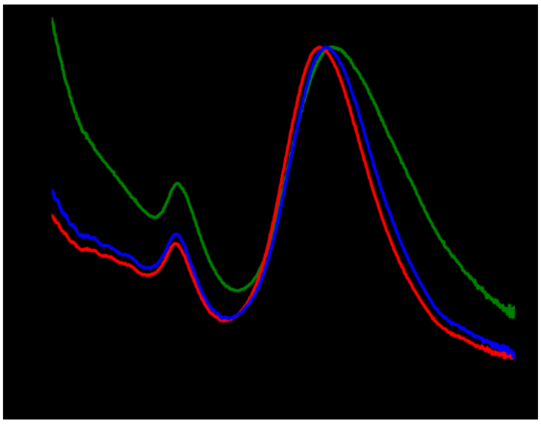

Figure 3. UV-vis-NIR spectra of gold nanorods (black curve) and gold nanorods coated $SiO_{1.5}SH$-shell with thickness 5 (red curve), 13 (blue curve) and 28 nm (green curve).

After sorption of cisplatin from aqueous solutions in $SiO_{1.5}SH$-shells, the plasmon characteristics of composite nanoparticles change only slightly, that indicates the aggregative stability of the dispersion.

Preliminary data on the peculiarities of cisplatin sorption are shown in Fig. 4. We should note that the sorption value is high enough and reaches is high enough (greater than 1 g/cm^3).

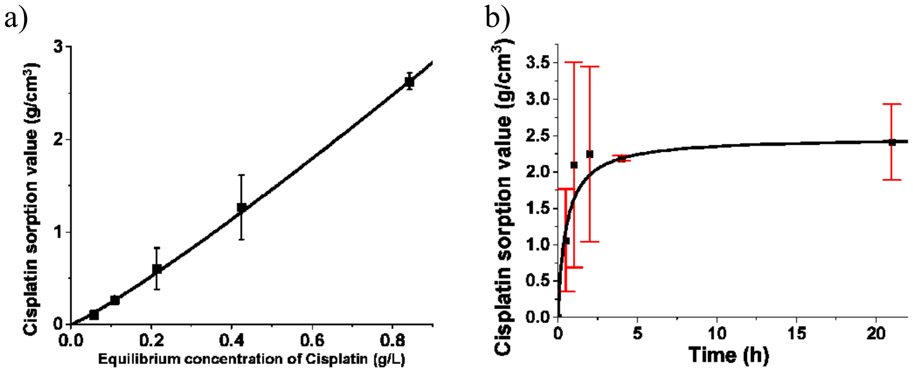

Figure 4. (a) isotherm of cisplatin sorption by organosilica shells; (b) kinetic curve of cisplatin sorption.

The loading of cisplatin into $SiO_{1.5}SH$-shells is confirmed by elemental mapping by energy dispersive analysis of X-rays. Besides the expected elements like Au, S, Si, the Pt is also detected in a rather high quantity.

The assumption that thiol groups are responsive for the high sorption value of cisplatin is confirmed by the data of FTIR spectroscopy. The band near 2560 cm^{-1}, corresponding to the stretching vibrations of the SH-group, disappears after the sorption of cisplatin.

CONCLUSION

Multifunctional composite nanoparticles with an anisotropic gold core and $SiO_{1.5}SH$-shell were synthesized. The sorption of the cytostatic cisplatin by such composite nanoparticles was studied.

ACKNOWLEDGMENTS

The reported study was funded by RFBR, project number 20-33-90266.

---

* Corresponding Author´s Email: gop--nick@yandex.ru

Chapter 17

Part 3: Nanotechnology in Medicine and Pharmacy

REFERENCES

[1] Dykman, L.A., and Khlebtsov, N.G. 2016. Multifunctional gold-based nanocomposites for theranostics. *Biomaterials*, 108:13–34.

[2] Salavatov, N.A., Dement'eva, O.V., Mikhailichenko, A.I., Rudoy, V.M. 2018. Some Aspects of Seedless Synthesis of Gold Nanorods. *Colloid Journal*, 80:541–549.

---

* Corresponding Author´s Email: gop--nick@yandex.ru

Albumin loaded PEG/HAp composite coatings with bone regenerative potential

A. Sobczak-Kupiec*[1], D. Słota[1], W. Florkiewicz[1]

[1] Faculty of Materials Engineering and Physics, Cracow University of Technology, Poland

ABSTRACT

The aim of the presented research was to create a ceramic-polymer coating, demonstrating bioactive properties, for potential use in bone tissue regeneration. For this purpose, hydroxyapatite, known for its osteoconductive properties and polymer phase, which was (PEG), were used. This system was then modified by the addition of bovine serum albumin. Hydroxyapatite was obtained by wet precipitation method and characterized using X-ray diffraction and FT-IR. Ceramic-polymer coatings with albumin were prepared using a photopolymerization method. Coatings were then incubated in simulated biological fluid (SBF) and the changes occurring due to the interaction of the material with the fluid were observed using SEM imaging. Analysis of the surface morphology demonstrated that new apatite layers appeared after 14 days of incubation. This satisfactory information confirms the interactions between the sample and the incubation fluid, thus demonstrating the bioactivity of the materials obtained.

Keywords: hydroxyapatite; ceramics; biomaterials; coatings; biomineralization

INTRODUCTION

Osteoporosis is a disease of civilization, manifested by decrease of bone density, thus when resorption processes occur faster than bone formation. It is estimated that currently more than 200 million people worldwide are affected and that it results in more than 8.9 million fragility fractures each year [1][2]. The disease affects people of both sexes, including one in five men and one in three women over the age of 50. Decreased oestrogen levels due to changes in hormone management after menopause contribute to the higher incidence in women [3]. Potentially the most effective way to treat osteoporosis and regenerate bone tissue are those containing bioactive agents.

Such a bioactive agent with great potential is hydroxyapatite (HAp). Synthetic HAp is used in dentistry and in orthopaedics to replace hard tissues. Particularly interesting is not only its biocompatibility and ability to bond with natural bone, but above all its ability to osteoinduction, which is a process leading to osteogenesis, i.e. the formation of new bone [4][5]. However, the primary factor limiting the application of hydroxyapatite itself is its high brittleness. Although, the solution to these problems, while maintaining the bioactive character of the material, is to create a composite with an elastic phase, exhibiting higher flexibility than Hap [6].

The polymer chosen for the present study is poly(ethylene glycol) (PEG), also known as poly(ethylene oxide) or poly(oxyethylene). It is one of the most widely used non-natural polymers in biomaterials designing field. PEG can reduce the adsorption of biomolecules and attachment of microorganisms [7]. What is more, it has the excellent biocompatibility which helps to realise the therapeutic effect. PEG-containing materials also reduce the risk of thrombus formation, by inhibiting platelet adhesion, while having no antigenicity or harmful effects on cells [8] [9].

Another well-known factor providing the appropriate conditions for cell growth is the protein-albumin. It is the most abundant human plasma protein, constituting over 50% of the total protein present in the bloodstream. Albumin not only has a high biological value because it consists of tryptophan, methionine, lysine, arginine and cystine but it is also inexpensive. In the form of bovine

---

* Corresponding Author´s Email: agnieszka.sobczak-kupiec@pk.edu.pl

serum albumin (BSA), it is obtained by purifying blood obtained as a by-product of the cattle industry [10] [11].

The aim of the presented work, was to create composite coatings based on PEG and HAp modified with the addition of BSA. The coatings were subjected to detailed physicochemical analysis and incubation studies in simulated biological fluid (SBF) to observe the changes occurring in the material due to interactions with the fluid.

EXPERIMENTAL/THEORETICAL STUDY

HYDROXYAPATITE SYNTHESIS

HAp was obtained via wet precipitation method. To Na_2HPO_4 (0.26 mol/L) few drops of ammonia water was added in order to obtain an alkaline pH value (pH>10). The mixture was then heated to boiling point and when the boiling point has been reached $(CH_3COO)_2Ca$ (0.128 mol/L) was added dropwise under constant stirring at a rate of 1 drop/s. After the reaction was completed, the powder was aged during 24 hours at room temperature. The sludge was then washed with distilled water an freeze-dried.

FT-IR ANALYSIS

To identify the functional groups in the HAp sample, infrared spectroscopy was used with a FT-IR spectrometer (Thermo Scientific, Nicolet iS5 FTIR, USA, Waltham) equipped with iD7 ATR accessory operated at room conditions in the range of 4000 cm^{-1} – 400 cm^{-1}.

XRD ANALYSIS

Crystallinity degree and phase composition of HAp were determined using the X-ray diffraction method (Rigaku SmartLab X-Ray Difractometer). The measurement was performed at the voltage of 40 kV and 30 mA in 2θ range of 10° - 60° and step size 0.002° 2θ.

PREPARATION OF COATINGS

A 20% PEG solution was prepared. Then, 0.5 g of HAp and 0.15 g of BSA were added to 10 mL of the solution. The mixture was stirred thoroughly. Afterwards PEGDA and 2-hydroxy-2-methylpropinophenone were added to the mixture to enable the polymerization reaction to occur. The prepared samples were placed under EMITA VP 60 lamp, 180 W for 3 minutes.

MORPHOLOGY ANALISYS

To determine the topography of HAp and coatings, the analysis of surface morphology by scanning electron microscopy (Jeol 5510LV Scanning Electron Microscope with EDS IXRF) was performed. The study enabled the detection of potential deposits formed on the surface of the samples as a result of interaction with individual ions of artificial biological fluids.

RESULTS AND DISCUSSION

Figure 1a shows the X-ray spectrum of the obtained ceramics. The performed study indicated that the only phase identified in the investigated material is HAp, and the visible background spectrum suggest that the substance is medium crystalline. The FT-IR spectroscopic analysis is presented in Figure 1b. The infrared analysis showed the presence of functional groups characteristic of HAp.

---

* Corresponding Author´s Email: agnieszka.sobczak-kupiec@pk.edu.pl

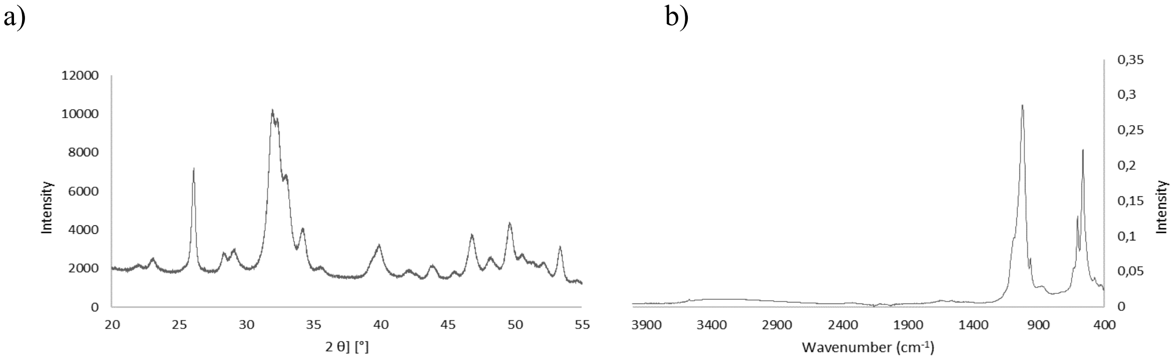

Figure 1. (a) XRD diffractogram of HAp; (b) FTIR spectra of HAp.

The results of incubation in SBF are shown in Figure 2. Samples were incubated in SBF for 14 days at 37 degrees. Figure 2a presents the surface of the coating before the incubation period, 2b and 2c are the incubation result for the coatings without and with the addition of BSA.

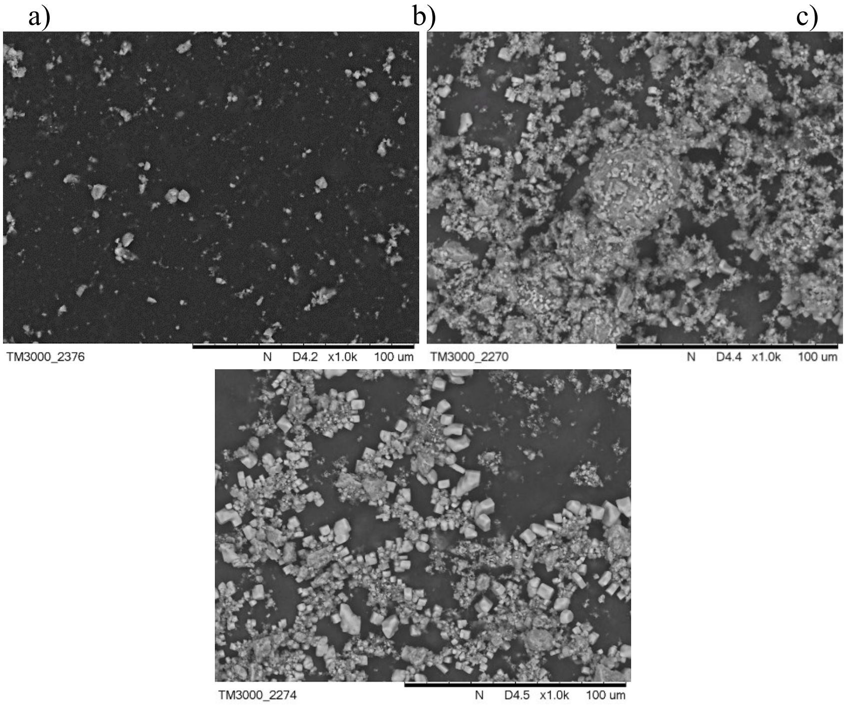

Figure 2. SEM image of: (a) surface morphology of coating before incubation; (b) surface morphology of coating after incubation in SBF; (c) surface morphology of coating with BSA after incubation in SBF.

Comparing the surface of the samples before and after the incubation period new apatite layers are clearly visible. Their appearance is the most desirable feature of biomaterials as it proves their bioactivity as well as confirms the existence of interactions between the sample and the incubation fluid. The addition of albumin affected the nature of the crystals formed on the surface. Considering these satisfactory results and the nature of polymer networks, the presented composite coatings may also find application in the transport of many other active substances such as antibiotics or drugs.

* Corresponding Author´s Email: agnieszka.sobczak-kupiec@pk.edu.pl

CONCLUSION

The work presented above focused on a brief physicochemical analysis of ceramic-polymer composite coatings. XRD and FT-IR analysis confirmed that the wet synthesis method used indeed yields HAp with satisfactory parameters. In vitro incubation in SBF, resulting in many new apatite layers observed on the surface, further confirmed the bioactivity of HAp. These promising results provide great potential for composite coatings as well as suggest further work on their modification and use in drug delivery systems.

ACKNOWLEDGMENTS

The "Multifunctional biologically active composites for applications in bone regenerative medi-cine" project is carried out within the TEAM-NET program of the Foundation for Polish Science financed by the European Union under the European Regional Development Fund. The authors gratefully acknowledge financial support.

REFERENCES

[1] Sözen, T., Özışık, L., Başaran, N.C. 2017. An overview and management of osteoporosis. *European Journal of Rheumatology*, 4:46–56.

[2] Ström, O., Borgström, F., Kanis, J.A., Compston, J., Cooper, C., McCloskey, E.V., Jönsson, B. 2011. Osteoporosis: Burden, health care provision and opportunities in the EU. *Archives of Osteoporosis*. 6:59–155.

[3] Ji, M-X., and Yu, Q. 2015. Primary osteoporosis in postmenopausal women. *Chronic Diseases and Translational Medicine*, 1:9–13.

[4] Kolmas, J., Krukowski, S., Laskus, A., Jurkitewicz, M. 2016. Synthetic hydroxyapatite in pharmaceutical applications. *Ceramics International*, 42:2472–2487.

[5] Murata, M., Hino, J., Kabir, M.A., Yokozeki, K., Sakamoto, M., Nakajima, T., Akazawa, T. 2021. Osteoinduction in Novel Micropores of Partially Dissolved and Precipitated Hydroxyapatite Block in Scalp of Young Rats. *Materials*, 14:196-204.

[6] Corcione, C.E., Gervaso, F., Scalera, F., Montagna, F., Maiullaro, T., Sannino A., Maffezzoli A. 2017. 3D printing of hydrox-yapatite polymer-based composites for bone tissue engineering. *Journal of Polymer Engineering*, 37:741-746.

[7] Zeng, G., Ogaki, R., Meyer, R.L. 2015. Non-proteinaceous bacterial adhesins challenge the antifouling properties of polymer brush coatings. *Acta Biomaterialia*, 24:64–73.

[8] Xu, L., Bauer, J.W., Siedlecki, C.A. 2014. Proteins, Platelets, and Blood Coagulation at Biomaterial Interfaces. *Colloids and Surfaces B: Biointerfaces*, 124:49–68.

[9] Ali, A., and Andriyana, A. 2020. Properties of multifunctional composite materials based on nanomaterials: A review. *RSC Advances*, 10:16390–16403.

[10] Rogalinski, T., Herrmann, S., Brunner, G. 2005. Production of amino acids from bovine serum albumin by continuous sub-critical water hydrolysis. *Journal of Supercritical Fluids*, 36:49–58.

[11] Hong, S., Choi, D.W., Kim, H.N., Park, C.G., Lee, W., Park, H.H. 2020. *Protein-based nanoparticles as drug delivery systems. Pharmaceutics*, 12:604-632.

---

* Corresponding Author´s Email: agnieszka.sobczak-kupiec@pk.edu.pl

Biodegradable polymeric materials with antimicrobial effects suitable for medical applications

K. Škrlová[1,2], K. Malachová[3], Z. Rybková[3], T, Stachurová[3], J. Zágora[1], Marta Fernández-García[4], and Daniela Plachá [1,5]*

[1]Nanotechnology Centre, CEET, VŠB–Technical University of Ostrava, 17. listopadu 15, 708 00 Ostrava-Poruba, Czech Republic;
[2]Center of Advanced Innovation Technologies, VŠB–Technical University of Ostrava, 17. listopadu 15, 708 00 Ostrava-Poruba, Czech Republic;
[3]Department of Biology and Ecology, Faculty of Science, University of Ostrava, Chittussiho 10, 71000 Ostrava, Czech Republic;
[4]Institute of Polymer Science and Technology (ICTP-CSIC), Juan de la Cierva 3, 28001 Madrid, Spain;
[5]ENET Centre, VŠB–Technical University of Ostrava, 17. listopadu 15, 708 00 Ostrava -Poruba, Czech Republic

ABSTRACT

Biodegradable polymers are promising materials for use in medical applications. The properties of these materials are comparable to commercial non-biodegradable polymers. This paper focuses on the preparation of biodegradable polymer composites based on polylactide, which are modified with antimicrobial fillers based on silicate and graphene matrices, which have been enriched with antimicrobial agents: Ag, hexadecyltrimethylammonion and hexadecylpyridinium cations. These composites have been investigated for their chemical-physical, degradable and antimicrobial properties.

Keywords: polylactide; antimicrobial; biodegradable; degradable; silver; medical applications

INTRODUCTION

Currently, polymeric materials are used for many medical applications - stents, catheters, fracture fixation screws and other implants. Polymers have a wide range of chemical, physical and mechanical properties that can be adapted and improved by modification with various fillers. Science deals with the development of composite materials based on biodegradable polymers such as polylactide, polycaprolactone or polyglycolide.

Polylactide (PLA) is currently one of the most studied biodegradable polymers, as it is the most stable biocompatible polymer. This material is comparable in properties to petroleum-based materials and is easily modifiable with various fillers that can give it new properties.

The main problem of biodegradable polymeric materials in medicine is the formation of a bacterial biofilm on the surface of the polymeric material. This biofilm is made up of colonies of bacteria that can cause extensive infection and endanger the patient's life. The solution to this problem is to modify the biodegradable polymer with an antimicrobial agent [1].

EXPERIMENTAL/THEORETICAL STUDY

Polylactide-based composite materials (PLA) were prepared from IngeoTM 4032D polylactide, supplied by RESINEX Czech Republic s.r.o. PLA was modified with Ag-enriched vermiculite fillers; hexadecyltrimethylammonium cations (HDTMA); hexadecylpyridinium cations (HDP). Furthermore, PLA was modified with graphene oxide (GO) enriched in Ag.

---

* Corresponding Author´s Email: katerina.skrlova@vsb.cz

The prepared fillers were characterized using FTIR, XRD, SEM, ICP-AES, TOC for basic chemical and physical properties. Furthermore, the fillers were characterized for their antibacterial properties.

Polymer composites were characterized by SEM, optical microscope, DSC, XRD, TGA, GPC. Furthermore, polymer composites have been characterized for their degradable and antimicrobial properties for common bacteria in the human body (*E. coli, P. aeruginosa, S. aureus, S.salivarius, C. albicans*).

RESULTS AND DISCUSSION

The characterization of antimicrobial fillers was performed using the disk method and proved the presence of antimicrobial agent in all prepared fillers and subsequently also antibacterial character. PLA was modified with these fillers. Homogenization took place in the melt and the same layers were extruded from the polymer composites. Using individual characterizations, the basic chemical and physical properties were clarified and the individual composites were found to be a stable material that could be used for medical applications. At the same time, the degradation of degradable properties was performed for 6 months, which showed that the polymer composites undergo gradual degradation in physiological saline and release antimicrobial fillers into their surroundings. This was subsequently confirmed also by antimicrobial testing using the disk method, which showed the antimicrobial character of the composites for all tested time intervals (0, 1, 2, 3 and 6 months).

Thus, it can be assumed that the prepared antimicrobial composite materials are suitable for temporary body implants such as stents or temporary fracture fixation devices.

CONCLUSION

In this work, antimicrobial fillers with vermiculite and graphene oxide matrix were prepared. The vermiculite matrix was modified with antimicrobial agents (Ag, HDTMA and HDP), the graphene oxide matrix was modified with Ag. The prepared fillers proved the antibacterial character of common bacteria in the human body. These fillers modified the biodegradable polymeric material - PLA. The prepared polymer composites were tested by conventional chemical-physical methods. At the same time, the characterization of degradable and antimicrobial properties of prepared composites was performed. The results showed that the prepared polymeric composite layers undergo degradation over time and release antimicrobial filler into their surroundings. At the same time, these composites themselves retain their antimicrobial character.

ACKNOWLEDGMENTS

This research was funded by MSMT projects No. CZ.02.1.01/0.0/0.0/17_049/0008441 "Innovative Therapeutic Methods of Musculoskeletal System in Accident Surgery" within the Operational Programme Research, Development, and Education financed by the European Union and by the state budget of the Czech Republic; Doctoral grant competition VSB - Technical University of Ostrava, reg. no. CZ.02.2.69/0.0/0.0/19_073/0016945 within the Operational Programme Research, Development and Education, under project DGS/TEAM/2020-001 "Development of antimicrobial biobased polymeric material using supercritical fluid technology; Programme i-LINK+ 2020: Design of novel antimicrobial biobased materials using supercritical fluids processes, LINKA20364.

REFERENCES

[1] Škrlová, K., Malachová, K., Muñoz-Bonilla, A., Měřinská, D., Rybková, Z., Fernández-García, M., Plachá, D. 2019. Biocompatible polymer materials with antimicrobial properties for preparation of stents. *Nanomaterials*, 9(11):1548-1578, doi:10.3390/nano9111548.

---

* Corresponding Author´s Email: katerina.skrlova@vsb.cz

Green synthesized silver nanoparticles: antibacterial activity, biocompatibility, and analyses of surface-attached proteins

J. Trzcińska-Wencel*[1], M. Wypij[1], M. Rai[1,2], P. Golińska[1],
[1]Department of Microbiology, Nicolaus Copernicus University, Poland
[2]Nanobiotechnology Laboratory, Department of Biotechnology, SGB Amravati University, India

ABSTRACT

In this study, the antibacterial and cytotoxic effect of AgNPs biosynthesized from filamentous actinobacterium, strain SF23, was evaluated against bacteria by determination of MIC, MBC and ATP level, as well as against cancer (MCF-7) and murine macrophages (RAW 264.7) using MTT assay, measurement of LDH release and determination of ROS level. Moreover, the capping proteins of NPs were identified by LC-MS/MS. Nanoparticles exhibited antibacterial activity (MIC of 8-128 µg mL^{-1}, MBC of 64-256 µg mL^{-1}) and significantly decreased ATP level in bacterial cells. The *in vitro* analysis showed dose-dependent cytotoxicity of AgNPs. Cell viability decrease was found to be 42.2-14.2% and 38.0-15.5% while LDH leakage 14.6-42.7% and 19.0-45.0%, respectively. Moreover, MCF-7 cells released a greater amount of ROS than RAW 264.7 macrophages during stimulation with AgNPs. The SDS-PAGE analysis revealed the presence of 5 protein bands at a molecular weight between 31.7 and 280.9 kDa. These proteins showed the highest homology to hypothetical proteins and porins from *E. coli, Delftia* sp. and *P. rhodesiae*. Obtained results suggest antimicrobial and anticancer potential of biosynthesized AgNPs in medical applications in the future.

Keywords: biogenic AgNPs; capping proteins; antibacterial and anticancer agents; cytotoxicity

INTRODUCTION

The increasing number of multi-drug-resistant bacteria and cancer cases, that are a real threat to humankind, forces research world to develop new weapons to deal with it. Biogenic silver nanoparticles (AgNPs) are considered as a solution to solve this problem. Biosynthesis of AgNPs is regarded as a green, eco-friendly, low-priced process that provides small and biocompatible nanostructures with antimicrobial and anticancer activities and potential application in medicine. The biocompatibility of these nanoparticles is related to the coating with biomolecules of natural origin [1].

EXPERIMENTAL STUDY

The synthesis of AgNPs from actinobacterial strain SF23 was confirmed using UV-Vis spectroscopy while their morphology, crystalline structure, stability and coating were characterized using TEM, XRD, Zeta potential and FTIR. Antibacterial activity of biogenic AgNPs was determined by estimation of minimum inhibitory and minimum biocidal concentrations (MIC and MBC) against *E. coli, K. pneumoniae, P. aeruginosa* and *S. aureus.* The potential mechanism of antibacterial action of AgNPs was determined by measurement of ATP level while the *in vitro* cytotoxicity of AgNPs on human breast cancer (MCF-7) and murine macrophage (RAW 264.7) cell lines by MTT (3-(4,5-dimethylthiazol-2-yl)-2,5-diphenyltetrazolium bromide) assay, cell LDH release and measurement of ROS level were assessed. The nanoparticle capping proteins were separated using SDS-PAGE electrophoresis and identified using LC-MS/MS.

---

* Corresponding Author´s Email: trzcinska@doktorant.umk.pl

RESULTS AND DISCUSSION

Biosynthesized nanoparticles were spherical in shape, small in size (mean 13.2 nm), showed crystalline nature, good stability (-18.7 mV) and presence of capping agents. The type, morphology, stability and aggregation of nanoparticles are the main properties determining their biological activity, including the toxic effect on biological systems [2, 3]. AgNPs exhibited antibacterial activity (MIC of 8-128 µg mL^{-1}, MBC of 64-256 µg mL^{-1}) and significantly decreased ATP levels in bacterial cells after treatment with different concentrations of AgNPs. This high toxicity of AgNPs toward microbial cell showed their potential as an antimicrobial agent. Similar findings were reported recently by other authors[4] who found that biogenic AgNPs significantly (about 3.5 times) decreased ATP synthesis in *P. aeruginosa* and *S. aureus* when compared to untreated cells. Such findings suggest that membrane ATPase is a potential target for AgNPs and its inhibition may affect metabolic activity in bacterial cell [4, 5]. The use of AgNPs for biomedical purposes, especially *in vivo* applications, requires determination of their cytotoxic effect. Although many studies on the toxicity of biogenic AgNPs in various cell lines have been reported, the mechanisms underlying the toxicity in eukaryotic cells are still unclear[1].The *in vitro* analysis showed that the AgNPs demonstrated dose-dependent cytotoxicity against RAW 264.7 macrophages and MCF-7 cancer cells but higher against the latter than the former. Cell viability decrease was found to be 42.2-14.2% and 38.0-15.5% while LDH leakage 14.6-42.7% and 19.0-45.0%, respectively. IC50 values calculated for MTT assay was found to be 16.3 and 12.0 µg mL^{-1} and for LDH assay 102.3 and 76.2 µg mL^{-1}, respectively. Moreover, MCF-7 cells released a greater amount of ROS than RAW 264.7 macrophages during stimulation with all tested concentrations of AgNPs (1.47-3.13 and 1.02-2.58 fold increase, respectively). The SDS-PAGE analysis revealed the presence of 5 protein bands at a molecular weight between 31.7 and 280.9 kDa. These proteins showed the highest homology to hypothetical proteins and porins from *E. coli, Delftia* sp. and *P. rhodesiae.* However, based on available reports, that the current knowledge on capping agents of nanoparticles, especially once of the bacterial origin, is still in their infancy [1]. Proteins associated with AgNPs change their physical and chemical properties, mainly surface charge and composition. Although the capping proteins can increase internalization of AgNPs into cells via endocytosis, regulate cellular uptake and bioavailability of AgNPs, they can also be responsible for the toxic activity of AgNPs [6,7].

CONCLUSION

These biogenic nanoparticles showed good stability, high antibacterial activity and inhibited ATP synthesis as potential antimicrobial mechanism of action. They showed cytotoxicity against breast cancer cells and macrophages but higher towards the former ones. Based on our findings, it can be concluded that biosynthesized silver nanoparticles from actinobacterial strain SF23 are capped with proteins and may be a potential cytotoxic agent against cancer cells and bacteria. In addition, presence of nanoparticle coating with many functional groups gives opportunities for further modifications to improve their biological activity, namely antimicrobial and anticancer ones, and biocompatibility. Considering the potential of these nanoparticles, they can be recommended for biomedical applications after further *in vivo* studies.

ACKNOWLEDGMENTS

This research was funded by National Science Centre (NSC), Poland, grant Preludium (no. 2016/23/N/NZ9/00247).

REFERENCES

[1] Wypij, M., Jędrzejewski, T., Trzcińska-Wencel, J., Ostrowski, M., Rai, M., Golińska, P. 2021. Green Synthesized Silver Nanoparticles: Antibacterial and Anticancer Activities, Biocompatibility, and

---

* Corresponding Author´s Email: trzcinska@doktorant.umk.pl

Analyses of Surface-Attached Proteins. *Frontiers in Microbiology*, 12:632505. doi: 10.3389/fmicb.2021.632505

[2] Rai, M., Gupta, I., Ingle, A.P., Biswas, J.K., Sinitsyna, V.O. 2018. Nanomaterials: What Are They, Why They Cause Ecotoxicity, and How This Can Be Dealt With? In *Nanomaterials: Ecotoxicity, Safety, and Public Perception*, edited by Rai, M. and Biwas J. K., 3-18. Switzerland: Springer Nature Switzerland AG: Cham.

[3] Jeevanandam, J., Barhoum, A., Chan, J.S., Dufresne, A., Danquah, M.K. 2018. Review on nanoparticles and nanostructured materials: history, sources, toxicity and regulations. *Beilstein Journal of Nanotechnology*, 9:1050–1074.

[4] Yuan, Y.G., Peng, Q.L., Gurunathan, S. 2017. Effects of Silver Nanoparticles on Multiple Drug-Resistant Strains of Staphylococcus aureus and Pseudomonas aeruginosa from Mastitis-Infected Goats: An Alternative Approach for Antimicrobial Therapy. *International Journal of Molecular Sciences,*18:569-590.

[5] Vardanyan, Z., Gevorkyan, V., Ananyan, M., Vardapetyan, H., Trchounian, A. 2015. Effects of various heavy metal nanoparticles on Enterococcus hirae and Escherichia coli growth and proton-coupled membrane transport. *Journal of Nanobiotechnology*, 13*:*69-77. doi: 10.1186/s12951-015-0131-3

[6] Ritz, S., Schöttler, S., Kotman, N., Baier, G., Musyanovych, A., Kuharev, J. 2015. Protein Corona of Nanoparticles: Distinct Proteins Regulate the Cellular Uptake. *Biomacromolecules,* 16:1311–1321.

[7] Barbalinardo, M., Caicci, F., Cavallini, M., Gentili, D. 2018. Protein Corona Mediated Uptake and Cytotoxicity of Silver Nanoparticles in Mouse Embryonic Fibroblast. *Nano and Micro Small*, 14:e1801219.

* Corresponding Author´s Email: trzcinska@doktorant.umk.pl

Mechanistic insights onto the synergetic effects of AgNPs and antibiotics

M. Wypij*[1,2], P. Golińska[1], V. Puntes[2]

[1]Department of Microbiology, Nicolaus Copernicus University, Poland

[2]Catalan Institute of Nanoscience and Nanotechnology (ICN2), Barcelona, Spain

ABSTRACT

The antimicrobial activity of silver nanoparticles (AgNPs) and combination of AgNPs with selected antibiotics (amikacin, colistin, tetracycline and vancomycin) was studied against Gram-positive (*Staphylococcus aureus*) and Gram-negative (*Escherichia coli*, *Pseudomonas aeruginosa*) bacteria. The minimum inhibitory concentrations (MICs) and minimum biocidal concentrations (MBCs) were evaluated using micro-dilution method. Combined effect was determined by estimation of FIC (Fractional inhibitory concentration) index. The antimicrobial activity of AgNPs strongly depended on their size and was noticed for those of 21 nm in size. The lowest MIC of AgNPs was noticed against *Escherichia coli* (58 µg ml^{-1}), followed by *Staphylococcus aureus* and *Pseudomonas aeruginosa* (both 178 µg ml^{-1}). The synergistic effect of antibiotics with silver nanoparticles against tested bacteria was found mainly for tetracycline. The obtained results clearly indicate that combination of selected antibiotics with nanoparticles enhances antibacterial activity in a way that traditional antibiotics cannot do.

Keywords: AgNPs; antibacterial agents; antibiotics

INTRODUCTION

Silver nanoparticles (AgNPs) display well documented broad spectrum of antimicrobial activity against Gram-positive and Gram-negative bacteria, including multi-resistant strains, and fungi [1]. Silver nanoparticles with their unique physiochemical properties provide new antibacterial modes of action [2]. Bactericidal activity of AgNPs strongly depends on their binding to microbial cells, including multidrug-resistant primary clinical isolates, such as *Staphylococcus aureus, Klebsiella pneumoniae* or *Enterococcus faecalis* [3]. Using controllable nanoparticle models, we found that nanoparticle-pathogen complex formation was enhanced by small nanoparticle size rather than material or charge, and was prevented by 'stealth' modifications [4].

EXPERIMENTAL STUDY

AgNPs of specific sizes and very narrow size distribution were initially synthesized by preparing silver seeds. They were synthesized by addition of $AgNO_3$ into a boiling water solution containing sodium citrate (SC) and tannic acid, then purified and re-suspended in a polyvinylpyrrolidone (PVP) solution to avoid aggregation and provide robust NP colloidal stability. The synthesis of AgNPs was confirmed using UV-Vis spectroscopy while their morphology, stability and structure were characterized using TEM, Zeta potential and DLS, respectively. Antimicrobial activity of AgNPs and antibiotics (tetracycline, colistin, amikacin and vancomycin) were determined against selected bacteria such as *Escherichia coli* (ATCC 8739), *Staphylococcus aureus* (ATCC 6538) and *Pseudomonas aeruginosa* (ATCC 10145) by the microdilution method recommended by Clinical Laboratory Standards Institute. The Fractional Inhibitory Concentration (FICs) index for determination of synergy

---

* Corresponding Author´s Email: mwypij@umk.pl

of tetracycline, colistin, amikacin and vancomycin combined with AgNPs were evaluated by checkerboard titration method in 96-well plates. All experiments were performed in triplicate.

RESULTS AND DISCUSSION

It is well known that capping agents such as PVP present over the nanoparticle surface prevent their aggregation. Single UV-vis absorption sharp peaks were observed for PVP and SC capped AgNPs at sizes of 21 and 46 nm, while for nanoparticles of 139.8 nm the quadrupolar peak appears on the left of a broadened dipolar peak due to the large size and small polydispersity of the nanoparticles. The peaks of PVP stabilized silver nanoparticles were right shifted (towards a longer wavelength) compared to SC stabilized nanoparticles. Zeta potentials for silver NPs of 21,46 and 139.8 nm coated PVP were –9,48, -26.4 and –33.5 mV, respectively). TEM analysis confirmed regular shape of AgNPs. The smallest AgNPs, unlike these of 46 and 140 nm, showed a clear antimicrobial activity. The strongest effect was observed against *E. coli* (MIC=58 µg ml^{-1}) while *S. aureus* and *P. aeruginosa* were less sensitive (MICs equal to 178 µg ml^{-1}, both). The MBCs of silver nanoparticles for *E. coli* was 256 µg ml^{-1}, while for *S. aureus*, and *P. aeruginosa* were higher than 256 µg ml $^{-1}$. These results are in line with those previously published [1, 5]. The test bacteria were sensitive to amikacin and tetracycline, and in exception of *E. coli* to colistin. Susceptibility of bacterial strains to vancomycin was low (MIC > 256 µg ml^{-1} for *S. aureus* and *E. coli*, equal to 256 µg ml $^{-1}$ for *P. aeruginosa*). The synergistic, non-synergistic or indifferent effects were observed when antibiotics were combined with AgNPs. Combined use of antibiotics with AgNPs revealed that antibacterial activity was significantly enhanced when silver nanoparticles were used with tetracycline (FIC 0.125 - 0.25) against all test bacteria, while with amikacin for *P. aeruginosa* (FIC = 0.5). For other combinations indifference effects were observed. Obtained results indicate that such combinations allow for two-, four, or eight-fold decrease of used antimicrobials when FIC equal to 0.5, 0.25 or 0.125, respectively. Enhanced activity of antibiotics suggests that AgNPs may increase the local concentration of antibiotics at the site of action [6]. Combination of silver nanoparticles with antibiotics, particularly with tetracycline, allowed for significant dose reduction of both antimicrobials together with keeping their antibacterial activity.

CONCLUSION

As solubility and reactivity of NPs is strongly dependent on NP size, the aim of our work was to synthesize silver nanoparticles with well-defined size to estimate their antimicrobial activity against selected Gram-positive and Gram-negative bacteria. The combination of AgNPs with four antibiotics of different classes, namely colistin (polymyxin E), vancomycin (glycopeptide), amikacin (aminoglycoside) and tetracycline (polyketide) was also studied to evaluate potential synergistic effects. These four antibiotics were selected due to their broad spectrum and two different modes of action. The first two interact with the bacterial cell membrane and cell wall, respectively. Both therefore, contribute in attachment and shuttle of the AgNPs into the bacteria. In this case, synergy would mean that the NP is a pharmaceutical active principle of the antibiotic, the targeting vector. Amikacin and tetracycline inhibit synthesis of proteins by blocking 30S and 50S subunits, respectively, indicating in this case that the NPs are mere Ag ions transporters which provide a sustained release of active species.

REFERENCES

[1] Wypij, M., Czarnecka, J., Świecimska, M., Dahm, H., Rai, M., Golinska, P. 2018. Synthesis, characterization and evaluation of antimicrobial and cytotoxic activities of biogenic silver nanoparticles synthesized from *Streptomyces xinghaiensis* OF1 strain. *World Journal of Microbiology and Biotechnology,* 34:23-35.

[2] Kumar, M., Curtis, A., Hoskins, C. 2018. Application of nanoparticle technologies in the combat against anti-microbial resistance. *Pharmaceutics* 10:11-27.

---

* Corresponding Author´s Email: mwypij@umk.pl

[3] Hemeg, H.A. 2017. Nanomaterials for alternative antibacterial therapy. *International Journal of Nanomedicine*, 12:8211–8225.

[4] Wang, L., Hu, C., Shao, L. 2017. The antimicrobial activity of nanoparticles: present situation and prospects for the future. *International Journal of Nanomedicine,* 12:1227–1249.

[5] Wypij, M., Golinska, P., Dahm, H., Rai, M. 2016. Actinobacterial-mediated synthesis of silver nanoparticles and their activity against 1 pathogenic bacteria. *IET Nanobiotechnology*, 11(3):336-342.

[6] Dakal, T.C., Kumar, A., Majumdar, R.S., Yadav, V. 2016. Mechanistic basis of antimicrobial actions of silver nanoparticles. *Froniers in Microbioogy*. 7:1831.

* Corresponding Author´s Email: mwypij@umk.pl

Part 4

Nanotechnology in Environmental Solution

Hetero- and homo-aggregation of ZnO nanoparticles in different size fractions of colloids extracted from agricultural soil

S. Kurtinová*

Institute of Laboratory Research on Geomaterials, Faculty of Natural Sciences, Comenius University in Bratislava, Slovakia

Slovak Spectroscopic Society, member of the Association of Slovak Scientific and Technological Societies

ABSTRACT

In the last few decades, there has been a significant increase in the application of zinc oxide nanoparticles (ZnO-NPs) in the agroindustry. This is due to their unique characteristics, which contrast behavior of non-nanosized and dissolved zinc forms. To highlight the risks of the increased deposition of NPs into the soil environment, we have studied the sorptive interactions of ZnO-NPs with a colloid fraction that was extracted from agricultural soil. Our initial results indicated contribution of both homo- and hetero-aggregation on the ZnO-NPs distribution in soil colloid fraction. Since both significantly affect the sedimentation rate, the obtained results can be helpful for better understanding of ZnO-NPs' behavior in soil environment.

Keywords: zinc oxide nanoparticles; size fractionation; soil colloids

INTRODUCTION

With the increasing application of nanofertilizers, there is also a higher risk of negative impact of NPs' exposure on development and growth of crops [1-7], which includes alteration in nutrient assimilation, chlorophyll production, and various other essential physiological processes [8-12]. Furthermore, the exposure of engineered NPs has generally more severe responses of crops in comparison to the effects of micro- and macro-sized analogues [13], therefore agricultural land can by at an ecological risk of ZnO-NP contamination. Nevertheless, it has been shown that NPs can alleviate the impact of biotic and abiotic stresses on crops, and increase crop production by improving their resistance to diseases and adverse environmental effects [14]. Whether the impact of NPs is negative or positive depends primarily on their physico-chemical properties, concentration and nature of their interactions with the environment, e.g., aggregation with soil components [15, 16]. Therefore, our experiment's objective is to address the importance of homo- and hetero-aggregation on the ZnO-NPs' mobility in the soil environment.

EXPERIMENTAL/THEORETICAL STUDY

The agricultural soils sample (calcic chernozem, pH_{H2O} 7,98) was collected in Senec (Slovakia) at a depth ranging between 5-15 cm. Soil extract was obtained using a solution of artificial rainwater[5]. The tested soil to solution ratio was 1:2.5. The mixture was shaken at 25 °C for 24 hours, and then centrifuged at 700g for 1 min to obtain a supernatant containing soil colloids (fraction below 1000 nm). Three parallel samples were prepared by filling 15 mL sealable plastic tubes with 9.5 mL of soil colloids and 0.5 ml of an aqueous suspension of commercial ZnO-NPs (~ 10–70 nm, Sigma Aldrich). Each sample contained approximately 20 $mg.L^{-1}$ ZnO-NPs. The tubes were placed in an ultrasonic bath for 15 min and then shaken. After 24 h, they were sequentially centrifuged at 3500g for 1 min, 3500g for 20 min, and 3500g for 30 min with ultrafiltration units to separate zinc aggregates into size fractions of 100-450 nm, 1-100 nm, and dissolved, respectively. The samples were decomposed in a mixture of HF, HNO_3 and H_2O_2 in a closed system at 150 °C. Subsequently, the concentrations of iron, manganese,

---

* Corresponding Author´s Email: kurtinova2@uniba.sk

zinc, aluminium and silicon in different size fractions were measured by flame atomic absorption spectrometry [17].

RESULTS AND DISCUSSION

The concentration of zinc in soil solution is primarily influenced by sorptive interactions, especially by sorption on the clay minerals, iron-, manganese- and aluminium-oxides and (oxy)hydroxides, and organic matter [18]. Therefore, in the context of ZnO-NPs mobility, the contents of iron, manganese, aluminium and silicon in the soil colloid were primarily monitored.

Our soil extract contained relatively high concentrations of aluminium and silicon, especially in relation to manganese content (Tab. 1). Thus, the probability of zinc's interaction with colloidal phases of aluminium and silicon (hetero-aggregation) is significantly higher than with phases containing manganese. Also, since the relative distribution of zinc and aluminium in all size fractions is almost identical (Fig. 1) and it correlates well ($R^2 = 0.998$). Therefore, we assumed that the hetero-aggregation of ZnO-NPs with aluminium-containing minerals, such as aluminosilicates, dominates in soil extract. This can be also confirmed by a very similar distribution of aluminium and silicon in all size fractions (Fig. 1), and relatively high proportion of clay fraction in our soil sample (approx. 20%).

The lowest concentrations of elements in the fraction below 100 nm can also be explained by homo- and hetero-aggregation of ZnO-NPs. The aggregation processes significantly affect the sedimentation rate; and since the particles with higher diameters are formed, their further transport in the soil extract is constrained.

Table 1. Characteristics of soil sample and soil colloid.

	Total concentrations in soil sample (mg. g^{-1})	Concentrations in soil colloid (mg. g^{-1})
Fe	25.7	3.75
Mn	0.60	0.05
Al	51.8	6.94
Si	Not measured	13.98
Zn	0.08	0.06

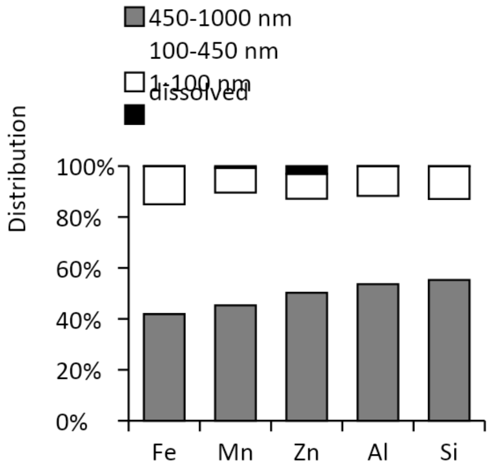

Figure 1. Distribution of elements in different size fractions of soil colloid.

However, the occurrence of hetero-aggregation is inconclusive, since it is contradicted by the experimental results obtained from the comparison of the size fractionation of zinc in soil colloid at different initial ZnO-NPs concentrations (9; 20; 88 20 mg.L^{-1}) (Fig. 2), and at different soil to solution ratios (1:2.5 vs 1:20) [19]. We concluded that with the higher concentrations of ZnO-NPs in the

---

* Corresponding Author´s Email: kurtinova2@uniba.sk

supernatant, the amounts of zinc in the 100-450 nm size fraction increased. Since there is negligible effect of concentration of colloids on the observed trend (Fig. 2), the occurrence of homo-aggregation of ZnO-NPs cannot be ruled out in this system.

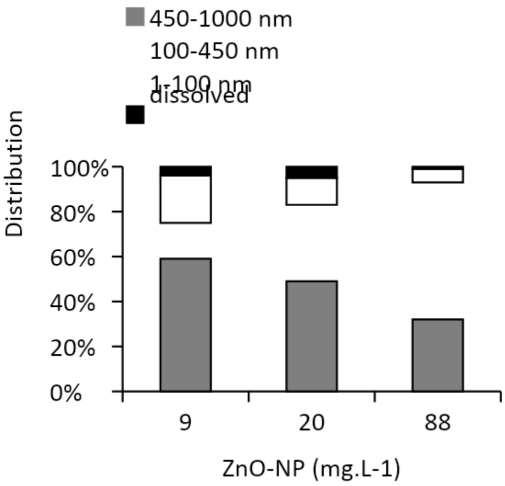

Figure 2. Distribution of ZnO-NPs in different size fractions of soil colloid.

CONCLUSION

ZnO-NPs are among the most tested NPs for the greater use in the agroindustry, therefore we find it necessary to understand their behavior and fate in complex environmental matrices, such as soil and soil colloids. Our results indicate that the ZnO-NPs in agricultural soil colloid were most likely associated with aluminosilicates/clay minerals. However, the homo-aggregation of ZnO-NPs also seems to have a significant contribution on the size fractionation and, thus, may also substantially influence the size distribution of ZnO-NPs in colloidal fraction extracted from agricultural soil. Nevertheless, homo- and hetero-aggregation could co-occur. However, according to our analysis, hetro-aggregation has probably more significant effect in ZnO-NPs size fractionation in soil colloid. These seemingly contradicting results should be addressed in more detailed research on ZnO-NPs' behavior in soil environment and, thus, provide the basis and inspiration for upcoming experiments.

ACKNOWLEDGEMENT

This work was supported by Comenius University grant UK/48/2021 and by Slovak Spectroscopic Society, member of the Association of Slovak Scientific and Technological Societies with following logo .

REFERENCES

[1] Kořenková, L., Šebesta, M., Urík, M., Kolenčík, M., Kratošová, G., Bujdoš, M., Vávra, I., Dobročka, E. 2017. Physiological response of culture media-grown barley (Hordeum vulgare L.) to titanium oxide nanoparticles. *Acta Agriculturae Scandinavica, Section B – Soil & Plant Science*, 67:285-291.

[2] Kolenčík, M., Ernst, D., Komár, M., Urík, M., Šebesta, M., Dobročka, E., Černý, I., Illa, R., Kanike, R., Qian, Y., Feng, H., Orlová, D., Kratošová, G. 2019. Effect of foliar spray application of zinc oxide nanoparticles on quantitative, nutritional, and physiological parameters of foxtail millet (Setaria italica l.) under field conditions. *Nanomaterials*, 9:1559.

---

* Corresponding Author´s Email: kurtinova2@uniba.sk

[3] Nemček, L., Šebesta, M., Urík, M., Bujdoš, M., Dobročka, E., Vávra, I. 2020. Impact of Bulk ZnO, ZnO Nanoparticles and Dissolved Zn on Early Growth Stages of Barley—A Pot Experiment. *Plants,* 9:1365-1379.

[4] Kolenčík, M., Ernst, D., Urík, M., Ďurišová, Ľ., Bujdoš, M., Šebesta, M., Dobročka, E., Kšiňan, S., Illa, R., Qian, Y., Feng, H., Černý, I., Holišová, V., Kratošová, G. 2020. Foliar application of low concentrations of titanium dioxide and zinc oxide nanoparticles to the common sunflower under field conditions. *Nanomaterials*, 10:1619-1639.

[5] Kolenčík, M., Nemček, L., Šebesta, M., Urík, M., Ernst, D., Kratošová, G., Konvičková, Z. 2021. Effect of TiO2 as plant-growth stimulating nanomaterial on crop production. In: *Plant Responses to Nanomaterials, Recent Interventions, and Physiological and Biochemical Responses*, edited by Singh, V.P., Singh, S., Tripathi, D.K., Prasad, S.M., and Chauhan D.K., 129 - 144, Switzerland: Springer Nature Switzerland AG: Cham.

[6] Šebesta, M., Illa, R., Zvěřina, O., Šeda, M., Diviš, P., Kolenčík, M. 2021. Effects of Titanium Dioxide Nanomaterials on Plants Growth. In: *Nanotechnology in plant growth promotion and protection*, edited by Ingle A.P., 17-44, Wiley.

[7] Urík, M., Kolenčík, M., Fujitake, N., Diviš, P., Zvěřina, O., Illa, R., Šeda, M. 2021. Effects of Natural Organic Matter on Bioavailability of Elements from Inorganic Nanomaterial. In: *Nanotechnology in plant growth promotion and protection*, edited by Ingle A.P., 113-128, Wiley.

[8] Kolenčík, M., Urík, M., Čaplovičová, M. 2014. Unexpected formation of Ag2SO4 microparticles from Ag2S nanoparticles synthesised using poplar leaf extract. *Environmental Chemistry Letters*, 12:551-556.

[9] Šebesta, M., Kolenčík, M., Bujdoš, M., Matúš, P. 2017. Transport Syntetických Nanočástic zlata v poľnohospodárskej pôde – modelovanie a použiteľnosť UV-VIS spektrofotometrie. In: *Aktuálne trendy geochemického štúdia geologického prostredia, edited by* Jurkovič, Ľ., and Kulikova, T., 117-120. Slovenská asociácia geochemikov, Bratislava (in Slovak).

[10] Kolenčík, M., Štrba, P., Šebesta, M., Kratošová, G., Urík, M., Vávra, I., Peikertová, P., Polláková, N., Šimanský, V., Feng, H., Qian, Y., Ramakanth, I. 2019. Journal of Nanoscience and Nanotechnology, 19:2983-2988.

[11] Šebesta, M., Urík, M., Bujdoš, M., Kolenčík, M., Vávra, I., Dobročka, E., Kim, H., Matúš, P. 2020. Fungus Aspergillus niger Processes Exogenous Zinc Nanoparticles into a Biogenic Oxalate Mineral. *Journal of Fungi*, 6:210-219.

[12] Šebesta, M., Nemček, L., Urík, M., Kolenčík, M., Bujdoš, M., Hagarová, I., Matúš, P. 2020. Distribution of TiO2 Nanoparticles in Acidic and Alkaline Soil and Their Accumulation by Aspergillus niger. *Agronomy,* 10:1833-1842.

[13] Šebesta, M., Kolenčík, M., Matúš, P., Kořenková, L. 2017. Transport a distribúcia syntetických nanočastíc v pôdach a sedimentoch. *Chemické Listy*, 111:322-328.

[14] Šebesta, M. 2020. Distribúcia nanočastíc kovov v pôdach a ich interakcia s rastlinami a hubami, VSB – Technical university of Ostrava.

[15] Almutairi, Z.M. 2019. Plant Molecular Defense Mechanisms Promoted by Nanoparticles against Environmental Stress. *International Journal of Agriculture & Biology*, 21:259-270.

[16] Šebesta, M., Kolenčík, M., Urík, M., Bujdoš, M., Vávra, I., Dobročka, E., Smilek, J., Kalina, M., Diviš, P., Pavúk, M., Miglierini, M., Kratošová, G., Matúš, P. 2019. Increased Colloidal Stability and Decreased Solubility—Sol—Gel Synthesis of Zinc Oxide Nanoparticles with Humic Acids. *Journal of Nanoscience and Nanotechnology*, 19:3024-3030.

[17] Šebesta, M., and Matúš, P. 2018. Separácia, stanovenie a charakterizácia anorganických syntetických nanočastíc v komplexných environmentálnych vzorkách. *Chemické Listy*, 112:583-589 (in Slovak).

[18] Šebesta, M., Urík, M., Kolenčík, M., Bujdoš, M., Matúš, P. 2020. Sequential Extraction Resulted in Similar Fractionation of Ionic Zn, Nano-and Microparticles of ZnO in Acidic and Alkaline Soil. *Forests,* 11:1077-1089.

[19] Šebesta, M., Nemček, L., Urík, M., Kolenčík, M., Bujdoš, M., Vávra, I., Dobročka, E., Matúš, P. 2020. Partitioning and stability of ionic, nano-and microsized zinc in natural soil suspensions. *Science of the Total Environment*, 700:134445-134455.

---

* Corresponding Author´s Email: kurtinova2@uniba.sk

Ca-palygorskite clay mineral for Fe^{2+} removal from water systems from molecular simulations point of view

C.V. Lazaratou*[1], D. Panagiotaras[2], G. Panagopoulos[3], M. Pospíšil[4], D. Papoulis[1]
[1]Department of Geology, University of Patras, Greece;
[2]Department of Environment, Ionian University, Greece;
[3]Department of Mechanical Engineering, University of the Peloponnese, Greece,
[4]Charles University, Faculty of Mathematics and Physics, Czech Republic.

ABSTRACT

Palygorskite was used for a testing of Fe (II) uptake from aqueous solutions under various experimental conditions. Palygorskite samples were characterized by following methods: X-ray diffraction, Fourier transform infrared spectroscopy, scanning electron microscopy, cation exchange capacity and molecular simulations. The fully saturated Ca-palygorskite samples were characterized as well and applied in batch kinetic experiments series.

It was shown that Ca-palygorskite was more efficient adsorbent for the lowest ferrous concentrations removal (5 mg/L). Especially when the highest solid: liquid ratio (20 g/l) have been applied, Ca-palygorskite reach 99.8 % removal within 10 min. The pH value affected the adsorption's efficiency, as Ca-palygorskite was more efficient adsorbent at acidic values (pH ~ 4– 6). The competitive ions, found to decrease Ca-palygorskite capacity for Fe (II), following the order of K<Na=Mn<Zn<Cu<Mg<Ba, highlighting their preference to the Fe cations. According to the thermodynamic analysis the Fe (II) uptake is a physical and spontaneous process. Ca- palygorskite was optimally fitted by the Langmuir isotherm indicating a monolayer sorption. This study of the palygorskite sample crystal structure and its characteristic, as well as the exact mechanism of a Ca-palygorskite efficient adsorption in detail was described by molecular simulation methods in Materials Studio 4.3. modelling environment.

Keywords: palygorskite; crystal structure; Ca exchange; Fe(II) removal

INTRODUCTION

Palygorskite is a 2:1 clay mineral with fibrous morphology, and may occur either in monoclinic or orthorhombic crystal structure [1]. Specifically, it is consisted by SiO_4 tetrahedral sheets which periodically present inversion in oxygens orientation, and by octahedral sheets that are discontinuous and broken in ribbons, linked to the inverted tetrahedrals by Si–O bonds [2]. The interruption of the octahedral layers, leads to the existence of empty channels where variable amounts of either cations or anions can be exchanged along with zeolitic water or with other existed exchangeable ions which balance crystal's charge [3]. The structure, basal spacing as well as the crystal morphology are the main causes of a palygorskite high specific surface area and an adsorption capacity enable it as the cost-effective adsorbent for a variety of contaminants from water systems.

Iron is an abundant element on the Earth and is a biologically essential component of every living organism [4]. Exceeded concentrations of iron are accompanied with reddish and blurred water, diminishing its quality and can be toxic for a human health and marine organisms as well [5]. An iron concentration in drinking water is normally less than 0.3 mg/l, but in some areas exceeds the limit because of the intensive use of iron containing materials and chemicals or from the disposal of iron rich industrial wastes [6], rendering its removal from water systems essential. Ca^{2+} in a literature was found to be an exchangeable cation with Fe(II) [7, 8], so it was selected for palygorskite modifications in order to gain enhanced Iron removal from water without any environmental impact.

---

* Corresponding Author´s Email: lachrist93@yahoo.gr

The present work aims to the insight description of Fe(II) removal from water by Ca^{2+}- treated palygorskite under various experimental conditions. Via molecular simulations, the exact crystal structure of palygorskite, Ca treatment and the affinity of Ca exchange with Fe were determined.

EXPERIMENTAL/THEORETICAL STUDY

Raw palygorskite was characterised with X-ray diffraction (XRD), scanning electron microscopy (SEM), Fourier transform infrared spectroscopy (FT-IR) and cation exchange capacity (CEC) methods. In order to enhance the CEC of palygorskite, it was treated with 1 M calcium chloride ($CaCl_2$) solution and was experimentally characterized again. Batch kinetic experiments were followed, were the effects of adsorbent dosage (i.e. 2 g/l, 4 g/l, 8 g/l, 20 g/l), Fe^{2+} concentrations (i.e. 5 mg/l, 10 mg/l, 20 mg/l and 100 mg/l), pH range (4-10), temperature (15 – 60 ºC) and competitive ions existence were determined. The experimental data were applied on the Langmuir and Freundlich isotherm models, as well as the thermodynamic analysis was conducted.

The monoclinic (C2/m) and orthorhombic (Pbmn) space groups of palygorskite were built in Materials Studio 4.3 modeling environment[9] based on the study of Giustetto and Chiari [10]. XRD patterns of both models were calculated and compared with the experimental XRD data. Based on an agreement, the monoclinic crystal structure was selected for subsequent investigation by molecular simulation methods with the following cell parameters: a = 13.337 Å, b =17.879 Å, c = 5.264 Å, β = 105.27°. An optimization of the initial models with the various positions and arrangements of iron cations in the palygorskite crystal structure was done in the cff97 force field [11]. Charges were calculated by the Charge equilibrium method [12]. Dynamics were run in the NPT ensemble at the temperature T = 298 K under the Andersen thermostat, under an atmospheric pressure kept by the Andersen barostat, time step was 0.2 fs and the total time of dynamics run was 1.2 ns. Dynamics were applied for the optimized models with interlayer cations and zeolitic water to test their stability because of symmetry of the cell was changed to P1 for calculation purposes. Palygorskite ribbon (Si–O) was kept fixed with a respect to the Cartesian coordinates. Cations, OHs and water molecules were not fixed to move without any constraints.

RESULTS AND DISCUSSION

According to XRD, Brunauer–Emmett–Teller (BET) and FT-IR methods the dominant mineralogical phase and the characteristic fibrous morphology of palygorskite were verified, while were not influenced after Ca-treatment. Ca-palygorskite presented a high Fe(II) removal efficiency with adsorbent dosage increase, especially for the lower examined Fe (II) initial concentrations. Specifically, 20 g/l of Ca-palygorskite removed almost 100 % of Fe(II) at a concentration range of 5 - 20 mg/l, instead of 50 % that was achieved for 100 mg/l Fe(II). The adsorption in this case found to be a rapid procedure, the Iron was diminished at 10 min, as well as the procedure found to be independent either at pH and temperature change, or at the competitive ions existence. Molecular simulations came in a perfect agreement with the experimental results. Particularly, a raw Mg-rich palygorskite structure was built in both orthorhombic and monoclinic systems and XRD pattern was calculated. In a comparison with the XRD pattern of the raw sample, better fit was reached for the monoclinic system, which is the most common system for palygorskite deposits, according to literature. The effectiveness of the Ca-treatment was also verified as it can be shown in Table 1, since Ca in the palygorskite structure presented similar energies with Mg, rendering its exchangeability and become enough stable cation for this structure (Fig. 1). Table 1 show that the Ca cations are not fully exchanged with Fe cations, since the total energy of fully exchanged models with Fe cation (4Fe) is higher than the total energy of models with Ca cations (Table 1). This behavior was confirmed by a sorption in the investigated real samples.

Nevertheless, the negative energies indicated the Fe(II) uptake is not only a surficial phenomenon and that the ion exchange took place in the inner space of palygorskite, coming in an agreement with

---

* Corresponding Author´s Email: lachrist93@yahoo.gr

the results from the thermodynamic analysis that characterized the Fe(II) adsorption on Ca-palygorskite as a physical procedure which is highly preferred [13].

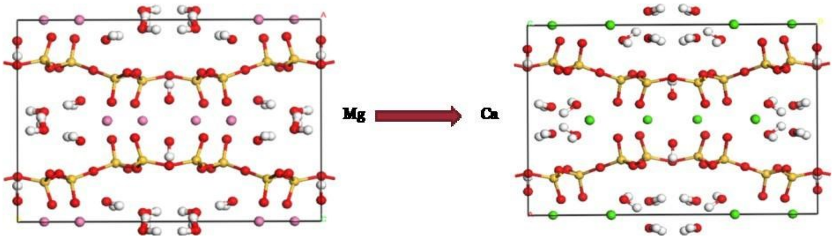

Figure 1. Molecular structure of Mg palygorskite and Ca- palygorskite. Mg is pink, Ca is green, Fe is blue, O is red, Si is yellow, H is white.

Table 1. Total sublimation energies of the calculated models of palygorskite in monoclinic system with various cations.

Model Type	Total energy [kcal/mol]	Binding energy per one cation [kcal/mol]
Mg palygorskite	-5487	-59
Ca palygorskite	-5488	-21
2Fein palygorskite	-5588	-42
2Feout palygorskite	-5297	-20
4Fe palygorskite	-5440	-46

The binding energies between cations and the rest of the whole crystal (surrounding of cations) were calculated according to the Equation 1.

$$E_{binding} = E_{total} - (E_{cations} + E_{surrounding}) \qquad (1)$$

CONCLUSION

The adsorption efficiency of the Ca treated palygorskite clay mineral was examined in order to estimate the removal capacity of iron ions from an aqueous solution with a respect to the different mass/volume ration, initial ions concentration, pH, temperature and a presence of other ions in a solution. The results indicate that Ca-palygorskite can be considered as an effective and low cost absorbent for the removal of Fe(II) ions from an aqueous solution and can be used in large scale applications for a water treatment, since with 20 g/l of Ca-palygorskite 5-20 mg/l of Fe(II) of the polluted water were zeroed. Moreover, molecular simulations found to be extremely useful at providing information about the Fe(II) removal mechanism insight, as well as to the detailed analysis of adsorbent's structural characteristics and properties, that could be applied in other cases of the heavy metals removal.

---

* Corresponding Author´s Email: lachrist93@yahoo.gr

REFERENCES

[1] Chisholm, J. 1992. Powder diffraction patterns and structural models for palygorskite. *Canadian Mineralogist*, 30:61–73.

[2] Giustetto, R., Wahyudi, O. 2011. Sorption of red dyes on palygorskite: Synthesis and stability of red/purple Mayannanocomposites. *Microporous and Mesoporous Materials*, 142:221–235.

[3] Galán, E. 1996. Properties and applications of palygorskite-sepiolite clays. *Clay Minerals*, 31:443–453.

[4] Lieu, P.T., Heiskala, M., Peterson, P.A., Yang, Y. 2001. The roles of iron in health and disease. *Molecular Aspects of Medicine*, 2:1–87.

[5] Berbenni, P., Pollice, A., Canziani, R., Stabile, L., Nobili, F. 2000. Removal of iron and manganese from hydrocarbon-contaminated groundwaters. *Bioresource Technology*, 74:109–114.

[6] WHO-World Health Organization. 1996. Guidelines for drinking-water quality, 2nd ed. Vol. 2. Health criteria and other supporting information. World Health Organization, Geneva.

[7] Charlet, L., Tournassat, C. 2005. Fe(II)-Na(I)-Ca(II) cation exchange on montmorillonite in chloride medium: Evidence for preferential clay adsorption of chloride - Metal ion pairs in seawater. *Aquatic Geochemistry*, 11:115–137.

[8] Lorenc-Grabowska, E., Gryglewicz, G., Gryglewicz, S. 2004. Development of mesoporosity in activated carbons viacoal modification using Ca- and Fe-exchange. *Microporous and Mesoporous Materials*, 76:193–201.

[9] Accelrys Software, 2003. Materials Studio Modeling Environment, Release 4.3 Documentation. Accelrys Software Inc, San Diego.

[10] Giustetto, R., Chiari, G. 2004. Crystal structure refinement of palygorskite from neutron powder diffraction. *European Journal of Mineralogy*, 16:521–532.

[11] Carpenter, J.E. 2002. Computation of pressure components due to class II force fields. *Journal of Computational Chemistry*, 23:667– 672.

[12] Rappé, A.K., Goddard III, W.A., 1991. Charge equilibration for molecular dynamics simulations. *Journal of Physical Chemistry*, 95(8):3358–3363.

[13] Lazaratou, Ch., Panagiotaras, D., Panagopoulos, G., Pospíšil, M., Papoulis, D. 2020. Ca-treated Palygorskite and Halloysite clay minerals for Ferrous Iron (Fe^{+2}) removal from water systems, *Environmental Technology & Innovation*, 19(6):100961.

---

* Corresponding Author´s Email: lachrist93@yahoo.gr

Chemically selective vapor sensing of structurally colored butterfly wings

G. Piszter*[1], K. Kertész[1], Z. Bálint[2], L.P. Biró[1]

[1]Institute of Technical Physics and Materials Science, Centre for Energy Research, Hungary;
[2]Hungarian Natural History Museum, Hungary

ABSTRACT

The photonic-crystal-type nanoarchitectures occurring in the wing scales of the butterflies are mainly composed of chitin and air, and the structural coloration they generate is determined by the periodicity and characteristic dimensions of the nanostructure, and also by the refractive indices of the building materials. Small changes in the refractive index or in the periodicity, like those induced by different vapors in the surrounding atmosphere, can generate color variation of the wings detectable with optical spectrophotometry. The mechanism behind vapor sensing is the capillary condensation of the volatiles into the nanocavities of the photonic nanoarchitecture which results in a reversible color change. In the present work, the general findings regarding the mechanism of sensitivity and selectivity, and the parameters influencing the sensing will be discussed. We demonstrated that the butterfly wing-based sensor materials allow chemically selective detection of single-component vapors as well as binary vapor mixtures. The sensitivity of the wings was tuned by modifying the surface of the photonic nanoarchitecture, and the effect of long-term vapor exposure and how these sensors work in real life conditions, for example in simulated environmental humidity, were investigated.

Keywords: photonic nanostructure; vapor sensing; butterfly; chemical selectivity

INTRODUCTION

Naturally occurring photonic nanoarchitectures may have remarkable optical properties [1,2] that are a vast source of inspiration for materials scientists. These intricate nanostructures have been documented in many animal species [3], but the most spectacular examples were found in the cuticle of insects [1]. Many butterfly species developed high-complexity photonic nanoarchitectures [4,5] that would be very time consuming and expensive if attempted to be implemented with our current technological level. Therefore, it is worth considering these structures as ready-made samples that can be used in our theoretical and experimental studies, and as well as in potential applications.

The optical properties of photonic nanoarchitectures depend on the refractive index of their components, and the characteristic size range and order/disorder of their periodicity [6]. In the case of insects, the nanoarchitectures are composed of mainly chitin and air which may be supplemented with an absorbing media (pigments). If the characteristic periodicity, which is comparable with the visible light's wavelength, or the refractive index of the components changes, this will result in the shift of the reflectance of the photonic nanoarchitecture. Therefore, the structurally colored wings of butterflies show an optical response when the vapor composition of the surrounding atmosphere changes [7,8]. This color change is reversible and can be observed using an optical spectrophotometer which makes them suitable as a vapor detector with optical readout [7,8]. In this work, the mechanism of this chemically selective color change and the parameters influencing the vapor sensing properties will be discussed in the case of Lycaenid butterfly wings.

---

* Corresponding Author´s Email: piszter@mfa.kfki.hu

EXPERIMENTAL

As it was reported earlier [9], a custom air-proof aluminum cell with a quartz window, with a gas inlet and outlet on opposite sides, was used in the vapor-sensing measurements. The wings were inserted in the cell, and their optical response was measured when the test substances were let through the vents. The saturated vapors for the mixtures used were generated in computer-controlled gas bubblers. The samples were illuminated through the quartz window of the cell by a deuterium-halogen (UV–Vis) light source under normal incidence. To avoid mirror-like reflection from the quartz window, the reflected light was collected under ~45° with an Avantes spectrophotometer.

RESULTS AND DISCUSSION

The males of many *Polyommatus* butterfly species have blue structural coloration on their dorsal wing surfaces that arise from complex photonic nanoarchitectures interacting spectrally selective way with the incident white light. These short-range ordered, so-called “pepper-pot”-type nanoarchitectures are typical for this genus as it can be seen in Fig. 1. We showed that both these nanoporous photonic nanostructures and the generated colors were species-specific [10, 11], stable over time [12] and over large geographic areas [13], and resistant to external environmental influences [14, 15] which makes them promising candidate for volatile organic compound (VOC) sensing applications.

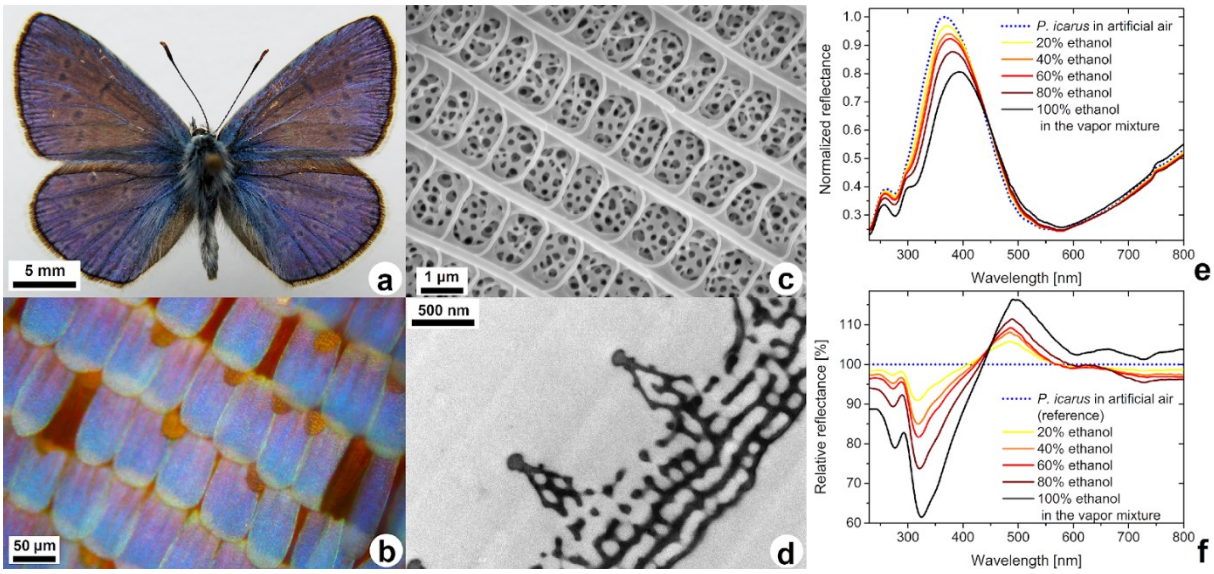

Figure 1. (a) Photograph of a *Polyommatus icarus* male and (b) the optical microscope image of the blue dorsal wing surface of this specimen. (c) SEM and (d) cross-sectional TEM images of the photonic nanoarchitecture located in the lumen of the cover scales. (e) The spectral change of the *P. icarus* wing reflectance when ethanol vapor was added to the surrounding atmosphere in different concentrations. (f) Optical response from the same vapor sensing measurement when the *P. icarus* wing reflectance was used as a reference.

The optical response of the wings during vapor exposure can be characterized by the color change of the photonic nanoarchitecture that was defined[7] as $\Delta R = (R/R_0) \times 100\%$, where the initial spectrum of the wings in air (R_0) was used as a reference during the measurements. The alteration of the reflectance spectrum measured in *Polyommatus icarus* male specimen when the surrounding atmosphere is changed to ethanol mixtures in different concentrations and the calculated optical responses are depicted in Fig. 1c,d.

We found that the nanoporous photonic nanoarchitectures of nine investigated polyommatine species allowed fast response time in the order of seconds during vapor sensing [16], which may be

---

* Corresponding Author´s Email: piszter@mfa.kfki.hu

tuned by the temperature of the butterfly wing [17]. The concentration dependence of the signal amplitude was nearly linear with a small hysteresis at higher concentrations, indicating that the mechanism behind sensing is based on capillary condensation of vapors into the wing scale nanoarchitectures [18], resulting in a higher-than-expected optical response.

We investigated the chemically selective VOC sensing properties of the photonic nanoarchitectures in *Polyommatus icarus* blue wing scales using seven test volatiles. The measured optical responses were analyzed using a three-dimensional chromaticity diagram based on the color vision of the polyommatine butterflies, and also using principal component analysis [9]. An almost perfect match of the two results was observed, clearly showing that the chromaticity diagram can be used very efficiently for the characterization of the spectral changes and to represent the substance-selective vapor sensing of the wings [9]. The detailed analysis showed that at lower concentrations the dominant process was capillary condensation, while at higher concentrations the swelling of the chitin nanostructure became dominant. This swelling can be terminated by coating the wing in a conformal Al_2O_3 layer using atomic layer deposition, resulting in the reduced sensitivity of the sensor at high vapor concentrations [19, 20].

To tune the sensitivity of the sensor material, modifications of the surface properties of the photonic nanoarchitecture were applied by pretreating them in several kinds of volatiles (ethanol, chloroform, IPA) [21]. This is a cheap way of altering the surface properties of the photonic nanoarchitectures and this procedure can be easily scaled up for practical applications. The vapor sensing measurements showed that ethanol pretreatment provided the most significant results – more than doubling the maximal spectral response compared to the untreated wing – while the chemical selectivity increased at lower vapor concentrations (<50%) and remained almost unchanged at higher (>50%) concentrations [21]. The treatment of the wings may be resulted in the functionalization of the epicuticle layer covering the photonic nanoarchitecture, which has become sensitized that way.

As the whole wings covered by scales are optically complex objects, we also investigated the behavior of single separated scales of *Albulina metallica* male specimen by using a microscope for individual characterization [22]. We found that the single blue and green cover scales exhibit similar chemically selective sensing both in reflected light and transmitted light as was found on the whole wings. By artificially stacking several layers of scales possessing photonic nanoarchitectures, we demonstrated that the magnitude of the sensing signal can be increased which may be used in the future to enhance the VOC detection properties of such microscopic sensor materials.

The structurally colored butterfly wings were also used for the detection not only of single component but of binary vapor mixtures [23]. It was found that the measured optical responses generated by the mixtures were the linear combination of the optical responses of the pure vapors, showing that biological photonic nanoarchitecture-based sensor materials can differentiate between vapor mixtures, as the generated optical response was found to be characteristic for each of them. It is also important to investigate how water vapor affects the optical response signal because this is the highest concentration vapor in ambient air. Therefore, the stability and the VOC sensing properties of butterfly wings were investigated under humid conditions [24]. It was demonstrated that the capability to detect VOCs was preserved in the presence of water vapor: high-intensity color change signals with short response times were measured in 25% relative humidity, similar to the one-component case, showing the possibility of utilization in real-life applications in the future.

CONCLUSION

We have investigated the vapor sensing properties of several polyommatine butterfly species with nanoporous photonic nanoarchitectures in their wing scales. Due to the open structure of the nanoarchitectures, the structural colors of these chitin–air nanocomposites changed rapidly when the vapor composition of the ambient atmosphere changed. By measuring this optical response, the nature and concentration of the test volatiles could be determined. It was found that during vapor exposure, capillary condensation took place, and due to the condensed liquid layer, swelling of the chitin nanoarchitecture occurred. This resulted in both a substance-specific optical response and higher-than-expected sensitivity, which also could be tuned in a controlled way. We have found that single wing scales can also detect VOCs with the same efficiency as whole wings. Finally, the complex sensing mechanism, based on condensation and swelling, allowed the detection of binary vapor mixtures, which provided the basis for detecting VOCs in atmospheric humidity. Based on these, VOC sensors can be made from the wings of butterflies that can endure long-term operation in atmospheric humidity and are capable of real-time analysis that meet the requirements of the potential applications, such as medical diagnostics or monitoring indoor activities and living environments.

ACKNOWLEDGMENTS

This research was supported by the Priority Project of the Centre for Energy Research.

REFERENCES

[1] Biró, L.P., and Vigneron, J.P. 2011. Photonic nanoarchitectures in butterflies and beetles: valuable sources for bioinspiration. *Laser& Photonics Reviews,* 5:27–51.

[2] Doucet, S.M., and Meadows, M.G. 2009. Iridescence: a functional perspective. Journal of The Royal Society Interface 6:S115–S132.

[3] Sun, J., Bhushan, B., Tong, J. 2013. Structural coloration in nature. *RSC Advances*, 3:14862–14889.

[4] Kinoshita, S., Yoshioka, S., Fujii, Y., Okamoto, N. 2002. Photophysics of Structural Color in the Morpho Butterflies. *Forma* 17:103–121.

[5] Kertész, K., Bálint, Z., Vértesy, Z., Márk, G., Lousse, V., Vigneron, J.P., Rassart, M., Biró, L.P. 2006. Gleaming and dull surface textures from photonic-crystal-type nanostructures in the butterfly Cyanophrys remus. *Physical Review E*, 74:021922-021936.

[6] Joannopoulos, J.D., Meade, R., Winn, D.J.N. 1995 Photonic Crystals: Molding the Flow of Light, Princeton University Press, Princeton, NJ, USA.

[7] Potyrailo, R.A., Ghiradella, H., Vertiatchikh, A., Dovidenko, K., Cournoyer, J.R., Olson, E. 2007. Morpho butterfly wing scales demonstrate highly selective vapour response. *Nature Photonics,* 1:123–128.

[8] Biró, L.P., Kertész, K., Vértesy, Z., Bálint, Z. 2008. Photonic nanoarchitectures occurring in butterfly scales as selective gas/vapor sensors. *Proceedings SPIE* 7057, 705706-705714.

[9] Piszter, G., Kertész, K., Vértesy, Z., Bálint, Z., Biró, L.P. 2014. Substance specific chemical sensing with pristine and modified photonic nanoarchitectures occurring in blue butterfly wing scales. *Optics Express*, 22:22649–22660.

[10] Piszter, G., Kertész, K., Vértesy, Z., Bálint, Z., Biró, L.P. 2011. Color based discrimination of chitin–air nanocomposites in butterfly scales and their role in conspecific recognition. *Analytical Methods*, 3:78–83.

[11] Bálint, Z., Kertész, K., Piszter, G., Vértesy, Z., Biró, L.P. 2012. The well-tuned blues: the role of structural colours as optical signals in the species recognition of a local butterfly fauna (Lepidoptera: Lycaenidae: Polyommatinae). *Journal of the Royal Society Interface*, 9:1745–1756.

[12] Piszter, G., Kertész, K., Bálint, Z., Biró, L.P. 2016. Variability of the structural coloration in two butterfly species with different prezygotic mating strategies. *PLoS One*, 11:e0165857.

[13] Kertész, K., Piszter, G., Bálint, Z., Biró, L.P. 2019. Biogeographical patterns in the structural blue of male Polyommatus icarus butterflies. *Scientific Reports*, 9:2338-2347.

[14] Kertész, K., Piszter, G., Horváth, Z.E., Bálint, Z., Biró, L.P. 2017. Changes in structural and pigmentary colours in response to cold stress in Polyommatus icarus butterflies. *Scientific Reports*, 7:1118-1129.

[15] Piszter, G., Kertész, K., Horváth, Z.E., Bálint, Z., Biró, L.P. 2019. Reproducible phenotype alteration due to prolonged cooling of the pupae of Polyommatus icarus butterflies. *PLoS One*, 14:e0225388.

[16] Kertész, K., Piszter, G., Jakab, E., Bálint, Z., Vértesy, Z., Biró, L.P. 2013. Selective optical gas sensors using butterfly wing scales nanostructures. *Key Engineering Materials*, 543:97–100.

[17] Kertész, K., Piszter, G., Jakab, E., Bálint, Z., Vértesy, Z., Biró, L.P. 2014. Temperature and saturation dependence in the vapor sensing of butterfly wing scales. *Materials Science Engineering C*, 39:221–226.

[18] Kertész, K., Piszter, G., Jakab, E., Bálint, Z., Vértesy, Z., Biró, L.P. 2013. Color change of Blue butterfly wing scales in an air – vapor ambient. *Applied Surface Science*, 281:49–53.

[19] Kertész, K., Piszter, G., Baji, Z., Jakab, E.,. Bálint, Z, Vértesy, Z., Biró L.P. 2014. Vapor sensing on bare and modified blue butterfly wing scales *Chemical Sensors*, 4:17-22.

---

* Corresponding Author´s Email: piszter@mfa.kfki.hu

[20] Piszter, G., Kertész, K., Vértesy, Z., Bálint, Z., Biró, L.P. 2014. Vapor sensing of pristine and ALD modified butterfly wings. *Materials Today: Proceedings*, 1:216–220.

[21] Piszter, G., Kertész, K., Bálint, Z., Biró, L.P. 2016. Pretreated butterfly wings for tuning the selective vapor sensing. *Sensors*, 16:1446-1455.

[22] Kertész, K., Piszter, G., Bálint, Z., Biró, L.P. 2018. Optical vapor sensing on single wing scales and on whole wings of the Albulina metallica butterfly. *Sensors*, 18:4282-4293.

[23] Piszter, G., Kertész, K., Bálint, Z., Biró, L.P. 2019. Optical detection of vapor mixtures using structurally colored butterfly and moth wings. *Sensors*, 19:3058-3069.

[24] Piszter, G., Kertész, K., Bálint, Z., Biró, L.P. 2020. Stability and Selective Vapor Sensing of Structurally Colored Lepidopteran Wings Under Humid Conditions. *Sensors*, 20:3258-3269.

---

* Corresponding Author´s Email: piszter@mfa.kfki.hu

Application of adsorbents modified by nanoparticels

J. Seidlerová*[1,2], M. Tokarčíková[1], R. Gabor[1]

[1]Nanotechlology Centre CEET, VŠB-TUO, Czech Republic

[2]Department of Physical Chemistry and Theory of Technological Processes, Faculty of Materials Science and Technology, VŠB-TUO, Czech Republic

ABSTRACT

Phyllosilicates are a promising group of materials since they are native, nontoxic, and applicable in numerous industrial sectors. Phyllosilicates can be used as carriers of photoactive, degradable, antibacterial, or fungicidal nanoparticles. They are efficient adsorbents of non-degradable pollutants due to their (e.g.) high specific surface area, chemical and mechanical stability, various structural and surface properties and higher cation exchange capacity. On the other hand, sorbent separation can be associated with substantial technological problems, mainly when the sorbent particles are of a very small size. However, the adsorbent can be modified by magnetically iron oxide micro/nanoparticles to facilitate removing the adsorbents from the solution – by using a magnet or magnetic field. The magnetically modified materials in this study were prepared from two montmorillonites and Ghassoul (a unique mixture of stevensite and sepiolite) using the microwave-assisted method of magnetic particle preparation. The adsorption of Sr^{2+} ions from water solution was studied. The experimental data were fitted by adsorption isotherms (Langmuir, Freundlich, and Sips). Results showed that the adsorption could be fitted by the Sips adsorption isotherm and, hence, the ion-exchange mechanism occurred. The presence of magnetic iron particles on the adsorbent surface does not always decrease the maximum adsorption capacity. The adsorption capacity depends on the type of clay and the way of adsorbent preparation.

Keywords: adsorption; modified phyllosilicates; remove strontium

INTRODUCTION

Water contaminants such as pesticides, personal care products, organic and inorganic compounds are usually present in concentrations ranging from a few nanograms per litre to several milligrams per litre. The occurrence of various pollutants in surface water could pose a problem during water treatment processes of drinking water preparation [1], especially since drinking water is becoming increasingly rare. Various procedures have been described and applied for pollutants removal from water, including hydrocyclone, filtration, flotation, and precipitation. Biological methods of wastewater purification have been in use for several years now.

For the removal of non-biodegradable pollutants dispersed in wastewater, sorption is applied as one of the most important and efficient techniques. Nevertheless, it is of constant interest to develop new sorbents to improve the sorption efficiency, decrease the price of the purification technology, and enhance the functionality of the applied material. Adsorbents of inorganic ions are usually based on carbon or active carbon, but clay minerals (phyllosilicates) and their modified forms (e.g. acid-activated) are also a group of excellent adsorbents. The phyllosilicates occur in several different forms. There is a very good knowledge of the sorption properties of serpentinite – kaolinite, vermiculite or smectite (primarily montmorillonite) in both literature and practice [2, 3]. Nevertheless, a mix of the mentioned structures can be used as well. Vermiculite, montmorillonite, and kaolinite are suitable sorbents due to their (e.g.) high specific surface area, chemical and mechanical stability, variety of structural and surface properties, and higher values of cation exchange capacity. They were successfully applied as sorbents of many ions [4-7]. On the other hand, the post-sorption separation of these sorbents can cause

---

* Corresponding Author´s Email: jana.seidlerova@vsb.cz

substantial technological problems, mainly when their particles are very small. These disadvantages can be removed by manufacturing their magnetically modified form.

Adsorption can be used for removing isotopes of strontium as one of the major radioactive contaminants in surface water and shallow groundwater. Many different materials were used before, carbon – nature or activated [8-11], biochar [12, 13] some biosorbents [14, 15], or various materials [16-19]. Several researchers successfully used zeolite [20-22], hydroxyapatite [23-24], or dolomite powder [25]. Clay minerals or their mixtures were used for strontium ions removal as well [26-30]. All authors described the adsorption of strontium ions as a very rapid process achieving equilibrium for several minutes. The experimental data is usually fitted by the Freundlich, Langmuir, and Dubinin-Radulhkevich adsorption isotherm. Some authors carried out experiments also with Na-saturated montmorillonite

When the mixture of kaolinite and montmorillonite contained more montmorillonite, the adsorption capacity increased [31]. On the other hand, the adsorption capacity of the illite and smectite mixture is very similar to the adsorption capacity of Na-smectite or Na-illite [32]. The main adsorption mechanism of heavy metal adsorption (including Sr ions) by such phyllosilicates as attapulgite, halloysite, montmorillonite, bentonite, and vermiculite was described by Gu in a review of research from 2013-2017 [33]. Various modifications of clay minerals were used as well [34-36].

The present study is unique as it deals with the adsorption of strontium ions using montmorillonite and special Moroccan clay – Ghassoul [37]. The magnetic modification form of mentioned minerals was prepared, and adsorption properties were compared with natural clays.

EXPERIMENTAL STUDY

Material

Adsorption experiments were carried out on nature and modified phyllosilicates - montmorillonites and Ghassoul. The first montmorillonite (M1) was obtained by water leaching from a product of the Beaufour Ipsen Industrie (France). The chemical composition summarized Table 1.

Table 1. The chemical composition of sample montmorillonite M1 expressed in oxides, LOI – loss of ignition.

		Na_2O	**MgO**	**Al_2O_3**	**SiO_2**	**P_2O_5**	**SO_3**
M1	(wt. %)	0.12±0.01	3.6±1.2	14.2±0.5	49.8±1.0	<0.03	0.04±0.01
		K_2O	**CaO**	**MnO**	**TiO_2**	**Fe_2O_3**	**L.O.I.**
M1	(wt. %)	0.17±0.01	3.6±1.2	14.2±0.5	49.8±1.0	<0.03	0.04±0.01

The second natural montmorillonite comes (M2) from the region Ivančice in Czech Republic, it is a clean montmorillonite with crystallochemical formula [38, 39]:

$(Ca_{0,15}Mg_{0,07}Na_{0,09}K_{0,03})(Al_{1,25}Fe^{3+}_{0,23}Mg_{0,5}Ti_{0,09})(Si_{3,99}Al_{0,01})O_{10}(OH)_2$

The Mg-rich clay Ghassoul (G) is a unique mixture of stevensite and sepiolite with several ingredients (sepiolite, quartz, clinoenstatite, dolomite, and celestine). It has been used for centuries as a natural soap in Maghreb and Middle-East, but for other scientists than geologists, it remained unknown until the 20th century [37]. Detailed characterization used G described previous paper [40].

Before the adsorption experiments and modification, particles of size under 40 µm were prepared from each clays.

---

* Corresponding Author´s Email: jana.seidlerova@vsb.cz

Chapter 25

Part 4: Nanotechnology for Environmental Solution

Methods of phyllosilicate/nano iron oxide composite preparation

Two different methods of magnetic composite preparation were used. The magnetically modified montmorillonite - MM1 and MM2 - was prepared from ferrofluid (a colloidal liquid made of nanoscale ferromagnetic/ferrimagnetic particles suspended in a carrier fluid, usually an organic solvent or water). A known amount of M1 or M2 was mixed with the ferrofluid water suspension for several minutes; then the prepared composite was separated using filtration or centrifugation [41, 42].

Clay composite of sample G were prepared using simple and fast microwave-assisted precipitation [43]. In the first step, it is necessary to prepare a suspension of magnetic iron oxides particles. Suspension of the particles was prepared from $FeSO_4$, and NaOH solution used microwave radiation to prepare the mixture of maghemite (γFe_2O_3) and magnetite (Fe_3O_4) [44]. After removing sulphate ions by decantation, the clay mineral was added to the suspension and mixed for several hours. The composite was then separated by filtration (PRAGOPORE filter with pore 0.40 µm). After drying at laboratory temperature, the material was used for experiments and characterization.

Method of characterization

All prepared composites were characterised using the basic methods listed here:

- Energy dispersive X–Ray fluorescence spectrometer, SPECTRO XEPOS
- Scanning transmission electron microscopy with EDS microanalyzer and in-situ AFM with correlation analysis (STEM), JEOL 2010F Plus
- X-ray powder diffractometer, BRUKER D8 ADVANCE
- Atomic emission spectrometer with inductively coupled (ICP), SPECTRO CIROS VISION
- Atomic absorption spectrometer with flame atomisation (AAS), UNICAM 969

The total Fe content was determined after decomposition by acids using ICP. The essential information was FeO content determined according to ČSN [45].

Adsorption experiments

All adsorption experiments were carried out using a batch method under laboratory temperature. A measured quantity of mineral (0.1 g) was added to the vessels containing a measured volume (25 mL) of defined concentration of strontium ions; then, the vessels were shaken for different times for the kinetic study (10–180 min) or 120 min for the equilibrium study. After that, the suspension was filtrated through a filter (PRAGOPORE filter with pore 0.40 µm), and the final concentrations of cations were determined. Modelled strontium solution was prepared from $Sr(NO_3)_2$ (p.a. min. 99 %, MACH chemical s.r.o.) in deionised water.

Data processing by adsorption isotherms

The amount of adsorbed Sr^{2+} ions on used samples at the equilibrium at experimental condition - q_e ($mg.g^{-1}$) - was calculated as follows:

$$q_e = \frac{(c_0 - c_e)}{m_g} \cdot V \qquad (1)$$

where c_0 and c_e ($mg \cdot L^{-1}$) are initial and equilibrium concentration Sr^{2+} ions in model solution, V (L) is the volume of model absorbed solution and m_g (g) is the mass of adsorbent.

Adsorption isotherms are essential to describe how solutes interact with adsorbent and critical in optimizing the use of adsorbent. Correlation of the isotherm data with empirical or theoretical equations is thus essential to practical operation. Equilibrium adsorption data were superposed to the Langmuir, Freundlich, and Sips adsorption isotherms.

The Langmuir model assumes that uptake of ions occurs on a homogenous surface by monolayer adsorption without any interaction between adsorbed ions. That model is described by a limiting maximum sorption capacity that is related to monolayer coverage of surface sites:

---

* Corresponding Author´s Email: jana.seidlerova@vsb.cz

$$q_e = q_m \frac{K_L \cdot c_e}{1 + K_L \cdot c_e} \qquad (2)$$

where q_e (expressed in mg·g^{-1}) is the amount of the adsorbed ions on the sorbent, c_e (expressed in mg·L^{-1}) is the unadsorbed adsorbate concentration in solution at equilibrium, q_m is the maximum amount of the adsorbate to form a complete monolayer bound on the surface and K_L is a constant related to the affinity of the binding sites (expressed in L·mg^{-1}).

The Freundlich isotherm fits most experimental adsorption–desorption isotherm curves robustly. The Freundlich model is often used to describe sorption onto heterogeneous surfaces, including liquid-solid phase:

$$q_e = K_F \cdot c_e^{1/n} \qquad (3)$$

where K_F and n are the Freundlich constants related to the indicator of adsorption capacity and adsorption intensity, respectively; and c is the equilibrium concentration of the adsorbed ions.

The Sips equation is a combination of the Langmuir and Freundlich adsorption models. It uses the heterogenous adsorption system and for prediction and describes the isotherm model of continuing increase in the adsorbed amount with the increase in concentration:

$$q_e = q_{ms} \frac{K_s \cdot c_e^m}{1 + K_s \cdot c_e^m} \qquad (4)$$

where q_{ms} and K_S are the Sips maximum adsorption capacity (mg·g^{-1}) and Sips equilibrium constant (L·mg^{-1}), respectively, and m is the Sips model exponent.

RESULTS AND DISCUSSION

Sorbent characterization

Experiments were carried out on six samples, two different montmorillonite clays, their modified forms, Moroccan clay (Ghassoul), and its modified form. The total content of Fe and FeO before and after the magnetic modification is shown in Table 1. The magnetic form of montmorillonite clays M1 and M2, were modified using the same method, but the resulting total content of iron and the content of FeO were different. As described in a previous paper [44], magnetic iron oxides cover the surface. The presented results proved that magnetic iron oxides have a different interaction with the different clay surfaces as well.

Table 2. Content of total iron and FeO in the sample

Analyt	unit	**M1**	**MM1**	**M2**	**MM2**	**G**	**MG**
Fe(tot)	(wt. %)	1.79	4.35	2.41	8.47	0.44	5.75
FeO	(wt. %)	2.00	2.80	0.24	1.46	0.12	1.50

Experimental data were fitted by the Freundlich, Langmuir, and Sips adsorption isotherm, the results summarized in Table 2 and Figs 1–3.

---

* Corresponding Author´s Email: jana.seidlerova@vsb.cz

Table 3.

Adsorption isotherm	Parameter	**M1**	**MM1**	**M2**	**MM2**	**G**	**MG**
Freundlich	K_F (mg.g^{-1})	1.898	1.924	3.384	4.849	2.104	1.770
	n	2.108	2.078	5.183	7.324	3.260	3.576
	R^2	0.966	0.986	0.873	0.732	0.749	0.593
Langmuir	q_m (mg.g^{-1})	93.2	97.7	11.0	11.5	15.3	9.11
	K_L (L.mg^{-1})	0.002	0.002	0.135	0.202	0.002	0.045
	R^2	0.885	0.923	0.864	0.969	0.921	0.815
Sips	q_{ms} (mg.g^{-1})	124	206	15.2	11.6	13.2	8.22
	K_S (L.mg^{-1})	0.016	0.011	0.196	0.222	0.002	0.001
	m	0.528	0.509	0.436	0.942	1.75	2.28
	R^2	0.918	0.966	0.908	0.969	0.954	0.895

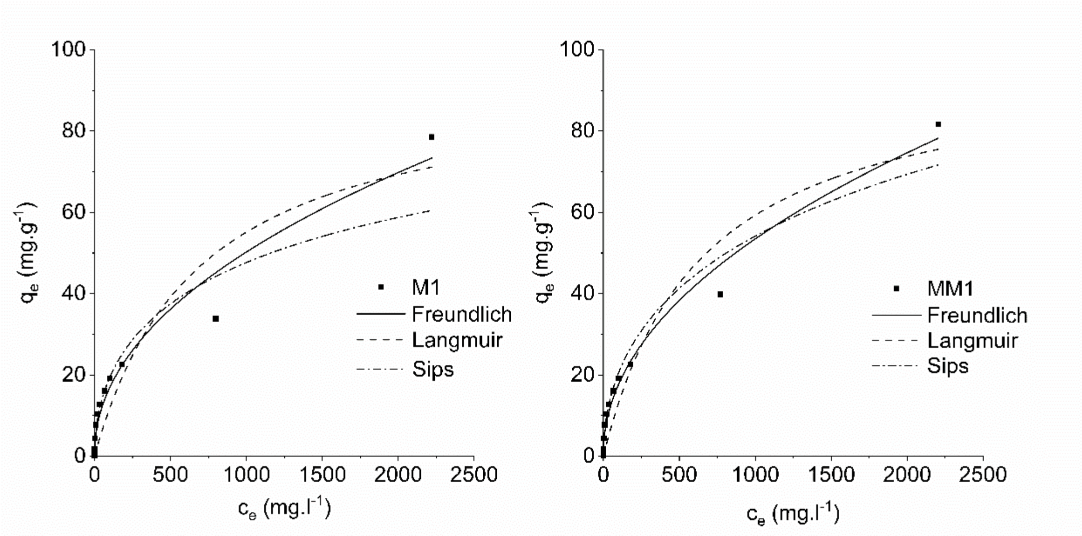

Figure 1. The three adsorption isotherms and the experimental data of Sr^{2+} ions adsorption on (a) M1 and (b) MM1.

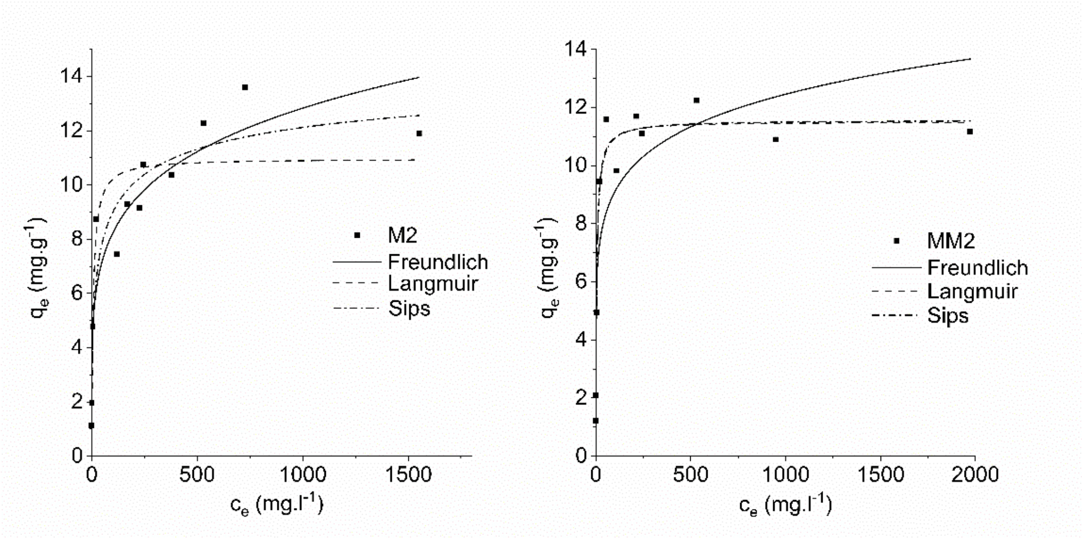

---

* Corresponding Author´s Email: jana.seidlerova@vsb.cz

Figure 2. The three adsorption isotherms and the experimental data of Sr^{2+} ions adsorption on (a) M2 and (b) MM2.

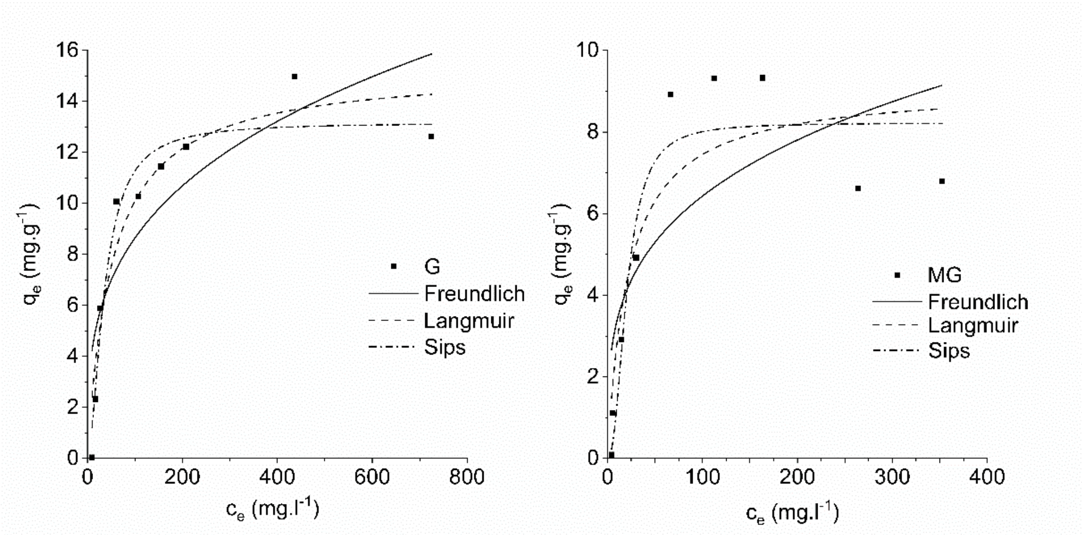

Figure 3. The three adsorption isotherms and the experimental data of Sr^{2+} ions adsorption on (a) G and (b) MG.

The coefficient determination of the isotherms differs, but the Freundlich isotherm was the best fit for M1 and MM1. On the other hand, the Sips isotherm can be considered a satisfactory model for the description of the adsorption on all the studied materials. Maximum adsorption capacity calculated using the Langmuir isotherms is similar to the maximum adsorption amount calculated by Sips isotherm only for M2, MM2, G and MG. The best adsorbent of Sr^{2+} ions is montmorillonite M1.

Adsorption capacity of M1, which was before the adsorption experiments modified by water leaching to remove glucose, saccharine, and vanilla [46], was lower - 7.9 mg.g^{-1}. The aforementioned preliminary study fitted the adsorption data by the Freundlich isotherm while the adsorption experiments were performed with initial Sr^{2+} ions concentration in the 0–300 mg.L^{-1} range only. These results support the theory that the adsorption is an ion-exchange process according to the following chemical equilibrium:

$$Na_2X + Sr^{2+} \leftrightarrow SrX + 2Na^{+}$$

where X is the adsorption site. Na^+ ions can be replaced with other exchangeable ions. If the M1 sample was in contact with water prior to the adsorption experiments, ion-exchange cations were flushed out. Subsequent adsorption is, then, likely to take place on the sample surface only.

The described adsorption capacities of Sr^{2+} ions on M1 does not support the results published so far. Khan and et al. described the adsorption of strontium by Langmuir isotherm, and their calculated sorption capacity is 28.7 mg of Sr per gram of bentonite (which consists of montmorillonite) [27].

Magnetic modification M1 increased the adsorption capacity by 66 %. On the other hand, the adsorption capacity of MM2 and MG due to magnetic modification decreased by 23.7 % and by 37.5 % respectively. It was caused by two reasons (a) removed ion-exchange ions during preparation magnetically modification and (b) the presence of magnetic iron particles on the clay surface.

The recently published article on adsorption properties of Morrocan natural clay (G) described the adsorption capacity of two divalent ions. The maximum adsorption capacity calculated by the Langmuir isotherm of Cu^{2+}, Co^{2+}, Ni^{2+}, and Pb^{2+} ions is 6.25, 5.92, 7.01, and 6.83 mg.g$^{-1,}$ respectively. In this study, the adsorption capacity of adsorbed Sr^{2+} ions was found to be higher ($q_m = 15.3$ mg.g^{-1} for G and 9.11 mg.g^{-1} for MG) than in the previous study. The review [37] showed that a Ghassoul composition varies significantly and that the maximum adsorption capacity probably depends on the stevensite content.

Figures 4 and 5 show Sr and Fe distribution on G and MG surfaces, respectively, determined by EMA and Table 4 shows the content of the elements on the surface. After magnetic modification of G, the content of Fe increased to 5.75 wt. % and it is apparent that the surface of MG (Fig. 5b) is covered by Fe more than the surface of G (Fig. 5a). Fig. 4a) shows that the Sr^{2+} ions covered the G surface more than the MG surface (Fig. 4b), which corresponds with q_{max} values derived from Langmuir and Sips adsorption isotherms (Tab. 3). It is evident from the figures that the Sr^{2+} ions do not adsorb on the surface occupied by ion oxides. Some authors described iron oxides as excellent adsorbents [47-48]. The assumption that the presence of iron oxides could increase the adoption capacity of the clays was, thus, confirmed on one sample only. The explanation will be the subject of further study.

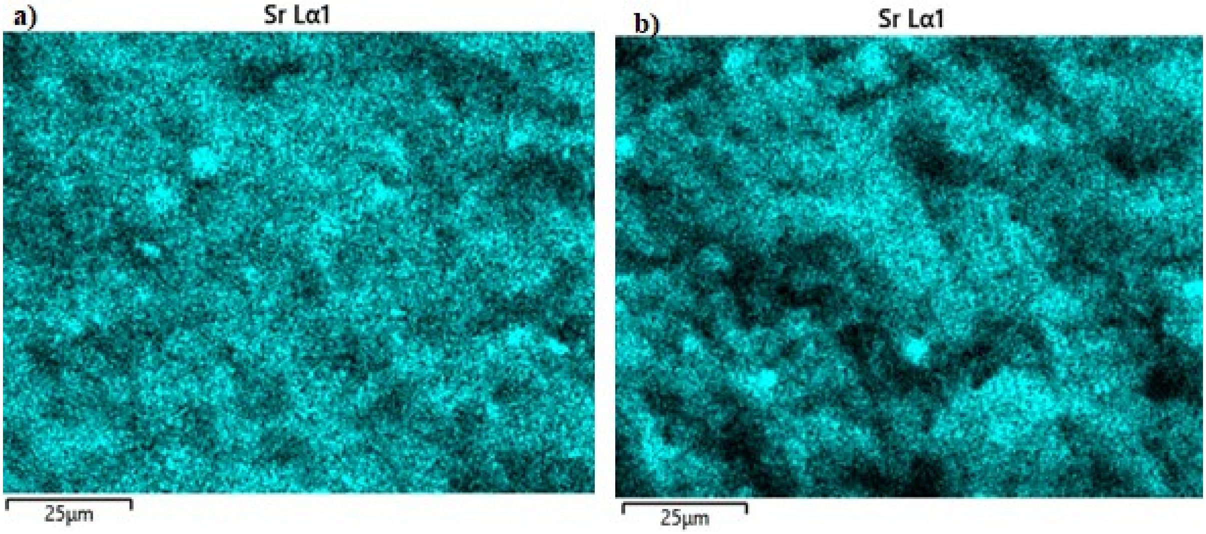

Figure 4. STEM mapping of Sr presence on the surface of (a) G and (b) MG sample.

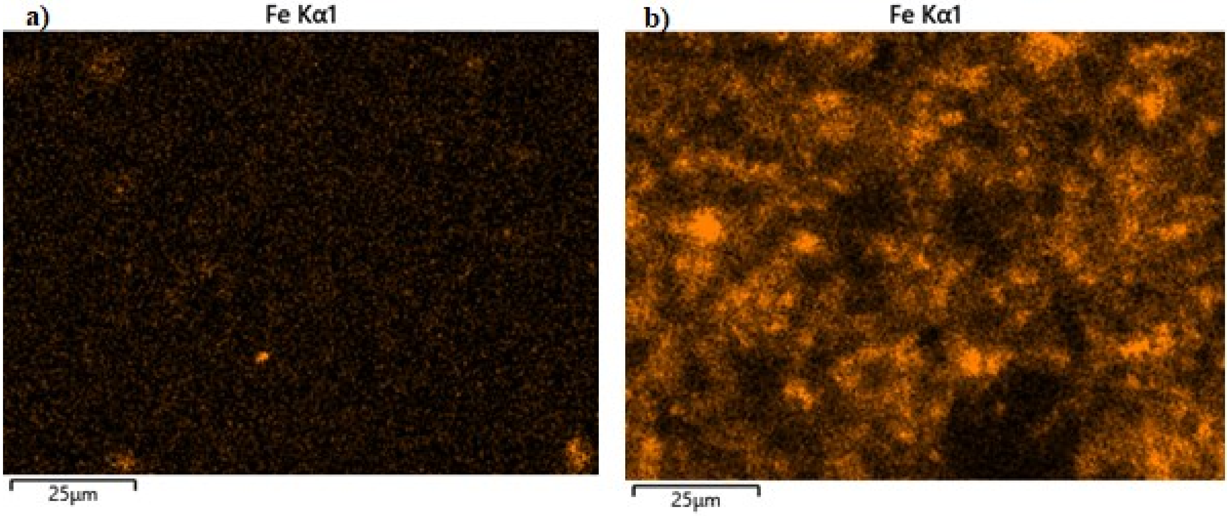

Figure 5. STEM mapping of iron presence on the surface of (a) G and (b) MG sample.

Table 4. Content of Fe and Sr on the surface G and MG samples determined by EDS.

Analyt	unit	G	MG
Fe	(wt. %)	1.12	26.0
Sr	(wt. %)	4.15	7.36

CONCLUSION

This study describes the adsorption of Sr^{2+} ions on two different montmorillonite clays and Ghassoul, and the preparation of their magnetically modified forms. The experimental data were fitted

---

* Corresponding Author´s Email: jana.seidlerova@vsb.cz

using the Langmuir, Freundlich, and Sips adsorption isotherms, and the amount of strontium ions adsorbed per unit weight of adsorbent was determined. The Sips adsorption isotherm fitted the experimental data of Sr^{2+} ions adsorption on all the used clay materials the best. The maximum adsorption capacity of the magnetically modified materials was lower than in the native minerals, but the difference was not significant. Even though the content of iron oxides could not increase the adsorption capacity of the clays, the present study showed that montmorillonite and Ghassoul and their magnetically modified forms can be used as a natural adsorbent for the removal of Sr^{2+} ions from aqueous solutions.

ACKNOWLEDGMENTS

This work was kindly supported by The Ministry of Education, Youth and Sports of the Czech Republic in the following projects Study and Development of Composite Nanomaterials and Nanofillers No. SP 2021/106 and project ERDF/ESF New Composite Materials for Environmental Applications (No. CZ.02.1.01/0.0/0.0/17_048/0007399). Authors thank to Dr. O. Motyka for language correction.

REFERENCES

[1] Galindo–Miranda, J.M., Guízar–González, C., Becerril–Bravo, E. J., Moeller–Chávez, G., León–Becerril, E., Vallejo–Rodríguez, R. 2019. Occurrence of emerging contaminants in environmental surface waters and their analytical methodology – a review. *Water Supply*, 19:1871–1884.

[2] Liu, L., Zhang, C., Jiang, W., Li, X., Dai, Y., Jia, H. 2021. Understanding the sorption behaviors of heavy metal ions in the interlayer and nanopore of montmorillonite: A molecular dynamics study. *Journal of Hazardous Materials*, 416:125976- 125987.

[3] Fedenko, Yu. 2021.Rgularities Of Sorption Cu (II) Ions By Natural And Activated Bentonite Clays. *Norwegian Journal of development of the International Science*, 6:28–30.

[4] Tokarčíková, M., Seidlerová, J., Motyka, O., Životský, O., Drobíková, K., Mamulová Kutláková, K. 2020. Easy and low-cost preparation method of magnetic montmorillonite/FexOy composite: initial study for future applications. *Monatshefte fur Chemie*, 151:1–10.

[5] Klika, Z., Seidlerová, J., Valášková, M., Kliková, C., Kolomazník, I. 2016. Uptake of Ce(III) and Ce(IV) on montmorillonite. *Applied Clay Science* 132:41–49.

[6] Tokarčíková, M., Tokarský, J., Mamulová Kutláková, K., Seidlerová, J. 2017. Testing the stability of magnetic iron oxides/kaolinite nanocomposite under various pH conditions. *Journal of Solid State Chemistry,* 253:329–335.

[7] Tokarčíková, M., Seidlerová, J., Motyka, O., Životský, O., Drobíková, K., Gabor, R. 2021. Experimental verification of regenerable magnetically modified montmorillonite and its application for heavy metals removal from metallurgical waste leachates. *Journal of Water Process Engineering*, 39:101691-101701.

[8] Kaçan, E. and Kütahyalı, C. 2012. Adsorption of strontium from aqueous solution using activated carbon produced from textile sewage sludges. *Journal of Analytical and Applied Pyrolysis*, 97:149–157.

[9] Chegrouche, S., Mellah, A., Barkat, M. 2009. Removal of strontium from aqueous solutions by adsorption onto activated carbon: kinetic and thermodynamic studies. *Desalination*, 235:306–318.

[10] Mironyuk, I., Tatarchuk, T., Naushad, M., Vasylyeva, H., Mykytyn, I. 2019. Highly efficient adsorption of strontium ions by carbonated mesoporous TiO2. *Journal of Molecular Liquids,* 285:742–753.

[11] Kaveeshwar, A., Kumar, P., Revellame, E., Gang, D., Zappi, M., Subramaniam, R., 2018. Adsorption properties and mechanism of barium (II) and strontium (II) removal from fracking wastewater using pecan shell based activated carbon. *Journal of Cleaner Production* 193:1–13.

[12] Jang, J., Miran, W., Divine, S., Nawaz, M., Shahzad, A., Woo, S., Lee, D. 2018. Rice straw-based biochar beads for the removal of radioactive strontium from aqueous solution. *Science of The Total Environment,* 615:698–707.

[13] Shin, J., Lee, Y., Kwak, J., Kim, S., Lee, S., Park, Y., Lee, S., Chon, K. 2021. Adsorption of radioactive strontium by pristine and magnetic biochars derived from spent coffee grounds. *Journal of Environmental Chemical Engineering,* 9:105119-105129.

[14] Ahmadpour, A., Zabihi, M., Tahmasbi, M., Bastami, T. 2010. Effect of adsorbents and chemical treatments on the removal of strontium from aqueous solutions. *Journal of Hazardous Materials,* 182(1–3):552–556.c

---

* Corresponding Author´s Email: jana.seidlerova@vsb.cz

[15] Choi, J., Cho, S., Choi, S. 2021. Ecofriendly, selective removal of radioactive strontium ions in aqueous solutions using magnetic banana peels. *Science of The Total Environment,* 778:146327-146336.

[16] Mironyuk, I., Tatarchuk, T., Naushad, M., Vasylyeva, H., Mykytyn, I. 2019. Highly efficient adsorption of strontium ions by carbonated mesoporous TiO2. *Journal of Molecular Liquids,* 285:742–753.

[17] Nur, T., Loganathan, P., Kandasamy, J., Vigneswaran, S. 2017. Removal of strontium from aqueous solutions and synthetic seawater using resorcinol formaldehyde polycondensate resin. *Desalination,* 420:283–291.

[18] Asgari, P., Mousavi, S., Aghayan, H., Ghasemi, H., Yousefi, T. 2019. Nd-BTC metal-organic framework (MOF); synthesis, characterization and investigation on its adsorption behavior toward cesium and strontium ions. *Microchemical Journal,* 150:104188-104196.

[19] Zhao, X., Meng, Q., Chen, G., Wu, Z., Sun, G., Yu, G., Sheng, L., Weng, H., Lin, M. 2018. An acid-resistant magnetic Nb-substituted crystalline silicotitanate for selective separation of strontium and/or cesium ions from aqueous solution. *Chemical Engineering Journal*, 352:133–142.

[20] Merceille, A., Weinzaepfel, E., Barré, Y., Grandjean, A. 2012. The sorption behaviour of synthetic sodium nonatitanate and zeolite A for removing radioactive strontium from aqueous wastes. *Separation and Purification Technology,* 96:81–88.

[21] Liang, J., Li, J., Li, X., Liu, K., Wu, L., Shan, G. 2020. The sorption behavior of CHA-type zeolite for removing radioactive strontium from aqueous solutions. *Separation and Purification Technology,* 230:115874.

[22] Abdel Moamen, O., Ismail, I., Abdelmonem, N., Abdel Rahman, R. 2015. Factorial design analysis for optimizing the removal of cesium and strontium ions on synthetic nano-sized zeolite. *Journal of the Taiwan Institute of Chemical Engineers,* 55:133–144.

[23] Nishiyama, Y., Hanafusa, T., Yamashita, J., Yamamoto, Y., Ono, T. 2016. Adsorption and removal of strontium in aqueous solution by synthetic hydroxyapatite. *Journal of Radioanalytical and Nuclear Chemistry,* 307:1279–1285.

[24] Xia, X., Shen, J., Cao, F., Wang, C., Tang, M., Zhang, Q., Wei, S. 2019. A facile synthesis of hydroxyapatite for effective removal strontium ion. *Journal of Hazardous Materials,* 368:326–335.

[25] Ghaemi, A., Torab–Mostaedi, M., Ghannadi–Maragheh, M. 2011. Characterizations of Strontium(II) and Barium(II) Adsorption from Aqueous Solutions Using Dolomite Powder. *Journal of Hazardous Materials,* 190(1–3):916–921.

[26] Ning, Z., Ishiguro, M., Koopal, L., Sato, T., Kashiwagi, J. 2018. Comparison of strontium retardation for kaolinite, illite, vermiculite and allophane. *Journal of Radioanalytical and Nuclear Chemistry*, 317(1):409–419.

[27] Khan, S., Riaz–ur–Rehman, Khan, M. 1995. Sorption of strontium on bentonite. *Waste Management*, 15(8):641–650.

[28] Baldermann, A., Grießbacher, A., Baldermann, C., Purgstaller, B., Letofsky–Papst, I., Kaufhold, S., Dietzel, M. 2018. Removal of Barium, Cobalt, Strontium, and Zinc from Solution by Natural and Synthetic Allophane Adsorbents. *Geosciences*. 8(9):309-331.

[29] Galamboš, M., Krajňák, A., Rosskopfová, O., Viglašová, E., Adamcová, R., Rajec, P. 2013. Adsorption equilibrium and kinetic studies of strontium on Mg-bentonite, Fe-bentonite and illite/smectite. *Journal of Radioanalytical and Nuclear Chemistry,* 298(2):1031–1040.

[30] Bilgin, B., Atun, G., Keceli, G. 2001. Adsorption of Strontium on Illite. *Journal of Radioanalytical and Nuclear Chemistry*, 250:323-328.

[31] Başçetin, E. and Atun, G. 2006. Adsorption behavior of strontium on binary mineral mixtures of Montmorillonite and Kaolinite. *Applied Radiation and Isotopes*, 64(8):957–964.

[32] Missana, T., Garcia–Gutierrez, M., Alonso, U. 2008. Sorption of strontium onto illite/smectite mixed clays. *Physics and Chemistry of the Earth, Parts A/B/C*, 33:S156–S162.

[33] Gu, S., Kang, X., Wang, L., Lichtfouse, E., Wang, C. 2019. Clay mineral adsorbents for heavy metal removal from wastewater: a review. *Environmental Chemistry Letters,* 17(2):629–654.

[34] Ma, B., Oh, S., Shin, W., Choi, S. 2011. Removal of Co2+, Sr2+ and Cs+ from aqueous solution by phosphate-modified montmorillonite (PMM). *Desalination,* 276(1–3):336–346.

[35] Jlassi, K., Eid, K., Sliem, M., Abdullah, A., Chehimi, M. 2021. Data on the fabrication of hybrid calix [4]arene-modified natural bentonite clay for efficient selective removal of toxic metals from wastewater at room temperature. *Data in Brief* 35:106799-106806.

[36] Wu, P., Dai, Y., Long, H., Zhu, N., Li, P., Wu, J., Dang, Z. 2012. Characterization of organo-montmorillonites and comparison for Sr(II) removal: Equilibrium and kinetic studies. *Chemical Engineering Journal,* 191:288–296.

[37] Tokarský, J. 2018. Ghassoul - Moroccan clay with excellent adsorption properties. *Materials Today: Proceedings,* 5(1):S78–S87.

---

* Corresponding Author´s Email: jana.seidlerova@vsb.cz

[38] Weiss, Z., and Kužvart, M. 2005. Jílové minerály: jejich nanostruktura a využití, Prag: Karolinum (In Czech).

[39] Valášková M. 2014. Vybrané vrstevnaté silikáty a jejich modifikované nanomateriály, Brno: Akademické nakladatelství CERM (In Czech).

[40] Seidlerová, J., Drobíková, K., Životský, O., Mamulová Kutláková, K., Tomášek, V. Magnetic modification of Ghassoul, in Materials Today: Proceedings: Nano Ostrava_2017, 2018, 5(1):S45–S54.

[41] Safarik, I., and Safarikova, M. 2010. Magnetic fluid modified peanut husks as an adsorbent for organic dyes removal. *Physics Procedia,* 9:274–278.

[42] Safarik, I., Horska, K., Pospiskova, K., Safarikova, M. 2012. One-step preparation of magnetically responsive materials from non-magnetic powders. *Powder Technology*, 229:285–289.

[43] Safarik, I., Horska, K., Pospiskova, K., Maderova, Z., Safarikova, M., 2012. Microwave assisted synthesis of magnetically responsive composite materials. *IEEE Transactions on Magnetics*, 49(1):213–218.

[44] Jiraskova, Y., Bursik, J., Seidlerova, J., Kutlakova, K., Safarik, I., Safarikova, M., Pospiskova, K., Zivotsky, O. 2018. Microstructural Analysis and Magnetic Characterization of Native and Magnetically Modified Montmorillonite and Vermiculite. *Journal of Nanomaterials*, 2018:1–14.

[45] ČSN 722041, part 11, Chemical alayses of slag, FeO determination.

[46] Kotlařová, I., and Seidlerová, J. 2016. Studies of Strontium Ions Sorption from Aqueous Solution. *Advanced Science Letters,* 22(3):711–713.

[47] Hua, M., Zhang, S., Pan, B., Zhang, W., Lv., L., Zhang, Q. 2012. Heavy metal removal from water/wastewater by nanosized metal oxides: a review. *Journal of Hazardous Materials*, 211-212:317–331.

[48] Dave P., and Chopda, L. 2014. Application of Iron Oxide Nanomaterials for the Removal of Heavy Metals. *Journal of Nanotechnology*, 2014:1–4.

---

* Corresponding Author´s Email: jana.seidlerova@vsb.cz

The role of guanidine in graphitic carbon nitride synthesis

A. Smýkalová[1,2], K. Foniok[1], K. Górecki[2], D. Cvejn[3], P. Praus*[1,2]
[1]Department of Chemistry, VŠB-TUO, Czech Republic;
[2]CEET, Institute of Environmental Technology, VSB-TUO, Czech Republic;
[3]CEET, Nanotechnology Centre, VSB-TUO, Czech Republic.

ABSTRACT

Graphitic carbon nitrides from mixtures of guanidine hydrochloride and melamine or guanidine hydrochloride and dicyandiamide with different weight ratios were synthetized. Obtained materials were characterized using UV/Vis diffuse reflectance spectroscopy, X-ray powder diffraction and Fourier transform infrared spectroscopy. The specific surface area and elemental com-position (C, H, N) were also measured. Photocatalytic activity of prepared materials was tested on Rhodamine B, Phenol and Amoxicillin. The photocatalytic experiments on all three pollutants showed a maximal activity for one sample with a specific ratio of precursors from each series. The specific surface area measurement of both sample series also showed the maximum correlating to the photocatalytic activity of samples. In order to understand the increase and decrease of photodegradation activity and specific surface area of materials more measurements and characterizations had to be carried out, for example, thermogravimetric analysis.

Keywords: graphitic carbon nitride; guanidine hydrochloride; amoxicillin; phenol; photocatalytic degradation

INTRODUCTION

A photocatalyst is a substance, a semiconductor, that is able to accelerate the reaction without being depleted and is activated by the adsorption of photons [1]. One of the semiconductors is graphitic carbon nitride which can be used as low-cost, green and highly efficient photocatalyst for photocatalytic degradation of organic pollutants in water [2]. Graphitic carbon nitride (g-C_3N_4) can be synthetized by simple heating of a precursors like melamine, dicyandiamide, thiourea and urea at temperatures around 550 °C. One of the precursors is also guanidine hydrochloride which should be able to alternate structure of a final g-C_3N_4 [3].

In a present paper, graphitic carbon nitrides from mixtures of guanidine hydrochloride and melamine or guanidine hydrochloride and dicyandiamide with different weight ratios were synthetized. XRD, and FT-IR were employed to characterize the morphology and structure of the synthesized g-C_3N_4 samples. Photocatalytic activity was tested on Phenol, Rhodamin B and Amoxicillin. To understand sample synthesis, TGA/DSC measurement was performed.

EXPERIMENTAL STUDY

Photocatalytic materials were synthetized by the facile method of direct heating melamine (M) and dicyandiamide (D) and their mixtures with guanidine hydrochloride (G) at 550 °C for 4h with heating rate of 3 °C min^{-1}. Typically, mixture (5g) of guanidine hydrochloride and melamine or guanidine hydrochloride and dicyandiamide with different weight ratios were placed in a ceramic crucible with a lid in a muffle furnace. Crucible was then cooled down to an ambient temperature out of furnace and ground in laboratory mill to a fine powder. All synthetized materials were compared to a bulk from

---

* Corresponding Author´s Email: petr.praus@vsb.cz

melamine, bulk from dicyandiamide and bulk from guanidine hydrochloride prepared by following the same steps as samples mentioned above.

Obtained materials were characterized using UV/Vis diffuse reflectance spectroscopy (DRS), X-ray powder diffraction (XRD), Fourier transform infrared spectroscopy (FTIR) and Scanning electron microscopy (SEM). The specific surface area (SSA) and elemental composition (C, H, N) were also measured. Thermogravimetric analysis with differential scanning calorimetry (TGA/DSC) was used for study of synthetized materials. Photocatalytic activity of prepared materials was tested on Rhodamine B, Phenol and Amoxicillin.

RESULTS AND DISCUSSION

After the synthesis (Fig. 1) and grounding, there were no significant visible differences between samples. Samples from mixtures of guanidine hydrochloride and melamine were labelled as GM 0,5 (0,5:1; G:M), GM 1 (1:1; G:M), GM 2 (2:1; G:M), GM 3 (3:1; G:M) and GM 4 (4:1; G:M). Samples from mixtures of guanidine hydrochloride and dicyandiamide were labelled the same way except from M letter was replaced with D letter which stands for dicyandiamide. Synthetized samples used for comparison were labelled as bulk M (bulk prepared from melamine), bulk D (bulk prepared from dicyandiamide) and bulk G (bulk prepared from guanidine hydrochloride).

Figure 1. Bulk from melamine (left); bulk from dicyandiamide (middle); bulk from guanidine hydrochloride (right).

The UV/Vis diffuse reflectance spectroscopy measurements were carried out to observe light absorption properties and mainly to determine the optical band gap energies of the synthetized materials. Band gap energies listed in Table 1. are moving in a range from 2.66 eV up to 2.73 eV and there is no chronological order of the values.

Table 1. Synthetized samples, their bang gap energies, specific surface areas, weight and molar ratio.

Sample	E_g (*eV*)	SSA (*m^2/g*)	Weight ratio (G:X) [1]	Molar ratio (G:X) [1]
G bulk	2.66	23	-	-
M bulk	2.69	12	-	-
D bulk	2.66	8	-	-
GM 0,5	2.69	25	0.5	0.2
GM 1	2.73	29	1	0.5
GM 2	2.71	54	2	0.9
GM 3	2.68	23	3	1.4
GM 4	2.70	23	4	1.9
GD 0,5	2.70	20	0.5	0.4
GD 1	2.71	34	1	0.7
GD 2	2.68	35	2	1.4
GD 3	2.71	23	3	2.1
GD 4	2.68	25	4	2.8

[1] X stands for melamine (M) for GM series and dicyandiamide (D) for GD series.

---

* Corresponding Author´s Email: petr.praus@vsb.cz

The specific surface area of synthetized samples was measured by the physisorption of nitrogen and was evaluated using the BET method. Bulk prepared from guanidine hydrochloride has the largest specific surface area of all bulks prepared only from one compound. Sample synthetized from the mixture of two parts of guanidine and one part of melamine (GM 2) had the highest values of specific surface area for GM series and GD 2 for GD series.

XRD patterns of synthetized samples were very similar to bulks synthetized from single compounds (Fig. 2.). A typical graphitic carbon structure was detected with the main diffractions at 31,9° and 14,8°.

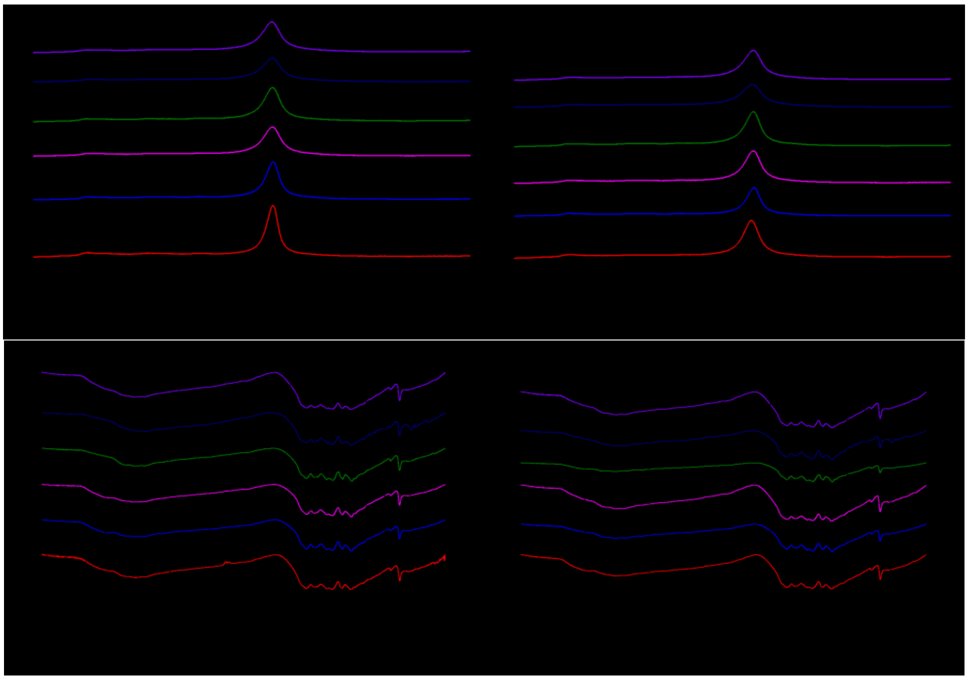

Figure 2. XRD patterns and FTIR spectra of bulks from various precursors.

The structure of prepared materials was studied by FTIR spectrometry as displayed in Fig. 3. Two regions A and B which are typical for graphitic carbon nitride were observed. The bands in the region A are related with the stretching vibrations of N-H bonds and bands in the region B are related with the stretching vibrations of C=N and C-N bonds of heterocyclic rings. Breathing mode of triazine units is visible around 810 cm^{-1}. The bands around 3500 cm^{-1} are related to the stretching vibrations of -OH groups. The FTIR spectra of all synthetized materials were similar and typical for graphitic carbon nitride.

Photocatalytic degradation of Rhodamine B, Phenol and Amoxicillin was performed. The experiments on photodegradation of Phenol (Fig. 3.) showed gradual increase and then decrease of photocatalytic activity with maximum for samples GM 2 and GD 2. The degradation experiments on Amoxicillin and Rhodamine B also confirmed that GM 2 and GD 2 are samples with the highest photocatalytic activity for both series. Results on photocatalytic degradation of Amoxicillin and Rhodamine B will be published in upcoming article.

---

* Corresponding Author´s Email: petr.praus@vsb.cz

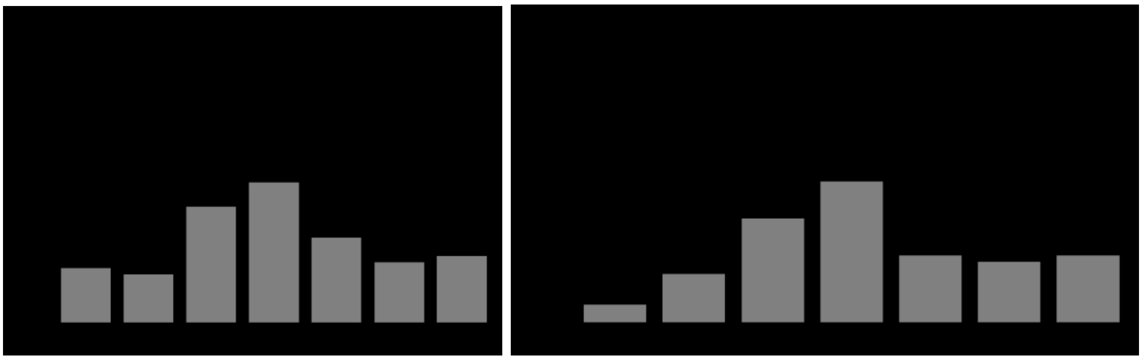

Figure 3. Photocatalytic experiments on Phenol.

TGA/DSC measurement was performed for all samples. In Firuge 4 are visible TGA and DSC curves for chosen samples. In 1. step, melamine and melamine derivates are presented. In 2. step, melem and melem derivates are formed. In 3. step g-C_3N_4 is being formed and in last 4. step the formation of g-C_3N_4 structures is finished.

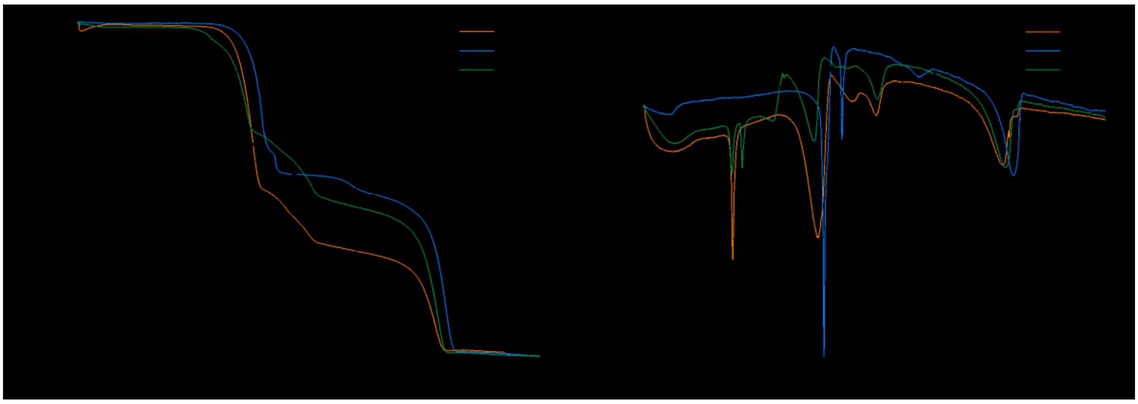

Figure 4. TGA and DCS curves of guanidine hydrochloride (G), melamine (M) and mixture of guanidine hydrochloride and melamine in weight ration 2:1 (GM2).

CONCLUSION

Three bulks for comparison and two series of 5 samples each were synthetized. All samples were synthetized under the same conditions and yet photocatalytic degradation of samples GM 2 and GD 2 was more efficient than of others. The specific surface area of these two samples was also the highest from the series. TGA/DSC showed that synthesis of g-C3N4 from GM and GD led through intermediate products (visible in 1. step in DSC graph for GM 2) that caused imperfections in structure that led to higher specific surface area and photocatalytic activity. The highest ratio of structural imperfections was obtained for samples GM 2 and GD 2.

ACKNOWLEDGMENTS

This work was supported by the Czech Science Foundation (project No. 19-15199S), EU structural funding in Operational Program Research, Development and Education (project No. CZ.02.1.01/0.0/0.0/16_019/0000853 „IET-ER") and by VŠB-TU Ostrava (Project No. SP 2021/46). The authors also thank the Large Research Infrastructure ENREGAT (project No. LM2018098).

---

* Corresponding Author´s Email: petr.praus@vsb.cz

Chapter 26

Part 4: Nanotechnology for Environmental Solution

REFERENCES

[1] Fox, M., 1988. Photocatalytic Oxidation of Organic Substances. In: *Photocatalysis and Environment: Trends and Applications*, edited by Schiavello, M. 445–467. New York: Kluwer Academic Publishers.

[2] Umar, M., and Abdul, H. 2013. Photocatalytic Degradation of Organic Pollutants in Water. In *Organic Pollutants - Monitoring, Risk and Treatment*, edited by Nageeb Rashed M., 195-208. Croatia: InTech. doi:10.5772/53699.

[3] Long, B., Lin, J., Wang, X. 2014. Thermally-induced desulfurization and conversion of guanidine thiocyanate into graphitic carbon nitride catalysts for hydrogen photosynthesis. *Journal of Materials Chemistry* A, 2:2942-2951. doi:10.1039/c3ta14339b.

---

* Corresponding Author´s Email: petr.praus@vsb.cz

Acknowledgement

This e-monography was supported by project: Technika pro budoucnost No. CZ02.2.69/0.0/0.0/16_015/0002338.

Autor:

kolektiv autorů: M. Čičkan, Q. Fang, A. Muhsan, L. Pazourková, S. Tamayo-Vegas, J. Zágora, K. Čech Barabaszová, S. Khammassi, I. Kopal, T. Luxbacher, G. Plohl, L. Bardoňová, L.V. Batyuk, S. Gerber-Lemaire, J. Jampílek, M. Pisarčík, N.A. Salavatov, A. Sobczak-Kupiec, K. Škrlová, J. Trzcińska-Wencel, M. Wypij, S. Kurtinová, C.V. Lazaratou, G. Piszter, J. Seidlerová, A. Smýkalová

Katedra, institut:

Centrum Nanotechnologií (9360), CEET, VŠB-TU Ostrava

Název:

Nanomaterials and Nanotechnology in 2021

Místo, rok, vydání:

Ostrava, 2021, 1. vydání

Počet stran:

143

Vydala:

Vysoká škola báňská-Technická univerzita Ostrava

Neprodejné

ISBN 978-80-248-4585-2